



# COOL2017 Bonn, Germany

**Proceedings of the 11th International Workshop on Beam Cooling and Related Topics**

## International Advisory Committee

Ilan Ben-Zvi	BNL
Yaroslav Derbenev	JLab
Jürgen Dietrich	Uni Dortmund
Daniel Kaplan	Illinois Institute of Technology
Takeshi Katayama	Nihon University
Yonehara Katsuya	FNAL
Igor Meshkov	JINR
Sergei Nagaitsev	FNAL
Akira Noda	
Vasily Parkhomchuk	BINP
Dieter Prasuhn	FZ Jülich
Markus Steck	GSI
Gerard Tranquille	CERN
Grigory Trubnikov	JINR
M. Wakasugi	RIKEN
Andreas Wolf	MPI Heidelberg
Xiaodong Yang	IMP Lanzhou
Yuhong Zhang	JLab

## Local Organizing Committee

Arthur Halama	FZ Jülich
Vesvolod Kamedzhiev	FZ Jülich
Dieter Prasuhn	FZ Jülich
Hannah Simonsen	FZ Jülich
Rolf Stassen	FZ Jülich
Hans Stockhorst	FZ Jülich
Raimund Tölle	FZ Jülich

## Editorial Team

Volker RW Schaa	GSI
Michaela Marx	DESY
Manuel Tilmont	SOLEIL

## Contents

<b>Preface</b>	<b>i</b>
Committees . . . . .	ii
Contents . . . . .	iii
<b>Papers</b>	<b>1</b>
MOA12 – The Muon Ionization Cooling Experiment . . . . .	1
MOA13 – Measurement of Phase Space Density Evolution in MICE . . . . .	6
MOA21 – Emittance Evolution in MICE . . . . .	11
MOA22 – Recent Results from MICE on Multiple Coulomb Scattering and Energy Loss . . . . .	16
TUM11 – Low Energy Electron Cooler for the NICA Booster . . . . .	22
TUM21 – High Voltage Cooler NICA Status and Ideas . . . . .	25
TUM22 – Model Development for the Automated Setup of the 2 MeV Electron Cooler Transport Channel . . . . .	28
TUP04 – Muon Intensity Increase by Wedge Absorbers for low-E Muon Experiments . . . . .	32
TUP06 – Stochastic Cooling as Wiener Process . . . . .	37
TUP08 – Preliminary Design of Electron Target for SRing at HIAF . . . . .	40
TUP09 – Project of High-Voltage System with Fast Changing Potential for DR Experiment . . . . .	44
TUP11 – The Interaction Between Electrons and Ions in Comoving and Static Electron Columns . . . . .	47
TUP12 – Simulation of Low Energy Ion Beam Cooling With Pulsed Electron Beam on CSRm . . . . .	50
TUP13 – Calculations of the Gun and Collector for Electron Cooling Systems of HIAF . . . . .	54
TUP14 – Investigation on the Suppression of Intrabeam Scattering in the High Intensity Heavy Ion Beam with the help of Longitudinal Multi-bunch Chain of Electron . . . . .	58
TUP15 – Experimental Demonstration of Electron Cooling with Bunched Electron Beam . . . . .	61
TUP16 – Latest News from Stochastic Cooling Developments for the Collector Ring at FAIR . . . . .	64
TUP17 – Design of Stochastic Pick-Ups and Kickers for Low Beta Particle Beams . . . . .	68
WEM12 – Development of a Bunched Beam Electron Cooler Based on ERL and Circulator Ring Technology for the Jefferson Lab Electron-Ion Collider . . . . .	72
WEM22 – Status of Proof-of-Principle Experiment of Coherent Electron Cooling at BNL . . . . .	77
THM13 – Commissioning of the Low Energy Storage Ring Facility CRYRING@ESR . . . . .	81
THM21 – NICA Project: Three Stages and Three Coolers . . . . .	84
THA11 – The HESR Stochastic Cooling System, Design, Construction and Test Experiments in COSY . . . . .	89
<b>Appendices</b>	<b>95</b>
List of Authors . . . . .	95
Institutes List . . . . .	99
Participants List . . . . .	102



# THE MUON IONIZATION COOLING EXPERIMENT\*

M. A. Uchida<sup>†</sup>, Imperial College London, UK  
*for the MICE collaboration*

## Abstract

The Muon Ionization Cooling Experiment (MICE) is designed to demonstrate a measurable reduction in muon beam emittance due to ionization cooling. This demonstration will be an important step in establishing the feasibility of muon accelerators for particle physics. The emittance of a variety of muon beams is measured before and after a "cooling cell", allowing the change in the phase-space distribution due to the presence of an absorber to be measured.

Two solenoid spectrometers are instrumented with high-precision scintillating-fibre tracking detectors (Trackers) before and after the cooling cell which measure the normalized emittance reduction.

Data has been taken since the end of 2015 to study several beams of varying momentum and input emittance as well as three absorber materials in the cooling cell, over a range of optics. The experiment and an overview of the analyses are described here.

## INTRODUCTION

The Muon Ionization Cooling Experiment (MICE) is a collaboration of over 100 scientists from 10 countries and 30 institutes around the world. Based at the Rutherford Appleton Laboratory in the UK it is designed to demonstrate a measurable reduction in emittance in a muon beam due to ionization cooling.

Ionization cooling [1] is the process of reducing the beam emittance (phase space) through energy loss in ionization as particles cross an absorber material, this combined with restoration of the longitudinal momentum of the beam through re-acceleration (using RF cavities) makes sustainable cooling.

Muon colliders and neutrino factories are attractive options for future facilities aimed at achieving the highest lepton-antilepton collision energies and precision measurements of parameters of the Higgs boson and the neutrino mixing matrix. Ionization cooling is the only practical solution to preparing high intensity muon beams for use in these facilities. Muon ionization cooling is necessary for a Muon Collider or neutrino factory [2,3], as the short lifetime of the muon ( $\tau_\mu \sim 2.2 \mu\text{s}$ ) and the large emittance of muon beams (as muons are tertiary particles) means that traditional beam cooling techniques which reduce emittance cannot be used and ionization cooling is the only viable technique to reduce the emittance of the beam within their lifetime.

MICE is currently the only experiment studying ionization cooling of muons.

\* Work supported by the (UK) Science and Technology Facilities Council and the (US) Dept. of Energy and National Science Foundation

<sup>†</sup> m.a.uchida@imperial.ac.uk

## MUON IONIZATION COOLING

Muon cooling can be characterized by the rate of change of the normalized emittance (phase space occupied by the beam). Where the muons lose both longitudinal and transverse momentum through ionization energy loss as they pass through the absorber, a proportion of the lost longitudinal momentum can then be restored using accelerating RF cavities that follow the absorber. Along with this cooling, however, there is a heating effect produced as a result of multiple scattering through the system, therefore, the net cooling is a balance between these two effects. This is described in Eq. (1), where the first term on the right hand side represents the cooling effect and the second term the heating effect:

$$\frac{d\epsilon_n}{ds} \sim -\frac{1}{\beta^2} \left\langle \frac{dE_\mu}{ds} \right\rangle \frac{\epsilon_n}{E_\mu} + \frac{1}{\beta^3} \frac{\beta_\perp (0.014 \text{ GeV})^2}{2E_\mu m_\mu L_R} \quad (1)$$

$\frac{d\epsilon_n}{ds}$  is the rate of change of normalized-emittance within the absorber;  $\beta$ ,  $E_\mu$  and  $m_\mu$  the ratio of the muon velocity to the speed of light, muon energy, and mass respectively;  $\beta_\perp$  is the lattice betatron function at the absorber; and  $L_R$  is the radiation length of the absorber material.

The effect of the heating and cooling terms defines an equilibrium emittance:

$$\epsilon_{n,eq} \propto \frac{\beta_\perp}{\beta X_0} \left\langle \frac{dE_\mu}{ds} \right\rangle \quad (2)$$

below which the beam cannot be cooled. However, as input emittance increases, beam scraping results in increased beam loss and so the two must be balanced.

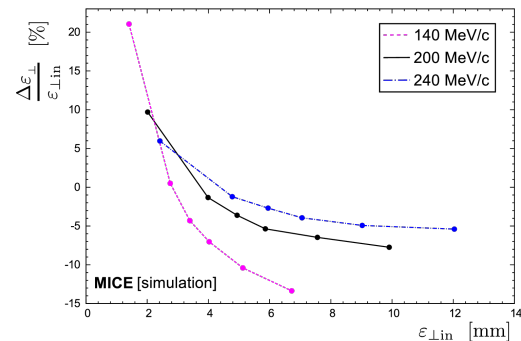


Figure 1: Change in emittance in percent vs. input emittance for a range of MICE beam momenta.

MICE will study this in order to obtain a complete experimental characterization of the cooling process, see Figs. 1 and 2. The cooling equation will be studied in detail for a variety of input beams, magnetic lattices and absorbers to demonstrate the feasibility of this technique. Since a typical

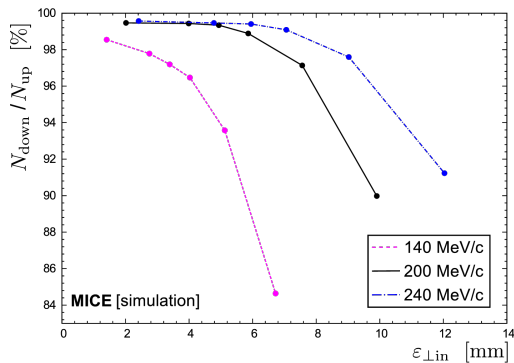


Figure 2: Change in transmission (in percent) vs. input emittance for a range of MICE beam momenta.

cooling channel will employ dozens to hundreds of cooling lattice cells, the precision with which the tails of distributions can be predicted will have important consequences for the performance of the channel.

### MICE

The MICE experiment shown in Fig. 3 passes a muon beam through a low-Z material (absorber), where the muons lose both longitudinal and transverse momentum through ionization energy loss.

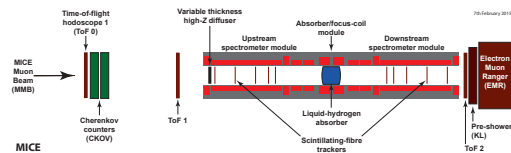


Figure 3: Schematic of the International Muon Ionization Cooling Experiment (MICE), with the beam entering from the left.

The muons produced in the MICE Muon Beam line first pass through the upstream particle identification (PID) detectors, are sampled and tracked upstream and downstream of the absorber by scintillating fibre trackers, before passing through the downstream PID detectors.

MICE is a single-particle experiment, meaning that there is no “beam” as such, instead, particles go down the beam line one by one. At each DAQ cycle, a single particle track is recorded and subsequently tracks are bunched at the analysis level. It is from this sample that the emittance is computed, see Fig. 4

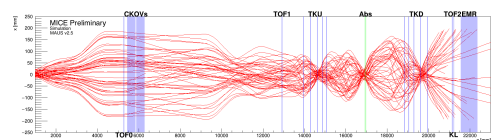


Figure 4: MICE is a single-particle experiment as particles go down the beam line one by one and are bunched at the analysis level.

### The MICE Muon Beam

The MICE Muon beam is produced using the ISIS 800 MeV proton beam [4], which delivers 4 μC of protons in two 100 ns long pulses, with mean current of 200 μA. A titanium target is dipped into the ISIS beam, producing pions (π<sup>+</sup>) which then decay into muons. MICE uses a decay solenoid to enhance the initial pion to muon decay process, dipole magnets for momentum selection and quadrupole magnets for beam focusing (Fig. 5).

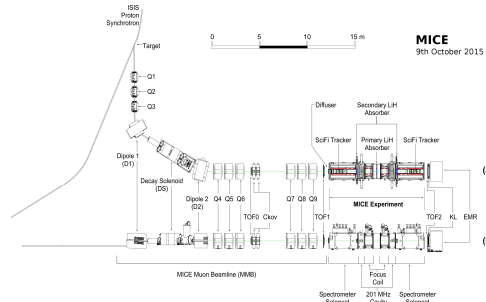


Figure 5: Schematic of the ISIS proton synchrotron and the MICE beam extraction magnets.

The MICE beam can be prepared as a π beam or μ beam with momentum between 140-450 MeV/c. The dip rate is 1 dip/1.28 s giving a maximum particle rate of: μ<sup>+</sup> ~ 120 μ/dip and μ<sup>-</sup> ~ 20 μ/dip. The final muon beam is a 3 ms wide spill, in two 100 ns long bursts every 324 ns.

The MICE muon beamline delivers a high purity beam with less than 1.4% pion contamination [5].

### The MICE Instrumentation

The MICE cooling channel (as shown in Fig. 6 consists of: two spectrometer solenoids which produce a magnetic field up to 4 T. Each has five coils: a central coil which surrounds the Trackers, two end coils on either side of the central coil and two matching coils nearest the absorber. All coils are wound onto the same bobbin and have a core temperature of 4 K and an operating pressure of 1.5 bar. In-between the solenoids is the absorber focus coil (surrounding the absorber). This “cooling channel” magnet chain can operate in flip or solenoid mode. The absorber is modular to allow a range of cooling materials to be used (liquid-hydrogen, lithium-hydride, xenon and empty).

The detector suite consists of three Time Of Flight detectors: TOF0, TOF1 and TOF2, giving precise timing and time of flight measurements; 2 cherenkov threshold counters; a downstream calorimeter made up of the Electron Muon ranger (EMR), to separate muons from decay electrons in collaboration with the KL KLOE-Light detector. There are two scintillating fibre trackers, one upstream and one downstream of the absorber, they measure normalised emittance reduction with a precision of 0.1% (beam emittance measured before and after cooling). This suite of detectors allow pion/muon separation up to 300 MeV/c.

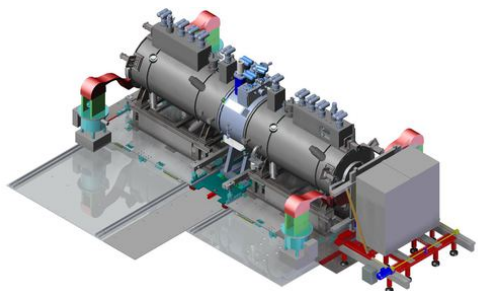


Figure 6: The MICE cooling channel showing the two spectrometer solenoids in grey and the absorber focus coil in blue.



Figure 7: The MICE Tracker detectors showing the 5 stations each consisting of three planes of WLS fibres.

The Trackers (Fig. 7, each sit within a spectrometer solenoid producing a variable magnetic field up to 4 T. Each Tracker is 110 cm in length and 30 cm in diameter and consists of five ‘stations’ with longitudinal space separation varying between 20–35 cm (the varied separation distance between the stations allows the muon pT to be determined). Each station has three planes of 350  $\mu\text{m}$  clear wavelength shifting fibres, each plane sits at 120 degrees to the next, providing a position resolution in the Trackers of 470  $\mu\text{m}$ .

### Data Taking

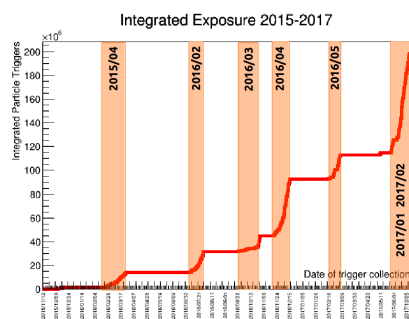


Figure 8: The MICE integrated particle triggers collected as a function of time. ISIS user cycles in which data were taken are highlighted in orange.

MICE has successfully taken data since December 2015. It has collected over 200 million integrated triggers over six ISIS user cycles with negligible down time. Figure 8 shows the MICE integrated exposure over time.

### DIRECT MEASUREMENT OF THE MICE MUON BEAM EMITTANCE

The MICE muon beam has high purity with less than 1.4% pion contamination and 0.05% decay electrons [5]. The time of flight between TOF0 and TOF1 is used to further improve the beam purity by removing other sources of contamination, such as decay positrons, from the final analysis sample. Tracker reconstruction using pattern recognition and a Kalman filter provides the best estimate of the particle position and momentum.

The time of flight between TOF0 and TOF1 is represented as a function of the total momentum reconstructed in the Tracker, shown in Fig. 9. The dotted line represents the ideal time of flight for a muon (with momentum loss as described by the Bethe-Bloch formula) between entering TOF1 and reaching the Tracker reference plane (closest to the absorber).

Due to the large aperture dipoles used to select the muon momentum distribution, the transported muon sample contains a large momentum spread,  $\sigma_{p_z} \approx 25.7 \text{ MeV}/c$ , for a mean longitudinal momentum of  $p_z = 195.4 \text{ MeV}/c$ . The emittance of the particle sample does not accurately represent the volume occupied by the particles (phase space), as muons with different longitudinal momenta occupy different regions of transverse phase space due to the presence of dispersion. The effect of this dispersion is removed by splitting the sample into momentum-coherent 8 MeV/c bins.

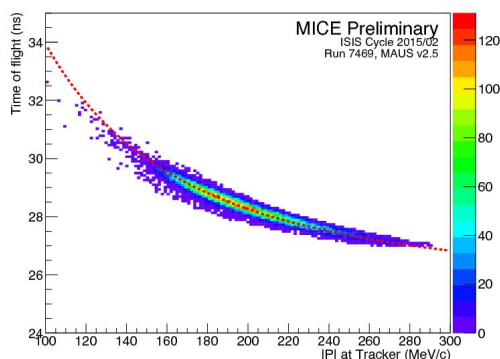


Figure 9: Time-of-flight distribution between TOF0 and TOF1 as a function of the total momentum measured in the upstream Tracker. The absence of other populations indicates selection of a pure muon sample.

The transverse normalised emittance was calculated for each 8 MeV/c bin as:

$$\epsilon_N = \frac{1}{m_\mu} \sqrt{\det \Sigma} \quad (3)$$

where  $m_\mu$  is the muon mass and  $\Sigma$  is the 4D transverse phase space covariance matrix.

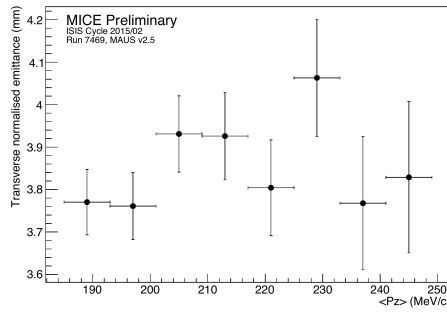


Figure 10: Transverse normalised emittance of 8 MeV/c longitudinal momentum bins.

The measured, momentum binned transverse normalised emittance is shown in Fig. 10. The horizontal error bars represent the limits of each momentum slice, while the vertical error bars are purely statistical errors on the measurements. A full systematics study is underway and preliminary results indicate that they are small in comparison. The binned emittance values are consistent across the range of studied momenta. The mean measured transverse normalised emittance for the whole sample is  $3.85 \pm 0.04$  mm.

### EMITTANCE EVOLUTION IN MICE

In order to demonstrate emittance reduction, MICE has measured the amplitude distribution upstream and downstream of the absorber. The single particle amplitude for each muon was reconstructed for each of the upstream, downstream and scraped ensembles. Initial beam emittances of 3 mm and 6 mm nominal emittance have been analysed so far. The resulting amplitude distributions are shown in Fig. 11.

The first bin is at the beam centre and hence is least affected by scraping. The 3 mm nominal emittance beam shows a clear reduction in the number of reconstructed muons downstream to upstream within the first bin, significantly above any scraping effects, which is characteristic of an emittance growth, or heating. Likewise muons with low amplitude upstream of the absorber are observed to move to higher amplitude when measured downstream, as the sample emittance is below equilibrium. Muons sampled from 6 mm 140 MeV beam show negligible change between the upstream and downstream reconstruction consistent with equilibrium emittance (and supported by simulation).

A full description of Emittance Evolution in MICE can be found in the relevant section of these proceedings.

### MULTIPLE SCATTERING MEASUREMENTS

Multiple coulomb scattering is a well known electromagnetic phenomenon experienced by charged particles traversing materials. However, recent measurements by the MuScat [6] experiment show that the available simulation codes, e.g. GEANT4 [7], overestimate the scattering of muons in low Z materials. This is of particular interest to MICE

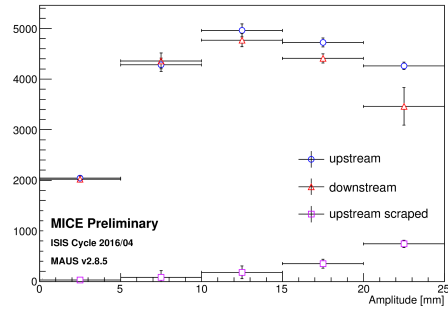
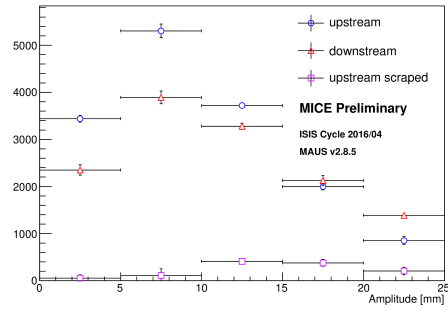


Figure 11: Change in amplitude distribution for the 3 mm 140 MeV configuration (above) and for the 6 mm 140 MeV configuration (below) are shown. Their transmission is  $\sim 90\%$  and  $80\%$  respectively. Blue circles show the amplitude of upstream events, red triangles show the amplitude of downstream events while magenta squares show the amplitude of upstream events that are not observed downstream.

which aims to measure the reduction of muon beam emittance induced by energy loss in low-Z absorbers. Multiple scattering induces positive changes in the emittance in contrast to the reduction due to ionization energy loss. It is, therefore, essential that MICE measures multiple scattering in all absorber materials; lithium hydride, liquid hydrogen and xenon; and validates this multiple scattering against known simulations.

To make the scattering measurements data was taken for a range of beam momenta (172 MeV/c (in order to compare with MuScat), 200 MeV/c and 240 MeV/c) and with the absorber in and empty (to ensure scattering in the windows of the absorber module are accounted for). A strict track selection criteria was imposed to ensure a pure, well understood muon sample. Bayesian deconvolution was applied to the selected data in order to extract the scattering distribution within the absorber material and subsequent comparisons to GEANT4 were made, as well as to the standalone scattering model developed by Carlisle and Cobb [8].

Data taken with the 200 MeV/c beam and, with and without, the LiH absorber (thickness of 65 mm,  $X_0 = 79.62 \text{ gcm}^{-2}$ ) and deconvolved using the GEANT model, are shown in Fig. 12. All contributions to the systematic uncertainty have been considered including: sensitivity to the thickness of the absorber, the time of flight cuts used in the momentum selection, detector alignment and the choice

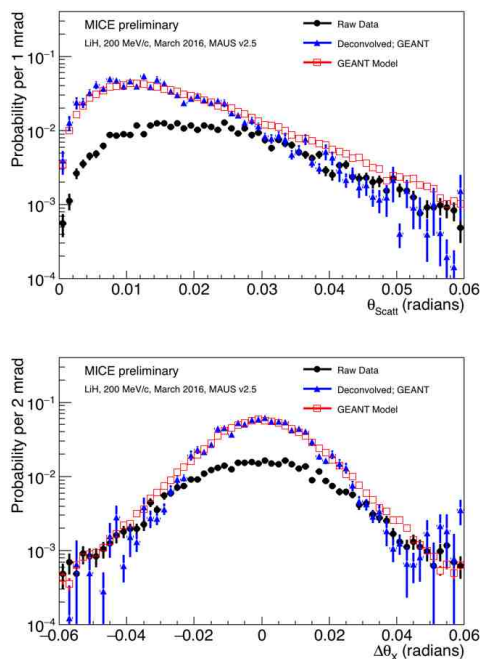


Figure 12: Projected (below) and 3D (above) scattering distributions of 200 MeV/c muons passing through the LiH absorber.

of fiducial volume cuts. The time of flight systematics are found to dominate. The scattering width taken from the scattering distributions projected in the X-Z and Y-Z planes are  $\theta = 20.3 \pm 0.2$  mrad at 172 MeV/c,  $\theta = 17.1 \pm 0.2$  mrad at 200 MeV/c and  $\theta = 13.8 \pm 0.1$  mrad at 240 MeV/c.

This preliminary analysis indicates that GEANT4 underestimates the scattering width, while the PDG model overestimates it. A full discussion can be found in the MICE Multiple Scattering discussion in these proceedings.

## CONCLUSIONS

MICE Step IV has been taking data since 2015. lithium hydride and xenon scattering data is complete and data tak-

ing with liquid hydrogen has begun. The cooling channel magnets have operated successfully taking data in flip and solenoid modes, throughout. The first direct measurement of emittance has been made in MICE, the dispersion effect is understood and there are several papers in preparation. The first emittance change measurements have also been made and are currently being finalised for publication. Multiple scattering results are progressing well and publication is also coming soon.

## REFERENCES

- [1] V. Parkhomchuck and A. Skrinsky, "Cooling Methods for Charged Particle Beams", *Rev. Accel. Sci. Tech.* 1 no. 1 (2008) 237.
- [2] S. Choubey *et al.* [IDS-NF Collaboration], "International Design Study for the Neutrino Factory, Interim Design Report", arXiv:1112.2853 [hep-ex].
- [3] M. Alsharo *et al.* *Phys. Rev. ST Accel. Beams*, 6:081001, Aug 2003.
- [4] M. Bogomilov *et al.* [MICE Collaboration], "The MICE Muon Beam on ISIS and the beam-line instrumentation of the Muon Ionization Cooling Experiment", *JINST* 7 (2012) P05009 doi:10.1088/1748-0221/7/05/P05009, [arXiv:1203.4089 [physics.acc-ph]].
- [5] MICE Collaboration, D. Adams *et al.* Pion contamination in the MICE muon beam, *JINST* 11 (2016) 03001.
- [6] MuScat Collaboration, W. J. Murray, "Comparison of MuScat data with GEANT4", *Nucl. Phys. Proc. Suppl.* 149 (2005) p.99-103.
- [7] GEANT4 Collaboration, S. Agostinelli *et al.*, "GEANT4: A Simulation toolkit", *Nucl. Instrum. Meth.* 265 A506 (2003) p.250-303.
- [8] T. Carlisle, "Step IV of the Muon Ionization Cooling Experiment (MICE) and the multiple scattering of muons", PhD Thesis, Oxford University (2013).

# MEASUREMENT OF PHASE SPACE DENSITY EVOLUTION IN MICE

F. Drielsma\*, Université de Genève, Geneva, Switzerland  
 D. Maletic†, Institute of Physics Belgrade, Belgrade, Serbia

## Abstract

The Muon Ionization Cooling Experiment (MICE) collaboration will demonstrate the feasibility of ionization cooling, the technique by which it is proposed to cool the muon beam at a future neutrino factory or muon collider. The position and momentum reconstruction of individual muons in the MICE trackers allows for the development of alternative figures of merit in addition to beam emittance. Contraction of the phase space volume occupied by a fraction of the sample, or equivalently the increase in phase space density at its core, is an unequivocal cooling signature. Single-particle amplitude and nonparametric statistics provide reliable methods to estimate the phase space density function. These techniques are robust to transmission losses and non-linearities, making them optimally suited to perform a quantitative cooling measurement in MICE.

## INTRODUCTION

Future facilities such as the Muon Collider and the Neutrino Factory will require high intensity and low emittance stored muon beams [1, 2]. Muons are produced as tertiary particles ( $p + N \rightarrow \pi + X$ ,  $\pi \rightarrow \mu + \nu$ ) inheriting a large emittance from the isotropic decay of the pions. For efficient acceleration, the phase space volume of these beams must be reduced significantly, i.e. “cooled”, to fit within the acceptance of a storage ring or accelerator beam pipe. Due to the short muon lifetime, ionization cooling is the only practical and efficient technique to cool muon beams [3, 4]. Each muon in the beam loses momentum in all dimensions through ionization energy loss in an absorbing material, reducing the RMS emittance and increasing its phase space density. Subsequent acceleration through radio frequency cavities restores longitudinal energy, resulting in a beam with reduced transverse emittance. A factor of close to  $10^6$  in reduced 6D emittance has been achieved in simulation with a 970 m long channel [5]. The rate of change in normalized transverse RMS emittance,  $\epsilon_N$ , is given by the ionization cooling equation [3]:

$$\frac{d\epsilon_N}{ds} \simeq -\frac{\epsilon_N}{\beta^2 E_\mu} \left| \frac{dE_\mu}{ds} \right| + \frac{\beta_\perp (13.6 \text{ MeV})^2}{2\beta^3 E_\mu m_\mu c^2 X_0}, \quad (1)$$

where  $\beta c$  is the muon velocity,  $|dE/ds|$  is the average rate of energy loss,  $E_\mu$  and  $m_\mu$  are the muon energy and mass,  $\beta_\perp$  is the transverse betatron function and  $X_0$  is the radiation length of the absorber material. The first term on the right can be referred to as the “cooling” term driven by energy loss, while the second term is the “heating term” that uses the PDG approximation for the multiple Coulomb scattering.

\* francois.drielsma@unige.ch

† Speaker

MICE [6] is currently taking data in the Step IV configuration in order to make detailed measurements of the scattering, energy loss [7] and phase space evolution at different momenta and channel configurations, with lithium hydride and liquid hydrogen absorbers. A schematic drawing of MICE Step IV is shown in Figure 1. MICE consists of two scintillating fiber trackers upstream and downstream of the absorber in strong solenoid fields to accurately reconstruct the position and the momentum of individual muons selected in a series of particle identification detectors, including 3 time-of-flight hodoscopes (ToF0/1/2), 2 threshold Cherenkov counters, a pre-shower calorimeter (KL) and a fully active tracker-calorimeter (EMR) [8–11].

## COOLING CHANNEL

The two spectrometer solenoid modules each generate a region of uniform 3 T field in which diagnostic trackers are situated and a matching region that transports the beam from the solenoid to the focus coil module. The focus coil module, positioned between the solenoids, provides additional focusing to increase the angular divergence of the beam at the absorber, improving the amount of emittance reduction that can be achieved. The magnetic field model is shown in Figure 2. The absorber was a single 65 mm thickness lithium hydride disk. Lithium hydride was chosen as an absorber material as it provides less multiple Coulomb scattering for a given energy loss.

In this paper the evolution of phase space density is reported for a single configuration of the cooling apparatus. Results from one transfer line configuration are reported, with the accumulated muon sample having a nominal emittance of 6 mm at momenta around 140 MeV/c in the upstream spectrometer solenoid, denoted as ‘6–140’.

As MICE measures each particle event individually, it is possible to select a particle ensemble from the collection of measured tracks. This enables the study of momentum spread and transverse beam parameters on the cooling. In this analysis, muons have been selected with:

- longitudinal momentum in the range 135 to 145 MeV/c;
- time-of-flight between TOF0 and TOF1 consistent with muons in this momentum range; and
- a single, good quality track formed in the upstream diagnostics.

In order to study the evolution of the phase space density through the whole cooling channel and across the absorber, a realistic simulation of the setting of interest was produced. The betatron function of the selected muon ensemble is shown for the Monte Carlo (MC) simulation, the

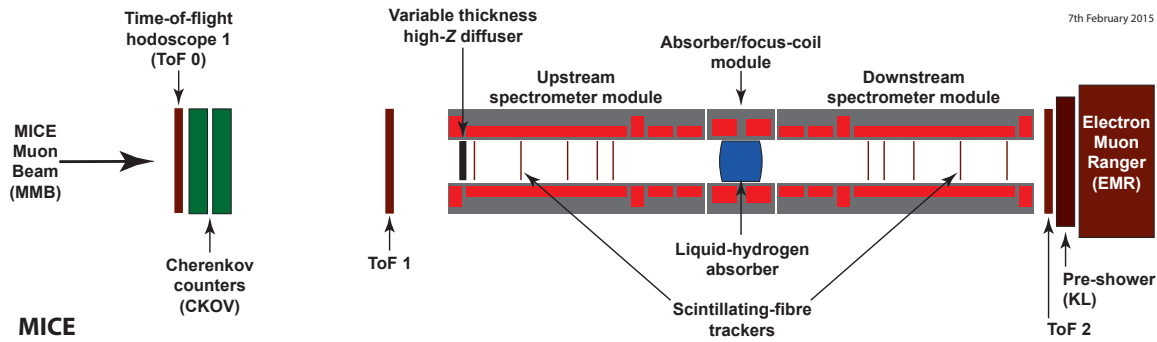


Figure 1: Layout of the MICE Step IV configuration, its absorber module, tracking spectrometers and PID detectors.

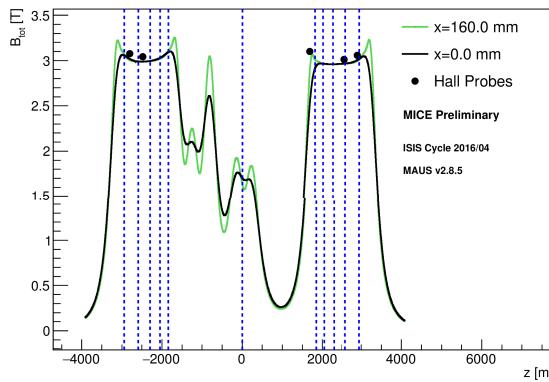


Figure 2: Modelled magnetic field for the configuration on the axis and with 160 mm horizontal displacement from the axis. Hall probes, situated 160 mm from the beam axis, show a 2% discrepancy with the model. Dashed lines show position of the tracker stations and absorber (at  $z = 0$ ).

reconstructed MC and the data for the ‘6–140’ setting in Figure 3. The graph shows a large growth of the beam size in the downstream section due to the absence of the downstream match coils in this configuration. The simulation closely reproduces the function measured in the data.

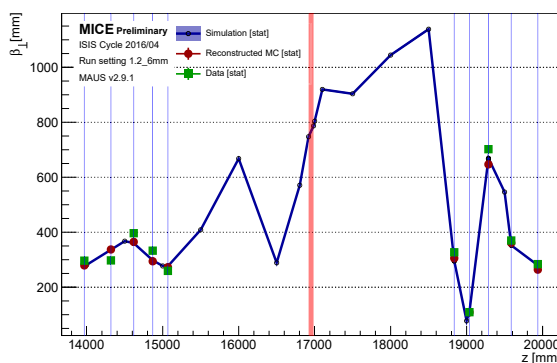


Figure 3: Beta function profile in the MC truth (blue line), reconstructed MC (red circles) and data (green squares).

## PHASE SPACE DENSITY EVOLUTION

### Emittance

The transverse normalized RMS emittance is the most common cooling figure of merit and is defined as

$$\epsilon_N = \frac{1}{m_\mu} |\Sigma|^{1/4}, \quad (2)$$

with  $m_\mu$  the muon mass and  $|\Sigma|$  the determinant of the 4D transverse phase space covariance matrix, i.e.  $\Sigma_{ij} = \langle ij \rangle - \langle i \rangle \langle j \rangle$  with  $i, j \in [x, p_x, y, p_y]$ . For a Gaussian beam, this quantity is directly related to the volume of the  $1\sigma$  RMS ellipse,  $V_{RMS}$ , through  $\epsilon_N = \sqrt{2V_{RMS}}/(m\pi)$ .

In a fully transmitted beam, emittance reduction is a clean signature of the contraction of transverse phase space volume. For a partially scraped beam, as shown for the ‘6–140’ setting in Figure 4, the emittance evolution exhibits apparent emittance reduction in the downstream section due to the loss of the tails of the distribution. It also experiences significant apparent growth in the downstream tracker due to high field gradient, causing filamentation in the beam.

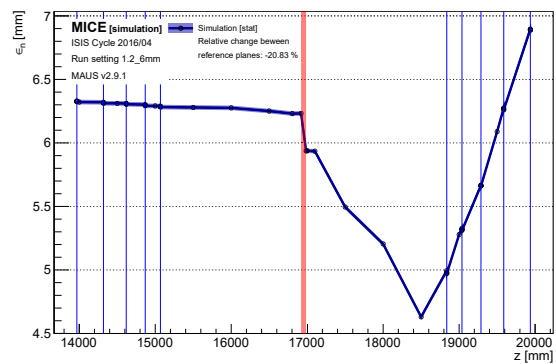


Figure 4: Normalized transverse RMS emittance evolution through the MICE cooling channel.

An alternative to RMS emittance is to study the evolution of the density distribution of the ensemble, as it allows for the selection of a defined and identical fraction of phase space upstream and downstream of the absorber.

## Amplitude

The 4D amplitude of a particle with phase space vector  $\mathbf{v} = (x, p_x, y, p_y)$  is given by

$$A_{\perp} = \epsilon_N (\mathbf{v} - \boldsymbol{\mu})^T \boldsymbol{\Sigma}^{-1} (\mathbf{v} - \boldsymbol{\mu}). \quad (3)$$

with  $\boldsymbol{\mu} = (\langle x \rangle, \langle p_x \rangle, \langle y \rangle, \langle p_y \rangle)$ , the beam centroid. In order to prevent the tails of the distribution from skewing the core, only those events with amplitude less than  $A_{\perp}$  have been included in the calculation of  $\boldsymbol{\mu}$  and  $\boldsymbol{\Sigma}$  for a given event. The high amplitude particles are iteratively removed from the sample first as they are calculated.

The distribution of muons is represented in Figure 5 in the tracker station that is furthest downstream in the  $(x, p_x)$  projection. The color of the points in the scatter plot represents the amplitude of the particle at that position. The distribution exhibits a clear Gaussian core of low amplitudes, while the tails are easily identified as high amplitude points.

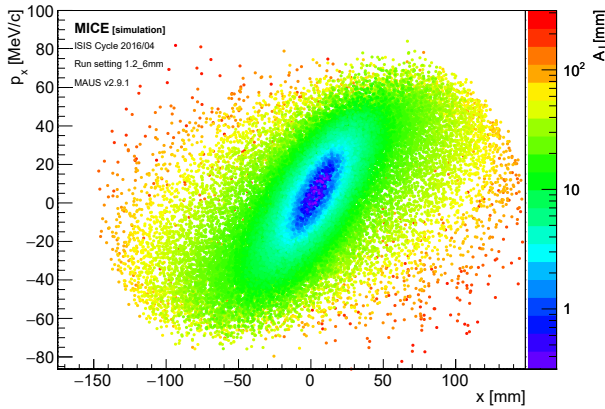


Figure 5: Scatter plot of the particles in the tracker station that is furthest downstream in the  $(x, p_x)$  projection. The color scale represents the individual particle amplitudes.

The amplitude of a particle in a Gaussian beam is related to its local density through

$$\rho(\mathbf{v}) = \frac{1}{4\pi^2 m^2 \epsilon_N^2} \exp\left[-\frac{A_{\perp}}{2\epsilon_N}\right]. \quad (4)$$

A low amplitude sample corresponds to the high density core of the beam.

## Subemittance

The  $\alpha$ -subemittance,  $e_{\alpha}$ , is defined as the RMS emittance of the core fraction  $\alpha$  of the parent beam. For a truncated 4D Gaussian beam of covariance  $S$ , it satisfies

$$\frac{e_{\alpha}}{\epsilon_N} = \frac{|S|^{\frac{1}{4}}}{|\boldsymbol{\Sigma}|^{\frac{1}{4}}} = \frac{1}{2\alpha} \gamma\left(3, Q_{\chi_4^2}(\alpha)/2\right), \quad (5)$$

with  $\gamma(\cdot, \cdot)$  the lower incomplete gamma function and  $Q_{\chi_4^2}(\cdot)$ , the 4-degrees-of-freedom  $\chi^2$  distribution quantiles.

If an identical fraction  $\alpha$  of the input beam is selected upstream and downstream, i.e. the same amount of particles, the measured subemittance change is identical to the normalized RMS emittance change. The evolution of the 9%-subemittance is represented in Figure 6. The choice of 9% is natural in four dimensions as it represents the fraction contained within the 4D RMS ellipsoid of a 4-variate Gaussian. This quantity exhibits a clean cooling signal across the absorber that is unaltered by transmission losses and nonlinearities. The only trade-off is that the relative statistical error on  $\alpha$ -subemittance grows as  $\alpha^{-\frac{1}{2}}$ . The estimated relative emittance change with this technique is  $-7.54 \pm 1.25\%$ , compatible with predictions.

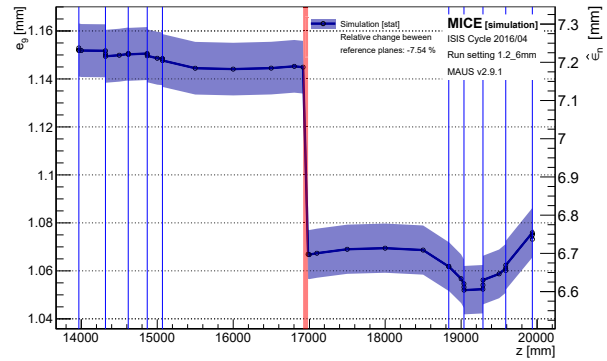


Figure 6: 9%-subemittance evolution through the MICE cooling channel.

## Fractional Emittance

The  $\alpha$ -fractional emittance,  $\epsilon_{\alpha}$ , is defined as the phase space volume occupied by the core fraction  $\alpha$  of the parent beam. For a truncated 4D Gaussian beam, it satisfies

$$\epsilon_{\alpha} = \frac{1}{2} m^2 \pi^2 \epsilon_N^2 Q_{\chi_4^2}^2(\alpha). \quad (6)$$

This volume scales as function of  $\alpha$  only and is proportional to the square of the normalized emittance. For a relative emittance change  $\delta = \Delta\epsilon_N / \epsilon_N^{UP}$ , one yields

$$\frac{\Delta\epsilon_{\alpha}}{\epsilon_{\alpha}^{UP}} = \delta(2 + \delta) \approx 2 \frac{\Delta\epsilon_N}{\epsilon_N^{UP}}. \quad (7)$$

The last approximation holds for small fractional changes. The volume of a fraction  $\alpha$  of the beam is reconstructed by taking the convex hull of the selected ensemble [12]. Figure 7 shows the evolution of the 9%-fractional emittance. The estimated relative emittance change with this technique is  $-7.85 \pm 1.08\%$ .

## Nonparametric Density Estimation

Nonparametric statistics are not based on parameterized families of probability distributions. Unlike parametric density estimation, such as amplitude, nonparametric statistics

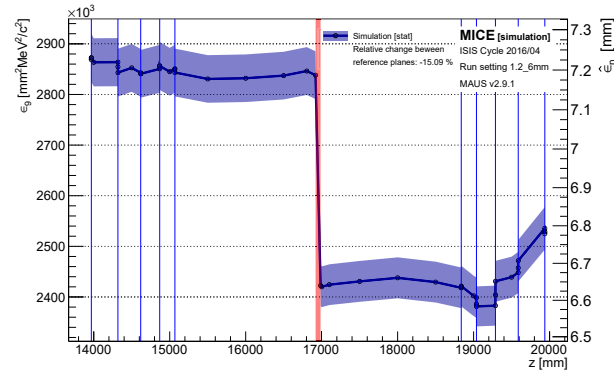


Figure 7: 9%-fractional emittance evolution through the MICE cooling channel.

make no assumptions about the probability distributions of the variables being assessed.

There are many classes of estimators that have been developed in the last century. Three of them have been considered in this study: optimally binned histograms,  $k$ -Nearest Neighbors ( $k$ NN) and Tessellation Density Estimators (TDEs) [13–16]. Systematic studies showed that the  $k$ NN method is the most efficient and robust technique in four dimensions. For a given phase space vector  $\mathbf{v} = (x, p_x, y, p_y)$ , find the  $k$  nearest points in the input cloud, calculate the distance to the  $k^{\text{th}}$  nearest neighbor,  $R_k$ , and evaluate the density as

$$\rho(\mathbf{v}) = \frac{k}{V_k} = \frac{k\Gamma\left(\frac{d}{2} + 1\right)}{\pi^{\frac{d}{2}} R_k^d}, \quad (8)$$

with  $d$  the dimension of the space,  $V_k$  the volume of the  $d$ -ball of radius  $R_k$  and  $\Gamma(\cdot)$  is the gamma function. The choice of parameter  $k = \sqrt{N}$  has been shown to be quasi-optimal in general [17] and is used in the following. This estimator is applied to the sample in the tracker station that is furthest downstream and is represented in the  $(x, p_x)$  projection for  $(y, p_y) = (0, 0)$  in Figure 8.

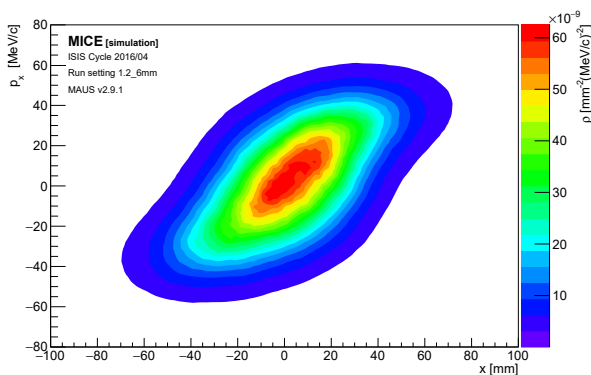


Figure 8:  $k$ -Nearest Neighbors estimate of the phase space density in the  $(x, p_x)$  projection for  $(y, p_y) = (0, 0)$  in the tracker station that is furthest downstream.

This method removes any underlying assumption about a Gaussian core and allows to reconstruct generalized probability contours. The volume of the  $\alpha$ -contour is the  $\alpha$ -fractional emittance, as defined above. An MC method is used to reconstruct the volume of a contour: select the densest fraction  $\alpha$  of the input points and record the level of the lowest point,  $\rho_\alpha$ . Sample  $N$  random points uniformly distributed inside a box that encompasses the contour and record the amount,  $N_\alpha$ , that have a density above the level, i.e.  $\rho > \rho_\alpha$ . The volume of the contour is simply  $\epsilon_\alpha = N_\alpha V_{box} / N$ , with  $V_{box}$  the volume of the 4-box. The 9%-contour volume evolution is represented in Figure 9. The estimated relative emittance change with this technique is  $-7.97 \pm 1.63\%$ .

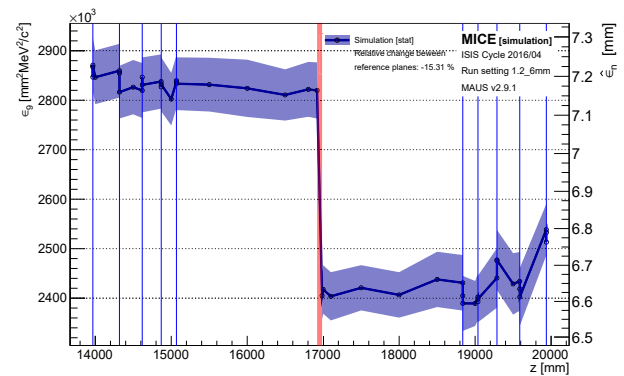


Figure 9: 9%-contour volume evolution through the MICE cooling channel.

## CONCLUSION

While the traditional normalized RMS emittance measurement is vulnerable to transmission losses and non-linearities in the particle ensemble, density estimation techniques provide the most viable option to recover quantitative cooling measurements. Amplitude-based techniques – subemittance and fractional emittance – rely on a well known quantity to select and study an identical fraction of the beam upstream and downstream of the absorber. Nonparametric density estimators allow to go one step further in removing any assumption on the underlying distribution. Both approaches yield compelling results when applied to a poorly transmitted and highly non-linear beams in a realistic simulation of one of the MICE cooling channel settings.

## ACKNOWLEDGEMENT

Work described here has been made possible through generous funding from the Department of Energy and the National Science Foundation (USA), the Istituto Nazionale di Fisica Nucleare (Italy), the Science and Technology Facilities Council (UK), the European Community under the European Commission Framework Programme 7, the Japan Society for the Promotion of Science and the Swiss National Science Foundation.

## REFERENCES

- [1] IDS-NF Collaboration, M. Apollonio *et al.*, “International Design Study for the Neutrino Factory”, *Nucl. Phys. Proc. Suppl.* 229-232 (2012) 515–515
- [2] Neutrino Factory and Muon Collider Collaboration, M. Alsharoa, *et al.*, “Recent progress in neutrino factory and muon collider research within the Muon collaboration”, *Phys. Rev. ST Accel. Beams* 6 (2003) 081001
- [3] D. Neuffer, “Principles and Applications of Muon Cooling”, *Part. Accel.* 14 (1983) 75–90.
- [4] V. Parkhomchuck and A. Skrinsky, “Cooling Methods for Charged Particle Beams”, *Rev. Accel. Sci. Tech.* 1 no. 1 (2008) 237
- [5] D. Stratakis and R. Palmer, “Rectilinear six-dimensional ionization cooling channel for a muon collider: A theoretical and numerical study” *Phy. Rev. ST Accel. Beams* 18 (2015) 031003
- [6] MICE Collaboration, “MICE: An International Muon Ionization Cooling Experiment”, MICE Note 21 (2003). <http://mice.iit.edu/micenotes/public/pdf/MICE0021/MICE0021.pdf>.
- [7] F. Drielsma, “Results from MICE Step IV”, in *Proceedings of “The 2017 European Physical Society Conference on High Energy Physics”* PoS(EPS-HEP2017)534
- [8] C. Heidt, “The tracker systems for the muon ionization cooling experiment”, *Nucl. Instr. Meth.*, vol. 718 (2014), 560–562.
- [9] U. Braver *et al.*, “MICE: the Muon Ionization Cooling Experiment. Step I: First Measurement of Emittance with Particle Physics Detectors”, <https://arxiv.org/abs/1110.1813>.
- [10] D. Adams *et al.*, “Pion contamination in the MICE muon beam”, *JINST* 11 (2016) P03001
- [11] D. Adams *et al.*, “Electron-muon ranger: performance in the MICE muon beam”, *JINST* 10 (2015) P12012
- [12] C.B. Barber, D.P. Dobkin, and H.T. Huhdanpaa, “The Quickhull algorithm for convex hulls”, *ACM Trans. on Mathematical Software*, 22(4) (1996) 469-483, <http://www.qhull.org>.
- [13] D.W. Hogg, “Data analysis recipes: Choosing the binning for a histogram”, <https://arxiv.org/pdf/0807.4820>
- [14] Y.P. Mack and M. Rosenblatt, “Multivariate k-nearest neighbor density estimates”, *Journal of Multivariate Analysis* Volume 9, Issue 1 (1979), 1–15
- [15] M. Browne, “A geometric approach to non-parametric density estimation”, *Pattern Recognition* 40(1) (2007), 134–140
- [16] M. Browne, “Regularized tessellation density estimation with bootstrap aggregation and complexity penalization”, *Pattern Recognition* 45(4) (2012), 1531–1539
- [17] D.O. Loftsgaarden and C.P. Quesenberry, “A nonparametric estimate of a multivariate density function”, *The Annals of Mathematical Statistics* Vol. 36, No. 3 (1965), 1049–1051

# EMITTANCE EVOLUTION IN MICE\*

M. A. Uchida<sup>†</sup>, Imperial College London, UK  
*for the MICE collaboration*

## Abstract

The Muon Ionization Cooling Experiment (MICE) was designed to demonstrate a measurable reduction in beam emittance due to ionization cooling. The emittance of a variety of muon beams was reconstructed before and after a “cooling cell”, allowing the change in the phase-space distribution due to the presence of an absorber to be measured.

The core of the MICE experiment is a cooling cell that can contain a range of solid and cryogenic absorbers inside a focussing solenoid magnet. For the data described here, a single lithium hydride (LiH) absorber was installed and two different emittance beam have been analysed. Distributions that demonstrate emittance increase and equilibrium have been reconstructed, in agreement with theoretical predictions.

Data taken during 2016 and 2017 is currently being analysed to evaluate the change in emittance with a range of absorber materials, different initial emittance beams and various magnetic lattice settings. The current status and the most recent results of these analyses is presented.

## INTRODUCTION

The International Muon Ionization Cooling Experiment (MICE) was designed and constructed to demonstrate the process of ionization cooling [1], applied to muon beams. It was constructed at the Rutherford Appleton Laboratory, and has been successfully taking data since 2015. Figure 1 shows the total number of integrated event triggers, as a function of time for the current configuration of the experiment.

MICE is a single particle experiment where each event contains a single muon passing through the beamline. Individual muon tracks are then reconstructed in each of the detectors. This data is aggregated at analysis in order to study the evolution of both individual track parameters and ensemble effects, when various absorber materials are placed within the cooling channel.

The primary goal is to measure the phase-space volume of the muon beam before and after a cooling cell by reconstructing the normalised, transverse RMS emittance (referred to simply as “emittance”). This corresponds the volume occupied by the central 68% of a gaussian-distributed ensemble of particles. This is easily calculated by constructing the covariance matrix for an ensemble,  $\Sigma$ , in the position-momentum phase-space, using the variables:  $x, p_x, y, p_y$ . The emittance can then be calculated as:

$$\epsilon_{\perp} = \frac{|\Sigma|^{\frac{1}{4}}}{m}, \quad (1)$$

\* Work supported by the (UK) Science and Technology Facilities Council and the (US) Dept. of Energy and National Science Foundation

<sup>†</sup> m.a.uchida@imperial.ac.uk

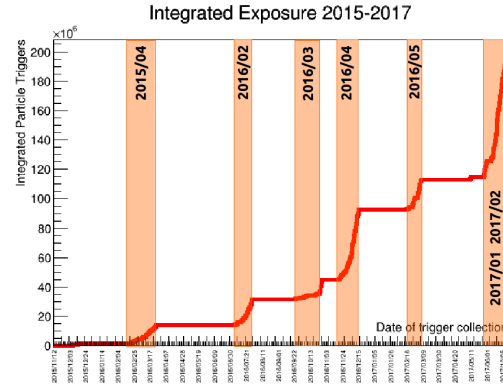


Figure 1: The integrated number of event triggers as a function of time. The ISIS user periods in which MICE is operational are highlighted.

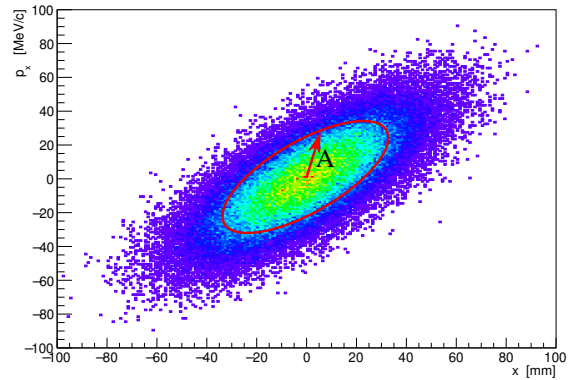


Figure 2: Example phase-space distribution with a contour of equal amplitude marked in red.

where  $\epsilon_{\perp}$  is the emittance, and  $m$  is the muon mass.

In order to analyse the effect of a single muon on the evolution of emittance, an additional quantity is defined: the single particle amplitude,  $A_{\perp}$ . This corresponds to the scalar distance a given particle is found from the centre of the beam (Figure 2). The definition is weighted by the covariance matrix such that amplitude is invariant under conservative transformations, e.g. focussing. It is defined by,

$$A_{\perp} = \epsilon_{\perp} \mathbf{v}^{\top} \Sigma^{-1} \mathbf{v} \quad (2)$$

where  $\mathbf{v} = (x, p_x, y, p_y)$  is the particle’s coordinate vector.

The behaviour of the beam emittance in the presence of an absorber material can be approximated by the cooling

Content from this work may be used under the terms of the CC BY 3.0 licence (© 2017). Any distribution of this work must maintain attribution to the author(s), title of the work, publisher, and DOI.

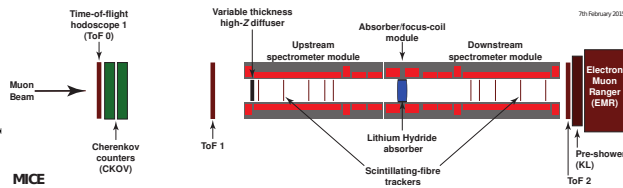


Figure 3: Layout of the MICE experiment in its current configuration. The upstream detectors are illustrated in the order in which the incoming beam crosses them, the solenoid magnet coils are marked in red and the absorber module is shown in blue.

equation,

$$\frac{d\epsilon_{\perp}}{dx} = -\frac{\epsilon_{\perp}}{\beta^2 E} \left\langle \frac{dE}{dx} \right\rangle + \frac{\beta_{\perp} (13.6 \text{ MeV}/c)^2}{2\beta^3 E m_{\mu} X_0}, \quad (3)$$

which describes the rate of change of emittance with respect to longitudinal position through a material with energy loss,  $\langle dE/dx \rangle$ , and radiation length,  $X_0$ .  $\beta$ ,  $E$  and  $m_{\mu}$  are the mean relativistic velocity, energy and mass of the muon beam and  $\beta_{\perp}$  is the betatron function.

## THE MICE EXPERIMENT

### Transfer Line

The muon beam used by the MICE experiment is produced by dipping a titanium target into the ISIS proton synchrotron. Three triplets of quadrupole magnets provide transverse focussing of the resultant pion and muon beams and a decay solenoid magnet is used to increase the capture efficiency of muons produced from pion decay (Figure 4).

Momentum selection is performed using two dipole magnets, the first selects the pion momentum before decay, and the second selects the resultant muon momentum. This allows for precise control over the final ratio between pions, muons and electrons that enter the cooling channel.

The final component, the variable beam diffuser, is found at the entrance to the cooling channel and is comprised of two brass and two tungsten irises that can diffuse the incoming muon beam via multiple Coulomb scattering. This provides a method to vary the initial beam emittance before entering the cooling channel.

### Diagnostics

A range of diagnostic detectors [2] are installed in order ensure that the species of particle can be precisely determined. Muons are selected with a high efficiency upstream of the cooling channel, and any muons that decay can be tagged downstream of the cooling channel.

Upstream, aerogel-based cerenkov detectors provide coarse velocity measurements and are used in conjunction with time-of-flight counters that identify muons, pions and electrons by their transit time between fixed points.

Downstream of the cooling channel, a third time-of-flight counter is used in addition to the Kloe-light (KL) and

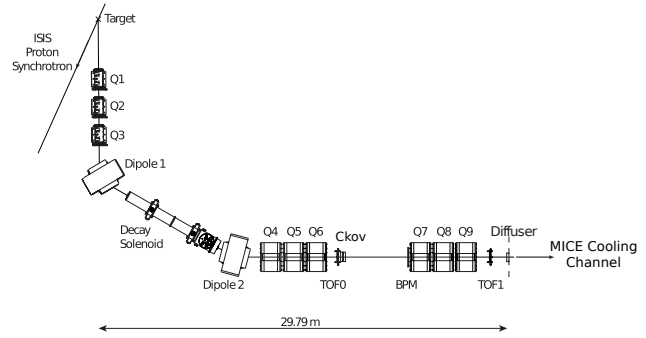


Figure 4: Layout of the transfer line from the ISIS synchrotron through to the MICE Cooling Channel.



Figure 5: Photograph of a scintillating fibre tracker under construction. The yellow light was required in order to prevent damage the fibres.

electron-muon ranger (EMR) calorimeters. The combination of precise time-of-flight measurements, and the identification of stopped particle tracks in the calorimetry systems, allows for better than 99% muon identification [3].

### The Trackers

The primary detectors used in the reconstruction of emittance are the scintillating fibre trackers [4]. They consist of five stations, which are in turn composed of the 3 planes of  $350 \mu\text{m}$  scintillating fibres. This allows for a position resolution better than  $0.5 \text{ mm}$ , and a transverse momentum resolution of approximately  $1 \text{ MeV}/c$  [5].

The fibres are read out using visual light photon counters (VLPCs) and processed to reconstruct position where overlapping channels are found across all three planes for a given station. This triplet requirement results in a noise rejection of better than 99.9%.

A Kalman filter based track fitting routine performs the final track fit for each tracker and allows precise determination of the track parameters at a reference plane. The reference plane for each tracker is defined as the plane that is closest to the absorber. This provides the nominal position at which results for different settings and configurations may be compared.

### Optics

The MICE cooling channel (illustrated in Figure 3), is composed of three solenoid magnets: spectrometer solenoid-upstream (SSU), absorber focus coil (AFC), and spectrome-

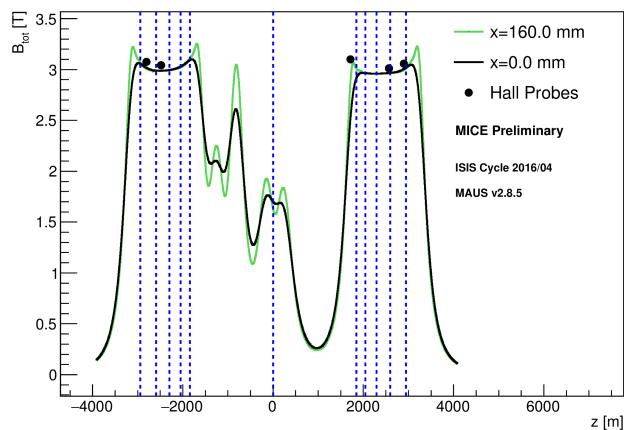


Figure 6: Magnetic field configuration of the MICE cooling channel in solenoid mode. The black line shows the mean, on-axis field and the green shows the mean field strength at the radius of the hall probe locations. Black points show the respective values from the hall probes within the magnet bore.

ter solenoid-downstream (SSD). The LiH absorber is located in the center of the AFC and the individual magnet coils are shown in red.

For the data discussed here, the two matching coils within SSD (those closest to the absorber) were not powered due to concerns over the quench protection system and related hardware issues. They have since been operated successfully.

The magnetic configuration of the channel that was used during data taking of the emittance-evolution data set is shown in Figure 6. A comparison between the model and hall probe measurements indicates that there is a small systematic error in the magnitude of the estimated field, the effective error of which was estimated using simulation data (section ).

Figure 6 also highlights the regions where there are significant field gradients, notably at  $z = 1000$  mm, the location of the unpowered downstream match coils. The combination of large betatron function (the transverse extent of the beam) and high field gradient is believed to cause filamentation within the beam (where different momentum muons are focussed by different amounts), leading to an apparent emittance growth.

The betatron function, estimated using simulation, is shown in Figure 7. Although well constrained in the upstream portion of the cooling channel, significant oscillations were present due the lack of focussing from the downstream match coils. The matching was optimised using a genetic algorithm to ensure good transmission through to the downstream tracking region, whilst maintaining the betatron function through the absorber.

## ANALYSIS PROCEDURE

### Event Selection

Each detector was read out and processed using specialised algorithms designed around the physical hardware.

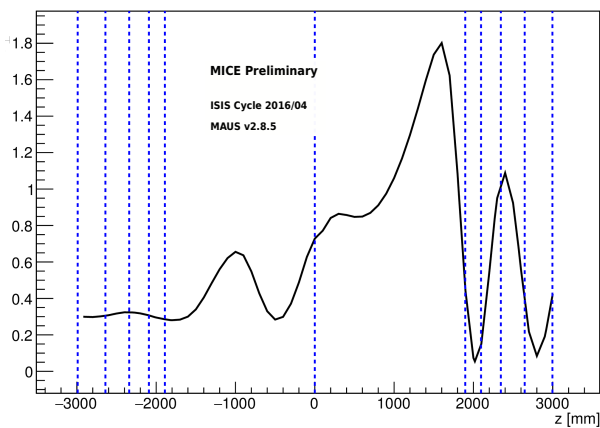


Figure 7: The betatron function from simulation for the magnetic configuration that was used during data taking. The blue dashed lines highlight the positions of the 5 tracker stations, upstream and downstream, in addition to the centre of the LiH absorber.

The resultant reconstructed spacepoints and tracks were then analysed and selected.

Individual events were primarily selected based on the time-of-flight between TOF0 and TOF1, the chi-squared per degree of freedom of the fitted upstream track and the momentum reconstructed at the reference plane of the upstream tracker. This provided a high-purity ensemble of muons that were well reconstructed by the trackers, with minimal statistical bias in the resultant measurement.

In order to validate the reconstruction of the time-of-flight and tracking detectors, the reconstructed momentum within the upstream tracker was plotted against the reconstructed time-of-flight of each muon entering the cooling channel that passed the selection criteria. The result is shown in Figure 8 and demonstrates very good agreement between the data and theoretical prediction (for the muon mass) shown by the red dashed line.

Additional statistical quantities were used to discriminate against bad events. Primarily, the reconstructed chi-squared value per degree of freedom,  $\chi_{NDF}^2$ , for the trackers. Events with  $\chi_{NDF}^2 > 5$  were excluded (both upstream and downstream) as this demonstrates a sub-optimal fit. This rejected less than 1% of potential events and was primarily due to rare hard-scatter events, in which a significant deflection in the track path is observed.

The event selection procedure was applied only to the upstream tracker, such that the result was unbiased by the preferential selection of events (that would demonstrate cooling). Events that scrape, i.e. interact with the apertures between modules or scatter into a magnet bore, were higher-amplitude particles. Hence, any selection based only on the particles that were transmitted would bias the resultant measurement towards those events that showed a net decrease in amplitude.

Content from this work may be used under the terms of the CC BY 3.0 licence (© 2017). Any distribution of this work must maintain attribution to the author(s), title of the work, publisher, and DOI.

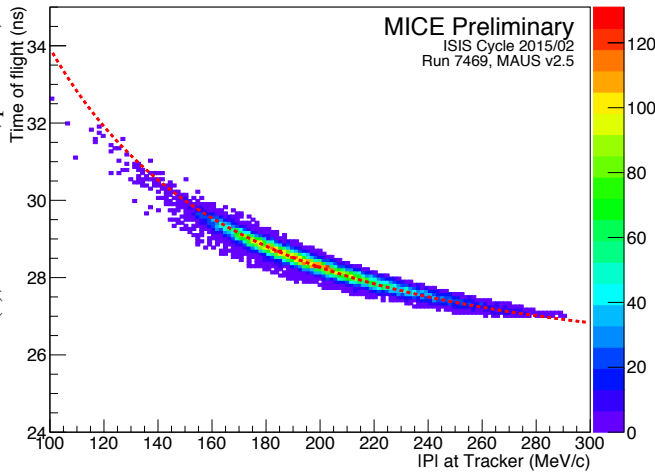


Figure 8: Comparison of the time of the flight between TOF0 and TOF1 and the momentum reconstructed within the upstream tracker. The red dashed line describes the theoretical results for a particle with the muon mass.

### Amplitude Reconstruction

For each event that passed the selection criteria (outlined above), the position and momentum components ( $x$ ,  $p_x$ ,  $y$ ,  $p_y$ ) were reconstructed at the reference plane of the upstream tracker. Similarly, each event for which an upstream track was found and transmitted through to the downstream tracker was reconstructed at the downstream reference plane.

For those events where a track was not located in the downstream tracker, the track was assumed to have been scraped out of the beam and therefore not included in the downstream reconstruction. Such events were flagged and reconstructed as an additional ensemble in the upstream tracker, such that the amplitude distribution of the scraped events could be compared against those that were transmitted.

At each of the upstream and downstream reference planes, the tracks that were selected were used to calculate the beam emittance and amplitude distribution using Equations (1) and (2) respectively.

The statistical error on the emittance was calculated using:

$$\sigma_{\epsilon_{\perp}} = \frac{\epsilon_{\perp}}{\sqrt{2(N-1)}} \quad (4)$$

where  $N$  is the number of events in the ensemble and  $\sigma_{\epsilon_{\perp}}$  is the standard error on the emittance. The results were used to estimate the statistical error for each bin in amplitude.

The systematic errors were estimated using a Monte Carlo simulation in which each tracker was analysed independently. A realistic reproduction of the data was performed starting from a model of the target. The momentum distributions were tuned to match those of the reconstructed data such that a accurate representation of the experiment was produced.

The simulated data was reconstructed such that for each bin in amplitude, the migration of events that were mis-reconstructed could be calculated. That is the number of events which should have been reconstructed in a given bin,

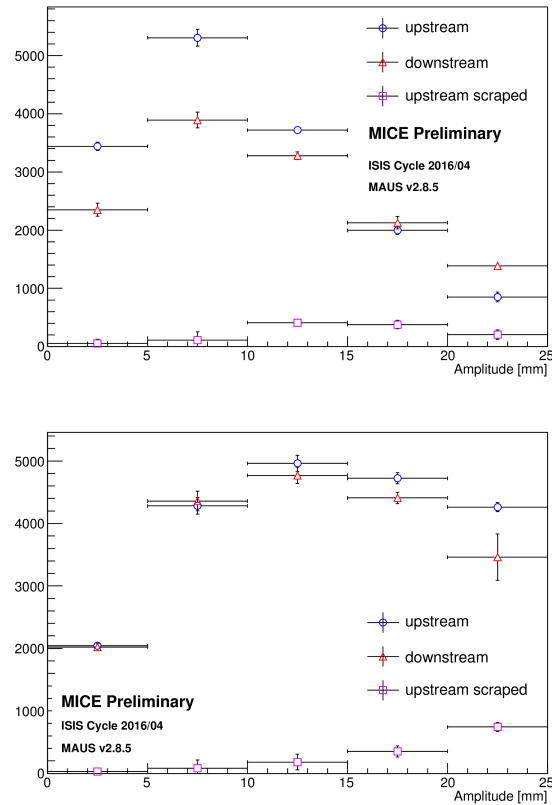


Figure 9: A comparison between the upstream and downstream amplitude distributions for the 3 mm nominal beam and the 6 mm nominal beam. The particles that were reconstructed upstream but were scraped before reaching the downstream tracker are also shown.

but were found in another bin. This is due to the intrinsic statistical precision of the trackers coupled with non-uniformities in the magnetic field.

Each bin in amplitude was then corrected according to the results of the model, and the associated errors were calculated.

## EMITTANCE EVOLUTION

The single particle amplitude for each muon was reconstructed for each of the upstream, downstream and scraped ensembles. Two different initial beams were studied: a 3 mm nominal emittance beam and a 6 mm nominal emittance beam. The resultant amplitude distributions are shown in Figure 9.

The region of interest is the core of the beam, where the effects of filamentation and scraping are weakest, which is well represented by the first bin in amplitude.

The result for the 3 mm nominal emittance shows a clear reduction within the first bin, significantly above any scraping effects, which is characteristic of an emittance growth i.e. heating. This is in agreement with predictions as lower emittance beam are more difficult to cool, in that they require

greater focussing and relative energy losses to achieve the same effect as a larger emittance beam.

The 6 mm result shows very little change between the upstream and downstream reconstruction in the first bin. The neighbouring bins are also consistent and no change within the effects of scraping and the statistical errors is observed. This demonstrates that the net movement of high amplitude particles to lower amplitude is approximately balanced by the net movement of low amplitude particles to higher amplitude. This is consistent with the expected equilibrium emittance for the cooling channel in this configuration at 6 mm.

## CONCLUSIONS

The first data for the study of emittance evolution through a LiH absorber has been taken and analysed. A muon beam sample has been selected and reconstructed for two different nominal beam emittances: 3 mm and 6 mm. The distributions of single particle amplitude have been produced and compared, resulting in effects consistent with emittance increase (for the nominal 3 mm beam) and emittance equilibrium (for the nominal 6 mm beam).

Monte Carlo simulations were used in order to validate the reconstruction and analysis techniques, in addition to modelling the errors present in the amplitude distributions.

The results were used to estimate the error for each bin in the amplitude distributions.

An additional 10 mm nominal beam is currently being analysed and initial indications show that this setting will demonstrate an increase in amplitude density at the core of the beam, a signal consistent with emittance reduction.

## REFERENCES

- [1] A. N. Skrinsky *et al.*, "Cooling methods for beams of charged particle," *Sov. J. Part. Nucl.*, vol. 12, no. 223, 1981.
- [2] D. Orestano, "The detector system of the MICE experiment," *Nucl. Inst. Phys. A*, vol. 617, pp. 45 – 47, 2010.
- [3] A. Dobbs *et al.*, "The reconstruction software for the mice scintillating fibre trackers," *Journal of Instrumentation*, vol. 11, no. 12, p. T12001, 2016.
- [4] C. Pidcott, "Multiple scattering and particle identification in the Muon Ionisation Cooling Experiment," PhD thesis, University of Warwick, 2017.
- [5] M. Ellis *et al.*, "The design, construction and performance of the MICE scintillating fibre trackers," *Nuclear Instruments and Methods in Physics Research Section A: Accelerators, Spectrometers, Detectors and Associated Equipment*, vol. 659, no. 1, pp. 136 – 153, 2011.

# RECENT RESULTS FROM MICE ON MULTIPLE COULOMB SCATTERING AND ENERGY LOSS

J. C. Nugent\*, P. Soler, University of Glasgow, Glasgow, United Kingdom  
 R. Bayes, Laurentian University, Sudbury, Canada

## Abstract

Multiple coulomb scattering and energy loss are well known phenomena experienced by charged particles as they traverse a material. However, from recent measurements by the MuScat collaboration, it is known that the available simulation codes (GEANT4, for example) overestimate the scattering of muons in low Z materials. This is of particular interest to the Muon Ionization Cooling Experiment (MICE) collaboration which has the goal of measuring the reduction of the emittance of a muon beam induced by energy loss in low Z absorbers. MICE took data without magnetic field suitable for multiple scattering measurements in the spring of 2016 using a lithium hydride absorber. The scattering data are compared with the predictions of various models, including the default GEANT4 model.

## INTRODUCTION

Results from atmospheric neutrinos at Super-Kamiokande [1] and from solar neutrinos at the Sudbury Neutrino Observatory [2] conclusively demonstrated that neutrinos have a non-zero mass and oscillate between different flavours. A facility promising precision measurement of neutrino oscillations parameters is the Neutrino Factory [3], where neutrinos would be produced via muon decay rings. Before the muons are injected into the storage ring the phase-space volume of the beam must be reduced. The only cooling technique which can act within the lifetime of the muon is ionization cooling and has shown in simulation to reduce the phase-space volume of the beam by a factor of 100,000 [4–6]. MICE Step IV is current taking data to provide the first measurement of ionization cooling. This demonstration is an essential part of the worldwide research effort towards building a Neutrino Factory. A Neutrino Factory is the only proposed facility with the capability to measure the CP violation phase,  $\delta_{CP}$ , with 5° accuracy.

## MICE BEAM LINE AND EXPERIMENT

The MICE experiment is located at the Rutherford Appleton Laboratory (RAL) in the UK and operates parasitically on the ISIS proton accelerator [7], producing beam for the newly built MICE Muon Beam (MMB) by the insertion of an internal pion-production target. MICE is a novel single particle experiment designed to perform high precision measurements of normalized emittance both upstream and downstream of the ionization cooling equipment. The MMB is composed of three quadrupole triplets, two dipole magnets, which select the momentum, and a decay solenoid

\* john.nugent@glasgow.ac.uk

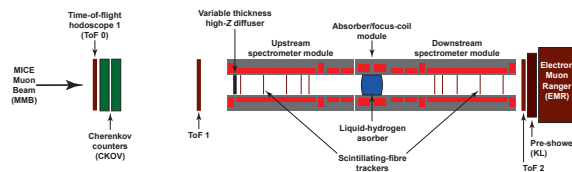


Figure 1: Schematic of Step IV of the MICE experiment, with the Absorber Focus Coil between the two Spectrometer Solenoids.

(DS), which increases the number of muons in the beam. The MICE Step IV setup is shown in Figure 1. It consists of an Absorber Focus Coil (AFC) located between two measurement stations. These stations are composed of particle identification suites including a total of three time-of-flight detectors (TOFs) [8], two Cherenkov detectors (Ckova and Ckvb) [9], the KLOE-type sampling calorimeter (KL) [10] and the Electron Muon Ranger (EMR) [11]. Each station has a Tracker with five planes of scintillating fibres inside a 4 T Spectrometer Solenoid (SS) to measure track and momentum information ( $x$ ,  $y$ ,  $p_x$  and  $p_y$ ), so as to reconstruct the emittance before and after cooling. In MICE Step IV the AFC module, which houses the liquid hydrogen or lithium hydride absorber within a focusing coil, is located between the two measurement stations.

## OVERVIEW OF MULTIPLE COULOMB SCATTERING

The PDG recommends an approximate multiple scattering formula [12, 13], which is found to be accurate to approximately 11%:

$$\theta_0 \approx \frac{13.6 \text{ MeV}}{p_\mu \beta_{\text{rel}}} \sqrt{\frac{\Delta z}{X_0}} \left[ 1 + 0.0038 \ln \left( \frac{\Delta z}{X_0} \right) \right], \quad (1)$$

where  $\theta_0$  is the rms width of the projected scattering angle distribution,  $X_0$  is the radiation length of the material and  $\Delta z$  is the thickness of the absorber,  $p_\mu$  is the momentum of the muon and  $\beta_{\text{rel}} = p_\mu c / E_\mu$ , with  $E_\mu$  its energy. From this an approximate cooling formula can be derived (ignoring the logarithmic term of Equation (1)),

$$\frac{d\varepsilon_n}{dz} = -\frac{\varepsilon_n}{E_\mu \beta_{\text{rel}}^2} \left\langle \frac{dE_\mu}{dz} \right\rangle + \frac{\beta}{2m_\mu \beta_{\text{rel}}^3} \frac{(13.6 \text{ MeV})^2}{E_\mu X_0}, \quad (2)$$

where  $\varepsilon_n$  is the normalised transverse (two-dimensional) emittance of the beam,  $\beta$  is the betatron function, and  $m_\mu$  the energy and mass of the muons [14]. Given that the goal of

MICE is to measure the reduction in normalised emittance with 1% precision, which requires an absolute emittance measurement precision of 0.1%, this approximate formula is not sufficient for the needs of MICE. This demands an accurate measurement of MCS for relevant low-Z materials, such as liquid hydrogen and lithium hydride, where simulations are not in good agreement with data. The MUSCAT experiment carried out a measurement of muon scattering in low-Z materials [15] and found significant differences between a number of models and the measured distributions.

The theory of Multiple Coulomb Scattering, developed by Rossi and Greisen [16] and Molière [17] considered the Rutherford scattering with a low angle cut-off

$$\frac{\theta_0^2}{z} = 16\pi N_A \frac{Z^2}{A} r_e^2 \left( \frac{mc}{p_\mu \beta} \right) \ln \left( 196 Z^{-1/3} \left( \frac{Z}{A} \right)^{1/6} \right) \quad (3)$$

$$\approx \frac{(21.2 \text{ MeV})^2}{p_\mu^2 \beta^2} \frac{1}{X_0}$$

where only interactions with the atomic nucleus are included, with a distribution proportional to  $Z^2$ , where  $Z$  is the atomic number of the scattering material. Bethe [18] adapted the Molière theory to include atomic electron scattering, which implied a proportionality of  $Z(Z+1)$  however this theory still assumed equal weight was given to both nuclear and atomic electron scattering. Early theories of MCS were reviewed by Scott [19]. Further modifications were made to the original theory by Lynch and Dahl to incorporate a path length dependance which resulted in the PDG formulae quoted in expression 1. Both the Molière and Bethe theories were compared to MCS data for a variety of absorbers in MUSCAT, and it was found that these theories did not describe low-Z materials adequately.

Most particle physics simulations use GEANT4 [20] to evaluate particle interactions with matter. GEANT4 makes a parameterisation of the scattering distribution for finite thickness of the material then proceeds stepwise through the simulated material calculating the contribution for each step. Multiple scattering in GEANT4 does not use a small angle approximation and relies on a Legendre polynomial expansion, where the default physics list evaluates the Urban cross-section [21, 22] for most particles and the Wentzel single-scattering cross-section for muons. This model works well for high-Z materials but overestimates scattering for low-Z materials. Alternative models which can overcome these shortcomings have been proposed, namely the Cobb-Carlisle model [14, 23] which samples directly from the Wentzel single-scattering cross-section and simulates all collisions with nuclei and electrons. This includes a cut-off for the nuclear cross-section and separate contributions from the nuclear and atomic electron scattering

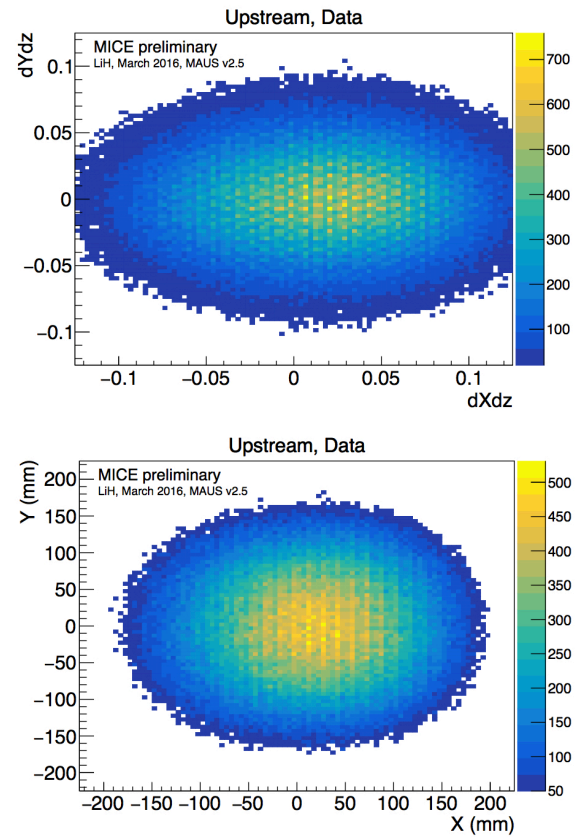


Figure 2: Upstream position distributions for a 200 MeV/c muon beam in the LiH data after particle selection.

$$\frac{\theta_0^2}{z} = 8\pi N_A \frac{Z^2}{A} r_e^2 \left( \frac{mc}{p_\mu \beta} \left[ \ln \left( \frac{\theta_2^2}{\theta_1^2} + 1 \right) - 1 \right] + \frac{1}{Z} \left[ \ln \left( \frac{\theta_2^e}{\theta_1^e} + 1 \right) - 1 \right] \right) \quad (4)$$

Therefore, MICE will need to measure MCS for low-Z materials, such as liquid hydrogen and lithium hydride, to perform an accurate measurement of ionisation cooling. The lithium hydride absorber has a thickness of 65 mm ( $6.7\% X_0$ ) where the lithium hydride composition is: 81%  ${}^6\text{Li}$ , 4%  ${}^7\text{Li}$ , 14%  ${}^1\text{H}$  with traces of C, O, and Ca.

## SCATTERING DATA

The MICE Muon Beam has been fully characterised [24] and has a pion contamination of less than 1.4% at 90% C.L. [25]. For the lithium hydride data the beam was operated in “muon mode” giving an almost pure muon beam at a variety of momenta. For this measurement a beam with a  $3\pi$  mm·rad emittance beam was selected. The lithium hydride MCS data taking period was during the 2015/04 ISIS user cycle from the 23rd of February until the 24th of March 2016. The volume between the absorber and the two trackers was filled with helium to minimise multiple scattering not due to the absorber. The measurements were carried out without a magnetic field either in the tracker volume or surrounding the absorber. During the 2015/04

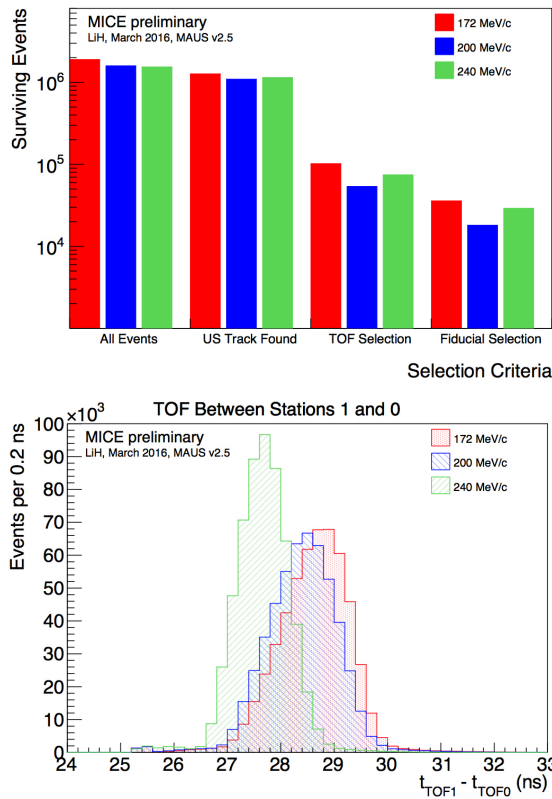


Figure 3: Left: The survival of muons after each stage of the selection. Right: The time of flight for muons between TOF0 and TOF1 for each of the nominal momentum points that MICE will measure scattering at.

data taking period, the channel was entirely empty when the lithium hydride was removed. Momentum measurements were carried out using the time-of-flight difference between TOF1 and TOF2. Only tracks that have hits in TOF1 in both planes, with one muon reconstructed in each event and within the time of flight window, are selected for the analysis. Tracks are projected downstream from the upstream tracker volume to the reference plane of the downstream tracker and must be within a 150 mm radius from the centre of the reference plane to be selected. The beam spot in the trackers after selection is shown in Figure 2 and the population of muons after each selection is shown in Figure 3.

## MOMENTUM CORRECTION

The two MICE trackers can measure the momentum of muons up- and downstream of the absorber when both spectrometer solenoids are energised. When the solenoidal magnetic fields are present in the channel muons follow a helical trajectory from which a momentum measurement can be made. In the case where there are no magnetic field in the cooling channel no measurement of momentum can be made with the trackers. In this scenario a momentum measurement is made with the MICE time of flight system using the expression:

$$p = \frac{m}{\sqrt{\frac{t_{12}^2 c^2}{L^2} - 1}} \quad (5)$$

However this expression makes several assumptions, namely that the muons are on axis and undergo no energy loss between the TOF stations. To account for these effects a correction is applied to the momentum as reconstructed by the TOF system to reconstruct the exact momentum at the centre of the absorber. The calculation is an analytic expression which is the second order expansion of the Taylor series in  $p/mc$  for the exact path of the muon between TOF stations. One caveat of this method is that constant energy loss is assumed. However even with this approximation good agreement between reconstructed momentum and that obtained from MC truth is shown in Figure 4 with the residuals shown in Figure 5.

## TRACKER ACCEPTANCE

The geometric acceptance of the scattering angles that can be measured by MICE are determined by the apertures of the cooling channel. The effect of this acceptance on the scattering distributions must be accounted for and is determined by considering Monte Carlo (MC) simulations of the

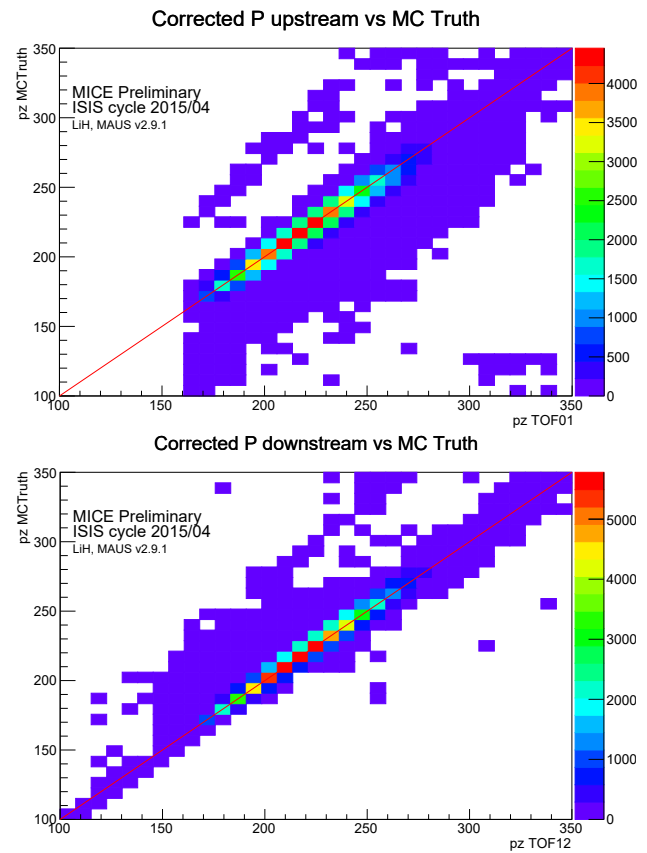


Figure 4: Figures showing the agreement between the momentum calculated by the correction up- (left) and downstream (right) and the momentum determined from MC truth.

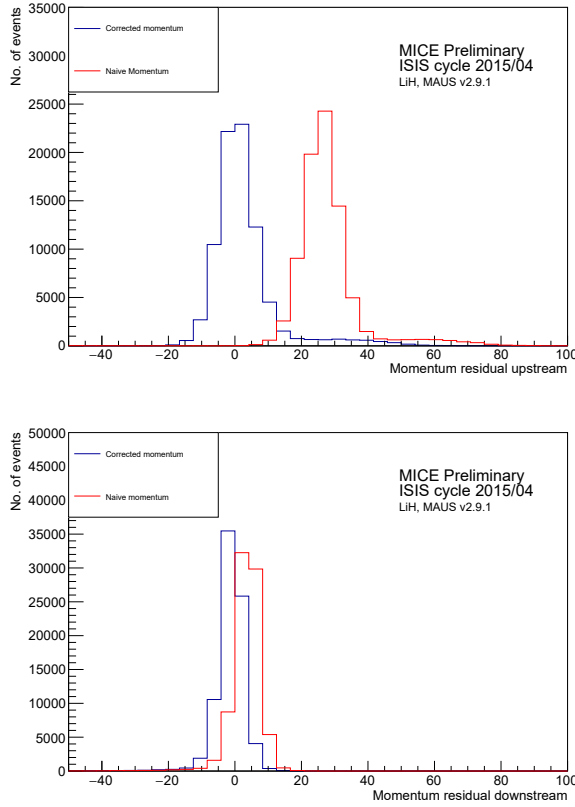


Figure 5: Figures showing the residual between the momentum before and after correction up- (top) and downstream (bottom) and the momentum determined from MC truth.

MICE beam. In simulation both the number of tracks which are expected (i.e. seen in MC truth) and number of tracks reconstructed (i.e. seen in the reconstructed data) is known. The full analysis chain is then run, tracks are matched upstream and downstream, the selection is performed and the scattering angle is calculated. The downstream acceptance is then defined as

$$\frac{\text{No. of tracks in } \theta \text{ bin MC Truth that are reconstructed}}{\text{No. of tracks in } \theta \text{ bin MC Truth}} \quad (6)$$

It is assumed that the upstream efficiency is 100%, as by construction if a track is never seen upstream then no scattering angle is ever measured. The measured acceptance is shown in Figure 6

## DECONVOLUTION OF RAW SCATTERING DATA

The scattering in the absorber material is the physical quantity of interest. To extract this information the effects of scattering in non absorber materials and detector resolution that will appear in the overall scattering measurement must be deconvolved from the required scattering distribution. A deconvolution algorithm using Bayesian statistics [26]

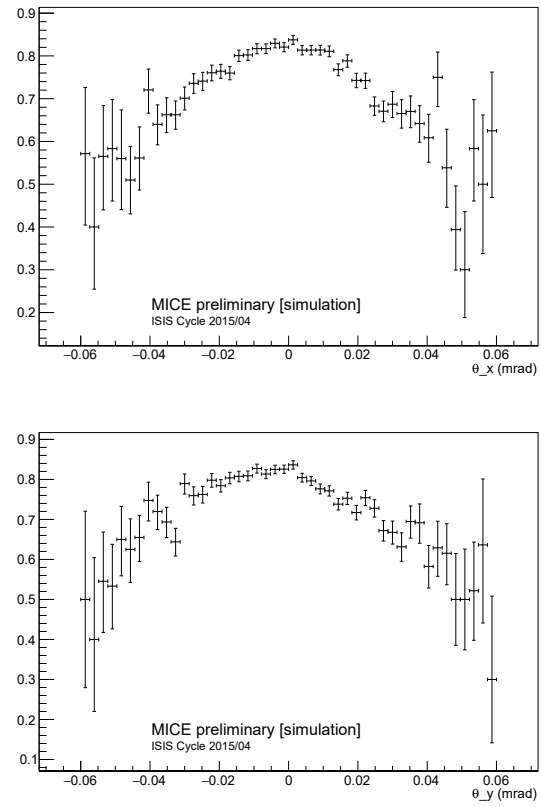


Figure 6: Figures showing the downstream tracker acceptance in  $\theta_x$  (top) and  $\theta_y$  (bottom).

has been used based on the implementation contained in the RooUnfold package [27]. This method uses the simulation to provide a probability of observing a given scattering angle from the trackers for a given true scattering angle in the absorber,  $P(\Delta\theta_j^{tracker}|\Delta\theta_i^{abs})$ . This conditional probability is then used to estimate the number of particles that experience an absorber scattering angle,

$$n(\theta_i^{abs}) = \sum_{j=1}^{n_E} n(\theta_j^{tracker})P(\theta_i^{abs}|\theta_j^{tracker}), \quad (7)$$

which requires the calculation of the conditional probability

$$P(\theta_i^{abs}|\theta_j^{tracker}) = \frac{P(\theta_j^{tracker}|\theta_i^{abs})P_0(\theta_i^{abs})}{\sum_{l=1}^{n_c} P(\theta_j^{tracker}|\theta_l^{abs})P_0(\theta_l^{abs})} \quad (8)$$

The estimate is refined through multiple applications of the algorithm by updating the prior probability by letting  $P_0(\theta_i^{abs}) = n(\theta_i^{abs})/\sum_{i=1}^{n_c} n(\theta_i^{abs})$  in iterations subsequent to the initial calculation in which a flat prior is used. The conditional probability  $P(\theta_j^{tracker}|\theta_i^{abs})$  is derived from the convolution where  $\theta_j^{tracker}$  is drawn from the sum of the reconstructed scattering angle in the empty absorber data and the scattering angle in the absorber from the convolution

Content from this work may be used under the terms of the CC BY 3.0 licence (© 2017). Any distribution of this work must maintain attribution to the author(s), title of the work, publisher, and DOI.

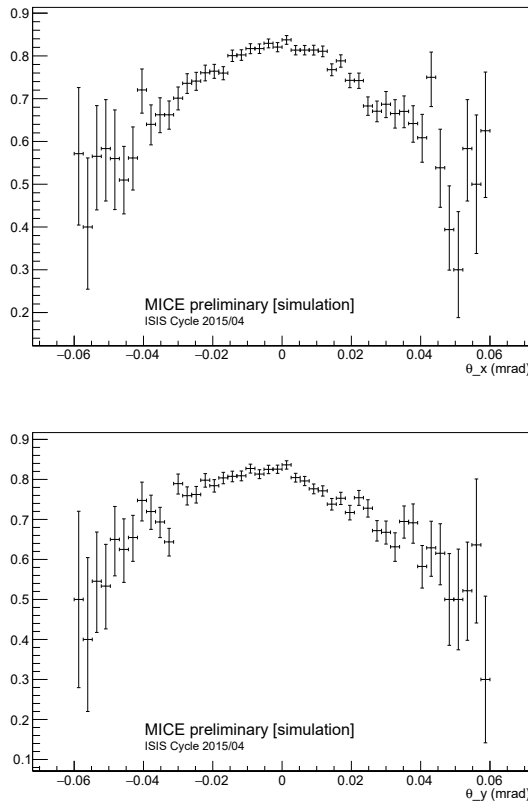


Figure 7: The results of the scattering analysis using data from all three nominal beam settings. Scattering widths are reported after application of deconvolution.

model, and  $\theta_i^{abs}$  is the scattering angle in the absorber alone. The final scattering distributions at each of the nominal momentum points are shown in Figure 7 and over the full momentum range in Fig. 8.

## CONCLUSION

MICE has measured multiple Coulomb scattering off a lithium hydride target for muons with momentum between 140 and 240 MeV/c. These data have been compared to popular simulation packages such as GEANT4 and other relevant models such as Moliere and Carlisle-Cobb. A study of the systematics is in progress with a MICE publication currently being prepared. Future work will include a measurement of multiple Coulomb scattering off liquid hydrogen, a measurement of scattering with magnetic field in the cooling channel and an energy loss measurement.

## REFERENCES

- [1] Y. Fukuda *et al.*, "Evidence for oscillation of atmospheric neutrinos", *Phys.Rev.Lett.*, 81:1562–1567, 1998.
- [2] Q. R. Ahmad *et al.*, "Direct evidence for neutrino flavor transformation from neutral current interactions in the Sudbury Neutrino Observatory", *Phys. Rev. Lett.*, 89:011301, 2002.

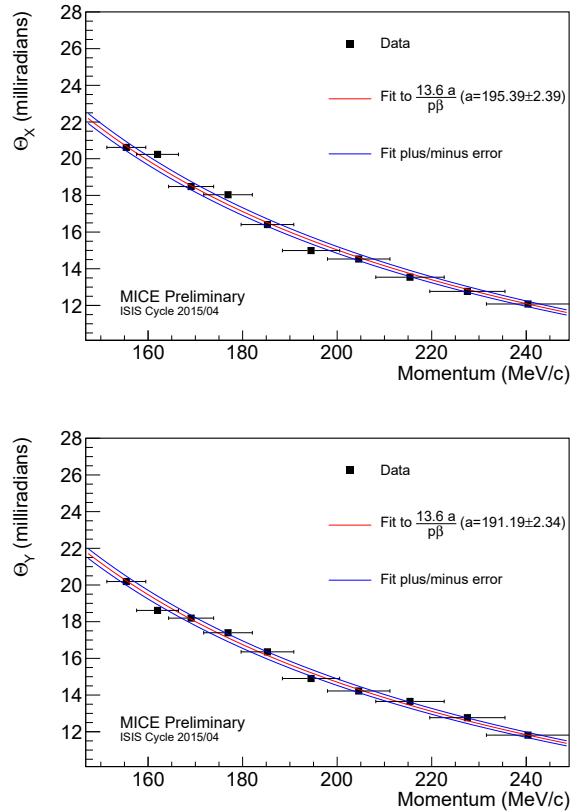


Figure 8: The results of the scattering analysis using data from all three nominal beam settings. Scattering widths are reported after application of deconvolution.

- [3] S. Geer, "Neutrino beams from muon storage rings: Characteristics and physics potential", *Phys. Rev.*, D57:6989–6997, 1998.
- [4] Diktys Stratakis, Richard C. Fernow, J. Scott Berg, and Robert B. Palmer. "Tapered channel for six-dimensional muon cooling towards micron-scale emittances", *Phys. Rev. ST Accel. Beams*, 16(9):091001, 2013.
- [5] Diktys Stratakis and Robert B. Palmer. "Rectilinear six-dimensional ionization cooling channel for a muon collider: A theoretical and numerical study", *Phys. Rev. ST Accel. Beams*, 18(3):031003, 2015.
- [6] Diktys Stratakis, "A hybrid six-dimensional muon cooling channel using gas filled rf cavities", *JINST*, 12(09):P09027, 2017.
- [7] M. Bogomilov *et al.*, "The MICE Muon Beam on ISIS and the beam-line instrumentation of the Muon Ionization Cooling Experiment", *JINST*, 7:P05009, 2012.
- [8] R. Bertoni *et al.*, "The design and commissioning of the MICE upstream time-of-flight system", *Nucl. Instrum. Meth.*, A615:14–26, 2010.
- [9] Lucien Cremaldi, David A. Sanders, Peter Sonnek, Donald J. Summers, and Jim Reidy, Jr., "A Cherenkov Radiation Detector with High Density Aerogels", *IEEE Trans. Nucl. Sci.*, 56:1475–1478, 2009.

- [10] M. Adinolfi, A. Aloisio, F. Ambrosino, A. Andryakov, A. Antonelli, *et al.*, "Calibration and reconstruction performances of the KLOE electromagnetic calorimeter", *Nucl. Instrum. Meth.*, A461:344–347, 2001.
- [11] D. Adams *et al.*, "Electron-Muon Ranger: performance in the MICE Muon Beam", *JINST*, 10(12):P12012, 2015.
- [12] K. A. Olive *et al.*, "Review of Particle Physics", *Chin. Phys.*, C38:090001, 2014.
- [13] Gerald R. Lynch and Orin I. Dahl, "Approximations to multiple Coulomb scattering", *Nucl. Instrum. Meth.*, B58:6–10, 1991.
- [14] Timothy Carlisle, "Step IV of the Muon Ionization Cooling Experiment (MICE) and the multiple scattering of muons", *DPhil thesis, University of Oxford*, 2013.
- [15] D. Attwood *et al.*, "The scattering of muons in low Z materials", *Nucl. Instrum. Meth.*, B251:41–55, 2006.
- [16] Bruno Rossi and Kenneth Greisen, "Cosmic-ray theory", *Rev. Mod. Phys.*, 13:240–309, 1941.
- [17] G. Moliere, "Theory of the scattering of fast charged particles. 2. Repeated and multiple scattering", *Z. Naturforsch.*, A3:78–97, 1948.
- [18] H. A. Bethe, "Moliere's theory of multiple scattering", *Phys. Rev.*, 89:1256–1266, 1953.
- [19] William T. Scott, "The theory of small-angle multiple scattering of fast charged particles", *Rev. Mod. Phys.*, 35:231–313, 1963.
- [20] S. Agostinelli *et al.*, "GEANT4: A Simulation toolkit", *Nucl. Instrum. Meth.*, A506:250–303, 2003.
- [21] Laszlo Urban, "A model for multiple scattering in Geant4", 2006. CERN-OPEN-2006-077.
- [22] V. N. Ivanchenko, O. Kadri, M. Maire, and L. Urban, "Geant4 models for simulation of multiple scattering", *J. Phys. Conf. Ser.*, 219:032045, 2010.
- [23] T. Carlisle, J. Cobb, and D. Neuffer, "Multiple Scattering Measurements in the MICE Experiment", *Conf. Proc.*, C1205201:1419–1421, 2012.
- [24] D. Adams *et al.*, "Characterisation of the muon beams for the Muon Ionisation Cooling Experiment", *Eur. Phys. J.*, C73:2582, 2013.
- [25] M. Bogomilov *et al.*, "Pion Contamination in the MICE Muon Beam", *JINST*, 11(03):P03001, 2016.
- [26] G. D'Agostini, "A Multidimensional unfolding method based on Bayes' theorem", *Nucl. Instrum. Meth.*, A362:487–498, 1995.
- [27] Tim Adye, "Unfolding algorithms and tests using RooUnfold", in *Proceedings of the PHYSTAT 2011 Workshop, CERN, Geneva, Switzerland, January 2011, CERN-2011-006*, pages 313–318, 2011.

# LOW ENERGY ELECTRON COOLER FOR THE NICA BOOSTER

Alexander Bublely, Maxim Bryzgunov, Vladimir Chekavinskiy, Anatoly Goncharov,  
 Konstantin Gorchakov, Igor Gusev, Vitalij Panasyuk, Vasily Parkhomchuk,  
 Vladimir Reva, Dmitriy Senkov, BINP SB RAS, Novosibirsk, Russia  
 Alexander V. Smirnov, JINR, Dubna, Moscow Region, Russia

## Abstract

The low energy electron cooler for the NICA booster has recently been installed at the booster ring of the NICA facility. The article describes results of various measurements obtained during its commissioning. In addition, some details of design and construction of the cooler are discussed.

## INTRODUCTION

NICA collider contains a big number of complicated systems and subsystems. One of them is gold ion booster which is located at the existing hall of former synchrotron, and new superconductive magnets sit inside old giant iron yokes [1]. Low energy cooler is one of the elements of the booster those provides sufficient improvement of the ion beam quality.

Main specifications of the cooler are listed below:

ions type	p+ up to $^{197}\text{Au}^{31+}$
electron energy, $E$	$1,5 \div 50$ keV
electron beam current, $I$	$0,2 \div 1,0$ Amp.
energy stability, $\Delta E/E$	$\leq 1 \cdot 10^{-5}$
electron current stability, $\Delta I/I$	$\leq 1 \cdot 10^{-4}$
electron current losses, $\delta I/I$	less than $3 \cdot 10^{-5}$
longitudinal magnetic field	$0,1 \div 0,2$ T
inhomogeneity of the field, $\Delta B/B$	$\leq 3 \cdot 10^{-5}$
transverse electron temperature	$\leq 0,3$ eV
ion orbit correction:	
displacement	$\leq 1,0$ mm
angular deviation	$\leq 1,0$ mrad
residual gas reassurement	$\leq 1 \cdot 10^{-11}$ mbar.

## MAGNETIC MEASUREMENT RESULTS

Magnetic system of the cooler consists of central solenoid, bending toroids, gun-collector solenoids and correctors [2]. Requirement for the magnetic field straightness is  $\Delta B/B \leq 3 \cdot 10^{-5}$  for the central (cooling) solenoid.

Measurements were performed with compass based measurement system [3].

The results of those measurements are shown on Fig. 1. Vertical and horizontal components of the magnetic field were measured several times during solenoid adjustment. Starting data (just after shipping of the cooler) are drawn as black curves. Red curves present final results of solenoid adjustment thus the requirement was fulfilled.

The solenoid was tuned at 1 kG of the longitudinal field as long as it is a middle of required field range. If we apply other values of magnetic field the vertical component

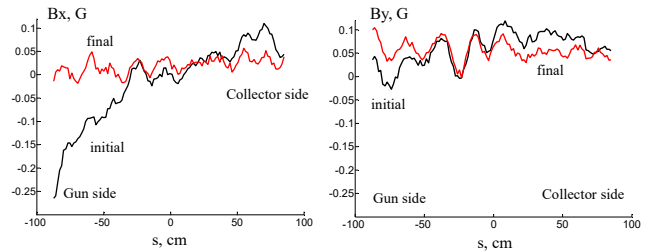


Figure 1: Horizontal (left) and vertical (right) magnetic field components before (black) and after (red) coils adjustment.

will change (Figs. 2 and 3). To improve the situation the cooler is equipped with linear correction coils attached along the solenoid so as each value of longitudinal field corresponds to amplitude of current applied to the linear corrector.

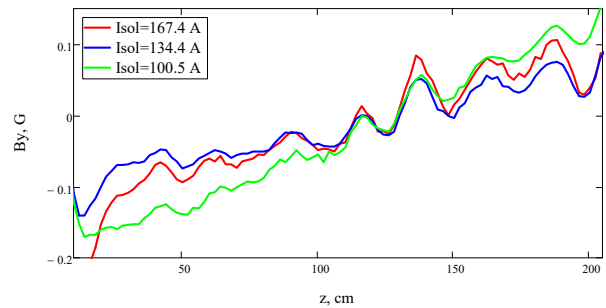


Figure 2: Vertical field component measured at different value of the longitudinal field. Red – 1 kG, blue – 800 G, green – 700 G.

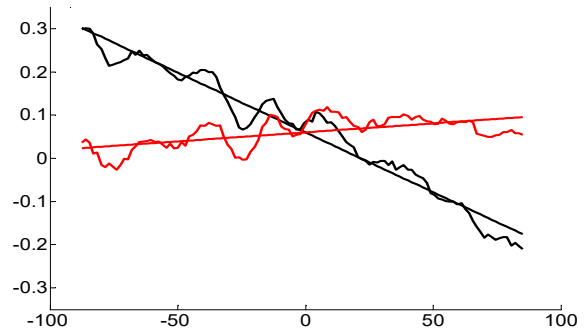


Figure 3: Linear (vertical) corrector calibration.

For the solenoid tuning its coils are slightly rotated or inclined depending on direction of the transverse field to be corrected. The movement of the coils on 0.1 mm corresponds to  $3 \cdot 10^{-4}$  in angle of the field that by order of magnitude higher than required accuracy.

Content from this work may be used under the terms of the CC BY 3.0 licence (© 2017). Any distribution of this work must maintain attribution to the author(s), title of the work, publisher, and DOI.



Figure 4: So-called pancake coils in cooling solenoid.

All coils in the solenoid have the supports on both sides those can be turned with two screws as shown in Fig. 4.

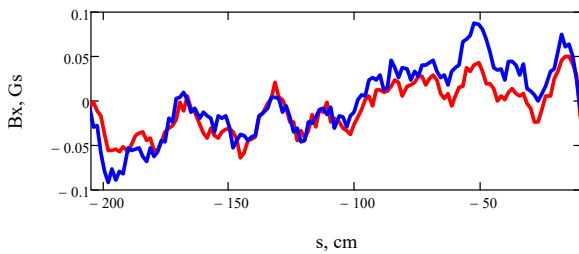


Figure 5: Horizontal field component before (red) and after (blue) all screws were tightened.

The position of the coils is very sensitive to those screws tension. Figure 5 showed the difference between two measurements of the field performed just before and after screws tightening.

One more important thing in reaching high straightness is residual field. Its value is rather high in comparison with acceptable transverse field distortion.

## ELECTRON GUN AND COLLECTOR

The electron gun design is similar (Fig. 6) to one taken from the 2 MeV cooler for COSY synchrotron [4]. Few changes were made to improve pumping of the inner volume and insulator was modified to meet HV requirement.

The collector consists of two parts. First is massive copper body with water cooling for primary electron beam accepting. Second one is metal-ceramics assembly providing 60 kV insulation and support for suppressor and pre-collector electrode. Both electrodes are intended to reduce the number of secondary electrons, reflected from collector.

The electron gun has four sectors control electrode what give an opportunity of the electron beam position measurement (with BPMs). Also it is possible to estimate the beam shape [4].

The volt-ampere characteristic of the gun is shown in Fig. 7. Control electrode voltage  $U_{grid}$  is divided on  $U_{anode}$ , and beam current  $I_{coll}$  on anode voltage  $U_{anode}^{1.5}$ . This scaling allow to compare data obtained at different anode voltage so curves are similar.

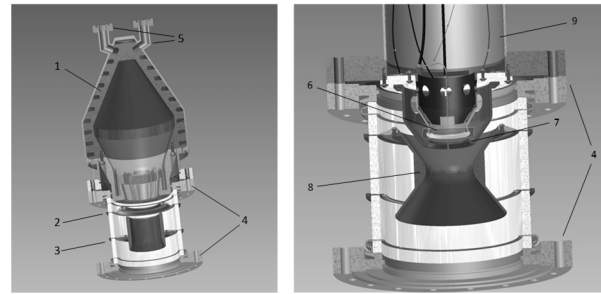


Figure 6: collector (left) and the gun (right). 1 – electron input, 2 – suppressor, 3 – pre-collector 4 – vacuum flanges, 5 – oil cooling tubes, 6 – cathode assembly, 7 – control electrode, 8 – anode, 9 – feedthroughs.

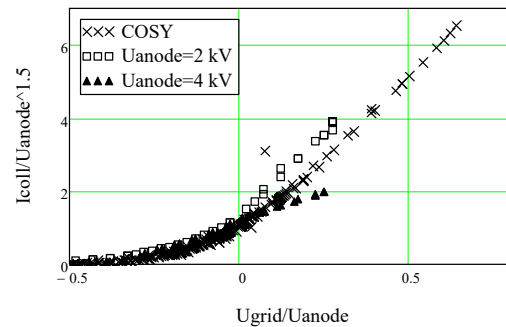


Figure 7: Volt-ampere characteristic of the gun at different setups of the cooler parameters.

## VACUUM GENERATION

The vacuum system of the cooler has a volume approximately  $0.2 \text{ m}^3$ . On the other hand, the internal surface of the vacuum chamber is very advanced as it contains bending plates and other various electrodes [5]. That leads to rather high outgassing rate. The scheme of the vacuum system is shown in Fig. 8.

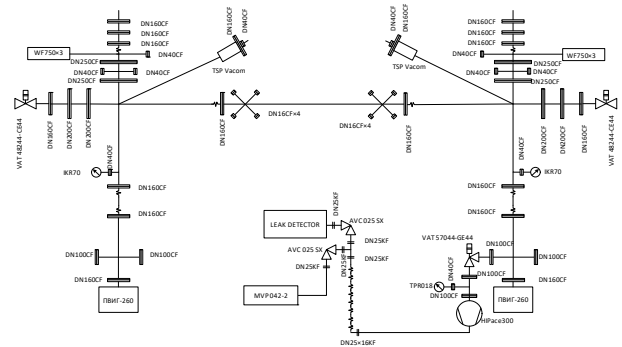


Figure 8: Scheme of the vacuum system.

For obtaining the required vacuum condition as  $\leq 1 \times 10^{-11}$  mbar following pumping equipment was included into the system.

1. Ion pump combined with TPS “PVIIG – 260” is most efficient in the range  $1 \times 10^{-6}$  to  $1,5 \times 10^{-8}$  Pa, total highest pumping speed 630 l/s.
2. Titanium sublimation pump TSP-IPG (“Vacom”) is used with special ambient screen with surface

area 1320 m<sup>2</sup>, which corresponds to approximately 2000 l/s of pumping speed.

- Every getter pump contains three modules of WP750-ST707. Data for one module: stripe surface 870 cm<sup>2</sup>, stripe thickness 0.2 mm, resistance 0.16 Ω, size 207×50×30 mm, pumping speed (H<sub>2</sub> - 330 l/s, CO - 130 l/s), sorption capacity (H<sub>2</sub>-660 torr<sup>-1</sup>, CO - 75 torr<sup>-1</sup>, activation current (450°C) is 27 amps.

All components of the vacuum system were baked out up to 300°C for about two days with back pumping (300 l/s turbopump). The heating as well as cooling speed was about 0.5 °C/min to protect numerous electric feed-throughs and other components contained ceramics. During cooling of the vacuum system the oxide cathode activation was performed and the NEG pump activation was done. After all those procedures were completed the system was closed from back pumping and ion pumps were turned on. Finally, the required vacuum condition was obtained.

## OXIDE CATHODE ACTIVATION

The oxide cathode, as required, was activated during the vacuum system bake-out with back pumping. The activation process is very sensitive to the vacuum condition when the cathode surface is overheated to provide necessary temperature. If the pressure is over required threshold so called, ‘cathode poisoning’ may occur. This leads to dramatic decrease of the emission ability of the cathode.

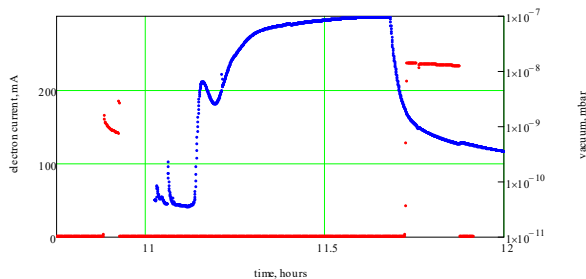


Figure 9: Electron current (red) and residual gas pressure (blue).

This experiment aimed at study the influence of the residual gases released during NEG regeneration on oxide cathode properties. The electron current was measured before and after regeneration process. Cathode filament was on during the experiment. Pressure measurement plotted on Fig.9 as a blue curve while electron current is red. Surprisingly the current significantly increased, that means the cathode surface was ‘cured’ with the hydrogen released from the NEGs.

The mass spectrogram of the residual gas composition is shown in Fig. 10. Blue bars in the figure correspond to the ions current at the cooler vacuum chamber; those are

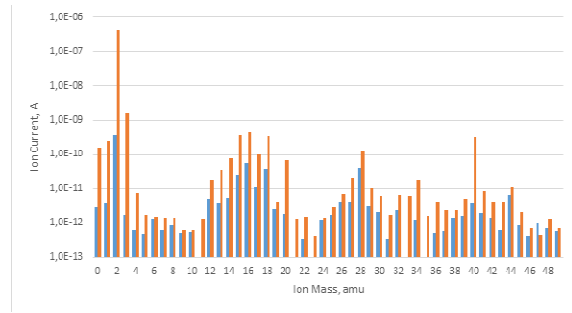


Figure 10: Residual gas mass spectrogram.

proportional to the partial pressure of the correspondent gas components. Red bars show the condition during NEGs regeneration. One may conclude that the hydrogen has pressure higher by 1000 times in comparison with other components.

## SUMMARY

The low energy electron cooler was successfully tested at BINP, shipped and partially commissioned at NICA booster.

During various measurements some techniques were improved. Nevertheless there are some points where the limits are reached and more efforts are needed to go further. One of them is magnetic lines straightness in the cooling solenoid. To get this parameter better than  $3 \cdot 10^{-5}$  for future projects following steps have to be made:

- improve design for coils support
- increase accuracy for mechanical movement
- residual field has to be compensated
- in-vacuum measurements are required.

## REFERENCES

- [1] N.Agapov, A.Butenko, *et al.*, “Booster synchrotron for NICA collider”, *Physics of Particles and Nuclei Letters*, 2010, Vol. 7, No. 7, pp. 723–730.
- [2] M. I. Bryzgunov, A. V. Bublei\*, A. D. Goncharov, *et al.*, “Status of Construction of the Electron Cooling System for the NICA Booster”, *Physics of Particles and Nuclei Letters*, 2016, Vol. 13, No. 7, pp. 792–795. © Pleiades Publishing, Ltd., 2016.
- [3] V. N. Bocharov, M. I. Bryzgunov, A. V. Bublei, V. G. Cheskidov, M. G. Fedotov, V. V. Parkhomchuk, V. B. Reva, “System of Measurement of magnetic field line straightness in solenoid of electron cooler for COSY”, in *Proceedings of COOL’11*, Alushta, Ukraine, 2011.
- [4] A. Bublei, A. Goncharov, A. Ivanov, *et al.*, “The electron gun with variable beam profile for optimization of electron cooling” in *Proceeding of EPAC 2002*, Paris, France, p.1357 - 1358.
- [5] M. I. Bryzgunov, A. V. Bublei\*, A. D. Goncharov, *et al.*, “Status of Construction of the Electron Cooling System for the NICA Booster”, *Physics of Particles and Nuclei Letters*, 2016, Vol. 13, No. 7, pp. 792–795. © Pleiades Publishing, Ltd., 2016.

## HIGH VOLTAGE COOLER NICA STATUS AND IDEAS

V.B. Reva<sup>1</sup>, M.I. Bryzgunov, A.V. Bublely, A.D. Goncharov, N.S. Kremnev, V.M. Panasyuk,  
 V.V. Parkhomchuk<sup>1</sup>, V.A. Polukhin, A.A. Putmakov BINP, Novosibirsk, Russia  
<sup>1</sup>also at Novosibirsk State University, Novosibirsk, Russia

### Abstract

The new accelerator complex NICA [1-2] is designed at the Joint Institute for Nuclear Research (JINR, Dubna, Russia) to do experiment with ion-ion and ion-proton collision in the range energy 1-4.5 GeV/u. The main regime of the complex operation is ion collision of heavy ion up to Au for study properties of dense baryonic matter at extreme values of temperature and density. The planned luminosity in these experiments is  $10^{27} \text{ cm}^{-2} \cdot \text{s}^{-1}$ . This value can be obtained with help of very short bunches with small transverse size. This beam quality can be realized with electron and stochastic cooling at energy of the physics experiment. The subject of the report is the problem of the technical feasibility of fast electron cooling for collider in the energy range between 0.2 and 2.5 MeV.

### SETUP DESCRIPTION

The NICA collider for study nuclear physics at range of relativistic physics 1-4.5 GeV/u requires powerful electron cooling system to obtain high luminosity. The basic idea of this cooler is to use high magnetic field along all orbit of the electron beam from the electron gun to the electron collector. At this case we have chance to have high enough the electron beam density at cooling section with low effective temperature. The schematic design of the setup is shown in Figure 1. The electron beam is accelerated by an electrostatic generator that consists of 42 individual sections connected in series. Each section has high-voltage power supplies with maximum voltage 60 kV and current 1 mA. The electron beam is generated in electron gun immersed into the longitudinal magnetic field. After that the electron beam is accelerated, moves in the transport line to the cooling section where it will interact with ions of NICA storage ring. After interaction the electron beam returns to electrostatic generator where it is decelerated and absorbed in the collector. Because the NICA is collider there are two electron lines for both ion beams located up and down. Both electron coolers are independent from each other.

The optics of 2 MeV cooler for NICA is designed close to the COSY high-energy coolers [3]. The motion of the electron beam is magnetized (or close to magnetized conditions) along whole trajectory from a gun to a collector. This decision is stimulated by requirement to operate in the wide energy range from 200 keV to 2.5 MeV. So, the longitudinal field is higher than transverse component of the magnetic fields. The essential challenge of this design is low value of the energy consumption of magnetic field 500-700 kW for both coolers. So, the volume of copper in

the coils is maximum as possible taken into account the small distance between beam lines. This distance is 32 cm. The length of the linear magnets is defined by the necessity to locate the electrostatic generator outside the shield area of the storage ring.

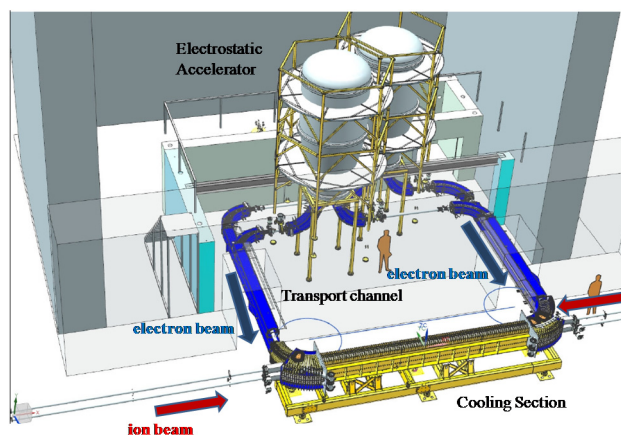


Figure 1: 3D design of 2 MeV COSY cooler.

The vacuum chamber will be pumped down by ion, getter and titanium sublimation pumps. The typical diameter of the vacuum chamber is 100 mm and the aperture in the transport channel and cooling section is close to this value. The diameter of the accelerating tube is 60 mm. The main parameters of NICA cooler can be found in Table 1.

Table 1: Specifications of NICA Cooler

Parameter	Value
Energy range	0.2÷2.5 MeV
Number of the cooling section	2
Stability of energy ( $\Delta U/U$ )	$\leq 10^{-4}$
Electron current	0.1÷1 A
Diameter of electron beam in the cooling section	5÷20 mm
Length of cooling section	6 m
Bending radius in the transport channel	1 m
Magnetic field in the cooling section	0.5÷2 kG
Vacuum pressure in the cooling section	$10^{-11}$ mbar
Height of the beam lines	1500/1820 mm
Total power consumption	500-700 kW

Content from this work may be used under the terms of the CC BY 3.0 licence (© 2017). Any distribution of this work must maintain attribution to the author(s), title of the work, publisher, and DOI.

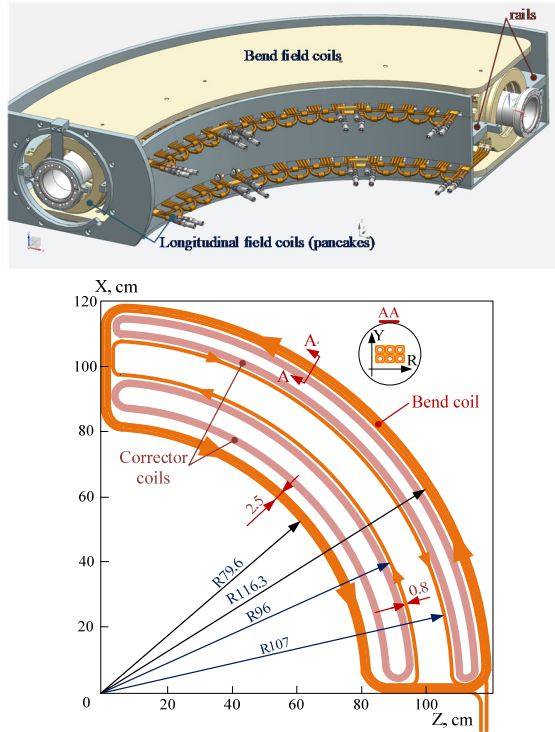


Figure 2: Design of bending magnets.

### MAGNETIC SYSTEM

The magnetic field in the accelerating tube is taken 500 G and this value is related to the maximum power that can be transfer to a high voltage potential with help of the cascade transformer. The value in the transport channel is located in the range 0.5 kG – 1 kG. The energy 2.5 MeV is high enough in order to don't have the complete adiabatic motion of the electrons because the magnetic field of the bend elements is chosen to provide the length of bend equal to integer number of Larmor lengths. In such case the kick on entry to bend is compensated by kick on leaving and the excitation of the transverse motion of the electron is small. So, it is convenient to change the longitudinal magnetic field according to the electron momentum. At attainment of the maximum magnetic field the transition to another integer number is implemented. Figure 2 shows the design of the 90° bending magnets. It consists of coils of the longitudinal magnetic field and coils of the bending field. The last shows separately on the bottom picture. The curve of the bending field should be very close to the centrifugal force  $F_c = pV/R$  (see Fig. 3). In this case the oscillation of the transverse motion of electrons is minimal. To decrease heating of the beam after transition through a bend, the length of the bend should be equal to integer number of Larmor length. In such a case kick on entry to bend in compensated by kick on leaving (see Fig. 4). Also field index  $n=0.5$  is required in order to prevent changing transverse shape of the electron beam. The field index is produced with help of bend coils with special shape.

It is clear that it is possible to set one value of energy of electron beam and to adjust cooler optics for this energy in

order to avoid high temperature of the electron beam in cooling section. But wide range of operating electron energy means that optics of the cooler must be easily adjustable for all energies. One method of realization of such system is to adjust optics manually for every value of energy. Number of parameters and correctors in our system allow us to do this, but this method is very time consuming. There is easier method which was proposed for this system. The idea of the method is to change magnetic field in the cooler synchronously with beam energy.

The magnetic field in the cooling section is taken 2 kG in order to have the maximum Larmor oscillation ( $\sim 20$ ) of the electron during its interaction with ion in order to have the magnetized Coulomb collisions even the highest electron energy 2.5 MeV. The cooling section consists of units with length 1 m. Each section contains coils of the longitudinal magnetic field, the correction coils of the transverse field, magnetic shield and magnetic shield support. Each vacuum section inside unit contains the BPM. So, the rough regulation of the magnetic force line is possible as result measurement of BPM with electron and ion beams. The ion beam is used as base line for the electron beam. The vacuum tube can be covered by NEG coats or contains NEG modules. The preliminary design of the cooling section is shown in Figure 5.

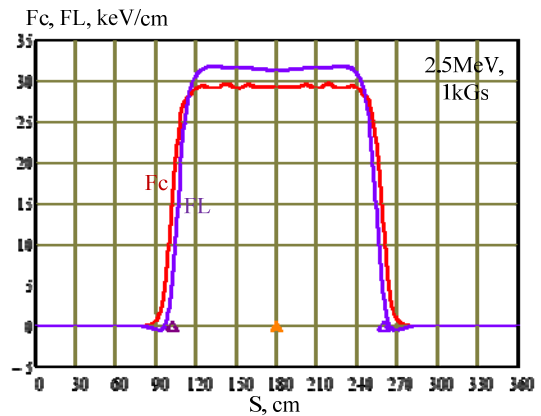


Figure 3: Centrifugal and Lorentz forces in 90 bend magnets.

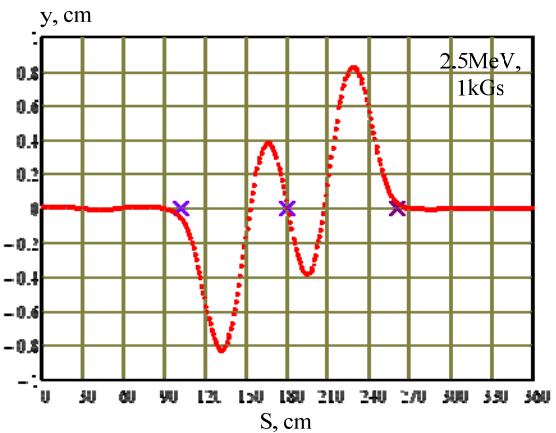


Figure 4: Oscillation of orbit in the bending magnet.

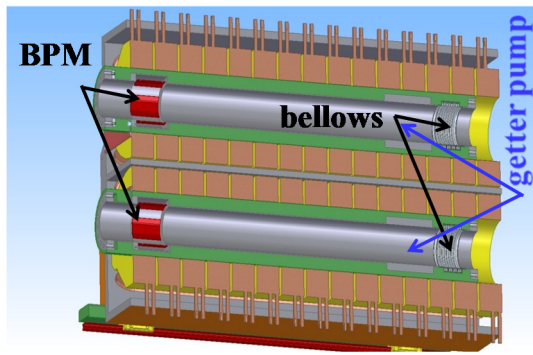


Figure 5: Design of the cooling section.

## ELECTROSTATIC ACCELERATOR

The design of the electrostatic accelerator is shown in Figure 6. The accelerating column consists of 42 identical high voltage sections. The column with high voltage terminal is placed in special vessel which was filled with SF<sub>6</sub> under pressure up to 10 bar. The section contains two magnetic coils producing guiding magnetic field for acceleration and deceleration tubes and the high voltage power supply producing up to 60 kV. Total power consumption of one section is about 300 W. The coils and the electronic components are cooled with transformer oil. Electrostatic accelerator of NICA cooler. It is divided on two parts. The middle section contains of vacuum pumping, BPM, correctors and mechanical support.

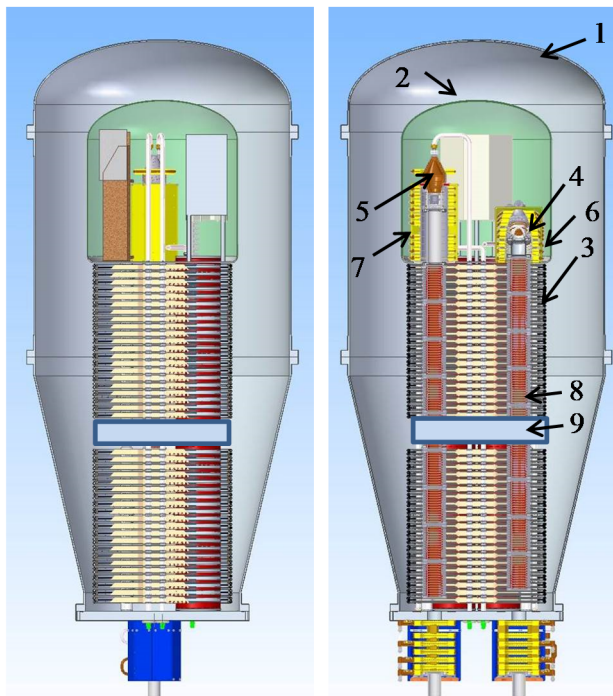


Figure 6: Design of the electrostatic accelerator of NICA cooler. High-pressure vessel for SF<sub>6</sub> is 1, high-voltage terminal (HVT) is 2, high voltage section is 3, electron gun is 4, electron collector is 5, magnetic system of the electron gun is 6, magnetic system of the electron collector is 7, acceleration tube is 8, middle section is 9.

The key problem of the accelerating/decelerating column is transfer energy to 42 sections, gun and collectors are located at high voltage potential. The base idea of the power supply is based on idea of a high frequency cascaded resonant transformer. The system consists of 42 transformers with cascaded connection. The electrical energy is transmitted from section to section from the ground to high-voltage terminal. Along this way the energy is consumed by the regular high-voltage section. The main problem of such decision is leakage inductance of the transformers. They are connected in series and the voltage from power supply is divided between inductance leakage and a useful load. In order to solve this problem the special compensative capacitance is used. This type of the transformer was used in COSY electron cooler [4]. Its length was 2 m and diameter 0.38 m. The length of NICA cooler is larger and power consumption is larger too. Because two transformer column was decided to use. One for collector and the other for the HV sections. Moreover each transformer column is divided by two in the middle section with technological point of view. In this case the transformer length is about 1.3 m that is more convenient for assembling and commissioning. Total length of one transformer column is about 2.6 m.

## CONCLUSION

The many problems of the electron cooler at 2.5 MeV (modular approach of the accelerator column, the cascade transformer, the design of the electron gun with 4-sectors control electrode, Wien filter etc) was experimentally verified during commissioning in COSY. But there is enough new decision induced by the problem of cooling two ion beams in the collider mode. At the end of work the NICA collider will obtain a powerful system of the cooling for luminosity improve.

## REFERENCES

- [1] G. Trubnikov, N. Agapov, V. Alexandrov, *et al.*, "Project of the Nuclotron-based Ion Collider Facility (NICA) at JINR", in *Proceedings of the 11rd European Particle Accelerator Conference (EPAC 08)*, Genoa, Italy, 2008, paper WEPP029, pp. 2581–2583.
- [2] V. Kekelidze, A. Kovalenko, R. Lednickiy, *et al.*, "Feasibility study of heavy-ion collision physics at NICA JINR", *Nucl. Instr. Meth. A*, 967 (2017), pp. 884-887.
- [3] V. B. Reva, N. Alinovskiy, T. V. Bedareva, *et al.*, "COSY 2 MeV Cooler: Design, Diagnostic and Commissioning", in *Proceedings of the 5th International Particle Accelerator Conference (IPAC'14)*, Dresden, Germany, 2014, <https://doi.org/10.18429/JACoW-IPAC2014-MOPRI075>, p. 777-779.
- [4] M. I. Bryzgunov, A. D. Goncharov, V. M. Panasyuk, *et al.* "Energy transfer in the high-voltage electron cooler for the COSY synchrotron ring", *Instruments and Experimental Techniques*, 2015, v.58, No 2, p.181-189.

# MODEL DEVELOPMENT FOR THE AUTOMATED SETUP OF THE 2 MeV ELECTRON COOLER TRANSPORT CHANNEL

A. J. Halama and V. Kamerdzhiev  
Forschungszentrum Jülich (FZJ), Jülich, Germany

## Abstract

The 2 MeV electron cooler allows for cooling the proton and deuteron beams in the entire energy range of COSY and thereby study magnetized high energy electron cooling for the HESR [1] and NICA [2]. Manual electron beam adjustment in the high energy, high current regime proves a cumbersome and time consuming task. Special difficulties are presented by the particular geometry of the e-beam transport channel, limited beam diagnostics and general technical limitations. A model has been developed to track electrons through the transport channel of the cooler. This allows the offline study of response schemes around any particular setting of the cooler. It is envisaged to control linear, dipole and quadrupole behavior of the e-beam. Application of the model will result in optimized e-beam transport settings for a lossless and cool beam transport. This will improve cooling and recuperation efficiency and allow quick adjustment of the e-beam to the various operational modes of the machine. A good relative agreement of the model and the cooler could be shown. Main focus lies now in overhauling the software and finding suitable initial conditions to improve the agreement to an absolute degree.

## MOTIVATION

In need of support for setting up the electron cooler, the model based approach offers a vast amount of advantages to the current manual way of operation. The model will at one point be able to predict the electron trajectory for any given machine setting. Additionally it will be able to calculate beam responses much faster than obtainable by measurements. The speed of obtaining responses scales progressively with the order of motion of the parameter of interest. Thus setting up the cooler will be faster, more reliable and will offer more information on the beam behavior throughout the transport channel, compared to the manual operation. The main objective of the model based adjustment is to achieve a brilliant electron beam quality for high cooling rates and optimal recuperation conditions. With respect to the safety during operation, this will result in improved vacuum conditions and causes less x-ray radiation. The model is embedded in a software suit that reads inputs from the cooler and is able to apply changes to the transport channel settings. With proper procedures and algorithms one will be able to compensate coupled effects between the different orders of beam motion types and to predict beam behavior also for yet unexplored beam regimes.

## OVERVIEW

### *Machine Characteristics and Limitations*

There are certain in and outputs available to handle the electron beam. The beam responds to the set currents i.e. the main currents and corrector currents. Main currents are internally called, “Cooling section”, “Longitudinal field”, “Bending field”, “Toroid 45° field”, and “Straight field”. Where it should be pointed out that the shown elements share the same current, as shown in Fig. 1. About 50 corrector currents are used to supply mostly dipoles, distributed along the transport channel and some more particular ones [3]. Feedback on the beams behavior is obtained by the Beam Position Monitor (BPM) system, and by the readouts from the vacuum system, leakage current and radiation monitors. Information on the beam shape can be obtained as the electron gun is capable of modulating the beam quadrant-wise [4], as only the modulated portion of the e beam is visible to the BPM system.

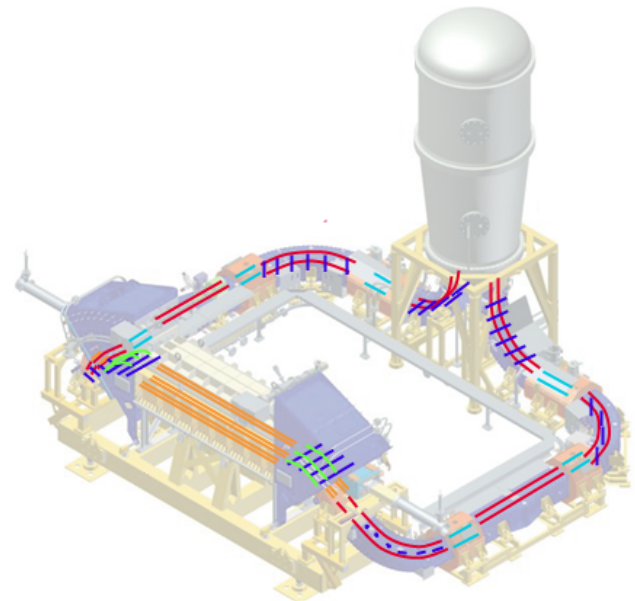


Figure 1: Image of the 2 MeV electron cooler. Equally colored symbolic field lines represent coils that share the same power supply. Orange: “Cooling section”, red: “Longitudinal field”, blue: “Bending field”, green: “Toroid 45° field”, and cyan: “Straight field”.

### *E Beam Parameters*

The e beam parameters of interest for the transport channel setup are the parameterized orders of motion, i.e. linear, dipole and quadrupole. There is only the possibility for an

orbit (linear) in-situ measurement, with the BPM system. The dipole motion, from now on called larmor rotation, is inevitably excited by the given geometry of the transport channel. The special condition of an integer number of larmor oscillations [3] to minimize the larmor excitation cannot be kept through all bending sections. Adjusting elements of different field straight distort the longitudinal profile so that a common optimal setting cannot be found. The larmor rotation can only be measured indirectly by sweeping the current of a straight section around the operating point and observing the resulting beam position shift over the set current or B-field. The amplitude of the motion is the larmor radius, which quantifies its magnitude. The highest order of motion is the so called galloping motion (quadrupole motion). It results from the passage of a non-adiabatic e beam through a B-field gradient section. Individual electrons are excited to carry out larmor rotation, whereas the envelope of the beam is wobbling as a result, because the individual larmor phases vary with their location within the beam as well as the larmor radius increases with distance to the center of charge of the beam. While the center of gravity is unaffected by the galloping motion one can measure the larmor rotation of the center as well as of one quadrant and simply subtract the coherent component to single out the pure galloping motion. The projections of the superposition of larmor rotation and galloping motion is shown in Fig. 2 For the currently foreseen scope of the model software, auxiliary data on the vacuum, leakage current, radiation signal will not be used for feedback schemes by default.

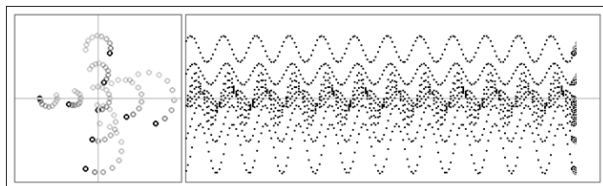


Figure 2: Trajectory cross sections to visualize the superposition of Larmor and galloping motion. Left in XY-Plane, right in YZ-Plane.

### *Current Way of Operation for Beam Setup and Adjustments*

The initial setup for the transport channel is found by setting main currents to empirically known values scaled by the beta-gamma relation for the given energy. Orbit optimization with focus on the reduction of leakage current as well as stable vacuum conditions is obtained at low e beam current. Larmor and orbit corrections are iteratively performed as the e beam current is slowly increased. The orbit changes are performed manually as for the operating needs by setting the currents of certain dipole correctors. As the shift translates throughout the transport channel, greater shifts have to be compensated further downstream. The Larmor rotation compensation is only carried out in the cooling section. There is only one pair of short dipole corrector kickers to

induce a larmor excitation that counteracts the accumulated larmor rotation in one selected section, in which the larmor radius is measurable. There is a set of seven corrector solenoids to counteract galloping motion in one of the so called matching sections. These coils ought to deliver such a field configuration to bridge the gradient region between the weaker magnetic field in the accelerator column and the strong longitudinal within the first bending section. There is no practical compensation scheme in place for the galloping motion as its measurement is a lengthy procedure and there are seven currents to sweep independently to find an optimal setting.

## MODEL

### *Implementation*

The model is embedded in a Java software package specifically in development for the operation of the 2 MeV electron cooler. At its core there are magnetic field maps calculated obtained from COMSOL Multiphysics 5.0 calculations, translated into equidistant grids for an eased access to specific field values at given coordinates. The equation of motion of the electron in such an environment is utilized in the integration of the instantaneous velocity of the particle. Special simplex arguments prevent blowup of the integration. Quantization of beam parameters from the model is taken care of by the trajectory fit of individual electrons with respect to the center of charge representing electron. This way one obtains linear, dipole and quadrupole terms for the entire beam and can compare those with measurement results.

### *Quality of Agreement*

During the proof of principle stage of the model software, it could be shown that there is a satisfying qualitative agreement between the model and the 2 MeV electron cooler. In the first order calibration deviations in the response behavior between the measured electron beam and calculated trajectories are used to scale the dipole magnets in the model. This accounts for errors and simplifications during modelling the coil configurations in COMSOL or installation misalignments of the coils. A quantitative comparison of a measured orbit response matrix and a calculated one showed after calibration RMS deviations of about 10 %. Although there is room for improvement for example by properly scaling also the longitudinal fields, such a deviation is small enough to still allow application of calculated orbit response schemes in feedback scenarios. The qualitative agreement can also be seen in the existence of anticipated effects of the short dipole kickers used for larmor excitation. Galloping motion can also be compensated within the model utilizing the previously mentioned matching section, consisting of seven coils. A simple algorithm sweeps the current of each coil slightly to determine the gradient of the galloping response. The current of each coil is successively set in the direction of the negative gradient. Progressing through several iterations the galloping growth rate is decreased significantly. This

Content from this work may be used under the terms of the CC BY 3.0 licence (© 2017). Any distribution of this work must maintain attribution to the author(s), title of the work, publisher, and DOI.

shows that the model is capable to find suitable settings for the matching section. The ability to compensate the galloping motion within the model is another solid hint for the good qualitative agreement. The compensation procedures can be carried out within the model, using its response to find optimised settings. Intermediate and final results of the stepwise procedure can be comprehended by means of the Fig 3.

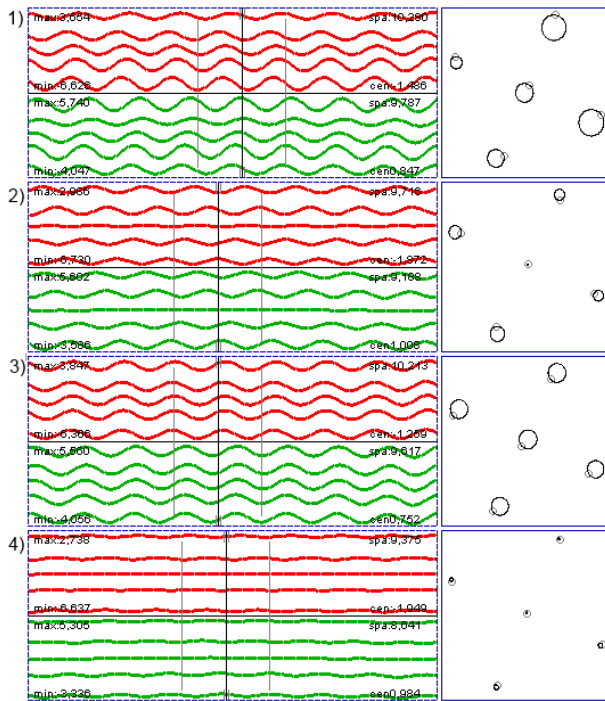


Figure 3: Trajectories in straight section. Red is projection in x, green is projection in y. First initial uncompensated beam, second larmor corrected, third galloping corrected, final larmor corrected again.

The corrector coils in the bending sections consists of two separate coil usually supplied with an equal current to satisfy a magnetic index of 0.5 in the bending sections, which ensures that there is no influence of the beam shape. As there are mismatches, beam shape influence can be seen. There is however the capability for beam shape restoration by applying antiparallel changes to the inner and outer bending corrector coil. The measured shape influence has been also compared to that of the model. The results show qualitative agreement only separated by a factor of two, which will be investigated in the near future.

### Space for Improvement

The model calculations are sensitive to the chosen time step width of the integration. Improvements of the underlying physics implementation could allow wider time steps which would speed up the calculation and guarantee its reliability. The included field maps extend partially up to one meter out from the magnetic element to reflect the diffusing fringe field. It has been observed that the electron motion in the order of micro meters is even sensitive to abruptly cut

off weak fringing field maps. To reflect the proper electron behavior the diffusion of the fringes as well as even wider extended regions could be implemented into the model. The transport channel is almost completely covered in a magnetic shielding. This acts additionally as a yoke, why its contribution has to be considered not only linearly but also as it can saturate or even pose with a remanence field due to hysteresis. Including saturation and hysteresis of the magnetic shielding would reflect a more accurate environment and improve the model.

### Calibration Schemes

As there is a relative agreement of the model and the electron cooler's beam behavior, one could already implement feedback loops to counteract coupled effects during manual or automated changes to the transport channel setup. But this has to be accompanied with steady measurements to verify the beam parameters. The relative calibration is simply given as the rescaling of magnetic field maps according to the deviations of measured and calculated response schemes. An absolute calibration of the model would allow for predictions of the trajectory and thereby all beam parameters. Key to the absolute calibration is the exact starting point of the electron. There are two approaches to determine proper injection conditions for the model calculation that will be presented. The general approach can be described as a least square fit to all measured beam positions. The variations lie within a positional spread and angular spread at each BPM location from where the electron trajectory is traced down- as well as upstream. The error of this error calibration lies within the BPM misalignments. The second approach is more specialized reflecting the transport channel geometry. It also focuses on calibrating the longitudinal model fields. As the larmor rotation can be measured in three straight sections, the position and angle of the e beam is known at the end of these sections. Tracing along straight sections is least prone to error. Because of that, position and angle of the e beam in the beginning of the straight sections can easily be determined. This gives additionally the special relation between the offsets of the present BPMs. In between these straight sections the model trajectory can be traced from one section to the next down- and upstream. Phase propagation differences between the model and the measurement can be picked up and corrected by repeating this procedure at varied settings for the inner magnetic bend elements and determination of scaling factors to calibrate the longitudinal model fields. The remaining trajectory can be traced upstream from the beginning of the first straight section and downstream from the end of the last straight section. This way one knows the most precise starting and end point of the model trajectory, which can be used for the model application and beam predictions.

### OUTLOOK

As the model offers plenty of new opportunities one can think of many adaptations, refinements and add-ons. One of

these is the implementation of the electron gun environment model or some of its crucial parameters. This way one could make use a better an understanding of the beam shape as well as to determine its absolute temperature. Collector components could also be included to the model to achieve and verify higher recuperation and collector efficiencies for higher currents. /newline The hard coded model could be generalized to support a sand box like feature. With help of such a feature any transport channel geometry could be constructed virtually on the fly. It could provide aid during the design of an electron cooler or be adapted to existing ones. This would include the possibility to plug in generic, numeric and analytic field maps. A step into a more analytic approach to find and optimize transport channel settings is the look at optics functions. For generalized adjustment schemes transfer functions could be obtained. Inversions of transfer matrices will eventually lead to optimized solutions. This way the entire trajectory could be described analytically.

## CONCLUSIONS

A model is under development to aid the transport channel setup of the 2 MeV electron cooler. The model is embedded in a Java software suit with a GUI to monitor beam parameters and set transport channel parameters. The model satisfies a qualitative agreement with the cooler and shows in this way the expected physical behavior. Properly scaled corrector dipoles within the model allow already application

of the model for orbit feedback loops. Successful use has been demonstrated during the proof of principle stage of the model. Absolute calibration is yet required to properly reflect the actual e beam trajectory with the model for each magnetic setting of the cooler. For this matter, calibration schemes are under development and will be implemented and tested soon. After successful calibration the core of the model will be operational.

## ACKNOWLEDGEMENT

Many thanks to V. Kamerdzheiv, B. Lorentz, C. Weidemann, V. Reva, and M. Bryzgunov.

## REFERENCES

- [1] A. Lehrach *et al.*, “Design Work for the High-Energy Storage Ring of the Future GSI Project”, in *Proc. PAC2005*, Knoxville, TN, USA, paper FPAE001.
- [2] V. Reva *et al.*, “The High Voltage Cooler for NICA, Status and Ideas”, presented at COOL’17, Bonn, Germany, Sep 2017, paper TUM21, this conference.
- [3] M. Bryzgunov *et al.*, “Magnetic System of Electron Cooler for COSY”, in *Proc. COOL’11*, Alushta, Ukraine, paper TUPS10.
- [4] M. Bryzgunov *et al.*, “Electron Gun with Variable Beam Profile for COSY Cooler”, in *Proc. COOL’11*, Alushta, Ukraine, paper TUPS06.

# MUON INTENSITY INCREASE BY WEDGE ABSORBERS FOR LOW-E MUON EXPERIMENTS\*

D. V. Neuffer<sup>#</sup>, D. Stratakis, J. Bradley<sup>&</sup>, Fermilab, Batavia IL 60510, USA

## Abstract

Low energy muon experiments such as mu2e and g-2 have a limited energy spread acceptance. Following techniques developed in muon cooling studies and the MICE experiment, the number of muons within the desired energy spread can be increased by the matched use of wedge absorbers. More generally, the phase space of muon beams can be manipulated by absorbers in beam transport lines. Applications with simulation results are presented.

## INTRODUCTION

Low energy muon experiments, such as the Fermilab-based mu2e [1, 2] and g-2 experiments, [3] have a limited phase space acceptance for useful muons. The mu2e experiment can only accept a small momentum slice of the incident muon momentum spectrum ( $P\mu < \sim 50$  MeV/c, see below). The g-2 experiment only accepts a momentum spread of  $\delta P = \pm 0.1\%$  around the design momentum of  $\sim 3.1$  GeV/c. Methods that can increase the number of muons within the momentum acceptance are desirable.

Similar or complementary constraints occurred in the exploration of ionization cooling for muons [4]. Wedge absorbers are needed to transform the intrinsic transverse cooling effect to include longitudinal cooling, and introduce exchanges between longitudinal and transverse phase space densities. In cooling channels incremental exchanges were developed so that large increases in phase space density could be obtained over a multistage system. In final cooling toward the extreme parameters needed for a high luminosity collider, it was noted that very large exchanges in single wedges were needed [5, 6]. In that limit it was noted that a wedge could be treated as an optical element in a transport system and large exchanges can occur with single wedges [7], which can be used to match the final beam to desired distributions (smaller transverse emittance with larger  $\delta p$  or vice versa). As an example the use of a wedge, and its effects in large exchanges, can be measured in the MICE experiment [8, 9].

The method can also be adapted for phase space matching into low energy muon experiments, and matched placement of wedges in the beam transport could obtain more muons within experiment acceptances. We note that use of a wedge to reduce  $\delta P$  increases the transverse emittance, and changes the matched optics. Some iterations in beam matching may be needed to increase the number muons accepted.

In this paper we first describe the wedge process and its approximation as a transport element

\*Work supported by FRA Associates, LLC under DOE Contract No. DE-AC02-07CH11359.

<sup>#</sup>neuffer@fnal.gov

<sup>&</sup> current address: University of Edinburgh, Edinburgh, Scotland.

The parameters of mu2e and g-2 are discussed and potential uses of wedge absorbers and their adaptation to increase acceptance into the experiments are described. Simulations that test these possibilities are presented and the results are discussed.

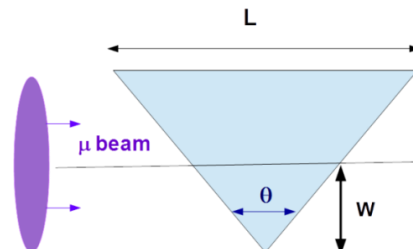


Figure 1: Schematic view of a muon beam passing through a wedge.

## WEDGE EFFECTS ON BEAM - FIRST ORDER ESTIMATES

Figure 1 shows a stylized view of the passage of a beam with dispersion  $\eta_0$  through a wedge absorber. The wedge is approximated as an object that changes particle momentum offset  $\delta = \Delta p/P_0$  as a function of  $x$ , and the wedge is shaped such that that change is linear in  $x$ . (The change in average momentum  $P_0$  is ignored in this approximation. Energy straggling and multiple scattering are also ignored.) The rms beam properties entering the wedge are given by the transverse emittance  $\epsilon_0$ , betatron amplitude  $\beta_0$ , dispersion  $\eta_0$  and relative momentum width  $\delta_0$ . (To simplify discussion the beam is focussed to a betatron and dispersion waist at the wedge:  $\beta_0' = \eta_0' = 0$ . This avoids the complication of changes in  $\beta'$ ,  $\eta'$  in the wedge.) The wedge is represented by its relative effect on the momentum offsets  $\delta$  of particles within the bunch at position  $x$ :

$$\frac{\Delta p}{P} = \delta \rightarrow \delta - \frac{2(dp/ds) \tan(\theta/2)}{P_0} x = \delta - \delta'x$$

$dp/ds$  is the momentum loss rate in the material ( $dp/ds = \beta^1 dE/ds$ ).  $2x \tan(\theta/2)$  is the wedge thickness at transverse position  $x$  (relative to the central orbit at  $x=0$ ), and  $\delta' = 2dp/ds \tan(\theta/2) / P_0$  indicates the change of  $\delta$  with  $x$ .

Under these approximations, the initial dispersion and the wedge can be represented as linear transformations in the  $x$ - $\delta$  phase space projections and the transformations are phase-space preserving. The dispersion can be represented by the matrix:  $\mathbf{M}_\eta = \begin{bmatrix} 1 & \eta_0 \\ 0 & 1 \end{bmatrix}$ , since  $x \Rightarrow x + \eta_0\delta$ .

The wedge can be represented by the matrix:  $\mathbf{M}_\delta = \begin{bmatrix} 1 & 0 \\ -\delta' & 1 \end{bmatrix}$ , obtaining  $\mathbf{M}_{\eta\delta} = \begin{bmatrix} 1 & \eta_0 \\ -\delta' & 1 - \delta'\eta_0 \end{bmatrix}$ . Writing the  $x$ - $\delta$  beam distribution as a phase-space ellipse:

$g_0 x^2 + b_0 \delta^2 = \sigma_0 \delta_0$ , and transforming the ellipse by standard betatron function transport techniques obtains new coefficients  $b_1, g_1, a_1$ , which define the new beam parameters[6]. The momentum width is changed to:

$$\delta_1 = \sqrt{g_1 \sigma_0 \delta_0} = \delta_0 \left[ (1 - \eta_0 \delta')^2 + \frac{\delta'^2 \sigma_0^2}{\delta_0^2} \right]^{1/2}$$

The bunch length is unchanged. The longitudinal emittance has therefore changed simply by the ratio of energy-widths, which means that the longitudinal emittance has changed by the factor  $\delta_1/\delta_0$ . The transverse emittance has changed by the inverse of this factor:

$$\varepsilon_1 = \varepsilon_0 \left[ (1 - \eta_0 \delta')^2 + \frac{\delta'^2 \sigma_0^2}{\delta_0^2} \right]^{-1/2}$$

The new values of

$$(\eta, \beta) \text{ are: } \eta_1 = -\frac{a_1}{g_1} = \frac{\eta_0 (1 - \eta_0 \delta') - \delta' \frac{\sigma_0^2}{\delta_0^2}}{(1 - \eta_0 \delta')^2 + \delta'^2 \frac{\sigma_0^2}{\delta_0^2}} \text{ and}$$

$$\beta_1 = \beta_0 \left[ (1 - \eta_0 \delta')^2 + \frac{\delta'^2 \sigma_0^2}{\delta_0^2} \right]^{-1/2}$$

Note that the change in betatron functions implies that the following optics should be correspondingly matched.

A single wedge exchanges emittance between one transverse dimension and longitudinal; the other transverse plane is unaffected. Serial wedges could be used to balance  $x$  and  $y$  exchanges, or a more complicated coupled geometry could be developed.

Wedge parameters can be arranged to obtain large exchange factors in a single wedge. In final cooling we wish to reduce transverse emittance at the cost of increased longitudinal emittance.

## APPLICATION TO MU2E

The mu2e experiment presents an unusual opportunity to exploit beam-cooling techniques to improve acceptance. The transport from target to detector includes a bent solenoid that produces a dispersion that invites the introduction of a wedge absorber to shape the transmitted energy distribution.

The mu2e experiment from target to detector is shown in Fig. 2. Particles produced in the target are directed along the production solenoid and into the bent solenoid transport solenoid, which selects beam that continues into the Al stopping target within the detector solenoid. The transport is designed to accept low energy  $\mu$ , mostly produced from  $\pi$  decay within the solenoids. The bent solenoid and associated collimators are tuned to accept  $\sim 0$ – $100$  MeV/c  $\mu$ ; stopped  $\mu$ 's are obtained from  $\sim 0$ – $50$  MeV/c  $\mu$ . Figure 3 shows the momentum distribution of muons reaching the detector solenoid, including the population of those that are stopped within the target. Peak stopped  $\mu$ 's are actually at 35–40 MeV/c (6–7 MeV kinetic energy). If we could put more of the beam from the  $\sim 50$ – $100$  MeV/c into the  $< \sim 40$  MeV/c region, the useable mu2e beam would increase.

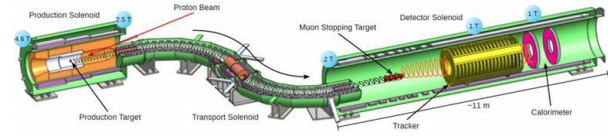


Figure 2: Overview of the mu2e experiment from production solenoid to transport solenoid to Detector Solenoid.

The transport solenoid (TS) consist of two bent solenoids with a short transition solenoid connecting them; collimators are in the transition solenoid. The equations of motion in a bent solenoid are:

$$x'' = h + by' \quad y'' = h - bx'$$

where  $b = B_0 / B\rho$  and  $h = 1/\rho_0$ , where  $\rho_0$  is the bending radius and  $B_0$  is the solenoidal field. In mu2e the bending radius is  $\sim 3$  m. The magnetic field is  $B_0 = 2.4$  T and  $B\rho$  (T-m) =  $p$  (GeV/c)/0.3. The total bend of each bent solenoid is  $90^\circ$ , but with opposite signs. The solutions of these equations are:

$$y(s) = C_1 - \frac{h}{b}s + \frac{h}{b^2} \sin(bs) + C_2 \frac{1}{b} \sin(bs) + C_4 \frac{1}{b} (\cos(bs) - 1)$$

$$x(s) = C_3 + \frac{h}{b^2} (1 - \cos(bs)) + C_2 \frac{1}{b} (1 - \cos(bs)) + C_4 \frac{1}{b} \sin(bs)$$

$C_1 = y(0)$ ,  $C_2 = y'(0)$ ,  $C_3 = x(0)$ ,  $C_4 = x'(0)$ . Starting at 0 in all coordinates, we obtain the solution:

$$y(s) = -\frac{h}{b}s + \frac{h}{b^2} \sin(bs); \quad x(s) = \frac{h}{b^2} (1 - \cos(bs))$$

At the end of the first bent solenoid, entering the transition,  $s = 4.6$  m. At that point the vertical position is linear with momentum  $p$ :  $y(p) = \sim 0.213$  ( $p$  (MeV/c)/100) m for negative muons. (opposite sign for positive muons). The oscillation amplitude  $h/b^2$  is a measure of beam oscillation within the focusing solenoid fields and is relatively small ( $\sim 0.16$  cm for  $p = 50$  MeV/c).

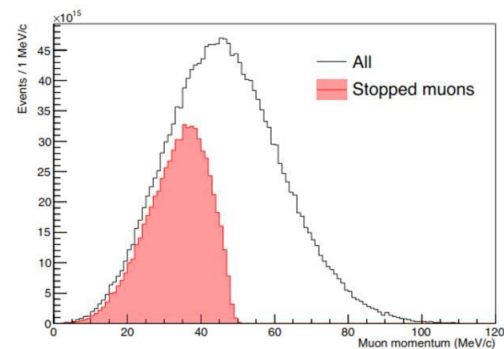


Figure 3: Simulated muons that reach the detector solenoid. Stopped muons that can provide mu2e candidate events are displayed in red (from Ref. 1).

Muons in the  $\sim 40$ – $100$  MeV/c momentum range can have their momenta moved toward the  $\sim 40$  MeV/c desired momentum by passing through an absorber with a thickness corresponding to the desired momentum loss. This can be done by using a wedge with a thickness that

Content from this work may be used under the terms of the CC BY 3.0 licence (© 2017). Any distribution of this work must maintain attribution to the author(s), title of the work, publisher, and DOI.

depends on vertical position. The requirement would be that the thickness as a function of  $y$  be such that  $P_\mu(y)$  is reduced to  $\sim 40$  MeV/c. This implies zero thickness for  $y < 8.5$  cm. Momentum loss in material is strongly momentum-related. From the Bethe-Bloch formula:

$$p(s) \equiv p_1 - \int_0^s 0.3071 \frac{Z}{A} \rho \left( \frac{p^2 + m_\mu^2 c^2}{p^2} \log \left( \frac{2p^2 c^2 m_e c^2}{I_e (m_\mu c^2)^2} \right) - 1 \right) \frac{\sqrt{p^2 + m_\mu^2 c^2}}{p} ds$$

We can choose the thickness as a function of position  $y$  by requiring that the integrated energy loss be equal to the amount necessary to reduce the momentum to  $\sim 40$  MeV/c.

$$\text{range}(40, p_1) = \int_{40}^{p_1} \frac{1}{\frac{dP}{ds}(p)} dp$$

Combining this with the relationship  $y(p_1) = \sim 0.213 (p_1 (\text{MeV}/c)/100)$  m, obtains the desired thickness as a function of  $y$ .

The choice of a wedge material is dependent on practical considerations that are not fully explored within this note. The material should be a relatively low- $Z$  material to minimize multiple scattering and must be mechanically compatible with the transport solenoid vacuum pipe. For an initial estimate we consider polyethylene ( $\sim \text{CH}_2$ ), with properties of  $Z/A = 0.57$ ,  $\rho = 0.94$ ,  $I_e = 57.4$  eV,  $X_0 = 47.45$  cm. This is a low cost material that is easily machined, and has actually been used to produce a wedge for the MICE experiment, (see Fig. 4.).



Figure 4: Polyethylene wedge piece machined for use in the MICE experiment. Wedge for mu2e would have similar dimensions. (Inner radius is  $\sim 20$  cm).

Evaluation of the range equation obtains an absorber with zero thickness for  $y < 8.5$  cm. For  $y = 0.213$  m ( $P_\mu = 100$  MeV/c), a thickness of 7.22 cm is required, for  $y = 24$  cm, 9.15 cm and for  $y = 15$  cm, 1.61 cm. A numerical solution and fitting within Mathematica obtains a thickness of a polyethelene absorber given by:

$$w = 0 \text{ for } y < 8.5 \text{ cm}$$

$$w \approx 0.133(y - 8.5) + 0.0296(y - 8.5)^2 \text{ cm for } y > 8.5 \text{ cm}$$

This nonlinear profile is roughly parabolic, see Fig. 5.

The TS has an inner radius of  $\sim 25$  cm, so the maximum thickness would be  $\sim 10$  cm. For denser materials (Be or  $\text{B}_4\text{C}$ ) the thickness would be  $\sim 5$ — $7$  cm. This maximum thickness could be reduced by reducing the maximum matched  $P_\mu$  to be reduced (3—5 cm for 100 MeV/c).

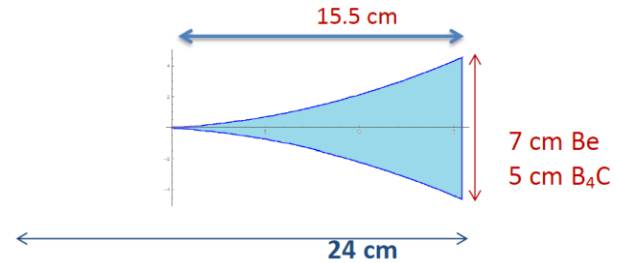


Figure 5: Cross-section of a wedge to be inserted at the high dispersion point of the mu2e transport solenoid. The wedge is offset from the center line by  $\sim 8.5$  cm so that low-energy  $\mu$ 's pass without touching the wedge; higher-momentum  $\mu$ 's lose energy toward  $P_\mu \sim 40$  MeV/c.

## APPLICATION TO G-2

The g-2 ring has a very small momentum acceptance for 3.1 GeV/c  $\mu$ 's ( $\delta P/P$  is  $\sim 0.1\%$ ). The beam transport into the g-2 ring (which includes the Debuncher ring has a much larger acceptance of  $\sim 1\%$ ). Reduction of that momentum spread before injection into the ring could increase the number of accepted  $\mu$ 's. This would require a wedge absorber at a point of the transport with non-zero dispersion. While larger dispersion is desirable, the transport as presently designed has dispersion  $\eta < \sim 1$  m. At that dispersion an offset of 0.001  $\delta P/P$  is 1 mm and to change momenta to the baseline requires a momentum loss of 3.1 MeV/c.

We would like the absorber thickness also to be less than a few mm, which means using a dense material (large  $dE/dx$ ). We note that  $dE/ds$  at 3.1 GeV/c is  $\sim 20\%$  larger than minimizing ionizing. We also want minimal multiple scattering, which would mean low- $Z$  materials. High-density low- $Z$  materials could include: Be ( $dE/ds = 3.8$  MeV/cm), Boron Carbide  $\text{B}_4\text{C}$  ( $dE/ds = 5.5$  MeV/cm) or diamond ( $dE/ds = \sim 8.4$  MeV/cm). Polyethelene would have  $dE/ds = 2.56$  MeV/cm. Since the absorbers are relatively thin, higher  $Z$  materials can be considered, such as Nickel ( $dE/ds = 18.2$  MeV/cm) or Iridium ( $dE/ds = 36$  MeV/cm). For reduction of energy offsets to zero (with small transverse emittance beam size) we require:  $2 \frac{dE}{ds} \eta \tan\left(\frac{\theta}{2}\right) = E_\mu$ .

For  $\eta = 1$  m,  $\theta = 161^\circ, 152.5^\circ, 141^\circ, 123^\circ, 81^\circ, 47^\circ$  for polyethelene, Be,  $\text{B}_4\text{C}$ , diamond, Ni, and Ir, respectively. For  $\eta = 0.65$  m,  $\theta = 168^\circ, 162^\circ, 154^\circ, 141^\circ, 105^\circ, 67^\circ$  for polyethelene, Be,  $\text{B}_4\text{C}$ , diamond, Ni, and Ir, respectively.

The transverse and longitudinal acceptances of the ring are limited by the ring aperture, which has an  $r = 4.5$  cm radius and the betatron functions ( $\beta_x = 8$  m,  $\beta_y = 18.4$  m,  $\eta = 8.2$  m). These are given by:

$$A_x = \frac{r^2}{\beta_x}, A_y = \frac{r^2}{\beta_y}, \text{ which is } 0.00025 \text{ m for } A_x \text{ and } 0.00011 \text{ m for } A_y.$$

This could be rewritten as an rms normalized emittance acceptance by multiplying by  $\beta_y = 30$  for  $P_\mu = 3.1$  GeV  $\mu$ 's and dividing by 6 ( $\epsilon_{\text{rms}} = A/6$ ), obtaining  $\epsilon_x = 0.00125$  m,  $\epsilon_y = 0.0005$  m. The transverse emittance increase induced by the absorber must be

significantly less than these aperture cuts. (Stricter aperture cuts are imposed by the injection optics.)

The increase in rms normalized emittance caused by multiple scattering in the absorber can be estimated by

$$\delta\epsilon_N = \beta_t \frac{E_s^2}{2\beta^3 \gamma (mc^2)^2} \frac{\Delta w}{L_R}$$

where  $E_s = 13.6$  MeV,  $\beta_t$  is the transverse beta function at the wedge,  $L_R$  is the material radiation length,  $\Delta w$  is the length of the absorber at central energy loss,  $mc^2 = 105.66$  MeV, and  $\beta$ ,  $\gamma$  are the relativistic kinematic factors ( $\beta \sim 1$ ,  $\gamma \sim 30$ ). If we require the energy loss at central momentum to be  $2 \times 3.1$  MeV, set  $\beta_t = 10$  m (typical for a transport line), then  $\delta\epsilon_N = \{0.00013, 0.00015, 0.00017, 0.0008, 0.0016\}$  m for Be, B<sub>4</sub>C, C, Ni, Ir, respectively. The geometric emittance change is  $\delta\epsilon_N / 29.3$  or  $\{4.4, 5, 6, 27, 53\}$  mm-mrad (geometric). While the low-Z materials may have tolerably small emittance increases, the higher-Z materials lead to emittance increases that are large when compared to the acceptances. They would not be recommended, unless  $\beta_t$  is significantly reduced. The application to g-2 appears to require low-Z materials, with large angle absorbers. Figure 6 shows a schematic view of the muon beam passing through a large angle absorber.

Figure 7 displays betatron functions for the transport into the g-2 ring. The transport to the ring has a horizontal dispersion of  $\sim 0.65$  m where  $\beta_x = \sim 2$  m and  $\beta_y = \sim 7$  m, and this might be an appropriate location for the wedge.

However the transverse beam size due to emittance is not small, even with  $\beta_x = \sim 2$  m. With an rms emittance of 12 mm-mrad, the rms beam size  $\sigma_x$  is 5 mm. A large transfer in emittance can occur if  $\eta\delta_0 \gg \sigma_x$ , where  $\delta_0$  is the initial beam width. At  $\delta_0 = 0.01$  and  $\eta = 0.65$  m,  $\eta\delta_0 = 6.5$  mm which is similar to the emittance beam size. Within the linear wedge model, the  $\delta'$  to obtain minimal  $\delta p_{\text{after}}$  is reduced from  $1/\eta$  to  $1/\eta \times ((\eta\delta_0)^2 / ((\eta\delta_0)^2 + \sigma_x^2))^{1/2}$ , and  $\delta p_{\text{after}}$

$$\text{is given by } \delta p_{\text{after}} = \delta_0 \left( 1 - \frac{(\eta\delta_0)^2}{(\eta\delta_0)^2 + \sigma_x^2} \right)^{1/2}$$

which is  $\sim 0.61\delta_0$  at the above parameters. Optimum  $\delta'$  is reduced by a factor of 0.63 from the zero beam size limit, which reduces the desired wedge angles substantially. For this optimum  $\delta'$ , the dispersion is matched to zero exiting the wedge; a lattice exploiting this feature could have significant advantages.

A larger dispersion function at the wedge would be more desirable, of course.



Figure 6: Schematic view of a muon beam incident on a large angle (160°) absorber.

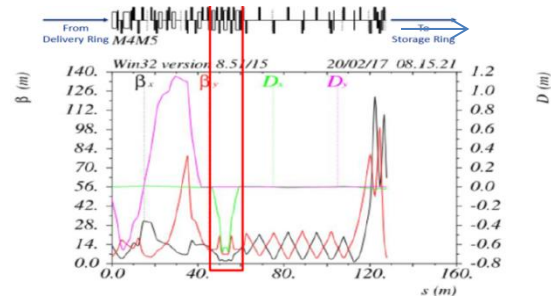


Figure 7: Betatron functions for the transport leading into the g-2 ring. Test wedges are inserted at high dispersion within the highlighted region in simulation.

## SIMULATION RESULTS

We have initiated simulations of the g-2 case. In these simulations, Beam was tracked using G4Beamline through the transport from the delivery ring into the g-2 ring. Wedges of various materials and dimensions were inserted in the high dispersion region and optimized for providing the most beam within a  $\pm 0.1\%$   $\delta p/p$  acceptance window through the transport.

As may be expected from the above discussion, the optimum wedge is a low-Z material (poly ( $\sim C_2H_4$ ) or LiH) with a shallow angle ( $\sim 150$ - $160^\circ$ ), and increases the beam within the acceptance by  $\sim 30\%$ . (see fig. 8) The wedge increases transverse emittance, and with the mismatched optics the larger amplitude particles were lost in the transport; the 30% net improvement included the losses.

The result is considered to be enough of an improvement to encourage further development, including further simulation and design and construction of moveable physical wedge inserts in the g-2 transport line at the high dispersion point.

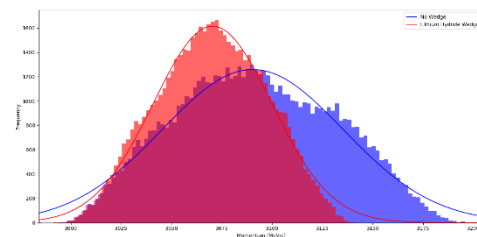


Figure 8: Momentum distribution of beam reaching the g-2 ring without (blue) and with (orange) a wedge. While total number of muons is reduced, the momentum width is reduced and beam within  $\pm 0.1\%$  is increased by  $\sim 30\%$ .

In the initial evaluations the beam optics was not rematched following the wedge, and a full simulation with matching into the g-2 ring and storage has not yet been completed. This must be done in the near future. Proper matching could increase acceptance significantly. A modified optics with larger dispersion at the wedge could also greatly improve acceptance.

## ACKNOWLEDGEMENT

We thank M. Syphers for helpful and encouraging discussions.

## REFERENCES

- [1] L. Bartoszek *et al.*, Mu2e Technical Design Report, Mu2e Doc 4299, arXiv 1501.0524 (2015).
- [2] Mu2e Conceptual Design Report, Mu2e Document 1169-v12 (2012).
- [3] C. Polly *et al.*, Muon g-2 Technical Design Report, Fermilab-FN-0992-E (2014).
- [4] D. Neuffer, H. Sayed, J. Acosta, T. Hart, and D. Summers, “Final Cooling for a High-Energy High-Luminosity Lepton Collider”, 2017\_JINST\_12\_T07003, *Journal of Instrumentation*, **12**, T07003 (2017).
- [5] D. Neuffer *et al.*, “A Wedge Absorber Experiment at MICE”, in *Proc. IPAC'17*, Copenhagen, Denmark, paper WEPAB133, p. 2888 (2017).
- [6] D. Neuffer *et al.*, in *Proc. IPAC'16*, Busan, Korea, paper THPOR025, p. 3832 (2016).
- [7] D. Neuffer, Fermilab Note MuCOOL-003 (1996).
- [8] M. Bogomilov *et al.*, *J. Inst.* **7**(5), P05009 (2012).
- [9] C. Rogers, P. Snopok, L. Coney, A. Jansson, “Wedge Absorber Design for the Muon Ionisation Cooling Experiment”, MICE 290 (2010).

# STOCHASTIC COOLING AS WIENER PROCESS

N. Shurkhno<sup>†</sup>, Forschungszentrum Jülich, Jülich, Germany

## Abstract

Traditional theoretical description of stochastic cooling process involves either ordinary differential equations for desired rms quantities or corresponding Fokker-Planck equations. Both approaches use different methods of derivation and seem independent, making transition from one to another quite an issue, incidentally entangling somewhat the basic physics underneath. On the other hand, treatment of the stochastic cooling as Wiener process and starting from the single-particle dynamics written in the form of Langevin equation seems to bring more clarity and integrity. Present work is an attempt to apply Wiener process formalism to the stochastic cooling in order to have a simple and consistent way of deriving its well-known equations.

## INTRODUCTION

There are two traditional approaches for theoretical description of the stochastic cooling process – studying parameter evolution of either a single particle or a particle distribution function [1].

The single particle approach involves ordinary differential equations for the rms-particle (i.e. having rms value of a given parameter). The equations are derived by calculation of the first two moments of the kick for a random particle. The cooling process is then described with a coherent effect, which is a particle's own signal, and incoherent effect, which includes all noises for the particle.

The other approach involves Fokker-Planck equations for the particle distribution functions. The derivation is either straightforward and based on the continuity equation analogues to the usual drift-diffusion equation derivation [2] or thorough and based on basic kinetic equations involving all other particle interactions with following simplifications [3]. In this case the cooling is described with quite similar coherent and incoherent terms, which are introduced as drift and diffusion coefficients of the Fokker-Planck equation.

The approach, involving treatment of particle distribution functions over given parameters, is more appropriate for the stochastic cooling simulation, unless we are interested in the initial cooling time or fast draft calculations. Nevertheless, single particle approach is the main tool for the betatron cooling simulation, since the diffusion term is defined by longitudinal dynamics and in this case could be considered constant (or defined by a function).

The connection of coherent and incoherent effects between different approaches was mentioned casually in [4], but it was never explicitly used. Eventually each approach requires its own derivation of coherent and incoherent terms. But both single particle and particle distribution function descriptions use the same underlying model of the cooling process, which involves particle beam, accelerator and stochastic cooling system. This process appears to be

a continuous Wiener process (or Brownian process), and corresponding formalism could be immediately applied to the stochastic cooling, giving a straightforward and clear way of deriving the equations and its' coefficients.

## LANGEVIN EQUATION

Consider an ensemble of non-interacting particles orbiting in an accelerator and undergoing a stochastic cooling. We are interested in the evolution of some parameter  $x$  (momentum spread, emittance, rms betatron amplitudes, etc.) of an arbitrary particle under influence of stochastic cooling system. On each revolution every particle receives a correction kick, or parameter change, from the cooling system, that is the sum of the self-signal of that particle (coherent signal  $x_c$ ) and some random noise signal due to signals from other particles and noises in the electronics (incoherent signal  $\tilde{x}_{ic}$ ):

$$\Delta x_{kick} = x_c + \tilde{x}_{ic}.$$

Since particle parameter depends solely on its present state and kick's interval (revolution period) in most cases could be considered much smaller than cooling time ( $T_0 \ll \tau_{cool}$ ), the process of stochastic cooling is a continuous Wiener process and all related formalism could be directly applied.

The starting point is then a derivation of a corresponding Langevin equation. The drift  $F$  and diffusion  $D$  coefficients could be defined in a usual way as:

$$F(x, t) = f_0 \Delta x_c(x, t),$$

$$D(x, t) = 1/2 f_0 \Delta x_{ic}^2(x, t),$$

where  $\Delta x_{ic}^2 = \langle \Delta x_{kick}^2 \rangle$ ,  $f_0$  – revolution frequency.

Then for the given model of stochastic cooling process with non-constant diffusion the corresponding Langevin equation will have the following form [5]:

$$\frac{dx}{dt} = F + \frac{1}{2} \frac{\partial D}{\partial x} + \sqrt{D} \xi(t), \quad (1)$$

where  $\xi(t)$  represents Gaussian white noise with the following statistics:

$$\langle \xi \rangle = 0,$$

$$\langle \xi(t) \xi(t') \rangle = 2\delta(t - t').$$

The summand with diffusion derivative in the Equation (1) is needed to compensate the effect of non-constant diffusion, a so-called *noise-induced drift*, which will be introduced later. The logic behind is the same as in explanation of Fick's law of diffusion, some additional details could be found in [5]. The Equation (1) could be used for tracking simulations in a software like Betacool in order to include

different effects like IBS or electron cooling altogether in the similar fashion.

### TIME-AVERAGED DIFFUSION

The standard procedure for deriving the equations within single-particle approach is to calculate the second moment of the kick, such treatment could be found for example in [4]. Here is given simpler, but not that mathematically strict derivation.

We anticipate that the incoherent effect for a given particle has a following statistics:

$$\begin{aligned}\langle x_{ic} \rangle &= 0 \\ \langle \bar{x}_{ic}^2 \rangle &= \Delta x_{ic}^2\end{aligned}$$

So, on the long-term average we expect that:

$$\frac{d}{dt} x^2 = \overline{\left( \frac{1}{2} \frac{\partial D}{\partial x} + \sqrt{D} \xi(t) \right)^2} = f_0 \Delta x_{ic}^2 = 2D.$$

By processing the derivative, formula for the incoherent dynamics is derived:

$$\frac{dx}{dt} = \frac{D}{x}.$$

Summing up coherent and incoherent effects for the single particle the following equation is derived:

$$\frac{dx}{dt} = F + \frac{D}{x}. \quad (2)$$

Such derivation is valid, because the white noise is considered. Equation (2) could be rewritten for the rms-particle (at a given time) in the more traditional form, involving cooling time  $\tau(t)$ :

$$\frac{1}{\tau} = -\frac{1}{x_{rms}} \frac{dx_{rms}}{dt} = -\frac{F}{x_{rms}} - \frac{D}{x_{rms}^2}.$$

Eventually, the single particle approach is completely described by the Equation (2). As a simple example, it can be shown that Equation (2) for oversimplified problem coincide with the well-known time-domain formula [4]. Consider:

- Flat distribution of  $N$  particles
- $\Delta x_c = -\lambda x$ , coherent correction is proportional to the particle's parameter value
- $\Delta x_{ic}^2 = \lambda^2 \cdot x^2 N_s + \lambda^2 \cdot \text{Thermal noise}$ , incoherent correction is proportional to the sum of particles' signals in the sample  $N_s = N/(2WT_0)$  and a thermal noise

Under given assumptions, the equation for the rms-particle simplifies to

$$\frac{1}{\tau} = \frac{W}{N} [2g - g^2(1 + U)],$$

where  $g = \lambda N_s$ ,  $U = \text{Therm. noise}/(x^2 N_s)$ .

### FOKKER-PLANCK EQUATION

Consider a following generic Langevin equation with the same statistics for  $\xi(t)$  as in Equation (1):

$$\frac{dx}{dt} = a(x, t) + b(x, t)\xi(t).$$

This generic Langevin equation has a corresponding deterministic Fokker-Planck equation of the form (see e.g. [6]):

$$\frac{\partial \Psi}{\partial t} = -\frac{\partial}{\partial x} \left[ \left( a + \frac{1}{2} b \frac{\partial b}{\partial x} \right) \Psi \right] + \frac{\partial^2}{\partial x^2} (b^2 \Psi).$$

The function  $\Psi$  is a probability distribution of a single particle, but mathematically it is identical to the particle distribution function when  $N \rightarrow \infty$ , which could be considered true for typical beam intensities. The summand under derivative  $\frac{1}{2} g \frac{\partial g}{\partial x}$  is a so-called noise-induced drift. To compensate this drift, the additional summand was added in the original Langevin Equation (1), otherwise diffusion term could lead to cooling.

Consequently, the corresponding Fokker-Planck equation for the given Langevin Equation (1) will have its traditional for stochastic cooling form:

$$\frac{\partial \Psi}{\partial t} = -\frac{\partial}{\partial x} (F\Psi) + \frac{\partial}{\partial x} \left( D \frac{\partial \Psi}{\partial x} \right).$$

While without this compensational term there would have been a different and incorrect form of the equation:

$$\frac{\partial \Psi}{\partial t} = -\frac{\partial}{\partial x} (F\Psi) + \frac{\partial^2}{\partial x^2} (D\Psi).$$

It was quite an issue in the early days, which form of equation is suitable for the stochastic cooling, and there was provided a dedicated experiment to verify the correct form of equation [7].

For the simplified example introduced earlier, the corresponding Fokker-Planck equation could be written in the following form:

$$\frac{\partial \Psi}{\partial t} = \frac{W}{N} \left[ 2g \frac{\partial}{\partial x} (x\Psi) + g^2(1 + U) \frac{\partial}{\partial x} \left( x^2 \frac{\partial \Psi}{\partial x} \right) \right].$$

### CONCLUSION

The stochastic cooling theory was formulated as continuous Wiener process. Such treatment derives the well-known equations in a clear and natural way, and besides it provides:

- Langevin equation for tracking simulations
- General form of equation for the single particle approach
- Explanation of the Fokker-Planck equation form
- Same well-established drift and diffusion coefficients for three theoretical approaches (incl. particle tracking).

## ACKNOWLEDGEMENT

I would like to heartily thank Anatoly Sidoren for the hint about Langevin equation, Hans Stockhorst for his great book and a lot of fruitful discussions, Rolf Stassen and Grigory Trubnikov, without whom this work would have never ever appeared.

## REFERENCES

- [1] H. Stockhorst, T. Katayama, and R. Maier, "Beam Cooling at COSY and HESR", Forschungszentrum Jülich GmbH, 2016.
- [2] T. Katayama and N. Tokuda, "Fokker-Planck Approach for the Stochastic Momentum Cooling with a Notch Filter", *Part. Accel.*, Vol. 21. p. 99, 1987.
- [3] J. Bisognano and C. Leemann, "Stochastic Cooling" in 1981 Summer School on High Energy Particle Accelerators, edited by R. A. Carrigan *et al.*, *AIP Conference Proceedings* 87, American Institute of Physics, Melville, NY, 1982, pp. 584-655.
- [4] D. Möhl, "Stochastic Cooling of Particle Beams", *Lecture Notes in Physics*, Vol. 866, Springer, 2013.
- [5] M. Doi and S. Edwards, "The Theory of Polymer Dynamics", Oxford University Press, 1988.
- [6] W. T. Coffey, Yu. P. Kalmykov, and J. T. Waldron, "The Langevin Equation: with Applications to Stochastic Problems in Physics, Chemistry and Electrical Engineering", *Series in Contemporary Chemical Physics*, Vol. 16, 2004.
- [7] L. Thorndahl *et al.*, "Diffusion in momentum space caused by filtered noise", Internal Report CERN/ISR-RF-TH, Machine Performance Report 19, 1977.

Content from this work may be used under the terms of the CC BY 3.0 licence (© 2017). Any distribution of this work must maintain attribution to the author(s), title of the work, publisher, and DOI.

# PRELIMINARY DESIGN OF ELECTRON TARGET FOR SRING AT HIAF\*

J. Li<sup>†</sup>, L. J. Mao, X.D. Yang, J. C. Yang, M.T. Tang, L. X. Zhao, H. Zhao, Z. K. Huang, S. X. Wang  
 Institute of Modern Physics, CAS, Lanzhou, China

## Abstract

A 13 Tm multifunction storage ring dedicated to nucleon and atomic experiment research - the SRing (Spectrometry Ring) is a significant part of the new heavy-ion research complex - HIAF (High Intensity heavy ion Accelerator Facility). In addition to an electron cooler and a gas internal target planned at the SRing, a beam of low temperature electron is also required to collide with the storage beam and to cool the decelerated ion beam at low energy. A magnetic adiabatic expansion is proposed to attain a low temperature by applying a 1.2 T longitudinal magnetic field upon the thermionic cathode at the electron gun. In this paper, preliminary design of the electron target is introduced.

## INTRODUCTION

The High Intensity heavy-ion Accelerator Facility (HIAF) is a new heavy ion accelerator complex under detailed design by institute of modern physics [1]. Two typical particles of  $^{238}\text{U}^{35+}$  and proton is considered in the design. The particles derive from a Superconducting Electron Cyclotron Resonance (SECR) ion source or an intense proton source, and are accelerated mainly by an ion linear accelerator (iLinac) and an booster ring (BRing). The iLinac delivers  $H_2^+$  at 48 MeV and  $^{238}\text{U}^{35+}$  at 17 MeV/u for the BRing that has a maximal rigidity of 34 Tm. The  $H_2^+$  is stripped into proton at the entrance of the BRing, after accumulation combined with two-plane painting and then is accelerated to the top plateau of 9.3 GeV. The  $^{238}\text{U}^{35+}$  is injected into the BRing by multi-turn two-plane painting scheme, after accumulation with the help of electron cooling, then accelerated to 0.2-0.83 GeV/u for extraction. At beam line of the HIAF FFragment Separator (HFRS), the ejected  $^{238}\text{U}^{35+}$  is stripped into  $^{238}\text{U}^{92+}$  and injected to the Spectrometer Ring (SRing) for high precision physics experiments. In addition, five external target stations of T1 - T5 are planned for nuclear and atomic experimental researches with an energy range of 5.8-830 MeV/u for the typical  $^{238}\text{U}^{35+}$  beam. Global layout of the HIAF complex is illustrated in Fig. 1.

### Overview of the SRing

The SRing is a 15 Tm spectrometer ring designed to collect secondary particles or stripped highly charged heavy ions like  $^{238}\text{U}^{92+}$  that derive from bombing the internal targets at HFRS. The typical particle of  $^{238}\text{U}^{92+}$  and proton can be stored at the upper limit of energy at 0.83 GeV/u and 9.3 GeV respectively. In addition, the deceleration to a low energy of  $^{238}\text{U}^{92+}$  to 30 MeV/u is also planned for

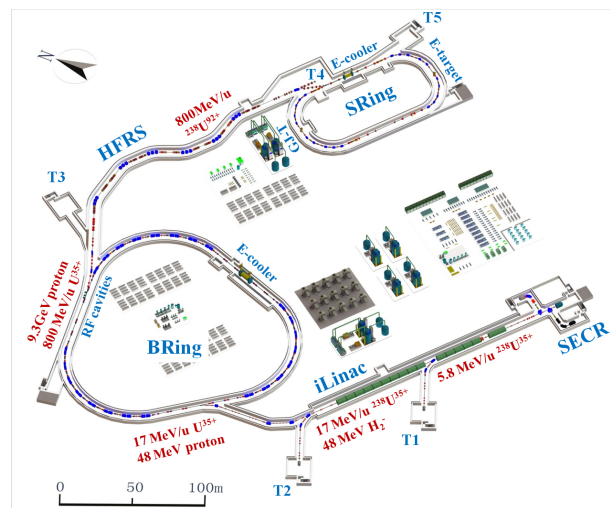


Figure 1: General layout of the HIAF complex.

atomic physics experiments. The ring has three operational modes of normal for cooling helped experiments with long life-time secondary particles, of internal for atomic physics experiments with electron-target (e-target), gas internal-target (GJ-Target), or laser cooling, and of isochronous for mass measurement of unstable nucleon with lifetime at tens of microsecond. Both electron cooler (e-cooler) and stochastic cooling system will be installed at the SRing. The e-cooler occupies one of the two longer straight section with a length of 11.2 m. The two shorter straight section are assigned to the e-target and gas-jet target. Main parameters of  $^{238}\text{U}^{92+}$  at the SRing are listed in Table 1.

Table 1: Main Parameters of  $^{238}\text{U}^{92+}$  at the SRing

Circumference	270.5 m
Magnetic rigidity	2-15 Tm
$\gamma_{tr}$	1.43-1.84
Energy	30-830 MeV/u
Acceptance ( $H/V, \delta p/p$ )	40/40 $\pi$ mmrad, $\pm 15\%$

### Electron Cooling System for SRing

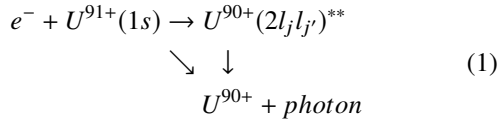
The e-cooler at SRing has a maximal energy of 460 keV that can cool the storage beam to an relative energy spread of  $3 \cdot 10^{-5}$  and transverse emittances of  $0.1 \pi$ mmrad at 0.83 GeV/u. The high precision measurement in dielectronic recombination (DR) experiment requires a continuous cooling at low energy. RF cavities are used to decelerate the storage beam. The cooling in DR experiments is mainly performed by the 460 keV e-cooler. In addition to act as a target, the e-target system also provides another approach of cooling that can cool the storage ion beam with energy up to 109 MeV/u.

\* Work supported by NSFC (Grant No. 11475235, 11611130016, 11575264, 11375245)

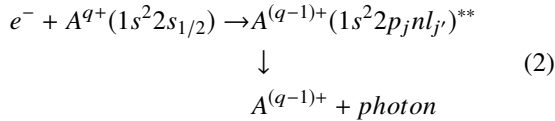
<sup>†</sup> lijie@impcas.ac.cn

## Experiments at E-target

Collision of storage ions with e-target at the SRing is mainly proposed by DR experiments on study of very heavy ions of  $H^-$  like



and ions of  $Li^-$  like



where  $q$  is the charge state, and  $A$  represents element. The double-asterisk denotes an intermediate doubly excited state in the process. The e-cooler is responsible for continuous cooling of collision ion beam and the e-target provide the low temperature electrons of energy detuned for the DR measurement or a supplementary cooling. Particularly, the transverse temperature of electron beam with order of milli-electron volts is demanded by the DR experiment while that of e-cooler is tens of times larger.

Besides, an electron density larger than  $1.0 \cdot 10^6 \text{ cm}^{-3}$  is also expected by DR experiment. The stored ions and electron beam overlap along the 1.3 m length of interaction solenoid. The de-excited  $A^{(q-1)+}$  ions are collected at e-target downstream after the dipole magnet when they are separated from the  $A^{q+}$  storage beam.

Table 2: Main Parameters of E-target Set-up

General Parameters	
Electron energy	1-60 keV
Maximal detuned energy	$\pm 10$ keV
HV ripple	$\pm 1 \cdot 10^{-5}$
Electron beam current (thermionic)	200 mA
Cathode diameter	10 mm
Maximal expansion factor	30
Magnetic field at electron gun	1.2 T
Magnetic field at collector	0.1 T
Magnetic field at interaction solenoid	0.04-0.1 T
Maximal electron beam diameter	55 mm
Interaction solenoid length	1.3 m
E-target installation length	4.5 m
$\beta_x/\beta_y$ at interaction section	21.6 m/15.3 m
Vacuum pressure	$1 \cdot 10^{-9}$ Pa
Typical Parameters for DR	
Expansion factor	25
Transverse electron temperature	5 meV
Electron beam density	$2 \cdot 10^6 \text{ cm}^{-3}$
Field at interaction section	0.048 T

## E-TARGET SYSTEM

The framework of e-target set-up follows the design of an traditional electron cooler [2]. It mainly consists of a

thermionic cathode electron gun section, two 90 deg toroid, an electron-ion interaction solenoid, and an collector section. The choice of thermionic cathode owing to its long lifetime and simplicity in maintain comparing to the photo-cathode. Main parameters of the e-target are listed in Table 2.

## Electron Gun and Collector Solenoids

On achieving the low temperature electron beam, we use a routine solenoid that can produce a magnetic field strength of 1.2 T. Typical field strength at interaction section in our design is 0.048 T. This allows an expansion of the electron beam with a factor of 25. The expansion also decrease the transverse electron beam temperature 25 times lower than that of the cathode, i.e.  $\sim 5$  meV at electron-ion interaction section. According to our calculation, the maximum power consumption by gun solenoid is 57.6 kW that will be cooled by water at a flow rate of 0.9 l/s. It is worth mentioning in Fig. 2 that the inner aperture of the gun solenoid is 120 mm that will limit size of electron beam. Thereafter, we set the cathode diameter as 10 mm.

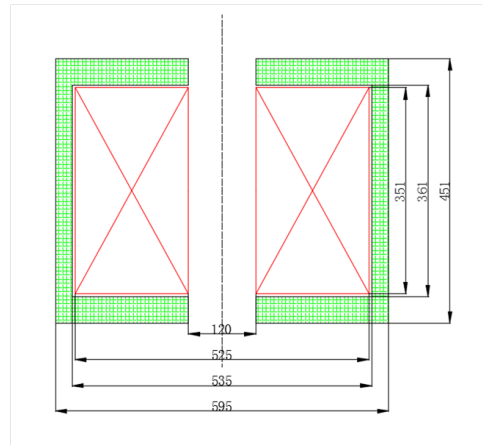


Figure 2: Cross section of the gun solenoid.

The guiding magnetic field at collector is set as 0.1 T. This allows an electron beam transport with a diameter of 34.6 mm at its maximum. That is 20 mm smaller than the aperture at the collector entrance. The heating power derives from electron beam bombing the collector will be taken away by cooling water.

## Guiding Magnetic Field and Bending in Toroid

The first consideration on selecting the optimized guiding magnetic field strength for toroid and interaction section is the attainable lowest transverse electron temperature in transport. The 90 deg bending of electron beam in toroid is a primary contribution after the adiabatic expansion.

Considering the routine design of e-cooler [2], we calculate contributions the parallelism from longitudinal field and added electro-static field for bending transport in the 90 deg toroid. In the following calculation, we set the electron start from four different phase advance of  $0, \pi/2, \pi, 3\pi/2$  in Larmor procession. The electrons have an kinetic energy

of 60 keV, an initial transverse temperature of 93 meV on cathode and adiabatic expanded temperature of 5 meV [3].

Figure 3 shows the calculation result of transverse electron temperature dependence upon the magnetic field strength after toroid in the case of with (upper) and without (lower) the electro-static bending field. The calculation shows that the transverse electron temperature has low value of 16 meV at 0.0495 T in the case with a electro-static deflector, and around 20 meV at 0.041 T, 5 meV at 0.048 T at the case of without the electro-deflector. This can be explained by the temperature contribution from  $\vec{E} \times \vec{B}$  drift.

On the other hand, the success experience of e-coolers at HIRFL-CSR and LEIR [2, 4, 5] show that bending with electro-static field can remarkably improve the collection efficiency. Thus, we take 0.04 T as the design minimal magnetic field strength for operation and 0.05 T as an optimized field when DR experiment is performed. Therefore, a dipole magnetic field is adopted to bend electron from electron gun to the interaction section and an electro-static deflector is used for bending in the toroid at collector side aiming at a higher collection efficiency.

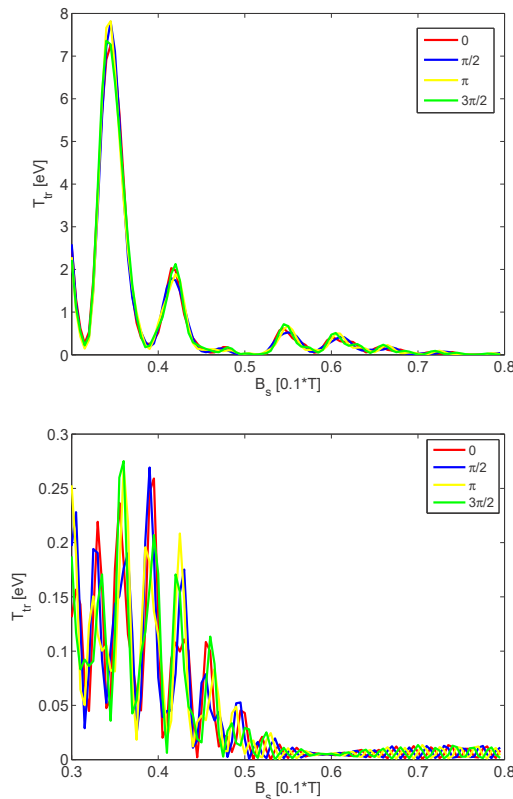


Figure 3: Dependence of transverse electron temperature upon the longitudinal magnetic field strength after toroid with (upper) and without (lower) the bending electro-static field. Electrons start from different initial phase advance of 0,  $\pi/2$ ,  $\pi$ ,  $3\pi/2$  in Larmor procession.

## Adiabatic Expansion of the Electron Beam

The electron beam dynamics from gun to toroid is calculated by USAM code [6]. As a typical case, the field strength around 1.17 T at electron gun and magnetic adiabatic expansion contribute a low temperature when 0.048 T guiding field is applied at the interaction section. The magnetic field strength  $B_s$  variation long the longitudinal axis  $s$  is shown by the black line in Fig. 4. The cathode temperature is set as 93 meV according to the derived result in e-cooler operation at main ring of the HIRFL-CSR [3]. Without the electro-static deflector, the transverse electron temperature  $T_{tr}$  and adiabatic parameter  $\xi = (\lambda_c/B_s) \cdot |dB_s/ds|$  variations along the longitudinal axis are shown in Fig. 4 where  $\lambda_c$  is the electron gyro wavelength. It is also shown in fig. 4 that the approach of low temperature electron beam less than 4 meV is attainable at the current design.

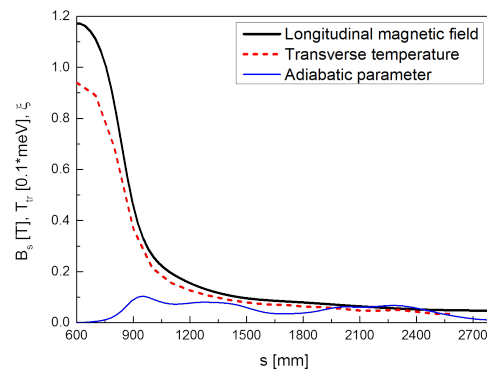


Figure 4: Variation of Longitudinal magnetic field  $B_s$ , transverse electron temperature  $T_{tr}$ , and adiabatic parameter  $\xi$  along the longitudinal coordinate  $s$ .

## CONCLUSION

An 1.2 T routine solenoid and adiabatic expansion is adopted to attain a beam of low temperature electrons for DR experiment at the SRing with an thermionic cathode being adopted. We introduce the preliminary design of e-target system. The calculation shows that the result matches the requirement to e-target in DR experiment.

## ACKNOWLEDGEMENT

The author would like thank fruitful knowledge from BINP electron cooling group and discussion with atomic group at our institute.

## REFERENCES

- [1] J.C. Yang *et al.*, "High Intensity heavy ion Accelerator Facility (HIAF) in China", *Nucl. Instr. and Meth. B*, vol. 317, p. 263-265, 2013.
- [2] V. Parkhomchuk, "Development of a New Generation of Coolers with a Hollow Electron Beam and Electrostatic Bending", *AIP Conference Proceedings*, Vol. 821, 249-258, 2005.

- [3] J. Li *et al.*, "Oxide-cathode activation and surface temperature calculation of electron cooler", *High Power Laser and Particle Beams*, Vol.23, p. 499-502, 2011.
- [4] X. D. Yang *et al.*, "Commissioning of electron cooling in CSRm", *Chinese Physics C*, Vol.33(2) p. 18-21, 2009.
- [5] G. Tranquille *et al.*, "Cooling result from LEIR", *Proceedings of COOL 2007*, p. 55-58, 2007.
- [6] A. Ivanov *et al.*, ULTRASAM - 2D code for simulation of electron guns with ultra-high precision", *Proceeding of EPAC2002*, p. 1634-1636, 2002.

Content from this work may be used under the terms of the CC BY 3.0 licence (© 2017). Any distribution of this work must maintain attribution to the author(s), title of the work, publisher, and DOI.

# PROJECT OF HIGH-VOLTAGE SYSTEM WITH FAST CHANGING POTENTIAL FOR DR EXPERIMENT

V.B.Reva<sup>1</sup>, D.N.Skorobogatov, A.Denisov<sup>1</sup>, V.V.Parkhomchuk<sup>1</sup>, A.Putmakov,  
 BINP, Novosibirsk, Russia  
 X.Ma, J.Li, L.Mao, IMP, Lanzhou, China  
<sup>1</sup>also Novosibirsk State University, Novosibirsk, Russia

## Abstract

A storage ring equipped with an electron cooler is an ideal platform for dielectronic recombination (DR) experiments [1]. In order to fulfil the requirement of DR measurements the system of the precision control of the relative energy between the ion beam and the electron beam should be installed in the electron cooler device. This report describes the project of such system that is designed with section approach like COSY electron cooler. Each section consist of the section of cascade transformer and two power supplies for low and fast detuning of potential of high-voltage terminal. This project can be used in CSRe [2] and future HIAF storage rings [3].

## MODULATION SYSTEM

The idea of the fast modulation of the electron beam energy is based on idea of two power supplies connected in series as it is shown in Figure 1. The power supply 300 kV produces the constant voltage (CPS) for the accelerating of the electron beam to the fixed energy. The pulse power supply (PPS) +/- 30 kV produces the fast switching between two values of the electron energy and realize the pulsing energy of the electron beam near the fixed value (see Fig. 2). Because of the high value of the pulse +/- 30 kV it is difficult to realize it as single unit power supply (PS). Such solution was used at design of the detuning system in EC-35 cooler (CSRm storage ring). Because of this, the PPS should be divided on the several sections with typical pulse voltage +/- 3 kV and CPS with typical continuous voltage + 30 kV also. So, the detuning system looks as a few section connected in series. Each section provides the DC voltage + 1 - + 30 kV and pulse voltage +/- 3 kV. Each section should have independent energy source isolated from ground and other sections. This energy source may be realized as section of the cascade transformer. Thus the construction of new detuning system for CSRe looks as the acceleration section of COSY electron cooler device [4].

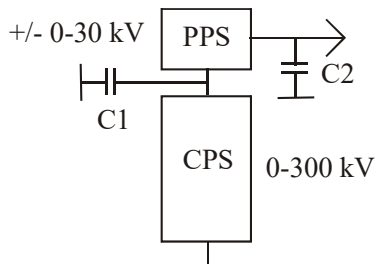


Figure 1: Idea of two power supply connected in series.

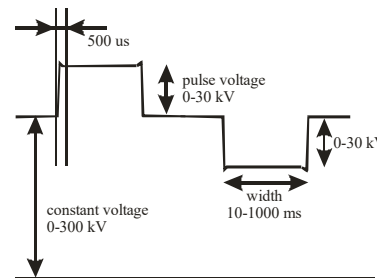


Figure 2: Shape of the detuning system.

The sketch of detuning system for CSRe is shown in Figure 3. It consists of 10 section connected in series. Each section contains CPS, PPS and section of cascade transformer. The high voltage terminal (HVT) contains all power supplies for the electron beam operation. The main problem of such system is inevitable presence of the slow feedback system of CPS (see Fig. 1). The fast change of potential is connected with the capacitance divider with parasitic capacitance C1, C2 of the HVT and 300 kV PS to ground. So after pulse not only the potential in the point B is change, but also the potential in the point A is change too. After that the CPS modules with slow feedback system of 300 kV set the potential of the HVT to the previous value. The parasitic capacitance C2 cannot be decreased from technician point of view. So, we have system with simultaneously operation of two feedback system - fast and slow and both systems see the action of each other.

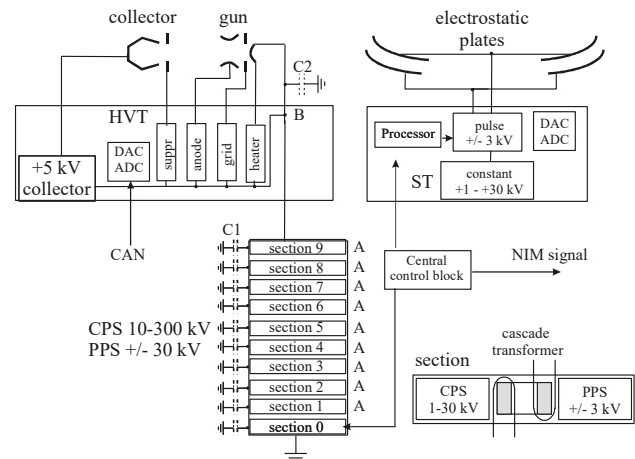


Figure 3: Pulsing system for fast changing of the electron beam energy.

High voltage pulse power supply with feedback can be produced with linear wideband transistor. In spite of the progress in semiconductor technique the transistors aren't

produced on full voltage that is needed for this task. So, the transistor should be connected in series. It leads to the following problems. The first, the voltage applied to each transistor should be less than datasheet value. The second, the transistors located at high potential should be provided by control circuit. The quality of control circuit is very important for obtaining wideband operation. The line of transistors connected in series and operated in linear regime can provide high rate of the switching process between energy levels and the possibility of the fine matching of the voltage for producing high-quality of output voltage. Such circuit can be named as high-voltage (HV) linear operational amplifier (HVA).

The screen shot of the oscilloscope signal from combination HV and HVA is shown in Figure 4. The yellow line is output voltage of the high voltage system, the green line is signal from divider of feedback system and the magenta line is signal of error of feedback system. The edges of pulse are shown in Figure 5. One can see that the transition process of voltage setting is about 400 us.



Figure 4: Signal from test-bench, the pulse amplitude  $\pm 2$  kV, the voltage of the main power supply is 20 kV.



Figure 5: Edges of pulse.

## CASCADE TRANSFORMER

The important problem of such section design is transfer of the electric power to many electronic consumers kept at a high and different electric potential. Several practical methods for solving this problem are possible. EC-300 (see Fig. 6) cooler is used transformer with large gap that are filled by SF<sub>6</sub> gas [5-6]. The experience of COSY [7] cooler shows that the cascade transformer with 33 sections has many benefits. In this case the high potential for electron acceleration can be received with high voltage power supplies connected in series. In this case the classical multiplier (Cockcroft–Walton generator) may have a large number of section but the problems of the

potential sagging and pulsation is decreased significantly because the multiplier section is powered independently. So, the high stability of the electron energy can be obtained.

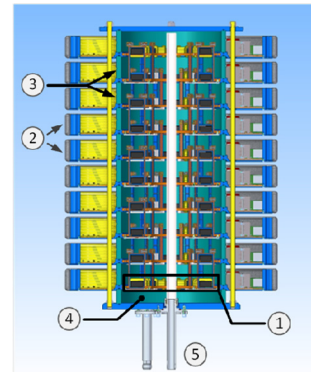


Figure 6: Design of high-voltage system. 1 - section transformer, 2 - electronic section, 3 - section transformer metal ring and ceramics, 4 - vessel filled by oil, input and output of oil.

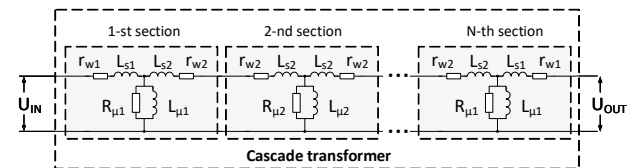


Figure 7: Equivalent circuit diagram of the cascade transformer.

The cascade transformer consists of alternating ceramic and metal rings (see Fig. 6). Inside a metal ring, there is a magnetic core with eight short circuit windings. The potential of the cascade transformer section is specified by the corresponding potential of the high-voltage section for which it acts as the power source. Transformer oil is pumped from the bottom of transformer. The total length of the cascade transformer in design is 0.9 m and the column diameter is 0.74 m. The geometrical sizes of iron (the outer and inner diameters) are 28 cm and 20 cm, thickness is 2 cm, iron mass is 4.8 kg, maximum magnetic induction is 2 kG, magnetic loss at an induction of 2.0 kG is 12 W/kg.

The electrotechnical and equivalent circuit diagrams are shown in Figure 7. It is apparent that the voltage value at the final load strongly depends on the scattering induction  $L_s$ . In order to decrease this value the large number of shot-circuit winding to top and bottom is located close to each other (see Fig. 6). This shot circuit is the primary and the secondary windings. So, the leakage of magnetic flux from one winding is compensated by the other. As result the leakage inductance is less than COSY design to factor 2. In this case the compensative capacitors can be installed outside of the cascade transformer. The variant with capacitors located on one side is shown in Figure 8, and variant with capacitor located on both side is shown in Figure 9. The impedance of the capacitors is equal to impedance of leakage current at resonance frequency 25 kHz.

Content from this work may be used under the terms of the CC BY 3.0 licence (© 2017). Any distribution of this work must maintain attribution to the author(s), title of the work, publisher, and DOI.

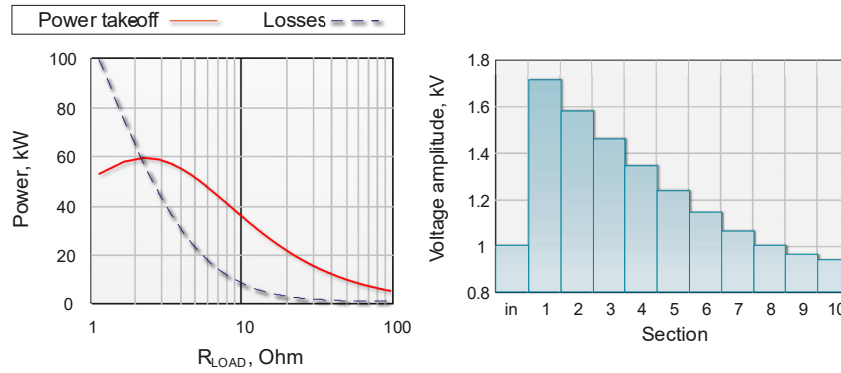


Figure 8: Transfer function of cascade transformer with compensative capacitor  $C_s = 180$  nF from one side.

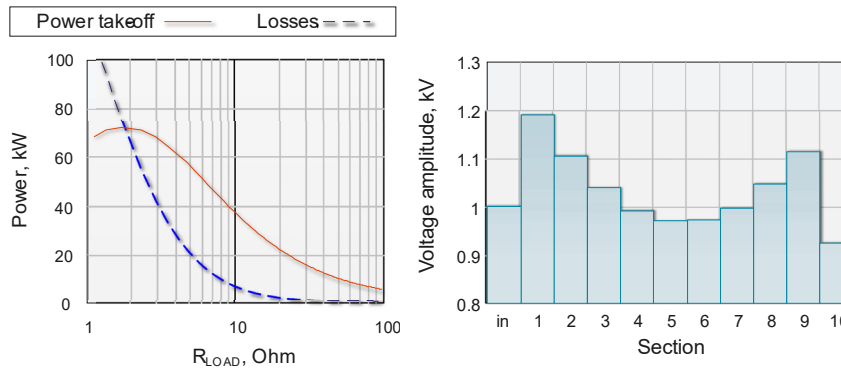


Figure 9: Transfer function of cascade transformer with compensative capacitor from both side.

So, reducing of the leakage inductance gives possibility to install compensative capacitance only outside of the cascade transformer. Such design essentially lighten manufacture and assembling of this device. The variation of voltage level from section to section is good enough (see Fig. 9). The transformer enables to transfer 40 kWt of power with 7 kWt losses according estimation. It is enough for HIAF and CSRe cooler operation. The power consumption of the coolers includes high-voltage modules and the collector power supply (about 15 kWt) for recuperation of the electron beam.

### ACKNOWLEDGEMENT

The reported study was partially funded by RFBR research project №16-52-53016.

### CONCLUSION

The use of section principle for electron cooling devices has a few benefits. It allow to decide together the problem of energy transfer to collector power supply and obtaining precise energy value of the electron beam. This energy can be stable or changing according specified function. This decision can be used in the electron coolers for CSRe and future HIAF storage rings.

### REFERENCES

[1] L.J Meng, X.W Ma, V.V Parkhomchuk, *et al.*, *Chinese Physics C* 2013, 37(1), p.17004:1-17004:8N.

[2] E. Bekhtenev, V. Bocharov, A. Bublely, *et al.*, in *Proceedings of the 9th European Particle Accelerator Conference (EPAC 04)*, Lucerne, Switzerland, 2004, pp. 1419–1421.  
 [3] L.J. Mao, J.C. Yang, J.W. Xia, *et al.*, *Nucl. Instr. Meth. A*, 786 (2015), p. 91-96.  
 [4] V.B. Reva, N. Alinovskiy, T.V. Bedareva, *et al.*, in *Proceedings of the 5th International Particle Accelerator Conference (IPAC 14)*, Dresden, Germany, 2014, p. 777–779.  
 [5] V.M. Veremeenko, R.V. Voskoboynikov, A.D. Goncharov, in *Proceedings of the RuPAC XX*, Novosibirsk, Russia, 2006, p. 97-99.  
 [6] E. Behtenev, V. Bocharov, V. Bublely, in *Proceedings of the RuPAC XIX*, Dubna, Russia, 2004, p.506-510.  
 [7] M.I. Bryzgunov, A.D. Goncharov, V.M.Panasyuk, *et al.*, *Instruments and Experimental Techniques*. 2015. v.58, No 2, p.9-17.

# THE INTERACTION BETWEEN ELECTRONS AND IONS IN COMOVING AND STATIC ELECTRON COLUMNS

V. A. Britten\*, M. Droba, O. Meusel, H. Podlech, A. Schempp, K. Schulte  
 Institute of Applied Physics (IAP), Goethe-University, Frankfurt am Main, Germany

## Abstract

The interaction between electrons and positive ion beams and its application in accelerator physics are investigated. A space charge lens called Gabor lens was developed which confines electrons in a static column by external fields. The confined electrons are used for focusing and support space charge compensation of ion beams. In this configuration the relative velocity between the ions and the electrons is maximal and corresponds to the beam velocity. In comparison an electron lens as at the Tevatron [1] is operated with a lower relative velocity in order to compensate the beam, to clean the beam abort gap or to excite the beam for beam dynamics measurements [2]. Another application is electron cooling, which needs the same velocity of the ion and the electron beam. The following study contains the superposition of electric and magnetic self-fields and their impact on the density distribution of the ion beam and of the electron beam. Recombination and ionisation processes are neglected. This is the beginning of an interface between these topics to find differences and similarities of the interaction between ions and electrons with different relative velocities. This will open up opportunities e.g. for the diagnostics of particle beams.

## INTRODUCTION

The investigated Gabor lens for a static electron column is used as a focusing element in a linear accelerator [3]. Future application is planned as space charge compensation device in ring accelerators. An electron lens also fulfils this purpose with a comoving electron beam. The advantage of a static electron column is that it does not require an electron gun and the undesired effects of the fringe fields are low. Early efforts to utilise a static electron column in a ring accelerator are done at IOTA [4]. To investigate the radius influence on the interaction between a proton beam with the initial radius  $r_p$  and a static electron column with radius  $r_e$ , the cases  $r_e < r_p$  and  $r_e > r_p$  were simulated.

## STATIC ELECTRON COLUMN

A static electron column can be confined by a superposition of electric and magnetic fields. An electrode system and e.g. a solenoid is used in a device called Gabor lens (Fig. 1).

The maximum electron density is limited in radial direction because of the Brillouin limit [5]

$$n_r = \frac{\epsilon_0 B_z^2}{2m_e} \quad (1)$$

\* virginia.a.britten@stud.uni-frankfurt.de

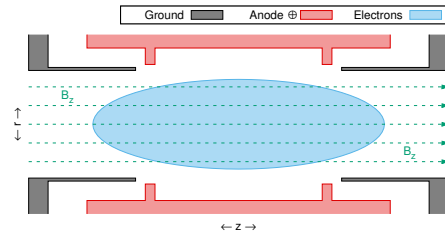


Figure 1: Schematic view of a Gabor lens to confine electrons with a superposition of magnetic and electric fields.

where  $\epsilon_0$  is the vacuum permittivity,  $B_z$  the maximum magnetic field in  $z$ -direction and  $m_e$  the electron mass.

In longitudinal direction the maximum density is limited by the anode potential  $\Phi_A$  and is given by

$$n_l = \frac{4\epsilon_0\Phi_A}{er_e^2 \left(1 + 2 \ln \frac{r_A}{r_e}\right)} \quad (2)$$

where  $e$  is the elementary charge,  $r_e$  the maximum radius of the electron column and  $r_A$  the inner radius of the anode.

An optimal confinement is achieved if both conditions (Eq. (1) and (2)) are fulfilled at once. This results in the working function for a Gabor lens [3]

$$\Phi_A = \frac{er_e^2 \left(1 + 2 \ln \frac{r_A}{r_e}\right) B_z^2}{8m_e} \quad (3)$$

With this system, it is possible to adjust the desired density in the static electron column by external parameters.

## INTERACTION WITH AN IDEAL STATIC ELECTRON COLUMN

Fringe field effects are neglected by assuming an infinite electron column along the longitudinal axis which is called ideal static electron column. In the following, the influence of the proton beam radius  $r_p$  in comparison to the radius of this ideal static electron column  $r_e$  is discussed.

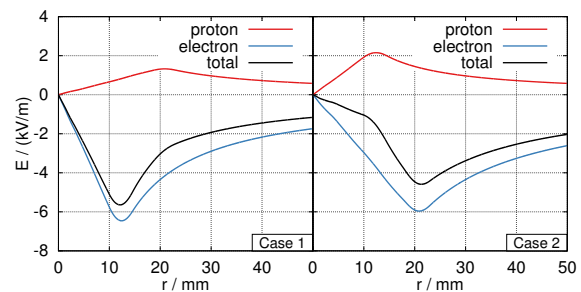


Figure 2: Radial electric fields of the initial homogeneous distributions for case 1 ( $r_e < r_p$ ) and case 2 ( $r_e > r_p$ ) split into the proton and electron part and the resulting field.

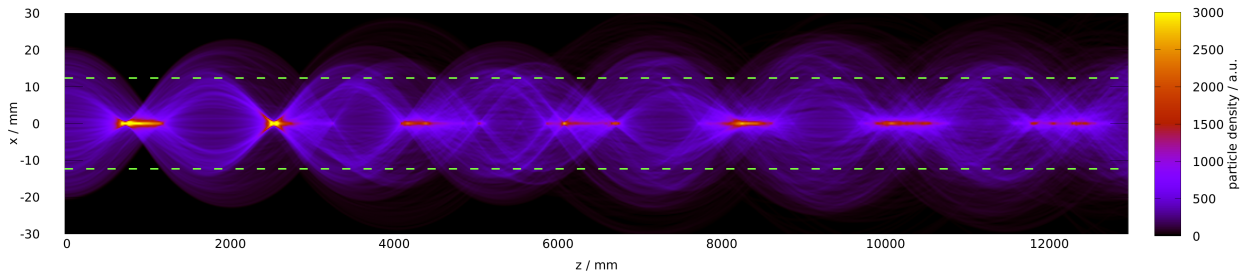


Figure 3: Particle density development for  $r_e < r_p$  of an initially homogeneous proton beam ( $I = 5$  mA,  $E = 50$  keV) which interacts with an ideal static electron column (edge with green dashed line) with a density ratio of  $n_e = 12n_p$ .

**Case 1:  $r_e < r_p$**

In this case, the radius of the static electron column is smaller than the initial radius of the proton beam. Both have a homogeneous distribution. The resulting fields at the beginning are shown on the left side in Fig. 2.

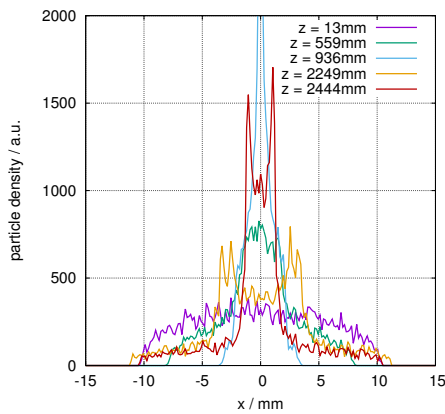


Figure 4: Beam profiles of a proton beam interacting with an ideal electron column for  $r_e < r_p$ .

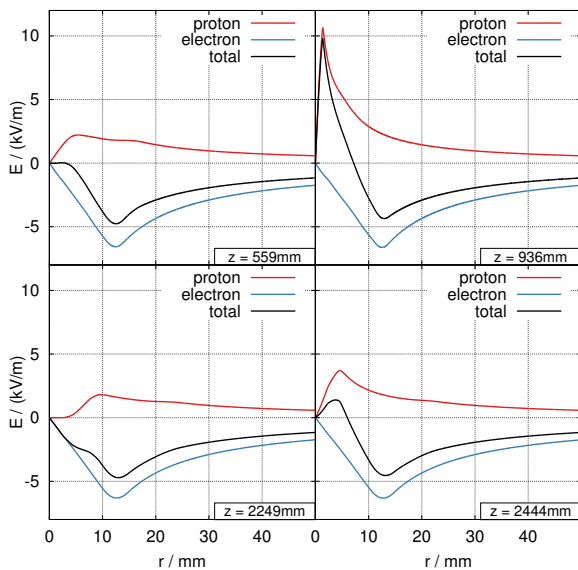


Figure 5: Electric fields for  $r_e < r_p$  at different  $z$ -positions.

The total electric field shows that only the inner part ( $r < r_e$ ) is linear. Outside the electron column, the protons

are exposed to a non-linear field. This leads to shifts in focus (Fig. 3) and changes of the proton beam distribution. After a transient effect the oscillation becomes even.

Some examples of beam profiles at different positions are shown in Fig. 4. The beam profile varies from the initial homogeneous distribution to a approximately Gaussian or to a hollow beam distribution while the beam is transported through the electron column.

The corresponding electric fields are shown in Fig. 5. These indicate the extent of further deformation of the distribution.

**Case 2:  $r_e > r_p$**

If the radius of the electron column is larger than the radius of the proton beam, the initial electric field, which has an effect on the protons, is entirely linear (Fig. 2, right).

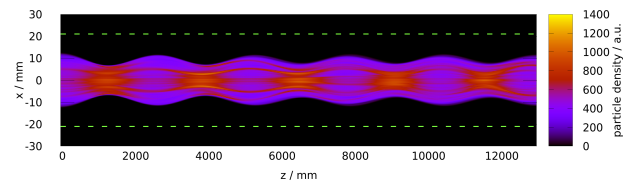


Figure 6: Particle density development for  $r_e > r_p$  of a proton beam through an ideal static electron column (edge with green dashed line).

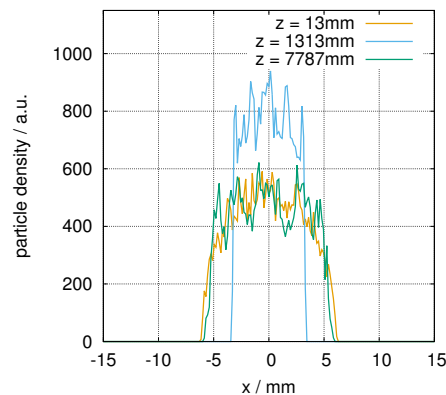


Figure 7: Beam profiles of a proton beam interacting with an ideal electron column for  $r_e > r_p$ .

For the simulation a proton beam with a current of  $I = 5$  mA and an energy of  $E = 50$  keV is chosen while the electron column has a density of  $n_e = 1.5n_p$ . The proton

Content from this work may be used under the terms of the CC BY 3.0 licence (© 2017). Any distribution of this work must maintain attribution to the author(s), title of the work, publisher, and DOI.

beam is compressed up to a density where the space charge force of the proton beam outweigh the compressing force of the electron beam and the proton beam becomes larger again. After reaching the initial radius the beam is compressed again. Typical oscillation behaviour is seen in Fig. 6.

In Fig. 7 selected beam profiles are shown to illustrate that the proton distribution is compressed and decompressed without changing the distribution substantially.

### Kurtosis and Emittance

If the beam radius is smaller or equal to the radius of the static electron column, the kurtosis barely changes because the beam distribution remains approximately homogeneous with a kurtosis value near two.

In the case that the static electron column is smaller than the proton beam, the kurtosis oscillates massively. In a beam focus the kurtosis takes high values, while for large beam radii the kurtosis reaches a local minimum. This local minimum rises and gets closer to a kurtosis value of 3, which means that the beam is approaching a Gaussian distribution. As a result, the non-linear field energy [6] rises.

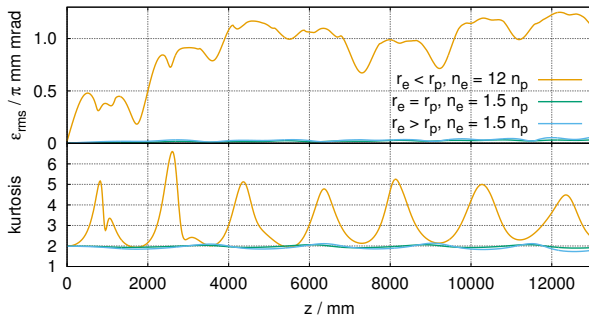


Figure 8: Development of kurtosis and emittance.

The emittance hardly changes for the case  $r_e \geq r_p$ . If the radius of the static electron column is smaller than the radius of the proton beam the emittance is growing (Fig. 8).

## INTERACTION WITH A REALISTIC STATIC ELECTRON COLUMN

To analyse the more realistic case of periodically separated static columns, a coupled Gabor lens is used for the simulations. The density distribution within the static electron column is shown in Fig. 9.

The proton beam has a homogeneous initial distribution, a current of  $I = 5$  mA and an energy of  $E = 300$  keV. The beam is passed through the electron columns several times. The resulting beam profiles are plotted in Fig. 10.

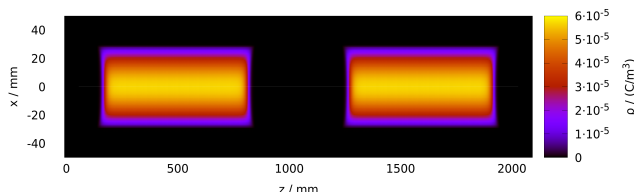


Figure 9: Electron density distribution of a double Gabor lens with  $B_z = 32$  mT and  $\Phi_A = 23$  kV.

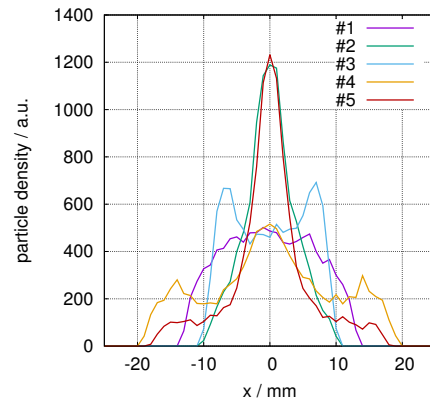


Figure 10: Beam profiles of a proton beam at different positions interacting with a realistic electron column.

In this case, the fringe fields of the electron column have an influence and it is more difficult to adjust a certain radius ratio due to the drift sections where the beam is exposed to its self-field. As a consequence, one part of the proton beam is inside of the column and the other part is outside. This corresponds to the case 1 where the static electron column is smaller than the proton beam. This explains why the resulting beam profiles are similar.

## CONCLUSION AND OUTLOOK

The first results from simulations of the interaction between a static electron column and a proton beam are presented. Further investigations include numerical calculations for different initial density distributions under close examination of non-linear field energies in connection with the change in emittance. The detailed knowledge of the interaction is necessary to apply static electron columns for space charge compensation of ion beams in ring accelerators reliably.

## REFERENCES

- [1] V. Shiltsev *et al.*, “Tevatron electron lenses: Design and operation.”, *Physical Review Special Topics - Accelerators and Beams*, 11.10(2008): 103501.
- [2] X. Zhang, V. Shiltsev, F. Zimmermann, and K. Bishofberger, “The Special Applications of Tevatron Electron Lens in Collider Operation”, in *Proc. PAC’03*, Portland, OR, USA, paper TPPB076.
- [3] K. Schulte, “Studies on the Focusing Performance of a Gabor Lens Depending on Nonneutral Plasma Properties”, Dissertation, Goethe-University Frankfurt, Germany, 2014.
- [4] C. S. Park, V. Shiltsev, G. Stancari, J. C. T. Thangaraj, and D. Milana, “Space Charge Compensation Using Electron Columns and Electron Lenses at IOTA”, in *Proc. NAPAC’16*, Chicago, IL, USA, paper THA3CO04.
- [5] L. Brillouin, “A Theorem of Larmor and Its Importance for Electrons in Magnetic Fields”, *Physical Review*, vol. 67, pp. 260–266, 1945.
- [6] J. Struckmeier, “Selbstkonsistente und nichtselbstkonsistente Phasenraumverteilungen intensiver Ionenstrahlen”, Dissertation, GSI Report 85-14, Darmstadt, Germany, 1985.

# SIMULATION OF LOW ENERGY ION BEAM COOLING WITH PULSED ELECTRON BEAM ON CSRm

H. Zhao<sup>1</sup>, L. J. Mao<sup>†</sup>, X. D. Yang, J. Li, M. T. Tang, J. C. Yang,  
 Institute of Modern Physics, Chinese Academy of Sciences, Lanzhou, China  
<sup>1</sup>also at University of Chinese Academy of Sciences, Beijing, China

## Abstract

The pulsed electron beam can be applied to high energy beam cooling and the researches of ion-electron interaction in the future. In this paper, we studied the pulsed e-beam cooling effects on coasting and bunched ion beam by simulation code which is based on the theory of electron cooling, IBS and space charge effect etc. In the simulation, a rectangular distribution of electron beam was applied to 7 MeV/u <sup>12</sup>C<sup>6+</sup> ion beam on CSRm. It is found that the coasting ion beam was bunched by the pulsed e-beam and the rising and falling region of electron beam current play an important role for the bunching effect, and similar phenomenon was found for the bunched ion beam. In addition, the analyses of these phenomena in simulation were discussed.

## INTRODUCTION

There are several high energy facilities that need electron cooler to acquire high quality, high intensity or short bunch length ion beam are under discussion or construction [1,2]. Classical DC cooler cannot satisfy these requirements because of the large power and the high voltage. The bunched electron beam from cooler or a Linac should be applied in that case. Before the application of high energy cooling, the investigation on low energy beam cooling with bunched electron beam is studied by simulation. It is observed that the grouping effect was happen for coasting or bunched ion beam and the rising and falling edge of e-beam has a strong effect on cooling rate and beam distribution. The simulation code is based on the theory of electron cooling, IBS and space charge effect. The simulation results and some analysis are given in the paper.

## COASTING ION BEAM COOLING

In the simulation, a pulsed electron beam was used to cool the coasting ion beam. The initial beam emittance and momentum spread are 0.3/0.2 pi mm.mrad and 2E-4. The parameters are listed in Table 1. It is observed that the coasting beam is bunched by pulsed electron beam and almost all of the particles are bunched into the region where have electrons as shown in Figure 1.

The revolution period of ion beam is about 4.44 us and the width of pulse electron beam is 2 us with peak current 30 mA. Considering the e-beam current increases linearly to peak with rising and falling time 10 ns, which will generate the electric field due to the space charge effect, and the longitudinal electric field in Laboratory Reference Frame (LRF) is given by

$$E_z(z) = -\frac{g}{4\pi\epsilon_0\beta c\gamma^2} \frac{dI_e(z)}{dz} \quad (1)$$

where  $g$  is the geometric factor. It is obviously the electric field only exist in the rising and falling region. The electric field in longitudinal is calculated ( $E_z=67.7$  V/m) as shown in Figure 1. When particles passing through cooling section, some of them meet the electric field will be kicked by the electric field and the effective voltage seen by the particle in this region is  $V_{\text{kick}}=E_z L_{\text{cooler}}=230.5$  V. It is found that the kick voltage plays a crucial role in the bunching process that all particles are bunched to the e-beam region, as shown in Figure 2. When using the pulse electron beam without the kick voltage, the bunch effect is so weak that only part of particles will be bunched. It can be explained by the barrier bucket theory that the particles are restricted in the region between the two barriers [3]. Because of cooling effect, all particles even that with large momentum spread will be cooled to that region and can't pass through the barrier during the motion in longitudinal phase space.

Table 1: Initial Parameters Used in Simulation

Name	Initial Value
Ion energy	7.0 MeV/u
Particle number per bunch	1E7
Emittance (RMS)	0.3/.2 pi mm mrad
Momentum spread (RMS)	2E-4
Betatron function @cooler	10/10 m
Cooler length	3.4 m
Transition gamma	5.42
E-beam current	30 mA
E-beam radius	3.0 cm
E-beam Temp.	0.2/1E-4 eV
Magnetic field @cooler	1000 Gs
Pulse width	2 us
Rising/falling time	10 ns

In the cooling section, the electrons at different radius inside the beam have different longitudinal velocities because of the space charge effect. Accordingly, the longitudinal velocity component of an ion at a certain radius should be corrected with respect to that of an electron at the same radius [4]. For coasting beam, most ions will be cooled down to positive momentum respect to the reference particle in the equilibrium status. Considering the electric field of electron beam, the motion of particles in phase space is a circle when it is cooled down to the poten-

<sup>†</sup> maolijun@impcas.ac.cn

tial well. So the distribution of particles show a non-uniform behaviour that most particles are accumulated in the beam head, as shown in Figure 2.

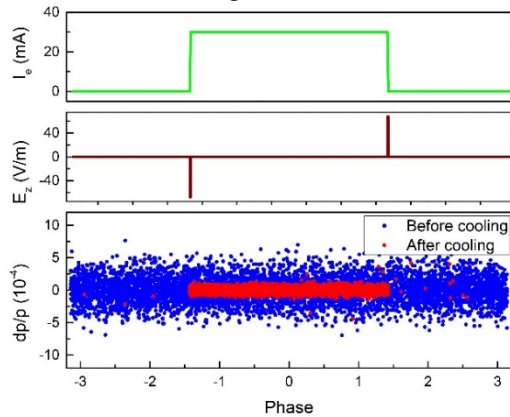


Figure 1: The distribution electron beam current and its electric potential at the edge, and distribution of particles in phase space when pulse e-beam is applied.

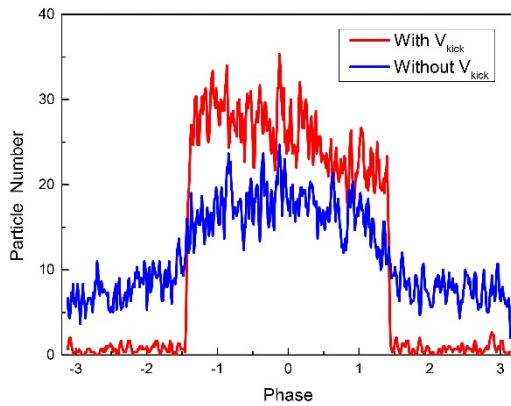


Figure 2: Final beam distribution after cooling with  $V_{kick}$  and without  $V_{kick}$ .

Similar to synchrotron motion in RF, the oscillation caused by the pulsed e-beam is shown in Figure 3. We can see that the potential field is a heating resource for the beam outside the electron beam. If there is no electron cooling force, only part of particles will be bunched to the region and the other particles that outside the region and that with larger momentum spread than the potential field will finally lost because of other heating resource like IBS and gas-scattering effect. When the cooling effect is applied, all particles will finally be cooled and bunched to the pulse region.

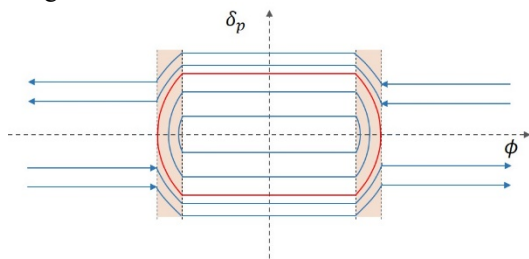


Figure 3: Particle motion in pulsed e-beam.

Since the particle motion in phase space is circle, we would like to study the period time of the bunched beam.

Firstly, the cycle time for a single particle that with momentum spread  $\Delta p/p$  include two parts: cooling section and e-beam edge section, and the period  $t_0$  is

$$t_0 = 2(t_{cool} + t_{edge}) \quad (2)$$

where  $t_{cool}$  is the period time in the cooling section which is determined by the momentum spread

$$t_{cool} = \frac{pulse\_width}{\eta \Delta p/p} \quad (3)$$

$\eta$  is the phase slippage factor.  $t_{edge}$  is the period time in e-beam edge section that can be calculated by

$$t_{edge} = \frac{2 \frac{\Delta p}{p} \beta^2 E}{e V_{kick} Z} \frac{A}{Z} T_0 \quad (4)$$

where the synchrotron mapping equation was used  $\delta_{n+1} - \delta_n = \frac{e V_{kick} Z}{\beta^2 E} \frac{Z}{A}$  [5]. Assuming the particles are been bunched in the cooling region and the distribution of momentum spread is Gaussian, the distribution of  $t_0$  can be calculated by [6]

$$g(t) = f[\phi_{cool}^{-1}(t)] |\Psi'_{cool}(t)| + f[\phi_{edge}^{-1}(t)] |\Psi'_{edge}(t)| \quad (5)$$

where  $f(\delta_p)$  is the beam momentum spread distribution, and  $\delta_p = \Psi(t) = \phi^{-1}(t)$ . Finally, we get the distribution of  $t_0$  as shown in Figure 4.

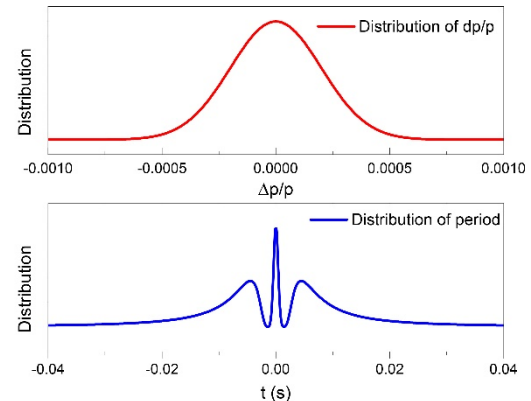


Figure 4: The distribution of momentum spread and period time for ion beam.

It is found that the distribution of period for particles have three peak value. One is the centre part which is correspond to the reference particle and that part is caused by the  $t_{edge}$ . The other two peaks beside the centre are caused by  $t_{cool}$ . It means there exist sidebands in the frequency domain and according to Eq. (5) the frequency sideband is proportional to  $\delta p/pulse\_width$ . In the simulation, we tracked several hundreds of particles for each turn and base on the particle momentum and Fourier transform, the beam spectrum was obtained as shown in Figure 5, in which the simulation results that with and without cooling are included. It is shows that the RMS momentum spread is decrease from  $2E-4$  to  $5E-5$  when cooling effect applied and when there is no cooling, it stays at around  $2.5E-4$ . The oscillation of the result and the little difference of the value at beginning in Figure 5 are caused by the potential at the

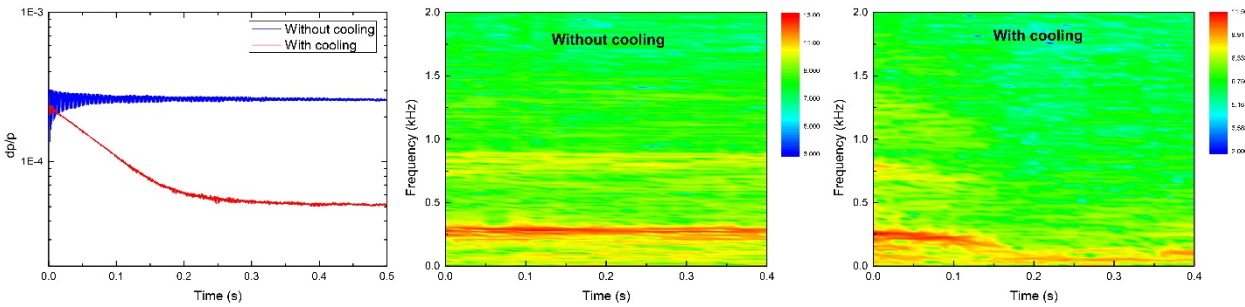


Figure 5: Beam spectrum in frequency domain for pulse e-beam cooling. The initial momentum spread and pulse width are  $2E-4$  and  $600$  ns respectively. The sidebands is caused by the oscillation within pulse electron beam.

edge. According to the calculation in Eq. (5), the sidebands should decrease from  $225\text{Hz}$  to  $56\text{ Hz}$  and stay at  $280\text{ Hz}$  respectively. The spectrum results show a good agreement with the calculation. Because the cooling time is quite small, the resolution of beam spectrum is not very good.

### BUNCHED ION BEAM COOLING

The simulation on ion beam cooling by pulsed electron beam combined with RF voltage was carried out. The ion beam is bunched by the RF voltage and the bunch length will decrease as the cooling process going on. There the pulse e-beam cooling can divided into two conditions: long pulse width which is larger than the RMS bunch length of the initial status before cooling and short pulse that close to the final bunch length of cooled beam.

The initial emittance and momentum spread of ion beam are  $0.3/0.2\text{ pi mm.mrad}$  and  $5E-4$  with the RF voltage  $1.0\text{ kV}$ . The parameters of pulsed electron beam are list in Table 1. Firstly, the initial RMS bunch length of ion beam is  $100\text{ns}$  and the pulse e-beam length is larger than that. The simulation results are shown in Figure 6. The cooling process and the particle distribution are given, which shows a little difference for different pulse e-beam. The cooling rate almost same with each other. It is due to the synchrotron motion of particles that each particle will meet the electron beam quickly, and with the cooling process the ion beam will fast cooled down to the pulse e-beam region where the cooling force is same with other conditions.

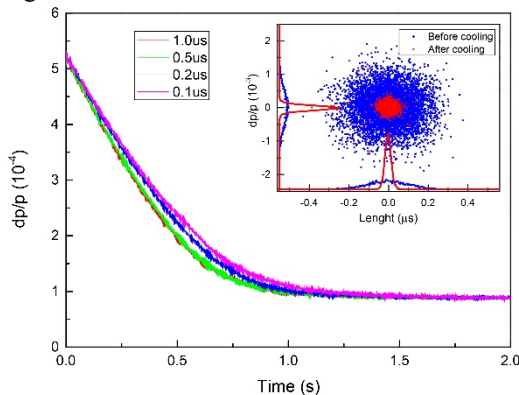


Figure 6: Cooling process with long pulse width of e-beam and the particle distribution before and after cooling.

For the short pulse beam cooling, a multi pulse e-beam with length  $20\text{ns}$ , interval  $10\text{ns}$  and rising/falling time  $10\text{ns}$  is applied. The simulation results are shown in Figure 7.

Because the RF voltage is so small in that small phase region that the distribution of ion beam will restricted by the potential voltage caused by pulse e-beam. So, the ion beam is cooled to two bunches, which are locate in two pulses potential well. In simulation, a single particle motion in phase space was tracked as shown in Figure 7. It is observed that the separatrix orbit of synchrotron is disturbed by the  $V_{\text{kick}}$ . As ion beam is cooling down, the particle will finally fall into one pulse region. However, some particles will be kicked out by the  $V_{\text{kick}}$ , so the electron beam peak current should carefully define in simulation.

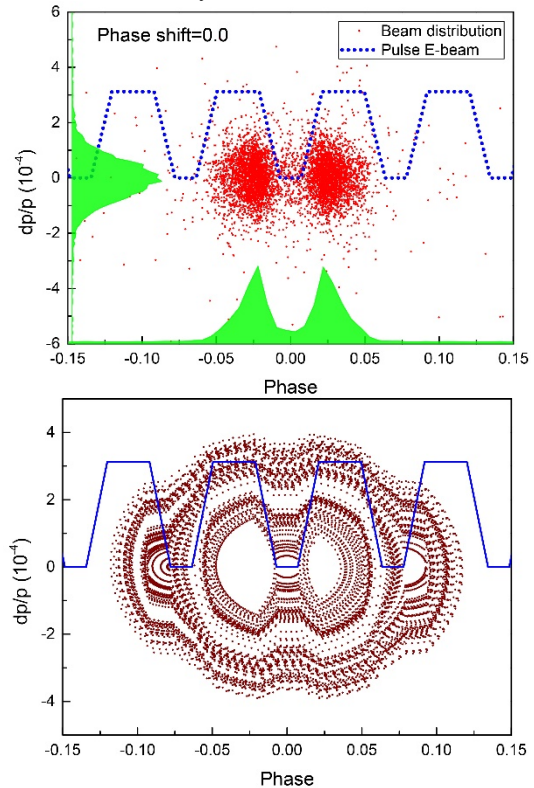


Figure 7: Beam distribution after cooled by short pulse e-beam with pulse width  $20\text{ ns}$  and single particle tracking in phase space.

We also tried to introduce a phase shift to the pulse electron beam which is not symmetrical in longitudinal. The result is shown in Figure 8. The bunched ion beam was cooled down to two bunches, but most particles was bunched to one side which is close to the synchronous

Content from this work may be used under the terms of the CC BY 3.0 licence (© 2017). Any distribution of this work must maintain attribution to the author(s), title of the work, publisher, and DOI.

phase ( $\Phi_s=0$ ). It indicates that the potential voltage  $V_{\text{kick}}$  is important for the status of ion beam. The finally distribution of ions can be modulated by the pulsed electron beam.

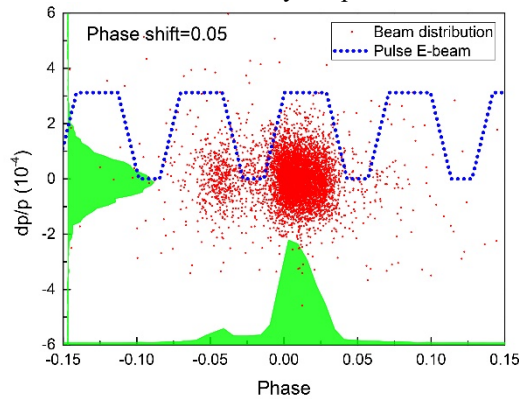


Figure 8: Beam distribution after cooling with the pulsed e-beam which have a phase shift (0.05) in longitudinal.

## CONCLUSION

In this paper, we simulated the low energy pulsed electron beam cooling on coasting and bunched ion beam. The grouping effect and some other phenomenon were found. These results are meaningful for the high energy electron cooling in the future.

## ACKNOWLEDGEMENT

The authors would like to express their thanks to Dr. Takayama and Dr. Smirnov for the help on the simulation code. This work is supported by the National Natural Science Foundation of China (Project No.11575264, No.11375245 and No.11475235) and the Hundred Talents Project of the Chinese Academy of Sciences.

## REFERENCES

- [1] LEReC  
[http://www.c-ad.bnl.gov/esfd/LE\\_RHICeCooling\\_Project/LEReC.htm](http://www.c-ad.bnl.gov/esfd/LE_RHICeCooling_Project/LEReC.htm)
- [2] JLEIC, [https://eic.jlab.org/wiki/index.php/Main\\_Page](https://eic.jlab.org/wiki/index.php/Main_Page)
- [3] C.M. Bhat, "Applications of barrier bucket RF systems at Fermilab", *Presented at No. FERMILAB-CONF-06-102-AD*, 45 2006.
- [4] Y. N. Rao, "Simulation of electron cooling and intrabeam scattering processes of a heavy ion beam in HIRFL-CSR", *Instrum. Methods Pys. Res., Sect. A*, Vol.391, no.42, p. 42, 1997.
- [5] S.Y. Lee, "Accelerator Physics", USA: World Scientific, 2006, p. 245.
- [6] J. Schiller, "Schaum's Outline of Probability and Statistics, Fourth Edition", McGraw Hill Professional, 3<sup>rd</sup> Edition, 2008.

# CALCULATIONS OF THE GUN AND COLLECTOR FOR ELECTRON COOLING SYSTEMS OF HIAF\*

Mei-Tang Tang, Li-Jun Mao<sup>†</sup>, He Zhao, Jie Li, Xiao-Ming Ma, Xiao-Dong Yang, Hai-Jiao Lu, Li-Xia Zhao, Institute of Modern Physics, Lanzhou, China  
 A. V. Ivanov, Budker Institute of Nuclear Physics, Novosibirsk, Russia

## Abstract

Two electron coolers are designed for the new project HIAF, one cooler with the highest energy 50keV is for the booster ring (BRing) to decreasing the transverse emittance of injected beams and another one with the highest energy 450keV is for the high precision Spectrometer Ring (SRing). In this paper the results of the gun and collector simulation for these two electron coolers are presented. After optimization, the gun can produce 2A profile variable electron beam. The one time collecting efficiency is higher than 99.99%. The results of electron motions in toroid calculated by a numerical method are also summarized in this paper.

## INTRODUCTION

The new accelerate facility HIAF is under design at the Institute of Modern Physics (IMP) [1], Chinese Academy of Sciences, which aimed to provide high intensity heavy ion beams for a wide range of research fields, such as high energy density physics, nuclear physics, atomic physics and so on. It consists of three ion sources (two Superconducting Electron Cyclotron-Resonance and (SECR) and a high intensity H<sup>2+</sup> ion source(LIPS)), a superconducting Ion Linac as a injector (iLinac), a Booster Ring (BRing), a high precision Spectrometer Ring (SRing) and some terminals for experiments. The schematic layout of the HIAF facility is shown in Fig. 1

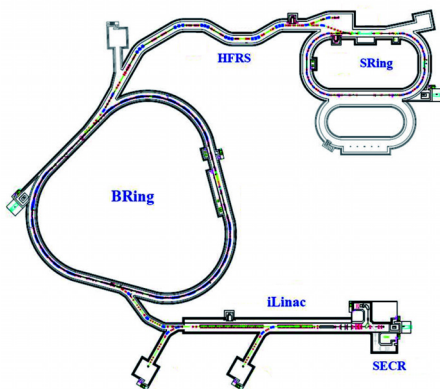


Figure 1: Layout of the HIAF accelerator facility.

Two magnetized electron cooling systems are planned to be used in the BRing and SRing to obtain intense ion

\* Work supported by the NSFC (Nos. 11575264, 11375245, 11475235, 1161130016)  
<sup>†</sup> maolijun@impcas.ac.cn

beams and to improve beam quality [2]. The main parameters of these two cooler are summarised in Table 1.

Table 1: Main Parameters of Electron Coolers of HIAF

Parameters	BRing	SRing
Maximum energy [keV]	50	450
Electron beam current [A]	2	2
Cathode radius [cm]	1.3	1.3
Maximum B <sub>gun</sub> [kGs]	2.5	4.0
Maximum B <sub>cool</sub> [kGs]	1.5	1.5
Maximum B <sub>coll.</sub> [kGs]	1.7	2.0
Effective cooling length [m]	7.4	7.4
Angle of toroid [deg.]	90	90
Radius of toroid [m]	1	1

## ELECTRON GUN

Electron guns designed for electron coolers of BRing and SRing have same geometry. The structure of the gun is shown in Fig. 2a. A convex cathode with the curvature radius equal to 48mm is used. A grid and an anode are used to control the electron beam current and the transverse distribution through changing the potential distribution nearby the cathode.

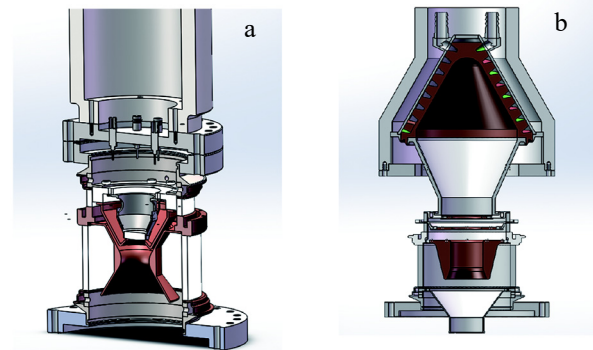


Figure 2: Structures of the electron gun and collector for cooler of HIAF.

Electron gun are calculated by code ULTRASAM [3]. Figure 3 shows the electron beam density distribution with different voltage on grid and anode relative to the cathode. The lines with different colours red, green, yellow and black respectively correspond the situation that voltage on grid equal to 2.5kV, 1.9kV, 1.7kV, 1kV and voltage on anode equal to 3.7kV, 7.7kV, 9.2kV, 13.7kV. When voltage is large enough, 2A parabolic beam and hollow beam can be produced by the gun.

Content from this work may be used under the terms of the CC BY 3.0 licence (© 2017). Any distribution of this work must maintain attribution to the author(s), title of the work, publisher, and DOI.

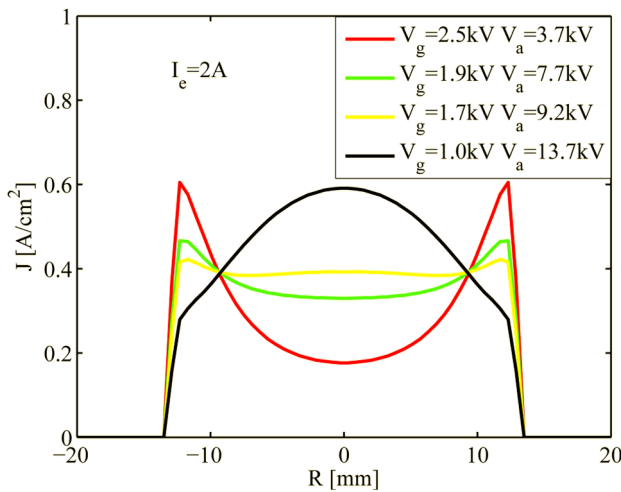


Figure 3: Electron beam current density distribution with different voltage on grid and anode.

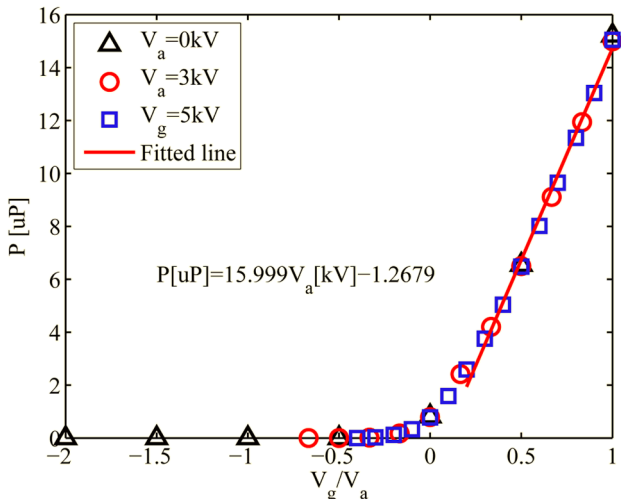


Figure 4: The variation of perveance with  $V_g/V_a$ .

Figure 4 shows the variation of the perveance with the ratio  $V_g/V_a$  ( $V_g$  is the voltage on grid relative to cathode,  $V_a$  is the voltage on anode relative to cathode). With the increase of the ratio  $V_g/V_a$ , the perveance of the gun increase. When  $V_g/V_a$  equal to 1 the perveance will reach about 15uP.

### ACCELERATION AND ADIABATIC EXPANSION

To let the maximum energy of the SRing's cooler reach 450keV, an additional accelerating tube is designed. However, the energy of BRing's cooler so low (50keV) that only one additional accelerating electrode is enough. Figure 5 shows the models used to simulate SRing's cooler.

The transverse electric fields ( $E_r$ ) at the  $r=1\text{mm}$  are calculated by ULTRASAM and also shown in Fig. 5. Calculations indicate that only the  $E_r$  at the end of the accelerating tube of SRing's electron gun has significant influence on the transverse electron beam temperature. To decrease the influence of the transverse electric field on the beam

temperature, the field of the gun region is optimized and an additional coil is used to enhance the local field.

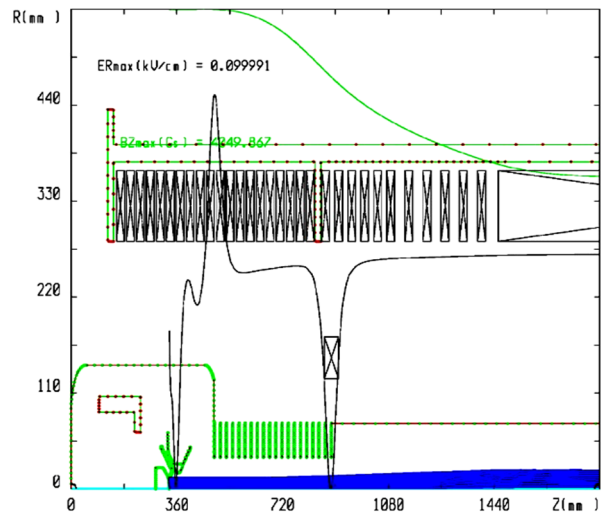


Figure 5: The geometry of the magnetic system for guns of SRing.

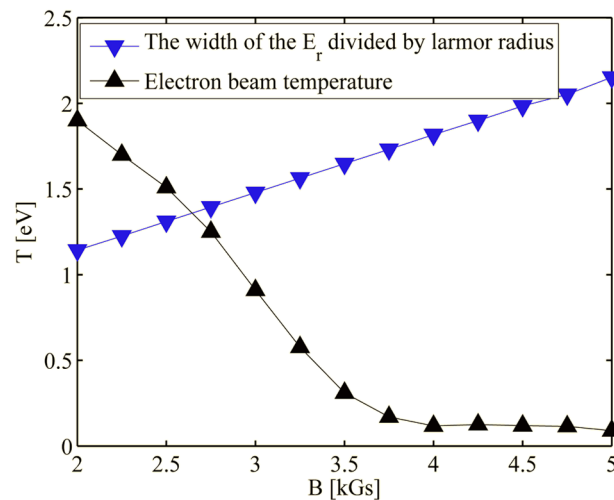


Figure 6: Dependency of the transverse temperature increase at the entrance of the toroid on the magnetic field in the gun region.

The temperature is calculated after beam is accelerated and adiabatically expanded. In calculations, the electron beam current is 2A, energy is 450keV and the magnetic field at entrance of toroid is 1kGs. The result is shown in Fig. 6. From Fig. 6 it can be found that when magnetic field in the gun region increases the temperature will decrease. One reason is that when the field increase the larmor radius of the electron beam will decrease, and beam will pass through the transverse field section more adiabatically, another reason is that the expansion factor of the system will increase when the field in gun section increase. Calculations indicate that when the field is larger than 4kGs, the field increasing will have less influence to the beam temperature, the temperature will keep at about 0.1eV. Therefore, for SRing's cooler the field in

Content from this work may be used under the terms of the CC BY 3.0 licence (© 2017). Any distribution of this work must maintain attribution to the author(s), title of the work, publisher, and DOI.

gun region for 450keV electron beam should not less than 4kGs. To further decrease the influence of  $E_r$ , the additional coil at the end of the accelerating tube should be used. More calculations show that with the help of the coil beam (2A 450keV) temperature can reach 0.05eV after the beam be adiabatically expanded.

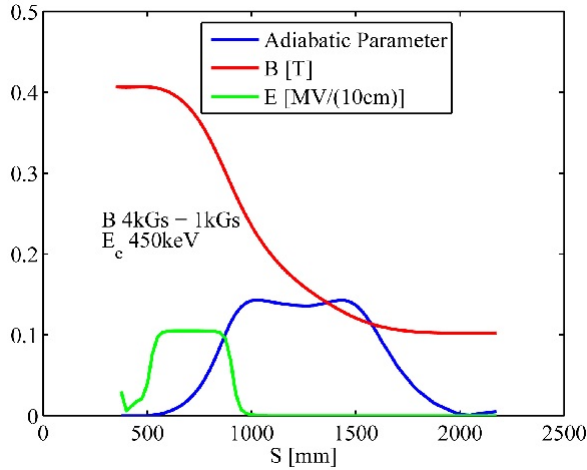


Figure 7: The adiabatic parameters for guns of SRing

Figure 7 shows the adiabatic parameter of SRing. It can be found that the adiabatic parameters are  $\ll 1$  for the 450keV electron beam.

## COLLECTOR

The structures of the collectors design for BRing and SRing's coolers are similar with the collector in the CSR. The magnetic systems for these two collectors are different with CSR's coolers, the maximum magnetic field is 1.7kGs for BRing's collector and the field is 2kGs for SRing's collector. Although the maximum magnetic field is different the magnetic systems in collector region is have same layout. One decelerating tube is used to decelerate beam energy to several keV for SRing's collector, for BRing's cooler the decelerating tube is not necessary.

Figure 2b and Figure 8 show the collector's structure, the layout of the magnetic coils, the field in the collector section and the beam profile in collectors. In calculation, the input beam energy are 50keV and 450keV for BRing and SRing's collector respectively, the beam current is 2A and the voltage on collector is 3.5kV relative to the cathode, the voltage on suppressor is -2kV relative to the collector, and the voltage on collector anode is same with the voltage on collector.

The efficiency of a collector can be estimated by following formula [4]

$$\frac{I_{loss}}{I_{beam}} = k \left( \frac{U_c}{U_0} \right)^2 \frac{B_c}{B_0} \quad (1)$$

Where  $U_{min}$  is the potential at the entrance of the collector,  $U_{coll}$  is the potential on the collector,  $B_c$  and  $B_0$  are the magnetic fields on the surface of the collector and at the entrance of the collector, respectively.  $k$  is a constant.

When voltage on collector is 3.5 kV relative to the cathode, the voltage on suppressor is -2 kV relative to the collector, the  $\frac{U_c}{U_0}$  will be 0.33, 0.40, and  $\frac{B_c}{B_0}$  will be 0.03, 0.04 respectively for BRing and SRing's collector. Taking  $k$  to be 0.1 and using formula (1) the one time secondary electron escape rate can be obtained, and it is  $3.3 \cdot 10^{-4}$  for BRing and  $6.4 \cdot 10^{-4}$  for SRing.

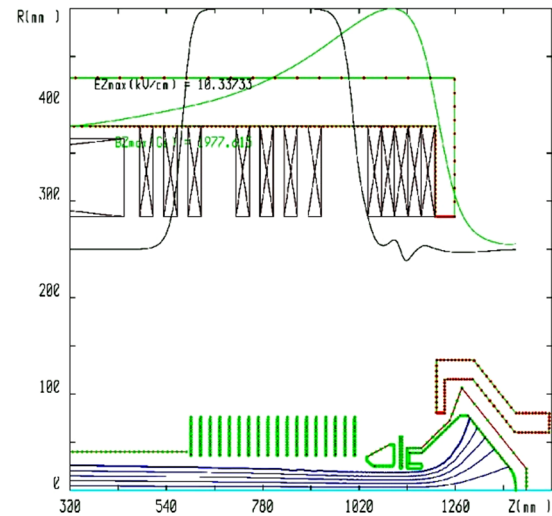


Figure 8: The collector structure of SRing, field in collector region, and beam profile in collector.

## ELECTRON MOTION IN TOROID

Electron beams motion in toroid is calculated by a numerical method. The follow approximate equations are used to calculate the motion of electrons in the orthogonal curvilinear coordinate system to the magnetic field  $B$  in the center of the magnetic system.

$$\left\{ \begin{aligned} \frac{dV_t}{ds} &= \frac{V_t}{2} \frac{\partial \ln B}{\partial s} + \left[ \left(1 - \frac{V_t^2}{c^2}\right) \frac{eE_t}{\gamma m} - V_s^2 K \right] \frac{\cos \theta}{V_s} \\ \frac{d\theta}{ds} &= \frac{1}{V_s} \left\{ W_H - \left[ \frac{eE_t}{\gamma m} - V_s^2 K \right] \frac{\sin \theta}{V_t} \right\} \\ \frac{ds}{dt} &= V_s \\ V &= \sqrt{V_s^2 + V_t^2} \end{aligned} \right. \quad (2)$$

Where  $V_t$  is the transverse velocity of a electron,  $\theta$  is the rotation angle around the field,  $V_s$  is the velocity along the field,  $K$  is the curvature of the  $B$ ,  $E_n$  is the elec-

tric field of the deflector used to compensate the electron beam drift in toroid.

Electron motion can be calculated by solving above equations. In calculations, the electron energy is equal to 450keV, the initial larmor velocity of electron is  $1.38 \cdot 10^7$  cm/s. Figure 9 show the the dependencies of the Larmor rotation velocity  $V_t$  at the end of the toroid on the magnetic field of toroid. Lines with different colours are the results with different initial rotation angles  $\theta = 0, \pi/2, \pi, 2\pi/3$ . It can be found that there are many magnetic field value can be selected to let the  $V_t$  be small. When the field increase the  $V_t$  will decrease. When field equal to 0.987kGs the 450keV electron will have a lowest larmor velocity increase after it passing the toroid.

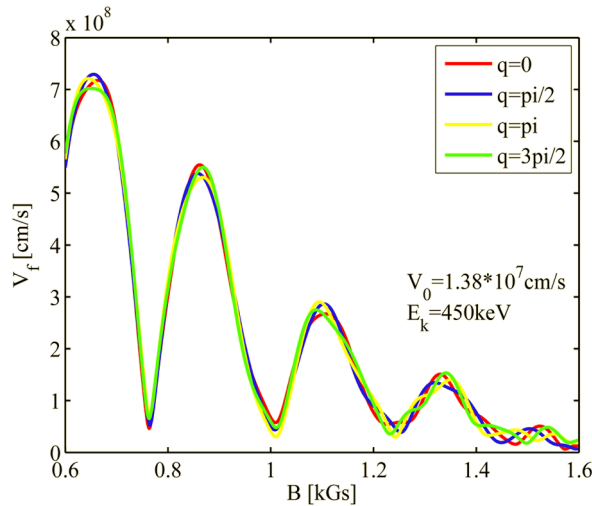


Figure 9: The dependencies of the velocity  $V_t$  on magnetic field.

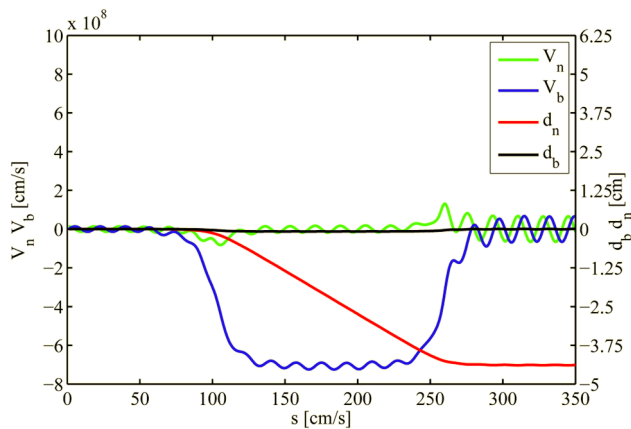


Figure 10: Variation of transverse velocity and electron displacements in two directions (without deflector).

Figures 10, 11 show the case without a electric deflector and the case with a deflector in toroid. It can be found that when there is no deflector there will be an about 4cm displacement after 450keV electron beam passing though the toroid.

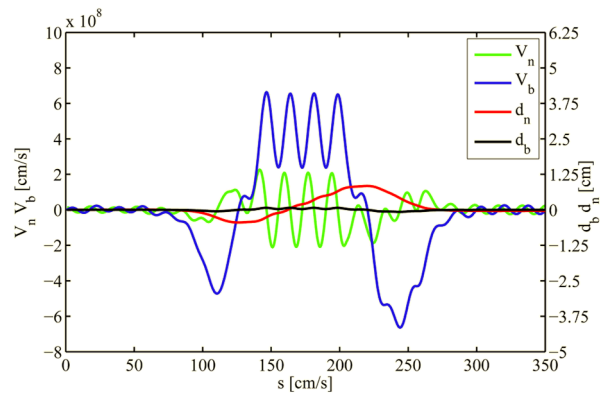


Figure 11: Variation of transverse velocity and electron displacements in two directions (with a deflector).

Further calculations indicate that when the optimum field is chosen the temperature increase will below 0.4eV for 450keV electron beam after it passing the toroid. For 50keV electron beam it's easy to let the beam temperature increase lower than 0.1eV when it passing the toroid.

## CONCLUSION

The basic design of gun and collector for HIAF has been finished. The beam motion in gun and collector are calculated by code ULTRASAM. The guns can produce 2A profile variable electron beam. The transverse temperature of the electron beam is control lower than 0.1eV. The magnetic system is design for the gun and collector, and the adiabatic parameters are nearly 0.1 for highest energy electron beam. The one time collecting efficiency of the collector is about 99.99%. The electron motion in toroid is calculated by numerical method. After optimizing the magnetic field in toroid, the temperature increase will below 0.4eV for 450keV electron beam and below 0.1eV for 50keV electron beam after the beam pass though the toroid.

## REFERENCES

- [1] J. C. Yang, J. W. Xia, G. Q. Xiao *et al.*, *Nuclear Instruments and Methods in Physics Research Section B*, 317 (2013) 263.
- [2] L. J. Mao, J. C. Yang, J. W. Xia *et al.*, *Nuclear Instruments and Methods in Physics Research Section A*, 786 (2015) 91–96.
- [3] A. Ivanov, and M. Tiunov, “ULTRASAM - 2D Code for Simulation of Electron Guns with Ultra High Precision”, in *Proc. EPAC'02*, Paris, France, 2002, pp 1634-1636.
- [4] M. I. Bryzgunov, A. V. Ivanov, V. M. Panasyuk *et al.*, “Efficiency improvement of an electron collector intended for electron cooling systems using a Wien filter[J]”, *Technical Physics*, 2013, 58(6): 911-918.

# INVESTIGATION ON THE SUPPRESSION OF INTRABEAM SCATTERING IN THE HIGH INTENSITY HEAVY ION BEAM WITH THE HELP OF LONGITUDINAL MULTI-BUNCH CHAIN OF ELECTRON\*

X. D. Yang<sup>†</sup>, L. J. Mao, J. Li, X. M. Ma, T. L. Yan, M. T. Tang, H. Zhao  
Institute of Modern Physics, CAS, Lanzhou, China

## Abstract

Intrabeam scattering is the main reason of degradation of the beam brightness and shortening of brightness lifetime in the collider, light source and storage ring. The intrabeam scattering presents dissimilar influence in the different facilities. Electron cooling was chosen to suppress the effect of intrabeam scattering and another unexpected effect happened during the cooling. The distribution of ion beam quickly deviates from the initial Gaussian type, then form a denser core and long tail. The ions standing in the tail of beam will loss soon owing to large amplitude. This solution will focus on the investigation on the suppression of intrabeam scattering in the high intensity heavy ion beam in the storage ring with the help of longitudinally modulated electron beam. The stronger cooling was expected in the tail of ion beam and the weaker cooling was performed in the tail of ion beam. The particle outside will experience stronger cooling and will be driven back into the centre of ion beam during which the ion loss will decrease and the lifetime will increase. The intensity of ion beam in the storage ring will be kept and maintain for a long time.

## INTRODUCTION

This solution will focus on the investigation on the suppression of intrabeam scattering in the high intensity heavy ion beam in the storage ring with the help of longitudinally modulated electron beam. The traditional DC electron beam in the electron cooler was modulated into electron bunch with different longitudinal distribution. The stronger cooling was expected in the tail of ion beam and the weaker cooling was performed in the tail of ion beam. The particle outside will experience stronger cooling and will be driven back into the centre of ion beam. The ion loss will lessen and the lifetime will be increased. The intensity of ion beam in the storage ring will be kept and maintain for a long time. Two functions will be combined into one electron cooler. The more short pulse, the more high intensity and more low emittance heavy ion beam was expected in the cooler storage ring. In the future, these results of this project will be constructive to the upgrade and improvement for existing machine and also be helpful to the design and operation for future storage and high energy electron cooler.

## SOME CONSIDERATIONS

The final equilibrium transverse emittance and longitu-

dinal momentum spread were determined by the cooling effect and intra-beam scattering heating effect together in the case of fixed ion energy and particle number. If we want to get more particle number, in other words, more intensive ion beam, a new parameters configuration will be necessary in the new equilibrium state. In the absence of electron cooling, the transverse ion beam will be blown-up due to not suppression intra-beam scattering effect. The transverse dimension and longitudinal length of ion beam will increase with time, as a result, some ion will loss and the lifetime of ion beam will become short.

## LIFETIME AND INTENSITY OF ION BEAM

The ion beam of  $^{238}\text{U}^{92+}$  with population  $1 \cdot 10^{11}$  particle was required in the high energy high intensity accelerator facility [1]. In this situation, the final emittance and momentum spread were the key parameters which the physics experiments concerned, more important parameters of ion beam were lifetime and the ion number in the detectors.

## MOTIVATION

Two essential questions should be certainly answered and clearly described in advance.

The first question concerned by physics experiment is that whether enough particle [2] be provided to the experiments terminals.

The second one concerned the lifetime [3] of the ion beam with so high intensity whether enough to satisfy the requirements of physics experiments, because it determines the efficiency of experiments.

## NEW SOLUTION PROPOSED

There are three points in this solution. The first point, the intensity of electron bunch presents certain distribution according to the ion bunch distribution in the longitudinal direction. The second point, the electron bunch distribution will change actively according to the ion beam distribution in the cooling process. As a result, the electron beam will provide different strength cooling in the different periods. The third point, the transverse intensity distribution can change also, the electron beam can present different transverse distribution according to the transverse distribution of ion beam in the cooling process. The purpose of this solution will aim to suppress the effect of IBS, increase the lifetime of ion beam and reduce

\* Work supported by The National Natural Science Foundation of China, NSFC (Grant No. 11375245, 11475235, 11575264)

<sup>†</sup> yangxd@impcas.ac.cn

the ion loss during cooling [4].

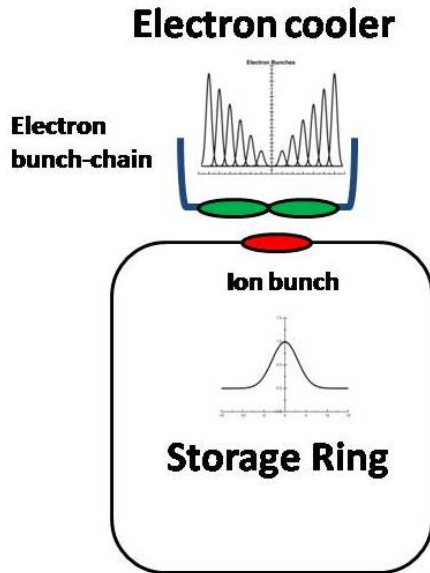


Figure 1: The longitudinal relation between the ion bunch in the storage ring and electron multi-bunch in the electron cooler.

In the interest of cooling the un-Gaussian distribution ion beam and suppressing the IBS in the ion beam, we plan to modulate the electron beam in longitudinal direction [5]. In the first step, two proximate electron bunches were delivered by the electron gun, and triggered isochronously. An ion bunch will be cooled by this two electron bunches, it was shown in Fig. 1. We hope this solution can provide stronger cooling in the tail of ion pulse, and relatively weaker cooling in the core of ion bunch. Further, the hollow electron beam will be united with the longitudinal electron bunches. We hope decrease the ion loss caused by recombination. The hollow electron beam in which the radial distribution of electron can be changed will be combined with the longitudinal modulated electron bunch chain in which the longitudinal distribution presents proper distribution as demonstrated in Fig.2.

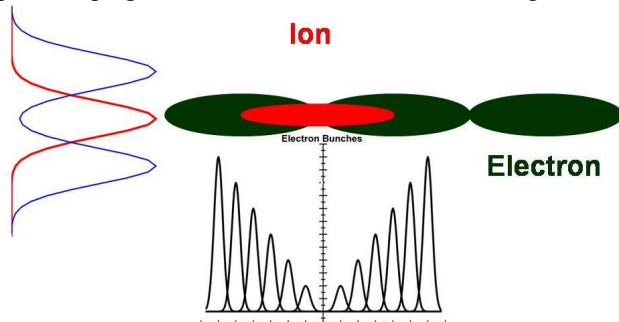


Figure 2: Diagram of ion bunch and electron multi-bunch distributions in the transverse and longitudinal directions respectively.

If we use the pulsed electron beam, as one possible result, we can use higher average electron density than the DC electron beam, the ion in the beam can experience higher cooling than DC electron beam, and these ion were

expected to be cooled down quickly, and to avoid escaping from the RF bucket.

### Betacool Simulation

Betacool program [6] has the ability to simulate the cooling and intrabeam scattering processes together in the various conditions, such as electron bunches and it can give the information about the lifetime of ion beam and final equilibrium emittance and bunch length, etc. Another function was developed for calculating the cooling and scattering intrabeam in the case of bunched electron beam.

According to the information from the IBS measurement results, the electron beam will be provided different distribution in the different periods, such as in the beginning of cooling and intrabeam scattering, before achieve the equilibrium and final equilibrium situation. In the beginning, the ion beam needs to cool down fast with the lowest ion loss, while before the equilibrium it needs modest cooling, and in the period of equilibrium, it just needs maintaining the proper cooling to counteract IBS effect.

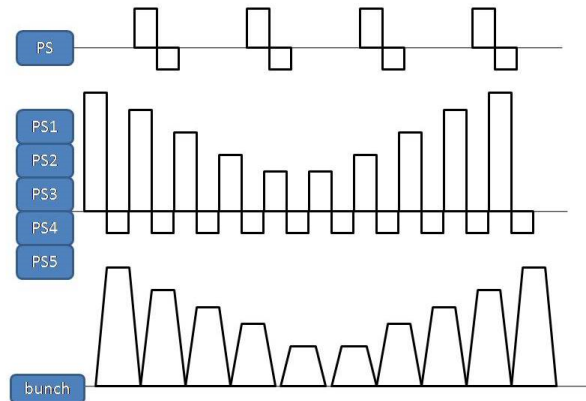


Figure 3: Sketch of ten electron bunches generated by five independent HV power supplies with the help of delay trigger.

### Scheme and Scenario

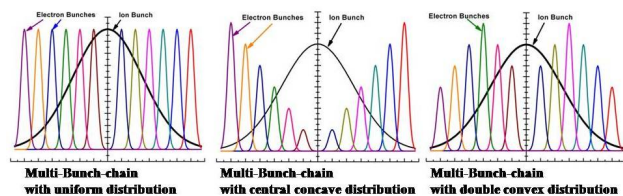


Figure 4: The longitudinal distributions of ion bunch and electron multi-bunch with different interval.

In order to get the multi-bunch with the certain frequency corresponding the ion beam revolution frequency, two independent HV power supplies were arranged in parallel connection. Delay trigger was used in this solution, as illustrated in Fig. 3. Every electron bunch was driven by the independent HV power supply, and the strength, width and space will be adjusted independently. In additional, the time relation between the multi electron bunch can be triggered slightly advance precede and trail

before and after the ion pulse in the electron cooler, and ion pulse will be timely, earlier or later.

### Implement

In order to optimize and improve the effect of this multi-bunch chain, we plan to vary the strength, interval of individual bunch and delay time with respect to the ion bunch to investigate the efficiency of cooling and suppression of IBS as presented in Fig. 4.

A multi-bunch chains were expected to deliver form the electron gun of cooler in order to implement the different cooling in the different position of ion beam, the ion in the centre of ion beam will be cooled mildly and the ion located in the tail of ion beam will be cooler intensively and fleetly. As a result, the ions outside of the beam was drug into the central part of ion beam, the ion loss caused by larger oscillation amplitude will be reduced, and the ion beam intensity was retained.

### Experimental Investigation

Intrabeam scattering not only depends on the lattice optical parameters of storage ring, but also depends on the parameters of ion beam, such as population, energy and charge state of ion. Furthermore, IBS depends on the condition and mode of cooling system.

The intrabeam scattering in the cases of different ion beam energy and population will be studies as well as the electron cooling process. The transverse emittance and longitudinal bunch length will be measured after the electron beam was switched off, the transverse growth rate and longitudinal growth rate, ion loss, and ion beam lifetime will be derived from these experiments.

The transverse emittance and longitudinal bunch length will be measured with the help of beam profile monitor and Schottky probe, and their developing with time will be recorded in the case of different energy and population in the ion beam with different initial ion beam parameters.

The normal uniform DC electron beam was chosen as the reference, the cooling time, equilibrium emittance and momentum spread will be measured in this condition, and the information of beam lifetime and beam loss during the cooling was derived from the data of beam current transformer.

The second step, the perform of a multi-bunch chain with a certain space but uniform distribution in transverse direction was studied.

The third step, the behaviour of transverse hollow electron beam with uniform longitudinal distribution will be investigated in CSRm.

The forth step, the perform of a multi-bunch chain with a certain space, and hollow distribution in transverse direction was studied.

The fifth step, the parameters of electron bunch amplitude, interval, width and delay time were varied to optimize and improve the cooling process.

### ACKNOWLEDGMENTS

We would like to thank Xiaolong Zhang for many useful discussions on this subject. We also acknowledge

collaboration on this subject with the power supplies group. Special thanks go to D. Q. Gao, Z. Z. Zhou, and J. B. Shanguan for many fruitful suggestions and very constructive comments on many aspects of this work.

### SUMMARY

The high energy and high intensity accelerator facility was required to provide high density and high charge state ion beam with long lifetime in the storage ring to satisfy the requirements of physics experiments. To maintain the ion beam density for longer time and reduce the ion loss, lifetime is the critical subject. Due to intrabeam scattering, the quality and the lifetime of ion beam will degrade during accelerating and storing. The electron cooling was chosen as a way to suppress the IBS and improve the quality of ion beam. There is a shortage point in the case of conventional DC electron cooling. The solution proposed in this paper was expected to overcome the deficiency of DC electron beam. The longitudinal modulated electron beam was adapted to suppress the IBS effects. The electron beam was constructed into certain strength distribution longitudinally. The stronger cooling was expected in the tail of ion beam, and the weaker cooling was applied in the core of ion beam. As a consequence, the ion loss was reduced and the lifetime of ion beam was lengthened. Meanwhile, the ion beam density was maintained for longer time in the storage ring, and ensued the certain luminosity in the physics experiment terminals. The detailed investigation will carry out in the future.

This exploration was expected to provide some helpful information for the design of electron cooler and operation parameters and mode in the case of high density high charge state ion beam.

### REFERENCES

- [1] J. C. Yang, J. W. Xia, G. Q. Xiao *et al.*, "High Intensity heavy ion Accelerator Facility (HIAF) in China", in *Nucl. Instr. and Meth. in Phys. Res. B* 317, p. 263–265, 2013.
- [2] V. V. Parkhomchuk, V. B. Reva, X. D. Yang, "Using Electron Cooling for Obtaining Ion Beam with High Intensity and Brightness", in *Proc. HB2010*, Morschach, Switzerland, paper MOPD25, pp. 110-114.
- [3] A. Krämer, O. Boine-Frankenheim, E. Mustafin *et al.*, "Measurement and Calculation of  $U^{28+}$  Beam Lifetime in SIS", in *Proc. EPAC 2002*, Paris, France, paper WEPL116, pp. 2547-2549.
- [4] L. J. Mao, J. C. Yang, J. W. Xia *et al.*, "Electron cooling system in the booster synchrotron of the HIAF project", in *Nucl. Instr. and Meth. in Phys. Res. A* 786, p. 91–96, 2015.
- [5] X. Yang, L. Mao, X. Ma *et al.*, "Formation of Bunched Electron Beam at the Electron Cooler of CSRm", in *Proc. COOL2015*, Newport News, VA, USA, paper TUYAUD03, pp. 85-88.
- [6] A. Sidorin, A. Smirnov, A. Fedotov *et al.*, "Electron Cooling Simulation for Arbitrary Distribution of Electrons", in *Proc. COOL 2007*, Bad Kreuznach, Germany, paper THAP01, pp. 159-162.

# EXPERIMENTAL DEMONSTRATION OF ELECTRON COOLING WITH BUNCHED ELECTRON BEAM\*

L. J. Mao<sup>†</sup>, H. Zhao, M. T. Tang, J. Li, X. M. Ma, X. D. Yang, J. C. Yang, H. W. Zhao  
Institute of Modern Physics, Lanzhou, China

A. Hutton, K. Jordan, T. Powers, R. A. Rimmer, M. Spata, H. Wang, S. Wang, H. Zhang, Y. Zhang  
Jefferson Lab, Newport News, Virginia, U.S.A.

## Abstract

Electron cooling at high energy is presently considered for several ion colliders, in order to achieve high luminosities by enabling a significant reduction of emittance of hadron beams. Electron beam at cooling channel in a few to tens MeV can be accelerated by a RF/SRF linac, and thus using bunched electrons to cool bunched ions. To study such cooling process, the DC electron gun of EC35 cooler was modified by pulsing the grid voltage, by which a 0.07-3.5  $\mu$ s of electron bunch length with a repetition frequency of less than 250 kHz was obtained. The first experiment demonstrated cooling coasting and bunched ion beam by a bunched electron beam was carried out at the storage ring CSRm at IMP. A preliminary data analysis has indicated the bunch length shrinkage and the momentum spread reduction of bunched 12C+6 ion beam. A longitudinal grouping effect of coasting ion beam by the electron bunch has also observed. In this paper, we will present the experiment result and its preliminary comparison to the simulation modelling.

## INTRODUCTION

Electron cooling, a well-established method proposed by Budker to improve the phase space densities of stored ion beams, was applied successfully in many proton, antiproton and ion storage rings [1]. The first electron cooling experiment was carried out at NAP-M (Novosibirsk) with protons at the energy of 68 MeV in 1974. After that, several electron cooling devices were built for low-energy proton and ion storage rings in twentieth century. The first relativistic electron cooling of 8.9 GeV/c antiprotons was demonstrated in 2005 at Fermi lab [2]. Later, a 2 MeV magnetized electron cooling device was installed in COSY at Juelich and a cooling of proton beam at the energy of 1.67 GeV/c was achieved [3]. Furthermore, various possibilities such as coherent electron cooling and micro-bunched electron cooling have been proposed for using the electron beam's instabilities to enhance cooling rate. A prototype based on ERL has been developing at BNL to demonstrate longitudinal cooling in coherent electron cooling mode [4]. All electron cooling systems which were in operation so far employed electron beam generated with an electrostatic electron gun in DC operating mode. Such conventional DC

electrostatic accelerator is quite possible to provide electrons of kinetic energies of up to about 5-8 MeV. For even higher energies the most promising approach would appear to be the RF accelerator of electron beam in an energy-recovering linac system and thus using bunched electron beam for cooling [5]. Some efforts were devoted to explore various aspects of such bunched electron beam cooling but experimental studies of such cooling are still lacking.

The first experiment to demonstrate electron cooling by a bunched electron beam was carried out in the storage ring CSRm at IMP. The 35keV conventional magnetized DC electron cooler provides pulsed electron beam by a modification of its high voltage platform. The electron beam is generated by a thermionic cathode. The grid electrode situated near the cathode edge can produce the negative electric field at the cathode thereby suppressing the emission of electrons. The grid electrode was originally designed for providing hollow electron beam to avoid instabilities of over-cooling beams. By varying the potential of this electrode it is possible to obtain electron beam with variable transverse profile. In our case, a pulsed voltage is applied on it to switch on and off the electron beam fast. Modifications are also made on the connection between grid and anode in order to have good characteristics for time pulse shape. Figure 1 provides a pulsed electron beam measurement by the modified 35 keV electron cooler.

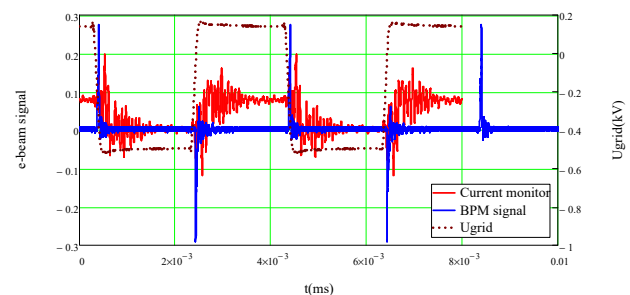


Figure 1: Modulated voltage on the grid electrode of the gun (dash line), pulsed electron beam current (red) and BPM signal generated by pulsed electron beam in the cooler.

In this experiment, a 7.0 MeV/u C<sup>6+</sup> ions provided by the cyclotron SFC were injected and accumulated in CSRm. The electron cooling system and the RF station can be switched on respectively to study the pulsed electron cooling of coasting or bunched ion beam. The main parameters of experiment are listed in Table.1.

\* Work supported by National Natural Science Foundation of China No. 11575264, No. 11375245, No. 11475235 and the Hundred Talents Project of the Chinese Academy of Sciences

<sup>†</sup> email address: maolijun@impcas.ac.cn

Table 1: Main Parameters of Experiment

Parameter	Unit	value
Ions		$^{12}\text{C}^{6+}$
Ion energy	MeV/u	7.0
Revolutions period	Us	4.4
Particle number		$10^8$
Initial bunch length	ns	700 or DC
Electron energy	keV	3.8
e-beam avg. current	mA	<50
e-beam pulse width	ns	70 - 3500
e-beam radius	cm	2.5

## COASTING ION BEAM COOLING

A pulsed electron beam was used to cool the coasting (DC) ion beam stored in CSRm firstly. The ions  $\text{C}^{4+}$  provided by the cyclotron was injected with a stripper, then we switched on the pulsed electron beam 1 or 2 seconds after then injection. Immediately we found the stored particles were lost, as shown in Figure 2.

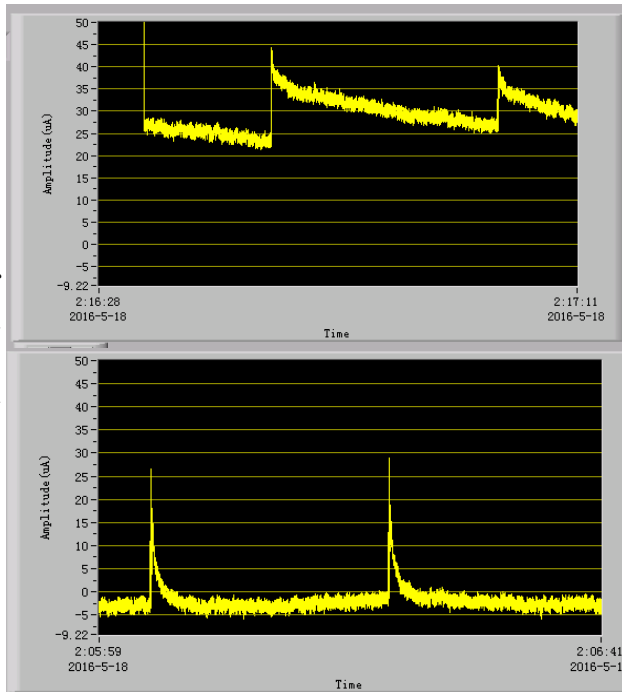


Figure 2: The DCCT signals of stored beam without (above) and with (below) pulsed electron beam.

By a scanning of the frequency of electron pulse, a dependence of beam lifetime on pulsed frequency was observed, as shown in Figure 3. The stored ions were stable only at synchronization point, for example, the frequency of pulsed electron beam is integer or half integer of the ion beam revolution period. It is easy to explain if a space charge field at the edge of pulsed electron beam was considered. Because of a density change, an opposite electric field was produced at rise/fall edge of electron pulse:

$$E_z(z) = -\frac{g}{4\pi\epsilon_0\beta c\gamma^2} \frac{dI_e(z)}{dz} \quad (1)$$

It is similar to a RF bucket around the electron beam. If there was no synchronization, ions can be kicked out by this RF voltage quickly, as shown in Figure 4.

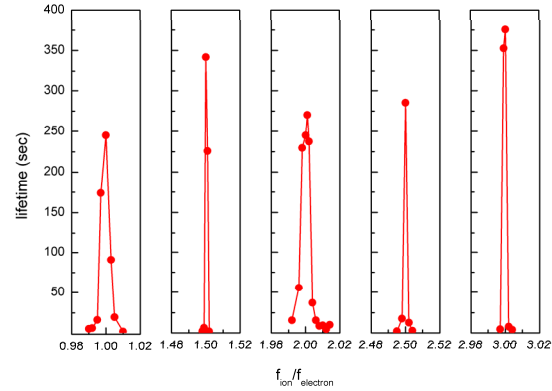


Figure 3: The dependence of lifetime on a synchronization between ion and electron pulses.

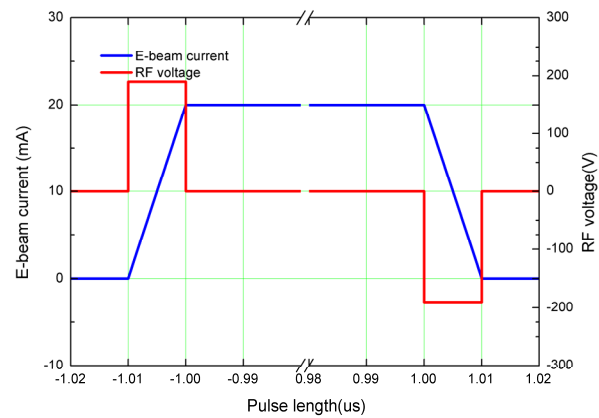


Figure 4: RF bucket with amplitude of 150V can be created by an electron pulse, the peak current is 50mA and the rise/fall time is 10ns.

During the cooling process with a synchronized electron pulse, an ion beam BPM signal was observed clearly and the amplitude increased step by step, as shown in Figure 5. It means ions were not only cooled into a small momentum spread, but also captured in a small longitudinal space, and cannot escape from the bucket, while the momentum is smaller than bucket amplitude. The width of ion beam pulse is the same as electron pulse, an integration of BPM signal also shown us the ion bunch length is equal to the electron pulse, which was called “grouping” effect, as shown in Figure 6. In addition, the linear density decreases from the beginning to the end of ion pulse. By considering of electron momentum spread caused by the longitudinal potential in different transverse position, a simulation result shown a same behaviour, but the details is still not very clear.

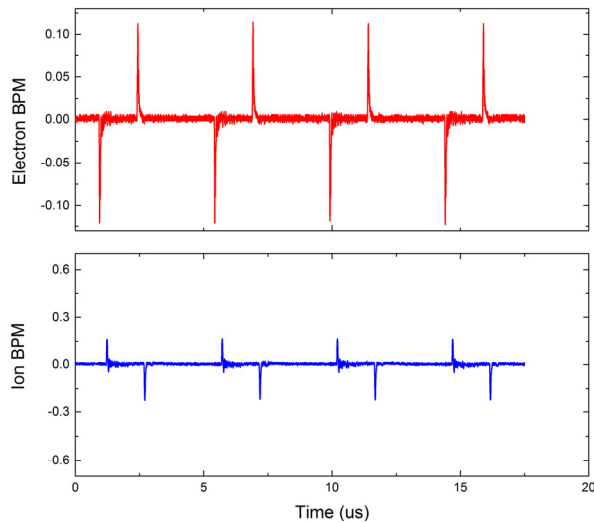


Figure 5: The BPM signal was observed clearly, even without RF system. The width is the same as electron pulse.

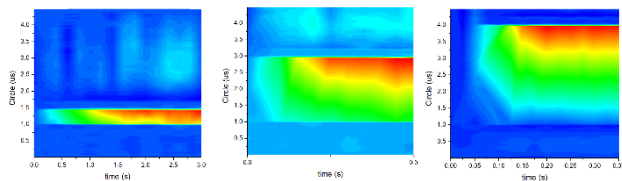


Figure 6: The BPM signal was observed clearly, even without RF system. The width is the same as electron pulse.

## BUNCHED ION BEAM COOLING

Cooling of bunched ion beam by pulsed electron beam was done due to study the cooling time depends on the parameters of electron beam, such as frequency, peak current, and pulse width. A sinusoidal RF voltage is applied. The RF voltage fixed to 1.0kV at 2 times of revolution frequency (454 kHz) is used to capture ions to the buckets, therefore there are two ion bunches in the ring. But because of limitation of pulse generator, electron pulse with repetition frequency less than 250 kHz can be obtained, which means only one ion bunch can be cooled in the ring, as shown in Figure 7.

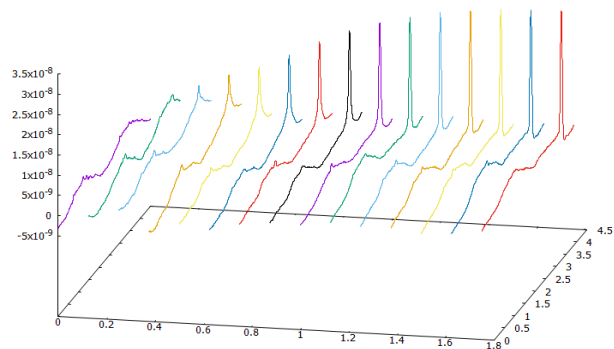


Figure 7: The ion bunch was cooled by pulsed electron beam. There are two ion bunches in the ring but only one was cooled by pulsed electron beam.

By changing of electron pulse parameters, such as width, peak current, a cooling process was studied. A preliminary data analysis shown some different, especially the cooling time of particles in tail depends on the width of electron pulse, as shown in Figure 8. More details should be studied according to further data analysis.

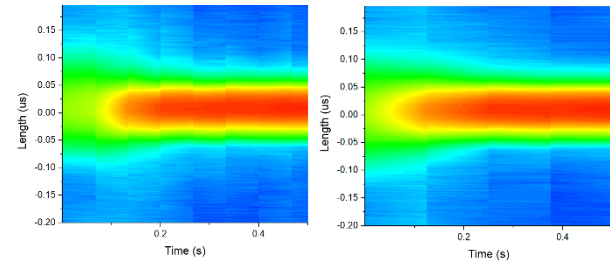


Figure 8: Preliminary data shows a difference of cooling process by different electron pulse width (2.5  $\mu$ s left and 1.0  $\mu$ s right).

## CONCLUSION

Cooling process of coasting and bunched ion beam by pulsed electron beam was studied at CSR storage ring. Cooling of coasting ion beam shows a grouping effect, which means particles are not only cooled to equilibrium, but also captured by electron pulse, finally a width equal to electron pulse was obtained. Cooling of bunched ion beam was done to study the cooling time dependence, a preliminary data analysis only shown some difference with vary parameters, details should be studied further.

## REFERENCES

- [1] H. Poth, "Electron Cooling: Theory, Experiment, Application", *Physics Reports*, 196.3-4 (1990): 135-297.
- [2] S. Nagaitsev *et al.*, "Experimental Demonstration of Relativistic Electron Cooling", *Physical Review Letters*, 96.4 (2006): 044801.
- [3] V. Kamerzhiev, J. Dietrich and V. V. Parkhomchuk, "Cosy 2 MeV Cooler: Design, Diagnostic and Commissioning", in *Proc. IPAC'14*, pp 777-779.
- [4] V. N. Litvinenko *et al.*, "Proof-of-Principle Experiment for FEL-Based Coherent Electron Cooling", Laboratory No. BNL-96405-2011-CP, Brookhaven National (BNL), Relativistic Heavy Ion Collider, 2011.
- [5] A. V. Fedotov, "Bunched Beam Electron Cooling for Low Energy RHIC Operation", *ICFA Beam Dyn. Newsletter*, 65, (2014): 22-27.

Content from this work may be used under the terms of the CC BY 3.0 licence (© 2017). Any distribution of this work must maintain attribution to the author(s), title of the work, publisher, and DOI.

# LATEST NEWS FROM STOCHASTIC COOLING DEVELOPMENTS FOR THE COLLECTOR RING AT FAIR

R. Hettrich, A. Bardonnier, R. Böhm, C. Dimopoulou, C. Peschke, A. Stuhl, S. Wunderlich  
 GSI Helmholtzzentrum für Schwerionenforschung, Darmstadt, Germany

F. Caspers, CERN, Geneva, Switzerland and European Scientific Institute (ESI), Archamps, France

## Abstract

The CR stochastic cooling system aims at fast 3D cooling of antiprotons, rare isotopes and stable ions. Because of the large apertures and the high electronic gain, damping within the 1-2 GHz band of the unwanted microwave modes propagating through the vacuum chambers is essential. It will be realised within the ultrahigh vacuum using resistively coated ceramic tubes and ferrites. The greatest challenge is increasing the signal to noise ratio for antiproton cooling by means of cryogenic movable (plunging) pickup electrodes, which follow the shrinking beam during cooling and then withdraw fast before the new injection. Linear motor drive units plunge synchronously the pickup electrodes on both sides of the ion beam (horizontal/vertical). Their technical concept is summarized. Their performance has been demonstrated in successive measurements inside testing chambers at GSI. Recent simulations of the critical antiproton cooling with the designed system are shown.

## CONCEPT OF PICKUP DRIVES

The concept of linear motor drives for plunging the pickups has been verified. Latest measurements and adjustments have shown that a safe drive concept, with inherent freeing of the aperture in case of an emergency power shutdown, can be built with a single mechanical construction for the all drive orientations.

The springs are the only parts which have to be adjusted for horizontal, vertical top or vertical bottom orientation. Due to the weight of the sliding mass in combination with the vacuum force, springs with three different strengths are needed. In a special test chamber the given forces have been measured and adjusted in order to optimize the dynamic performance. The basic idea is that the drives for the plunging electrodes are outside the vacuum chamber and the movement is decoupled with fatigue enduring bellows. This imposes the full static vacuum force of about 440 N on the drives. To avoid dropping the electrodes onto the beam axis in case of power failure, these vacuum forces are over-compensated with pre-compressed springs. This concept induces an outgoing force on the drives, which increases proportionally to the distance from the outer edge position. The slope of this increase should be as low as possible. The limit is given by the part of the drive length, which can be used for spring pre-compression. In order to get zero total static force at the outer edge position the springs were chosen with maximum length left for pre-compression and spring constants as low as possible. Further, the static forces of the drives including the electrodes and a dummy weight

to account planed enhancements have been measured. Then, adequate spacers for precise adjustment of the springs pre-compression have been inserted into the spring enclosure. Thus, for all three orientations a minimum static force configuration has been achieved. The plots for the orientations with the highest and lowest slope of the force versus the ‘distance-from-beam-axis’ are shown in Fig. 1.

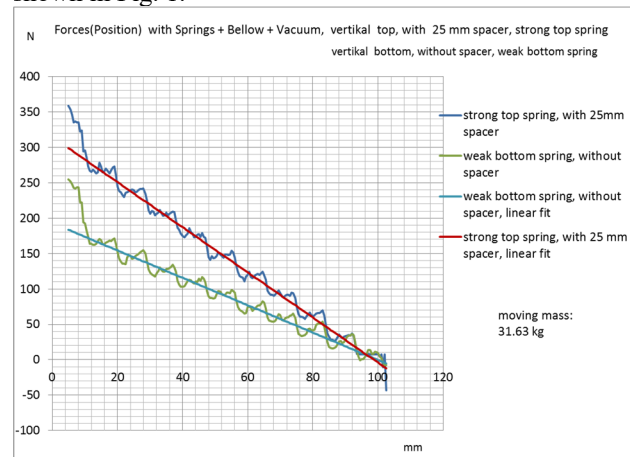


Figure 1: Static forces push out with a ripple from the permanent magnetic field of the motor (current off).

## PLUNGING TRAJECTORIES

For the most critical case with the highest slope, the static force could be kept about 100 N below the maximum static force of the motor. This is enough to achieve a 70 mm full scale movement within 120 milliseconds without additional mechanical shock from the inner to the outer edge of the tank in vertical top orientation. This is shown in Fig. 2.

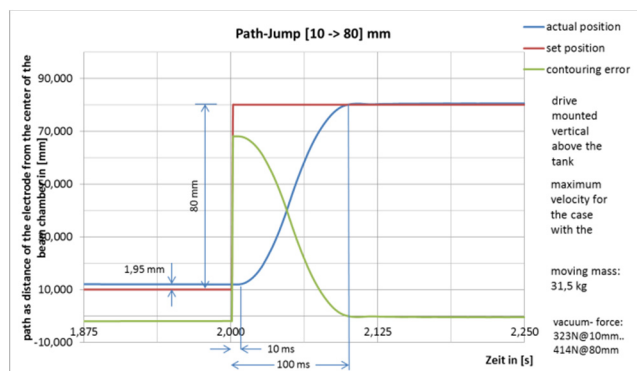


Figure 2: Minimum settling time response (blue) to a full drive distance path jump (red).

To avoid mechanical damage to the extremely sensitive electrodes in a long-term operation, the plunging should work on a jerk-free trajectory. Despite several optimized solutions, we used the profile with the following functions for all practical test sequences. This profile is very common in many other industrial applications and provides a representative mechanical stress situation.

$$s(t) = S_0 + S \left[ \frac{t}{T} - \frac{1}{2\pi} \sin\left(\frac{2\pi}{T} t\right) \right],$$

$$S_0 = 10 \text{ mm}, S = 70 \text{ mm}, T = \{0.2 - 1\} \text{ s}$$

$$v(t) = \frac{S}{T} \left[ 1 - \cos\left(\frac{2\pi}{T} t\right) \right] = 2 \frac{S}{T} \sin^2\left(\frac{\pi}{T} t\right),$$

$$a(t) = 2 \pi \frac{S}{T^2} \sin\left(\frac{2\pi}{T} t\right)$$

This results in a maximum velocity of  $2 \frac{0.07 \text{ m}}{0.2 \text{ s}} = 0.7 \frac{\text{m}}{\text{s}}$  and in a maximum acceleration of  $6.28 \frac{0.07 \text{ m}}{0.04 \text{ s}^2} = 11 \frac{\text{m}}{\text{s}} = 1.12 \text{ g}$ . A typical movement cycle with the given profile is shown in Fig. 3.

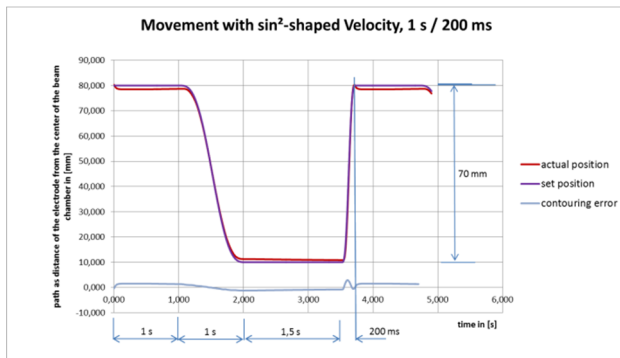


Figure 3: Movement cycle with  $T = [1\text{s} \text{ (in)}, \text{break of } 1.5\text{s}, 0.2\text{s} \text{ (out)}, \text{break of } 1\text{s}]$ .

## HARDWARE CONFIGURATION FOR SYNCHRONOUS DRIVING

To achieve synchronous movement of eight drives inside the tank the following control scheme was applied. Each drive is controlled by a separate industrial drive controller. A common computer with a real-time operating system sends set values to each drive controller, receives the actual values of a programmed control loop in equidistant 1 ms time-steps. The transport of all position values is made by a bus system, called ‘EtherCAT’. This system uses the common physical layer of the Ethernet standard, combined with a protocol derived from the Internet Protocol.

In order to achieve sufficient accuracy in positioning the drives, a drive control system with position measurement and feedback of the actual position was used. The drive control scheme is shown in Figure 4.

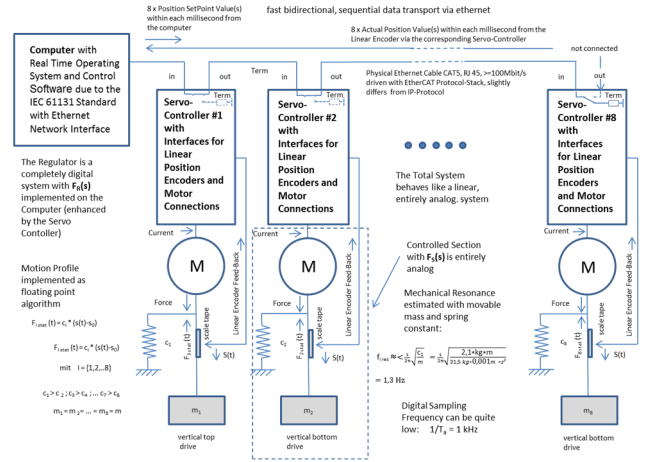


Figure 4: Linear drive control scheme for the CR stochastic cooling pickup tanks.

Unfortunately, the moving mass with the springs for vacuum force compensation is a resonant system with a very low resonance frequency and almost no damping.

$$f_{res} = \frac{1}{2\pi} \sqrt{\frac{c}{m}} = \frac{1}{2\pi} \sqrt{\frac{2.1 \text{ kg m}}{31.5 \text{ kg } 0.001 \text{ m}^2 \text{ s}^2}} = 1.3 \text{ Hz}$$

Such a system cannot be moved as fast and precise as specified above without some kind of damping. The solution was to implement an electronic damping system by a special control loop design. This design overrides the build-in hardware regulator of the industrial drive controller by replacing it by a precompiled PID regulator which is contained in the real-time operating system. Thus, the full parameter set of the regulator can be used to adjust the moving system with sufficient damping. The scheme of the corresponding control loop is shown in Figure 5.

## A CONTROL LOOP FOR PRECISION, SPEED AND DAMPING

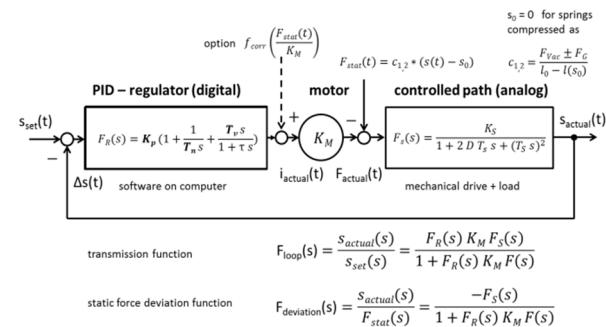


Figure 5: Stable adjustable control loop model with PID regulator and 2-pole path.

The optimal damping is achieved by putting a path jump  $s(t) = 20 \text{ mm} \cdot 1(t)$  (for instance) to the control loop. Then, the loop reacts with a damped movement like the one shown in Figure 6.

Content from this work may be used under the terms of the CC BY 3.0 licence (© 2017). Any distribution of this work must maintain attribution to the author(s), title of the work, publisher, and DOI.

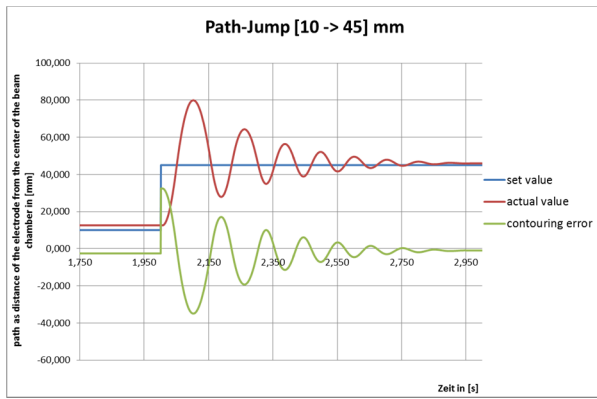


Figure 6: Damped oscillation at the beginning of the control loop adjustment.

After some trials by varying the parameters  $K_p$ ,  $T_n$  and  $T_v$  ( $T$  is set about 10% of  $T_v$ ), the expected ringing can be decreased and the movement can be made faster by increasing  $K_p$  short below an oscillation. Probably several iterations are necessary until the drives follow the position jump in a rectangular shape. The adjustment procedure behaves similar to the adjustment of a probe of an oscilloscope.

A new adjustment is necessary after each mechanical change concerning the moving mass until the mechanical construction is final. With the right adjustment and the estimated final moving mass of 31.5 kg, the movements shown in the pictures 2 and 3 are possible.

The violet curve on Figure 3 shows the set values in our movement cycle, the red curve shows the corresponding actual values. The comparison reveals a lag of the actual value behind the set value. In the given example, the actual value does not reach the inner or outer target position during the break sequences of 1.0 and 1.5 s, but has a slight slope towards the target position. This slope corresponds to the integration time constant of the regulator (about 3 s in the given adjustment). So, at least 3 s break is needed to reach the target position. The residual position difference of less than 2 mm cannot be zeroed by decreasing the integration time constant, because the needed damping depends on the value of the actual adjustment. The maximum error for the middle-point of two opposite synchronous drives with respect to the beam axis can be estimated by dividing this residual error by two. This results in a deviation of 1 mm for several seconds after reaching the target position. This is fully acceptable for the long cooling times and the broad distributions of the particle beams in the CR.

As an outlook, a correction is achievable: The residual position difference is caused by the static spring forces. These are proportional to the position itself. Therefore, it is possible to develop a correction function, which can be easily subtracted in the numerical path of the loop, if the known force is divided by the motor current-to-force constant  $K_M=78 \text{ N/A}$ . The precise correction function is a weighted response of the loop to the moving profile and the static spring force. A calculation would require a complete model of the not yet designed mechanics in

combination with an inverse Laplace transformation of the static force deviation function. The Laplace transform of the loop transfer function and the static force deviation function are shown in Figure 5.

## DAMPING OF UNWANTED MICROWAVE MODES

Large-aperture vacuum chambers admit many propagating waveguide modes. The operation with high gain (>130 dB) and a short distance between Palmer pickup and kicker favour self-excitation of the loop. To avoid self-excitation, sufficient microwave damping in the operating frequency band (1-2 GHz and above) is necessary inside the beam chambers. Materials like ferrites and resistively coated ceramics are used for this purpose [1]. They must be acceptable inside ultrahigh vacuum (UHV).

Table 1 summarizes the damping requirements, Figure 7 shows a possible layout of ceramic tubes in the magnet chambers and the space occupied by the beam.

Table 1: Electrical Gain and Required Damping

values for hexagonal quadrupole and sextupole chambers	slotline pickups to kicker	Palmer pickup to kicker
max. gain	150 dB	133 dB
min. damping	135 dB	130 dB
$\Sigma$ length of all chambers	19.6 m	12.7 m
min. damping per length	6.9 dB/m	10.2 dB/m

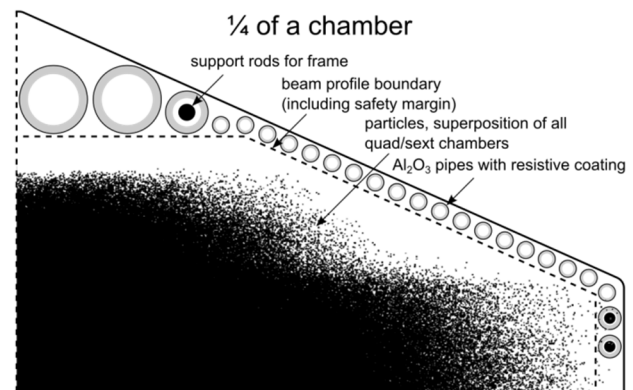


Figure 7: Topography of beam and tubes inside the hexagonal quadrupole/sextupole chamber.

The damping of microwave modes inside the magnet chambers has been simulated (HFSS) with 4 x 24 resistively coated  $\text{Al}_2\text{O}_3$  tubes (4 diameters from 6 to 24 mm). The result is shown in Fig. 8. The non-dotted lines present the dangerous TM-modes, whose electrical field has the same direction as kicker/pickup field whereas the dashed lines represent the less dangerous TE-modes. A sheet

resistance of  $R_{sq} = 150 \Omega/\text{square} \pm 30\%$  has been chosen for sufficient damping of all modes.

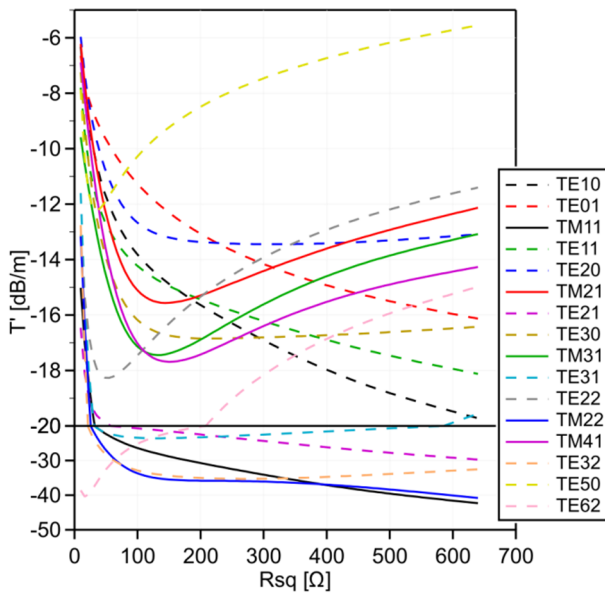


Figure 8: Dependence of damping on sheet resistance.

Ferrites are suitable damping materials inside the pickup and kicker tanks. First, the microwave damping of various ferrite samples was checked by putting them on a microstrip line and measuring the insertion loss. The attenuation corrected by the properties of the microstrip line without ferrite was sufficient in the 1-3 GHz band for all ferrites.

Second, the static specific resistance  $\rho$  was measured by contacting planes with a precise  $\Omega$ -meter. The expected discharging time is given by multiplication with the dielectric constant  $\epsilon_r \cdot \epsilon_0$  ( $\epsilon_r=12.9$ ). Acceptable values below 1 ms lie below the red line in Fig. 9.

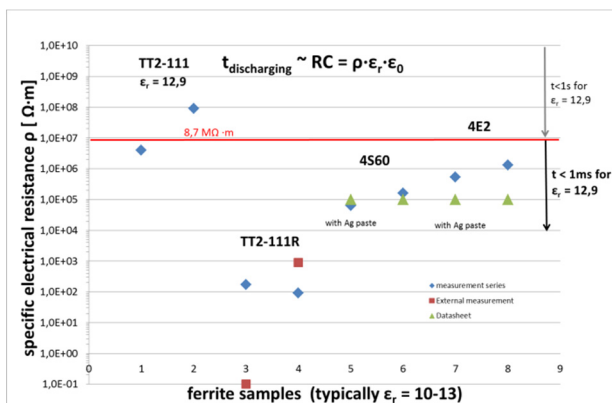


Figure 9: Specific electrical resistance of tested ferrites. The min. and max. values for TT2-111R at room temperature (red squares) are from [2].

The ferrites TT2-111R (Transtech) and 4S60 (Ferroxcube) have been approved for the desired damping of more than 130 dB inside the pickup and kicker tanks. Their outgassing rate was measured and found UHV-acceptable: 2-3 times that of stainless steel ( $<1.6 \cdot 10^{10}$  mbar l/s  $\cdot$  cm<sup>2</sup> after 1 week of pumping without bake out).

## SIMULATIONS OF THE STOCHASTIC COOLING PROCESS IN THE CR

Simulations of antiproton cooling performance for the most critical case ( $10^8$  protons at 3 GeV, cooling for 10 s all 3 phase-space planes) are shown in Fig. 10. The cooling performance is close to the design limits of the HESR downstream the CR. This is already achieved without plunging the electrodes in these simulations, so there is some margin. The power requirements however are not relaxed since they depend on the initially hot beams.

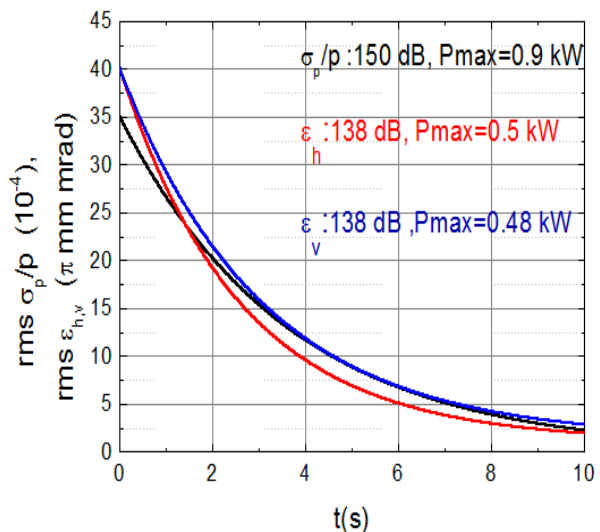


Figure 10: Evolution of rms parameters of the antiproton beam for simultaneous cooling in all 3 planes.  $P_{max}$  is the initial cw power at the kicker within the 1-2 GHz band. Four times this value (i.e. to account for statistical beam signal fluctuations) is just within the installed microwave power of 8 kW (power amplifiers at kickers).

## REFERENCES

- [1] F. Caspers, "Experience with UHV-compatible microwave absorbing materials at CERN", CERN, Geneva, Switzerland, Rep. CERN/PS 1993-10, Feb. 1993.
- [2] E. Chojnacki *et al.*, "DC Conductivity of RF Absorbing Materials", in *Proc. SRF'09*, Berlin, Germany, September 2009, paper THPPO035, pp. 643 - 647.

# DESIGN OF STOCHASTIC PICK-UPS AND KICKERS FOR LOW BETA PARTICLE BEAMS

B. Breitschneid†, R. Stassen, H. Stockhorst  
 Forschungszentrum Jülich, 52425 Jülich, Germany

## Abstract

The COSY facility hosts experiments for the JEDI (Jülich Electric Dipole moment Investigations) collaboration. Polarized deuteron beams with a momentum of 970 MeV/c are stored in the ring. To achieve polarization times in the order of several minutes, small emittances and momentum spread are crucial. Therefore, the beam is pre-cooled with the 100-kV electron cooler. To further improve the spin coherence time, cooling during the experiments would be desirable. That way, the beam blow-up due to intra beam scattering could be compensated. But since the focusing solenoids in the e-cooler may not be perfectly compensated, it cannot be used to cool during the experiments. The existing stochastic cooling (SC) system is not sensitive at low beam velocities. Thus, it is proposed to build a dedicated SC system for low beta beams. This work presents the proposed system. It emphasizes the design process of pick-up and kicker hardware. Starting from the slot-ring structures that have been developed for HESR, an optimization towards a high sensitivity at a beta of 0.46 is undertaken.

## INTRODUCTION

The discovery of an electric dipole moment (EDM) of hadrons would constitute a breakthrough in the search for CP violations. Since the proposed values of less than  $10^{-24}$  e·cm are hard to resolve, great effort is done to design high precision experiments.

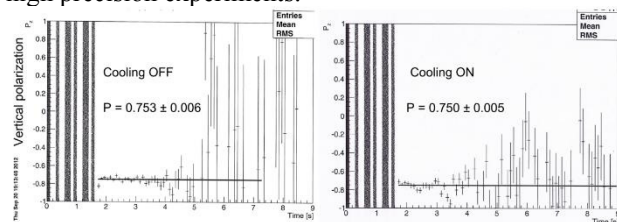


Figure 1: Vertical polarization measurement results after 30 minutes beam storage time, once without and once with vertical stochastic cooling.

The JEDI collaboration faces this task by investigating polarized beams in storage rings [1]. The precursor experiments currently done at COSY use vertically polarized deuterons at momenta of 970 MeV/c [2]. The goal is to increase the polarization lifetime up to the order of 1000 seconds. The beam is pre-cooled with the 100-kV electron cooler to reduce the beam emittances and momentum spread, and consequently increase the spin coherence time [3]. Unfortunately, the focusing in the e-cooler is done by a solenoid, which applies an unwanted longitudinal po-

larizing force to the beam. Thus, the solenoid is compensated by two additional solenoids before and after the beam intersection range. But this compensation is not perfect, and may not fulfil the desired accuracies.

To avoid such depolarization problems, the use of stochastic cooling (SC) instead of electron cooling is investigated. SC systems do not need focusing magnets at all. Thus, the cooling may be applied even during the experiment, counteracting the beam blow-up caused by intra-beam-scattering (IBS).

The influence of the SC system itself on the beam polarization was investigated in [4], concluding that no depolarizing influence is to be expected. To verify this result, vertical cooling was applied to a vertically polarized proton beam (1,965 MeV/c,  $N = 3 \times 10^8$ ). Vertical cooling causes horizontal magnetic RF-fields, thus a horizontal polarization may build up. But after 30 minutes of cooled flat-top, no vertical polarization loss was investigated in comparison to an uncooled setup, as shown in figure 1. It is expected that this will be also true for low energy deuterons in EDM experiments.

## PAST AND PRESENT STATE OF COSY COOLING SYSTEMS

The COLer SYnchrotron (COSY) of the Forschungszentrum Jülich started its operation in 1993 [5]. Protons and deuterons are accelerated in the 184-m long ring and stored at momenta from 0.3 to 3.7 GeV/c. Remarkable features are polarized sources for both deuterons and protons, and the eponymous beam cooling systems.

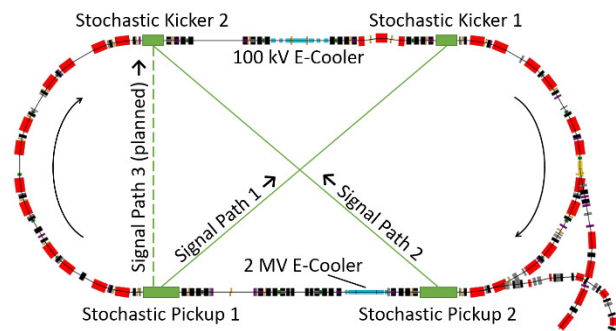


Figure 2: Cooling systems at COSY: Two electron coolers, the high energy SC system at signal path 1, the deprecated vertical and longitudinal system at path 2, and the planned low energy system at path 3.

In figure 2, an overview of the installed cooling systems is given. The initial configuration of COSY consisted of a 100-kV e-cooler for low energies, and a 3D SC system for the upper energy range.

† b.breitschneid@fz-juelich.de

Content from this work may be used under the terms of the CC BY 3.0 licence © 2017. Any distribution of this work must maintain attribution to the author(s), title of the work, publisher, and DOI.

The e-cooler has a typical beam current of 250 mA, and can cool momenta up to 0.6 GeV/c per nucleon [6]. The original SC system is meanwhile disassembled to make space for new installations. It was designed for fast particles starting from 1.5 GeV/c [7]. It consisted of two separate sub-systems, one for the vertical plane at position “1”, and one for the horizontal at “2”. Furthermore, filter cooling was implemented as well at position 1 for the longitudinal plane. The roughly four-meter-long pick-up (PU) tanks and two-meter-long kicker (KI) tanks contained quarter-wave couplers as electrodes. They could be moved to increase the aperture for low energies, and the coupling impedance during cooling at high energies. The PUs were cooled below 30 K to increase the signal-to-noise ratio. The system was split to two frequency bands, i.e. 1 to 1.8 GHz and 1.8 to 3 GHz.

In 2013, the cooling capabilities of COSY were extended by a second e-cooler [8]. It covers to a wide voltage range from 0.025 to 2 MV, which corresponds to the complete energy range of COSY.



Figure 3: PU / KI of the high energy SC system for HESR. Right: One stack of 16 slot rings. Center: eight combiner boards are attached to the electrode lines. Right: Two stacks, boards are combined pairwise.

The original SC system was disassembled to make space for the new high energy system [9]. It was developed for the High Energy Storage Ring (HESR) at the Facility for Antiproton and Ion Research (FAIR) [10], and was successfully tested at COSY [11].

The PU and KI hardware was newly developed. Instead of quarter-wave couplers, it consists of slots that resemble iris-loaded linac cells [12]. This static aperture approach is possible due to the small HESR aperture of only 89 mm. The simulated longitudinal shunt impedance per length is more than twice as high as of a comparable quarter-wave structure.

Each cell is equipped with eight electrodes which couple to the magnetic field of the beam. Every electrode loads the slot with 50 ohms, resulting in a large bandwidth of one octave, i.e. from 2 to 4 GHz. The single cells are manufactured separately and stacked afterwards in groups of 16 (figure 3, right). Then, 16-to-1 combiner boards are attached directly onto the stack, combining the electrodes of

each row with static delay lines corresponding to a beam velocity of  $\beta = 0.93$ . Finally, adjacent rows are combined in pairs, which can be connected from the outside via four outlets.

Each tank consists four such stacks, combined to one large shaft (figure 3, left). A network of hybrids and delay lines outside of the tank allows to adjust the delay between the stacks to fit an antiproton momentum range of 3.8 to 15 GeV/c. The hybrids combine the opposing pairs, so that the horizontal and vertical plane can be operated in push-pull configuration separately, or all electrodes in sum mode. This allows for a simultaneous cooling of all three planes in one single structure, reducing the needed length additionally by a factor of two.

Since the system is designed for HESR, it is not suited for slow particles at all. The combiner boards are not very broadband since they have static delay lines. For  $\beta = 0.46$ , the combination loss is more than -13dB. Furthermore, the shunt impedance of the single slot rings drops below 1  $\Omega$  in the frequency band of 2-4 GHz. Thus, an additional dedicated system for slow particles is inevitable.

All HESR tanks are tested at COSY before they get shipped. One pair of PU and KI at a time is installed at signal line 1. Thus, line 2 is now free for new installations. Nevertheless, it was decided to install a new signal path for a low energy SC system, labelled “3” in the floor plan. That is because the sensitivity of the slot-rings strongly depends on the aperture. PU position 2 is too close to the injection point, and the full COSY aperture of 150 mm is needed during injection. At position 1, the high energy system already reduces the aperture. Since the new PU is much shorter than the old one, sufficient space is left for a second PU at the same position. The phase advance between the two kickers is almost exactly  $2\pi$ , thus the transverse cooling condition is met between PU 1 and KI 2 as well. Furthermore, the deuterons are comparatively slow, so they still do not outrun the signal despite the shorter orbit length.

## DESIGN OF NEW PICK-UP AND KICKER HARDWARE

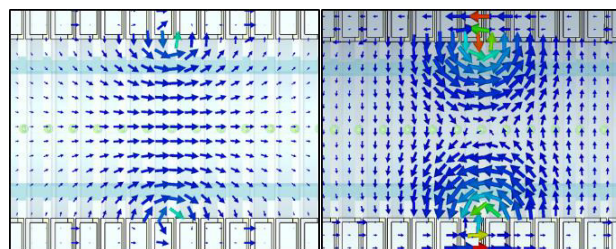


Figure 4: Transverse cut through a slot-ring kicker, with electric field of one excited cell. Left: All electrodes in phase (longitudinal). Right: Top and Bottom electrode in push-pull (vertical).

Starting from the design of the high energy slot ring kicker, the geometry was optimized for slow particles. For cooling band, the frequency range from 350 to 700 MHz was chosen. This is a comparatively small bandwidth, but simulations showed a Schottky band overlap starting from

Content from this work may be used under the terms of the CC BY 3.0 licence (© 2017). Any distribution of this work must maintain attribution to the author(s), title of the work, publisher, and DOI.

800 MHz. Furthermore, higher frequencies lead to low transit time factors for such slow particles.

The electromagnetic fields have been simulated with CST Microwave Studio 2016/2017 [13]. The structure was optimized for longitudinal shunt impedance. Therefore, structures with many cells, typically 31, have been modelled. The ends of the structure are connected to beam pipes, and terminated with waveguide ports. Only the center cell, in this example cell number 17, is excited. All electrodes of the cell are fed with signals of the same phase. The pulses are mostly reflected at the shorted ends of the electrodes, but some field reaches the beam axis, accelerating, or decelerating the beam (figure 4, left).

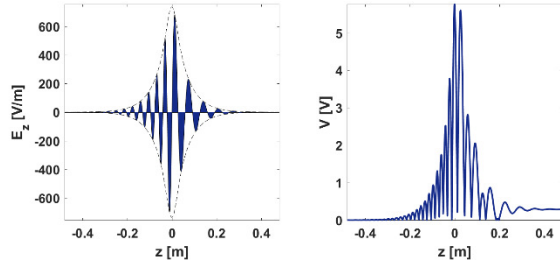


Figure 5: Left: Electric field observed by a slow particle passing through the HESR kicker, excited with 4 watts at 3 GHz. Right: cumulated voltage.

Although the frequency is far below cut-off of the aperture, a strongly damped  $TM_{01}$ -mode propagates along the structure, absorbed by the electrodes in the neighboring cells. The simulated structure length was chosen such that virtually no field reaches the beam pipe, to neglect end-effects. It is assumed that those end-effects are comparatively small, thus the quantities simulated for this center cell can be multiplied by the number of cells of the final structure to calculate the performance of the whole tank.

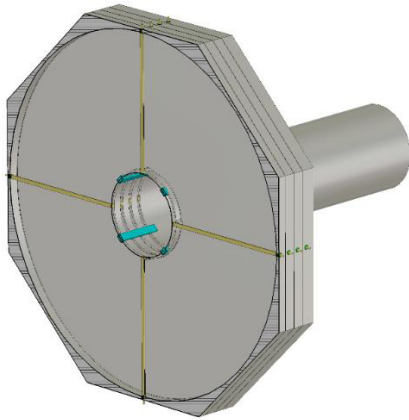


Figure 6: Low energy SC kicker as resulting from the optimization process.

The complex electric field along the beam axis was used to calculate the longitudinal shunt impedance according to [14]. The particles passing the structure observe an effective accelerating voltage,

$$V = \int e^{j\omega \frac{z}{\beta c_0}} E_z(z) dz. \quad (1)$$

This voltage is maximized for indefinitely fast particles. But since the electric field is oscillating during transit, its value drops strongly with transit time. To illustrate this, figure 5 shows the electric field that a particle with  $\beta = 0.46$  experiences in the HESR KI at 3 GHz. The field changes its direction multiple times while the particle passes, and accelerating and decelerating periods almost cancel out. The cumulated voltage oscillates, resulting in a very small net acceleration. This shows that the HESR system is not suited for slow particles.

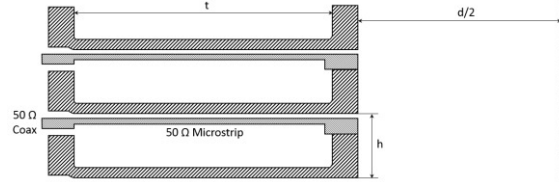


Figure 7: Cut through the cells of a slot ring coupler.

A cut through the slot of a cell is shown in figure 7. Thinking in terms of pick-ups, the image current of the beam must flow perpendicular to the slots, resulting in a voltage drop over the gap of the slot. This voltage is measured by the electrode, which forms a 50 ohms microstrip line with the upper neighboring cell and leads the signal to a coaxial transmission. Higher frequencies lead to bigger induced voltages over the slit, until the stray capacitances counteract this behavior.

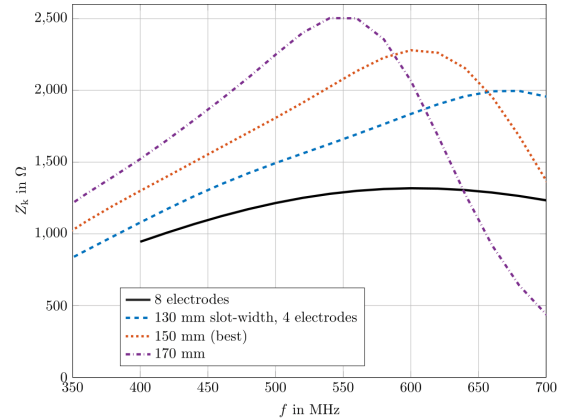


Figure 8: Longitudinal shunt impedance of a slot ring kicker for some variations of the tuning parameters. The longitudinal shunt impedance  $Z_k$  is given for a 64-cell long structure.

The longitudinal shunt impedance is a measure for the beam voltage that is achieved by a given input power. It is defined by

$$Z_k = \frac{1}{2} \frac{|V|^2}{P_{in}}. \quad (2)$$

The kicker geometry was optimized for  $Z_k$  by variation of different parameters. The result is displayed in figure 6. The aperture was set to 90 mm, to not further reduce the value given by the high energy PU. The most sensitive parameter is the slot width  $t$ . It defines the additional length for the image current and thus can be used to tune the resonant frequency to the desired band, as can be seen in the diagrams in figure 8.

The cell height  $h$  is sensitive as well. Slimmer cells have a smaller impedance, but a higher impedance per length. Very slim cells are not advisable, because the combiner boards get more complex. As a trade-off, we stuck to 12.5 mm as for the high energy kicker.

The number of electrodes per ring was reduced to 4. The diagrams show that the bandwidth is still sufficient, and besides, the peak sensitivity is higher. Furthermore, the number of combiner boards is reduced by a factor of two. This gives space for the larger Wilkinson combiners and longer delay lines that are needed for the low frequencies.

The structure is comparatively huge with a diameter of approx. 40 cm. The stiffness was adjusted by increasing the thickness of the base plates to 2 mm, and adding plastic supports between the rings and around the electrode outlets. Simulations showed a negligible influence on the electromagnetic properties.

After optimization of the longitudinal shunt impedance, the transverse impedance was checked. The cell was excited in push-pull mode. The transverse impedance can be derived from the gradient of the beam voltage by utilizing the Panofsky-Wenzel-theorem [14]:

$$Z_{k,x} = \frac{1}{2\bar{P}_{in}k^2} \left( \frac{\partial \tilde{V}}{\partial x} \right)^2 \quad \text{with } k = \frac{\omega}{c_0} \quad (3)$$

Values of 1.6 k $\Omega$  or more were found for the whole band. This is sufficient for transverse cooling, thus no further optimization was done.

## SYSTEM SIMULATION

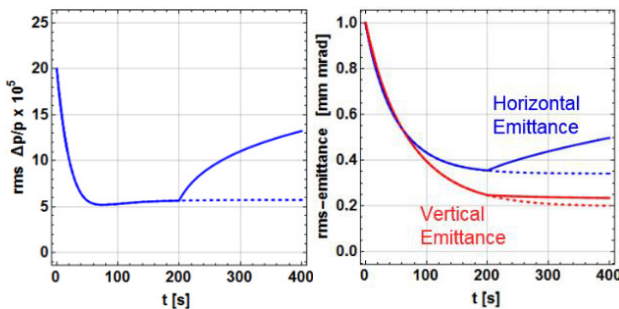


Figure 9: Momentum spread, horizontal and vertical emittance during 3D-cooling for 200 s, and beam blow-up when cooling is turned off.

The field simulation results have been used to simulate the cooling performance of the proposed system. A beam of  $10^9$  deuterons at 970 MeV/c was cooled in all three planes simultaneously, with filter cooling for the longitudinal plane. As can be seen in figure 9, an equilibrium state of  $6 \times 10^{-5}$  is reached for the momentum, and 0.35 or 0.2 mm mrad for the horizontal and vertical emittance. The longitudinal time constant is roughly 30 s and the transverse 80 s. When cooling is turned off, the strong influence of intra beam scattering is observed. This shows that permanent cooling during the experiment is desirable.

Another remarkable result of the simulation is the amount of RF cooling power, which turned out to be comparatively low. Of-the-shelf 5-watt power amplifier are

sufficient for operation, thus an essential cost factor is omitted.

## OUTLOOK

A set of test rings is under construction. The aim is to find out if the stiffness is sufficient, or whether the large plates will warp during the milling process. In parallel, new combiner boards will be developed that are suited for the new frequency band.

## REFERENCES

- [1] JEDI Collaboration, <http://collaborations.fz-juelich.de/ikp/jedi/>.
- [2] D. Eversmann *et al.*, “New Method for a Continuous Determination of the Spin Tune in Storage Rings and Implications for Precision Experiments”, *Phys. Rev. Lett.*, vol. 115, no. 9, p. 94801, Aug. 2015.
- [3] G. Guidoboni *et al.*, “How to Reach a Thousand-Second in-Plane Polarization Lifetime with 0.97 – GeV/c Deuterons in a Storage Ring”, *Phys. Rev. Lett.*, vol. 117, no. 5, p. 54801, Jul. 2016.
- [4] H. Stockhorst *et al.*, “Stochastic Cooling of a polarized Proton Beam at COSY”, in *Proc., International Workshop on Beam Cooling and Related Topics (COOL’13)*, Mürren, Switzerland, Jun. 2013, paper TUAM1HA02, pp. 44-48.
- [5] R. Maier, “Cooler synchrotron COSY — Performance and perspectives”, *Nucl. Instruments Methods Phys. Res. Sect. A Accel. Spectrometers, Detect. Assoc. Equip.*, vol. 390, no. 1–2, pp. 1–8, May 1997.
- [6] H. Soltner, H. J. Stein, V. Kamerzhiev, J. G. de Villiers, J. L. Conrady, and J. Dietrich, “Three-Dimensional Numerical Field Analysis for the Magnets of the 100-keV Electron Cooler at COSY-Jülich”, *IEEE Trans. Appl. Supercond.*, vol. 24, no. 3, pp. 1–4, Jun. 2014.
- [7] R. Stassen, U. Bechstedt, and J. Dietrich, “The Stochastic Cooling System and its Application to Internal Experiments at the Cooler Synchrotron COSY”, *EPAC98*, 1998.
- [8] V. Kamerzhiev, J. Dietrich, and V. Parkhomchuk, “COSY 2 MeV Cooler: Design, Diagnostic and Commissioning”, in *Proc. 1st Int. Particle Accelerator Conf. (IPAC’14)*, Dresden, Germany, Jun. 2014, paper MOPRI075, pp. 777-779.
- [9] R. Stassen, F. J. Etkorn, R. Maier, D. Prasuhn, and H. Stockhorst, “COSY as ideal Test Facility for HESR RF and Stochastic Cooling Hardware”, in *23th Particle Accelerator Conference*, 2009, pp. 861–863.
- [10] HESR “Baseline Technical Report”, [http://www.fair-center.eu/fileadmin/fair/publications\\_FAIR/FAIR\\_BTR\\_1.pdf](http://www.fair-center.eu/fileadmin/fair/publications_FAIR/FAIR_BTR_1.pdf)
- [11] R. Stassen *et al.*, “First Experiences with the HESR Stochastic Cooling System”, in *Proc., International Workshop on Beam Cooling and Related Topics (COOL’17)*
- [12] R. Stassen *et al.*, “Recent Developments for the HESR Stochastic Cooling System”, in *Proc., International Workshop on Beam Cooling and Related Topics (COOL’07)*
- [13] CST Microwave Studio, <https://www.cst.com/products/cstmws>
- [14] D. A. Goldberg and G. R. Lambertson, “Dynamic devices. A primer on pickups and kickers”, in *AIP Conference Proceedings*, Vol. 249, 1992

# DEVELOPMENT OF A BUNCHED BEAM ELECTRON COOLER BASED ON ERL AND CIRCULATOR RING TECHNOLOGY FOR THE JEFFERSON LAB ELECTRON-ION COLLIDER\*

Stephen Benson<sup>†</sup>, Yaroslav Derbenev, David Douglas, Fay Hannon, Andrew Hutton, Rui Li, Robert Rimmer, Yves Roblin, Chris Tennant, Haipeng Wang, He Zhang, Yuhong Zhang,  
 Jefferson Lab, Newport News VA, USA

## Abstract

Jefferson Lab is in the process of designing an electron ion collider with unprecedented luminosity at a 45 GeV center-of-mass energy. This luminosity relies on ion cooling in both the booster and the storage ring of the accelerator complex. The cooling in the booster will use a conventional DC cooler similar to the one at COSY. The high-energy storage ring, operating at a momentum of up to 100 GeV/nucleon, requires novel use of bunched-beam cooling. There are two designs for such a cooler. The first uses a conventional Energy Recovery Linac (ERL) with a magnetized beam while the second uses a circulating ring to enhance both peak and average currents experienced by the ion beam. This presentation will describe the design of both the Circulator Cooling Ring (CCR) design and that of the backup option using the stand-alone ERL operated at lower charge but higher repetition rate than the ERL injector required by the CCR-based design.

## INTRODUCTION

The JLEIC electron-ion collider is designed to produce extremely high luminosity at 45 GeV center-of-mass (CM) energy in electron ion collisions [1]. To accomplish this, the proton or ion beams must be cooled during the operation of the collider. The ion and proton energy is as high as 100 GeV so an electron cooling beam must have an energy of 55 MeV to match the velocity of the protons. To produce a beam of such an energy requires an RF accelerator so the electron beam used to cool the protons/ions must be bunched rather than CW.

We have attempted to design an electron cooling system for JLEIC that strongly cools the ion or proton beams. The specifications for the cooler are shown in Table 1 for the electron and Table 2 for the proton beams for two different CM energies. The electron beam parameters are difficult to achieve due to both the very high charge and high average current. Space charge forces, coherent synchrotron radiation, and wakes tend to create large energy shifts in the electrons. The layout of the cooling complex is shown in Fig. 1. The ion ring is cooled by a Circulating Cooler Ring (CCR) that circulates high-charge bunches 11 times through the ion or proton beam.

\*Authored by Jefferson Science Associates, LLC under U.S. DOE Contract No. DE-AC05-06OR23177, the Office of Naval Research and the High Energy Laser Joint Technology Office. The U.S. Government retains a non-exclusive, paid-up, irrevocable, world-wide license to publish or reproduce this manuscript for U.S. Government purposes.

<sup>†</sup>felman@jlab.org

The bunches are injected from an Energy Recovery Linac (ERL) via a harmonic kicker [2]. After 11 round trips, the electron bunches are extracted and decelerated in the ERL and diverted to the dump. The gun frequency is then one eleventh of the cooling ring frequency.

At full CM energy (63.5 GeV), the colliding beams are reduced to one third of their usual frequency while the proton bunch charge is tripled. This is the worst case for cooling so we will consider that case first.

Table 1: Electron Specifications for Strong Cooling

Parameter	Value
Energy	20–55 MeV
Charge	3.2 nC
CCR pulse frequency	476.3 MHz
Gun frequency	43.3 MHz
Bunch length (tophat)	2 cm (23°)
Thermal emittance	<19 mm-mrad
Cathode spot radius	2.2 mm
Cathode field	0.1 T
Gun voltage	400 kV
Norm. hor. drift emittance	36 mm-mrad
<i>rms</i> Eng. spread (uncorr.)*	$3 \times 10^{-4}$
Energy spread (p-p corr.)*	$<6 \times 10^{-4}$
Solenoid field	1 T
Electron beta in cooler	36 cm
Solenoid length	4x15 m

Table 2: Proton Specifications for Strong Cooling

Parameter	63.5 GeV CM	45 GeV CM
Energy	100 GeV	100 GeV
Particles/bunch	$2.0 \times 10^{10}$	$6.6 \times 10^9$
Repetition rate	158.77 MHz	476.3 MHz
Bunch length (rms)	2.5 cm	1.0 cm
Normalized emittance (x/y)	1.2/0.6 mm-mrad	1.0/0.5 mm-mrad
Betatron function	100 m	100 m

Note that we have chosen to use a magnetized beam in the cooler [3]. In a magnetized source, the cathode is immersed in a solenoid. The gun generates an almost parallel (laminar) electron beam. This beam state is then transplanted to the solenoid in the cooling section. The

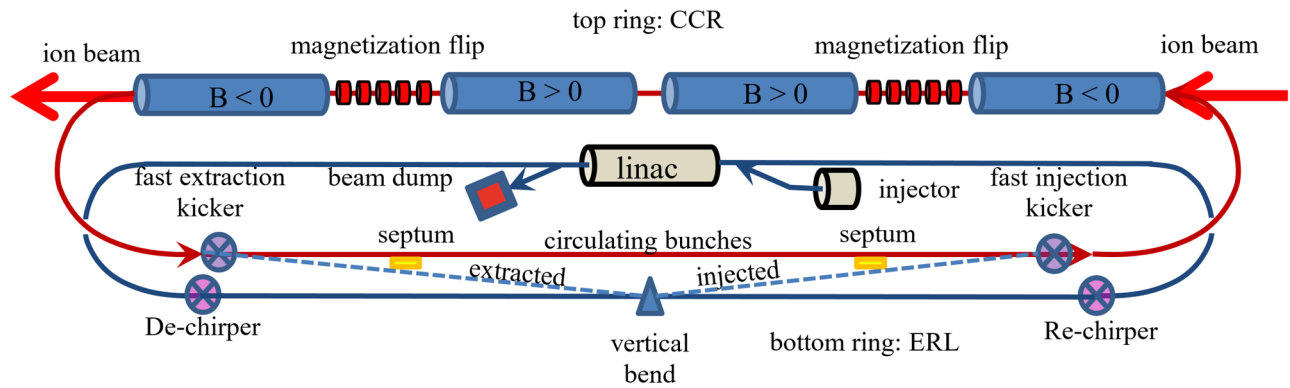


Figure 1: Layout of the Circulating Cooler Ring (CCR) concept. The ion ring is cooled by a magnetized beam circulating for 11 passes of the CCR and fed by an Energy Recovery Linac (ERL) producing and recovering high charge, magnetized bunches at a 43.3 MHz repetition rate.

ratio of the solenoid fields at the gun and cooler can be adjusted to match the e-beam size to the ion beam size. We do not, however, maintain the solenoid field from cathode to dump, so this Canonical Angular Momentum (CAM) beam must be transported in such a way that the magnetization is preserved between the gun and cooler. Derbenev has shown that this is possible if the transport is axisymmetric [4].

The helicity of the angular momentum is flipped in two transport sections between the cooler solenoids. This preserves the spin in the collider ring.

Magnetization has the following advantages over a non-magnetized gun/cooling solenoid):

- It has significantly stronger cooling than non-magnetic case [5].
- There is a large reduction (by a factor 20 – 30) of the deleterious impact of space charge on dynamics in the CCR (e.g, the tune shift).
- There is a strong suppression of the CSR micro-bunching/energy spread growth (though CSR can still increase the correlated energy spread) [6].
- It suppresses the deleterious impact of high electron transverse velocity spread and short-wave misalignments to cooling rates (thanks to ion collisions with “frozen” electrons at large impact parameters).

## COOLING SIMULATIONS

A simulation code JSpec, which uses algorithms similar to BETACOOOL [7], was used to simulate cooling in the ring for the 65 GeV CM parameters [8]. The calculated cooling and Intra-Beam-Scattering (IBS) rates are shown in Table 3.

Table 3: Sample Cooling Rates and Intra-Beam Scattering Rates for a 63.5 GeV Center-of-Mass Energy

	Units	x	y	z
Cooling rate	$10^{-3}$ 1/s	-0.431	-1.434	-1.605
IBS rate	$10^{-3}$ 1/s	3.192	0.102	0.618
Total rate	$10^{-3}$ 1/s	2.761	-1.332	-0.987

Note that the transverse heating in the x-direction is much larger than the cooling and the opposite is true for the vertical direction. The longitudinal cooling is also much stronger than the heating. If we cool with these cooling and heating strengths, the bunch becomes shorter and the IBS increases so that the horizontal emittance starts to increase very rapidly after about 20 minutes of operation.

Changing the partition of the cooling and heating might be accomplished by using skew quad coupling between vertical and horizontal axes for the proton beam. This must be done in such a way that the luminosity is not degraded. Transverse dispersion at the solenoid might also be able to couple the transverse and longitudinal cooling. The JSpec code must be modified to do this accurately.

## ERL SIMULATION RESULTS

### Weak Focusing Results

Historically, we first studied a weak cooling solution without the CCR. This had just an ERL with higher average current but lower charge than the ERL used with the CCR. The ERL design accelerates on the rising side of the acceleration phase and debunches the beam in an arc with non-zero  $M_{56}$ . An RF cavity operated at zero crossing is then used to remove the energy chirp on the beam. After going through a 30-meter solenoid the helicity is reversed in a magnetization reversing set of skew quads. The beam is then sent through a second 30-meter solenoid before going through a chirping cavity and a second arc, where the beam is bunch down to the proper length for the decelerating pass of the ERL. At the end of the second pass through the linac the beam is separated and sent to a 5 MeV dump.

This system was simulated from the cathode to the dump (Start-to-End) and from the exit of the injector booster to the dump (Injector-to-End). In the latter case, an ideal super-Gaussian distribution was used for the electron bunches.

Content from this work may be used under the terms of the CC BY 3.0 licence (© 2017). Any distribution of this work must maintain attribution to the author(s), title of the work, publisher, and DOI.

In Fig. 2 we show the *rms* bunch size vs. position for the Injector-to-End simulations both with and without CSR. With the very long bunch it is not clear that the CSR will have such a large effect because CSR shielding may reduce the CSR forces [9], but the dominant effect so far is to cause some mismatches, which can be rematched to optimize the system. The beam is well behaved through the ERL. The transverse Larmor emittance grows from an initial value of 2 mm-mrad to 4.4 mm-mrad without CSR and 7.8 mm-mrad with CSR. Both are well within the specifications in Table 1. The emittance growth is dominated by the growth in the merger between the booster and the linac. The longitudinal behaviour is also acceptable. The addition of CSR leads to some tilt in the phase-energy phase space but this can easily be removed by changing the de-chirper phase a bit. The start-to-end simulations do not achieve a smooth super-Gaussian distribution at the booster exit but the resulting distribution is maintained well through the machine and the transverse emittances are similar to the ideal Injector-to-End case.

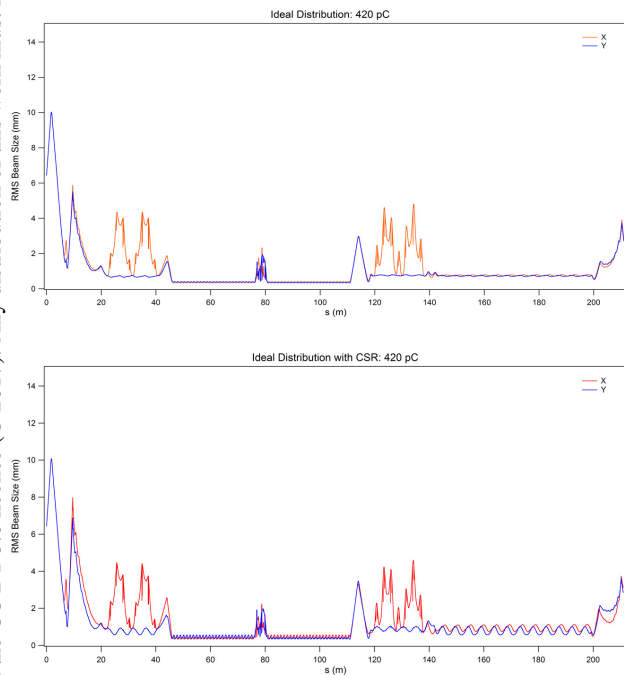


Figure 2: Simulation of the transport of the magnetized bunches from the exit of the injector booster to the dump both without (top) and with (bottom) CSR effects.

### Strong Focussing Results

In the CCR design, the charge per bunch is increased from 420 pC to 3.2 nC. This strongly enhances the effects of CSR and space charge. The arcs must also now be isochronous since the bunch length and shape have to be maintained for 11 turns.

Designing an isochronous arc with equal two-plane focussing is quite difficult due to the rather weak focussing in the double focusing dipoles. We have therefore explored the used of globally symmetric arcs. In such an

arc, the transport matrix from the beginning to the end of the arc is a unit matrix. The design does use quadrupoles however, which are explicitly asymmetric. We have found that magnetization can be maintained even with a globally symmetric arc.

Though the transverse properties of the beam are maintained in the arc, the longitudinal properties are badly degraded by CSR. This is shown in Fig. 3 for 5, 10, and 20 passes through the CCR. The bunch develops a strong energy chirp due to the CSR wake.

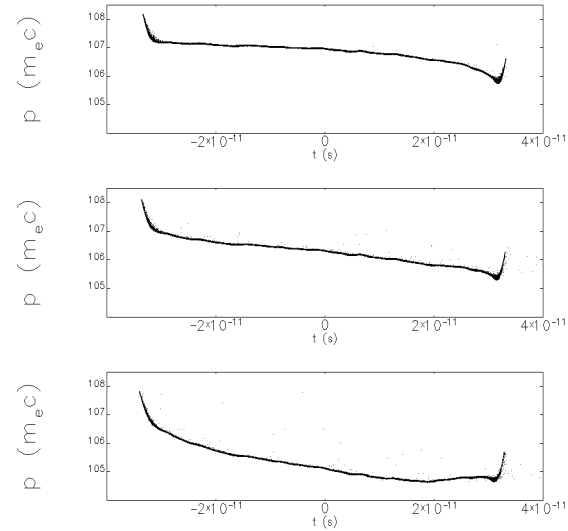


Figure 3: Longitudinal phase space for 5 (top), 10 (middle), and 20 (bottom) passes through the CCR. This assumes a super-Gaussian distribution in the ring.

Since the CSR effects appear to be fairly linear it is worth exploring whether an RF cavity can be used to compensate some of the energy loss and chirp. This was done with some success. The result is shown in Fig. 4. Note that we expect that the CSR will be at least partially shielded so the longitudinal distortion in both Fig. 3 and Fig. 4 should be much less when shielding is added.

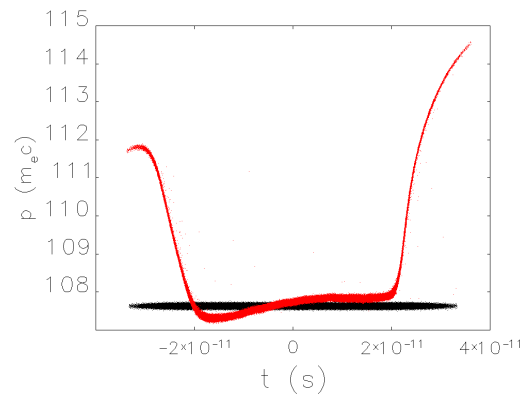


Figure 4: Longitudinal phase space after 20 passes with an RF cavity compensating the energy loss and chirp. The compensation is not perfect but it is possible to get close to the correlated energy variation specification in Table 1 of  $6 \times 10^{-4}$  peak-to-peak.

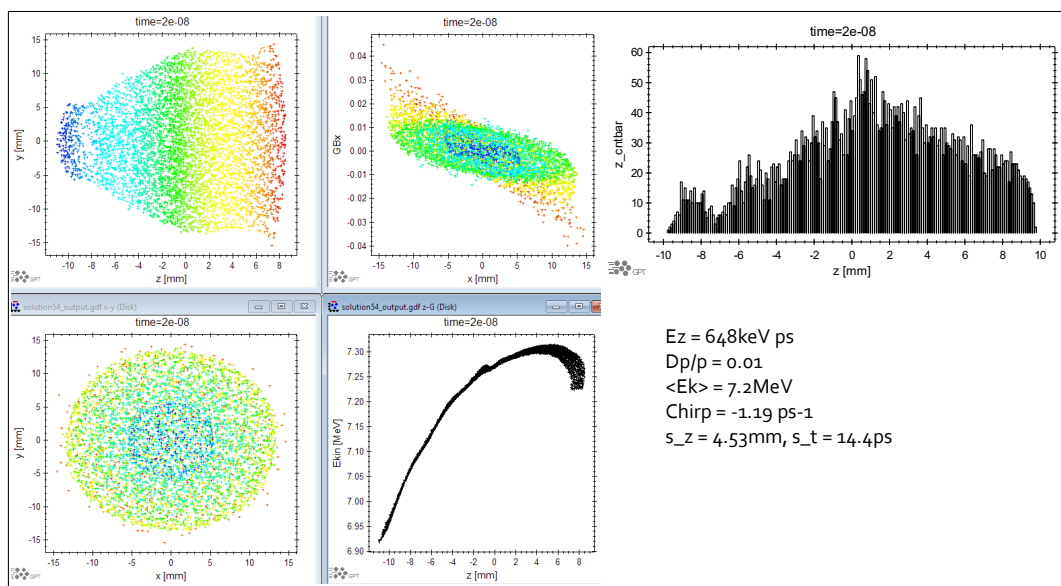


Figure 5: Particle distributions at the end of the booster for the injector. Each slice of the distribution has good magnetization but the slices do not have the same Twiss parameters so the projected emittance is larger than the specification.

### Exchange Region

The beam is kicked into the CCR and back out to the ERL using two harmonic kickers [2]. The kickers provide a 2.5 mrad kick to one of 11 bunches and no net kick on any of the others. There is some variation of the kick around zero for each of the bunches but the two kickers are separated by  $180^\circ$  of betatron phase shift so the slope and curvature of the kicker pulse cancels out.

It is possible that there may be some residual effects on the un-kicked bunches after traversing the exchange region several times. We have modelled the effects of the kickers and the intervening transport on the beam over 11 passes through the CCR. There are some small effects due to chromaticity but the bunches maintain their *rms* properties.

### Injector Simulations

The current injector layout consists of a 433 MHz NCRF gun (ten times the bunch frequency) followed by a 433 MHz buncher, a 952.7 MHz buncher, and a booster module with 4 2-cell 952.7 MHz cavities. There are solenoids in the first part of the line to create a magnetized beam. The longitudinal magnetic field must go down to zero before the superconducting cavities of the booster. The results of optimized simulations are shown in Fig. 5. The optimization algorithm tried to produce a uniform distribution with a very linear longitudinal phase space. It was found that the two tend to be inversely related, i.e. a more uniform distribution has worse longitudinal phase space distribution and vice versa. Note the strong variation in bunch size vs. micropulse position. This variation leads to projected emittance growth.

One way to address the non-uniformity in the micro-bunches would be to go to a lower frequency. We will be doing this next to find a more optimum configuration.

## CONCLUSIONS

The Cooler ring design is not yet complete, though we have made progress in several areas. The following are items that must be pursued before a complete design can be established:

- We have to find the proper cooling partition that matches the cooling to the Intra-Beam Scattering.
- An injector design that preserves the beam quality of the beam from the cathode must be derived. It is our expectation that we must use lower frequency RF.
- The longitudinal match to the CCR must be derived. If the injector bunch is too long we might have problems with getting the energy spread to match the specifications.
- CSR and space charge shielding effects must be added to the simulations to show if CSR can be managed in the arcs.
- The mergers at several points in the machine must be designed. There are many possible designs that might be used, including some that do not bend the injected beam at all.

The weak cooling design is almost complete but the strong cooling design has priority for now.

## REFERENCES

- [1] S. Abeyratne *et al.*, “MEIC Design Summary”, ArXiv 1504.07961 (2015).
- [2] Y. Huang, H. Wang, R. A. Rimmer, S. Wang, J. Guo, “Multiple Harmonic Frequencies Resonant Cavity Design and Half-Scale Prototype Measurements for the Fast Kicker in JLEIC”, *Phys. Rev. ST Accel. Beams*, **19**, 122001 (2016).
- [3] G. I. Budker and A. N. Skrinsky, *Sov. Phys. Usp.* **21**, 277 (1978).
- [4] A. Burov, S. Nagaitsev, A. Shemyakin, and Ya. Derbenev, “Optical Principles of Beam Transport for Relativ-

Content from this work may be used under the terms of the CC BY 3.0 licence (© 2017). Any distribution of this work must maintain attribution to the author(s), title of the work, publisher, and DOI.

istic Electron Cooling”, *Phys. Rev. ST Accel. Beams*, **3**, 094002 (2000).

[5] A. Burov, V. Danilov, Ya. Derbenev, and P. Colestock, *Nucl. Instrum. Methods Phys. Res.* **A441**, 271 (2000).

[6] C.-Y. Tsai, Ya. S. Derbenev, D. Douglas, R. Li, and C. Tennant, “Vlasov Analysis of Microbunching Instability for Magnetized Beams” *Phys. Rev. ST Accel. Beams*, **20**, 054401 (2017).

[7] I. Meshkov *et al.*, *Nucl. Instrum. Methods Phys. Res.* **A558** 325 (2006).

[8] <https://github.com/zhanghe9704/electroncooling>

[9] G. Stupakov and D. Zhou, “Analytical Theory of Coherent Synchrotron Radiation Wakefield of Short Bunches Shielded by Conducting Parallel Plates”, *Phys. Rev. ST Accel. Beams*, **19**, 044402 (2016).

## STATUS OF PROOF-OF-PRINCIPLE EXPERIMENT OF COHERENT ELECTRON COOLING AT BNL

V.N.Litvinenko<sup>1,2,#</sup>, I.Pinayev<sup>1</sup>, J.Tuozzollo<sup>1</sup>, J.C.Brutus<sup>1</sup>, Z.Altinbas<sup>1</sup>, R.Anderson<sup>1</sup>, S. Belomestnykh<sup>1</sup>, K.A.Brown<sup>1</sup>, C.Boulware<sup>3</sup>, A.Curcio<sup>1</sup>, A.Di Lieto<sup>1</sup>, C.Folz<sup>1</sup>, D.Gassner<sup>1</sup>, T.Grimm<sup>3</sup>, T.Hayes<sup>1</sup>, R.Hulsart<sup>1</sup>, P.Inacker<sup>1</sup>, J.Jamilkowski<sup>1</sup>, Y.Jing<sup>1,2</sup>, D.Kayran<sup>1,2</sup>, R.Kellermann<sup>1</sup>, R.Lambiase<sup>1</sup>, G.Mahler<sup>1</sup>, M.Mapes<sup>1</sup>, A.Marusic<sup>1</sup>, W.Meng<sup>1</sup>, K.Mernick<sup>1</sup>, R.Michnoff<sup>1</sup>, K.Mihara<sup>1,2</sup>, T.A.Miller<sup>1</sup>, M.Minty<sup>1</sup>, G.Narayan<sup>1</sup>, P.Orfin<sup>1</sup>, I.Petrushina<sup>1,2</sup>, D.Phillips<sup>1</sup>, T.Rao<sup>1,2</sup>, D.Ravikumar<sup>1,2</sup>, J.Reich<sup>1</sup>, G.Robert-Demolaize<sup>1</sup>, T.Roser<sup>1</sup>, B.Sheehy<sup>1</sup>, S.Seberg<sup>1</sup>, F.Severino<sup>1</sup>, K.Shih<sup>1,2</sup>, J.Skaritka<sup>1</sup>, L.A.Smart<sup>1</sup>, K.Smith<sup>1</sup>, L.Snydstrup<sup>1</sup>, V.Soria<sup>1</sup>, Y.Than<sup>1</sup>, C.Theisen<sup>1</sup>, J.Walsh<sup>1</sup>, E.Wang<sup>1</sup>, G.Wang<sup>1,2</sup>, D.Weiss<sup>1</sup>, B.Xiao<sup>1</sup>, T.Xin<sup>1</sup>, W.Xu<sup>1</sup>, A.Zaltsman<sup>1</sup>, Z.Zhao<sup>1</sup>

<sup>1</sup>Collider-Accelerator Department, Brookhaven National Laboratory, Upton, NY, USA

<sup>2</sup>Department of Physics and Astronomy, Stony Brook University, Stony Brook, NY, USA

<sup>3</sup>Niowave Inc., 1012 N. Walnut St., Lansing, MI, USA

### Abstract

An FEL-based Coherent electron Cooling (CeC) has a potential to significantly boosting luminosity of high-energy, high-intensity hadron-hadron and electron-hadron colliders. In a CeC system, a hadron beam interacts with a cooling electron beam. A perturbation of the electron density caused by ions is amplified and fed back to the ions to reduce the energy spread and the emittance of the ion beam. To demonstrate the feasibility of CEC we pursue a proof-of-principle experiment at Relativistic Heavy Ion Collider (RHIC) using an SRF accelerator and SRF photo-injector. In this paper, we present status of the CeC systems and our plans for next year.

### INTRODUCTION

An effective cooling of ion and hadron beams at energy of collision is of critical importance for the productivity of present and future colliders. Coherent electron cooling (CeC) [1] promises to be a revolutionary cooling technique which would outperform competing techniques by orders of magnitude. It is possibly the only technique, which is capable of cooling intense proton beams at energy of 100 GeV and above.

The CeC concept is built upon already explored technology (such as high-gain FELs) and well-understood processes in plasma physics. Since 2007 we have developed a significant arsenal of analytical and numerical tools to predict performance of a CeC. Nevertheless, being a novel concept, the CeC should be first demonstrated experimentally before it can be relied upon in the upgrades of present and in the designs of future colliders.

A dedicated experimental set-up, shown in Fig. 1, has been under design, manufacturing, installation and finally commissioning during last few years [2-4]. The CeC system is comprised of the SRF accelerator and the CeC section followed by a beam dump system. It is designed to cool a single bunch circulating in RHIC's "yellow" ring (indicated by yellow arrow in Fig. 1). A 1.5 MeV electron beam for the CeC accelerator is generated in an 113 MHz SRF quarter-wave photo-electron gun and first focussed by a gun solenoid. Its energy is chirped by two 500 MHz room-temperature RF cavities and ballistically compressed in 9-meter long low energy beamline comprising five focusing solenoids. A 5-cell 704 MHz SRF linac accelerates the compressed beam to 15 MeV. Accelerated beam is transported through an achromatic dogleg to merge with ion bunch circulating in RHIC's yellow ring. In CeC interaction between ions and electron beam occurs in the common section, e.g. a proper coherent electron cooler. The CeC works as follows: In the modulator, each hadron induces density modulation in electron beam that is amplified in the high-gain FEL; in the kicker, the hadrons interact with the self-induced electric field of the electron beam and receive energy kicks toward their central energy. The process reduces the hadron's energy spread, i.e. cools the hadron beam. Fourteen quadrupoles are used to optimize the e-beam interaction with the ion beam and FEL performance.

Finally, the used electron beam is bent towards an aluminium high power beam dump equipped with two quadrupoles to over-focus the beam.



Figure 1: Layout of the CeC proof-of-principle system at IP2 of RHIC.

#vl@bnl.gov

## COMMISSIONING OF THE CEC SYSTEM

The CeC accelerator SRF system uses liquid helium from RHIC refrigerator system, which operates only during RHIC runs, typically from February till end of June every year. Hence, the commissioning and operation of CeC accelerator is synchronized with RHIC runs.

The commissioning of the CeC accelerator was accomplished during three RHIC runs: Runs 15, 16 and 17.

During the run 15, only SRF gun and a part of the low energy beam line had been installed and commissioned. The installation of the equipment was continued during the RHIC maintenance days. We went through a steep learning curve of how to condition and operate an SRF gun with CsK<sub>2</sub>Sb photocathode and how to prevent its QE degradation. The run was very successful and the SRF gun generated electron bunches with 1.15 MeV kinetic energy and 3 nC charge per bunch.

The major installation of the CeC system, including all common section with FEL, occurred during RHIC shutdown in 2016. We had received 5-cell SRF linac cryostat from Niowave Inc, and three helical wigglers for our FEL amplifier from BINP, Novosibirsk, Russia. The latter were assembled, magnetically measured and tuned to design performance at BNL (see [5]).

Installation of 5-cell SRF linac system suffered from two major problems. First, after installing the cryostat into the CeC system we discovered that the integrity of the linac helium system and the cryostat cooling circuits was destroyed during truck transportation from Lansing, MI to BNL. Specifically, the cavity fell from its support inside the cryostat because of the major shocks during transportation and cracks appeared in the liquid helium and nitrogen systems. The cryostat was partially taken apart and leaks repaired in situ. The second even was even more damaging – an incompetent person opened the inside of the SRF cavity to a dirty air in the tunnel. The latter resulted in excessive field emission and limited the maximum operational voltage to about 6-7 MV, instead of design value of 20 MV. The 5-cell cavity, built by Advanced Energy Systems, demonstrated voltage close to 20 MV in prior vertical tests and we decided to take the SRF linac apart and re-clean it after the end of the Run 16.

Nevertheless, the CeC team managed to make significant progress in CeC accelerator commissioning during RHIC Run 16. Electron beam from the SRF gun was properly analysed, its emittance was measured and we had first clear indication that the SRF gun is generating electron beam of exceptionally high quality.

We also were discovering complexity of operating SRF quarter-wave gun with CsK<sub>2</sub>Sb photocathode. We discovered that while in a normal (high 1 MV scale voltage) mode of operation the SRF gun naturally has excellent vacuum, at low voltage it has a number multipacting (MP) zones. One of these zones – in the range from 28 kV to 40 kV of the gun accelerating voltage - was very strong and we frequently prevented us from passing to operational voltage using 2 kW power amplifier. In addition to annoying incapability of getting to the operational voltage, MP was spoiling

the gun vacuum and was destroying photocathode's QE. Lastly, this process was also enhancing the strength of MP, presumably by depositing high second-emission-yield (SEY) material from the photocathode to the surrounding surfaces. More details about our findings can be found in [6-7], but as the result of our experiences we increased the power of our transmitter to 4 kW and also developed a dedicated LLRF procedure providing for a single-shot pass through the most dangerous 40-kV multipacting barrier. After the passing the barrier, the gun was kept at operation voltage all the time and was intentionally turned down only for access to the RHIC IP2, where the gun is located. Accidental turning off the gun voltage – either by operator errors or system failures – were infrequent. If, by a chance, the gun was caught at MP level (mostly because of operator mistakes) and the MP barrier went above 4 kW of available power, keeping the gun idle for about 30 minutes was solving the problem.

As the results, during CeC Run 17 (February-June 2017) the CsK<sub>2</sub>Sb photocathodes QE ~ 3-4% was stable for months of operation. We used only two cathodes for five month of continuous operation and the change was done simply to explore an additional cathode. Our SRF gun had generated electron beam with charge up to 4 nC per bunch and extremely high quality. The best measured normalised emittance of 1.56 MeV (total energy), 0.5 nC electron bunch was 0.32 mm mrad [8].

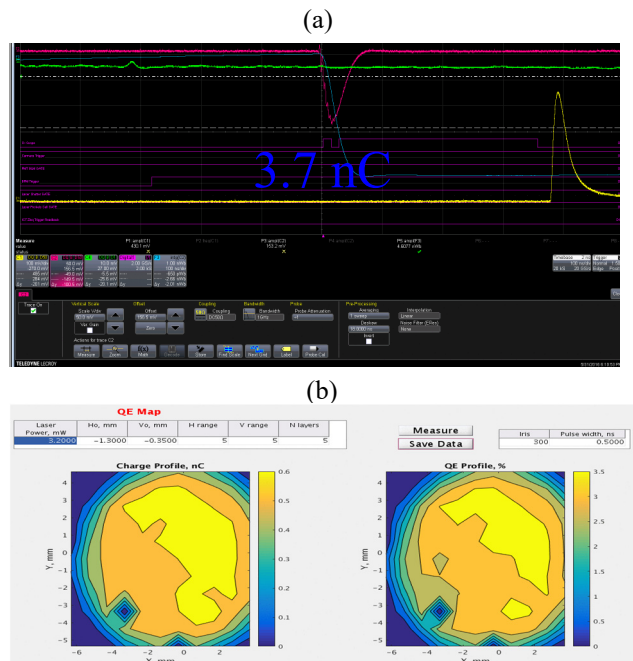


Figure 2: (a) A typical digital scope trace showing the electron bunch pulse (from integrated current transformer, red trace) and delayed trace of laser pulse (from a slow photodiode sensor); (b) a measured QE map of CsK<sub>2</sub>Sb photocathode after two months of operating in the SRF gun.

The main efforts during the shutdown period between Runs 16 and 17 were dedicated to complete disassembly of the SRF linac cryostat (done by BNL SRF group), re-cleaning of the 5-cell cavity system (which was perform at ANL

Content from this work may be used under the terms of the CC BY 3.0 licence (© 2017). Any distribution of this work must maintain attribution to the author(s), title of the work, publisher, and DOI.

Table 1: Main Parameters of the CeC System

Parameter	Design	Status	Comment
Species in RHIC	Au <sup>+79</sup> , 40 GeV/u	Au <sup>+79</sup> 26.5 GeV/u	To match e-beam
Particles/bucket	10 <sup>8</sup> - 10 <sup>9</sup>	10 <sup>8</sup> - 10 <sup>9</sup>	✓
Electron energy	21.95 MeV	15 MeV	SRF linac quench
Charge per e-bunch	0.5-5 nC	0.1- 4 nC	✓
Peak current	100 A	50 A	Sufficient for this energy
Pulse duration, psec	10-50	12	✓
Beam emittance, norm	<5 mm mrad	3 - 4 mm mrad	✓
FEL wavelength	13 μm	30 μm	New IR diagnostics
Rep-rate	78 kHz	26 kHz**	Temporary**
e-beam current	Up to 400 μA	40 μA	Temporary**
Electron beam power	< 10 kW	600 W	Temporary**

SRF facility), to reassemble the cryostat (at BNL) and to install it back onto CeC accelerator system. Unfortunately the SRF linac could operate only at voltage below 13.5 MV and exhibited typical hard quench behaviour above this level. The quenching characteristics are typical for a cavity defect near its equator, which cannot be repaired. Hence, this setback with the SRF linac limited the energy of electron beam from CeC accelerator to about 15 MeV. This created a major obstacle in commissioning of the CeC FEL system by shifting its wavelength from 13 μm to 30 μm and rendering all our IR diagnostics practically useless: its vacuum out-coupling window had cut off above 16 μm.

Nevertheless, we had fully commissioned the CeC accelerator and propagated CW beam through the entire CeC system – including FEL system - to the high power dump with very low losses. Table 1 summarizes the main parameters of the CeC system and its electron beam.

The second consequence of the low energy of the electron beam was mismatched between the frequency of the SRF and revolution frequency of 26.5 GeV/u gold ions,  $f_{rev}$ . The nearest of the harmonics of the revolution frequency was outside of the available tuning range provided by movable gun's FPC [9, 10]. In order to test interaction of electron beam with ion beam circulating in RHIC we had tuned the gun at frequency  $(n+1/3) f_{rev}$ , resulting in the e-beam rep-rate of 26 kHz. This problem will be fixed before the next RHIC run by mechanically retuning the gun frequency. Using this set-up, we synchronised the electron

beam with ion bunch circulated in RHIC's "yellow" ring and scanned electron beam energy. In this case, ion beam was overlapping with electron bunch at each third turn. Beams were overlapped both the temporarily and spatially. The recorded beam parameters during the scan are shown in Fig. 3. Without IR diagnostics we did not had chance to CeC cooling – it would require scan of 10 parameters, but we managed to detect weak energy-dependent interaction between the beams.

### PLANS FOR RUN 18

At the moment we are pursuing a program of modifications and small repairs to the CeC system. The main advances to the CeC capabilities will come from new IR diagnostic system, which would be coupled, to FEL via an SVD diamond window transparent in the entire IR spectrum. Other modification are aimed to improving accuracy of SRF controls and orbit correction in low-energy transport beamline.

We expect to start CeC operation in January 2018 and finish the run in mid-June 2018. First, we plan to establish a stable phase, amplitude and timing operation of RF and laser system to reliably deliver a stable electron beam. After that we plan to commission our new IR diagnostics and establish FEL operation/amplification. This will be followed by synching electron beam with 26.5 GeV/u gold ion beam, aligning them transversely and synchronizing the ion and electron beams energies using IR diagnostics. Specifically, we will observe energy-dependent increase in the intensity of FEL radiation. Finally, we plan to test and characterize Coherent electron Cooling.

### CONCLUSION

We successfully commissioned SRF-based CeC electron accelerator with beam parameters sufficient for CeC demonstration experiment [11-12]. We plan to undertake the challenging task of experimentally demonstrating coherent electron cooling during next RHIC run.

Work is supported by Brookhaven Science Associates, LLC under Contract No. DEAC0298CH10886 with the U.S. Department of Energy, DOE NP office grant DE-FOA-0000632, and NSF grant PHY-1415252.

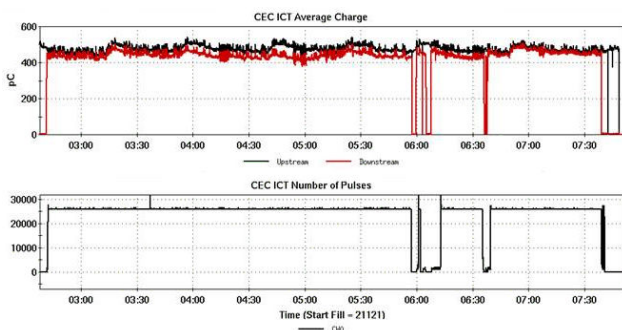


Figure 3: The charge per bunch and repetition rate during the interaction experiment.

## REFERENCES

- [1] V.N. Litvinenko and Y.S. Derbenev, *Physical Review Letters* **102**, 114801 (2009)
- [2] V.N. Litvinenko *et al.*, “Proof-of-principle Experiment for FEL-based Coherent Electron Cooling”, in *Proc. PAC’11*, paper THOBN3.
- [3] I. Pinayev *et al.*, “Present Status of Coherent Electron Cooling Proof-of-principle Experiment”, in *Proc. COOL2013*, paper WEPP014.
- [4] I. Pinayev *et al.*, “First Results of the SRF Gun Test for CeC PoP Experiment”, in *Proc. of FEL2015*, paper TUD03.
- [5] I. Pinayev, Y. Jing, V.N. Litvinenko, G. Wang, P. Vobly, *et al.*, “Helical Undulators for Coherent Electron Cooling System”, presented at FEL’17, Sante Fe, NM, USA, paper WEP051.
- [6] I. Petrushina, T. Hayes, Y. Jing, D. Kayran, V.N. Litvinenko *et al.*, “Novel Aspects of Beam Dynamics in CeC SRF Gun and SRF Accelerator”, presented at FEL’17, Sante Fe, NM, USA, paper TUP034.
- [7] I. Petrushina, T. Hayes, V.N. Litvinenko, G. Narayan, I. Pinayev, F. Severino, K.S. Smith, “Mitigation of Multipacting in 113-MHz Superconducting RF Photoinjector”, in preparation for submission to *PR AB*
- [8] K. Mihara, Y. Jing, V.N. Litvinenko, I. Pinayev, G. Wang, I. Petrushina, “Emittance Measurements from SRF Gun in CeC Accelerator”, presented at FEL’17, Sante Fe, NM, USA, paper WEP025.
- [9] G. Wang, Y. Jing, V.N. Litvinenko, J. Ma, “Electron Beam Requirements for Coherent Electron Cooling FEL System”, presented at FEL’17, Sante Fe, NM, USA, paper TUP039.
- [10] Y. Jing, V.N. Litvinenko, I. Pinayev, “Simulation of Phase Shifters Between FEL Amplifiers in Coherent Electron Cooling”, presented at FEL’17, Sante Fe, NM, USA, paper TUP072.
- [11] T. Xin, J. C. Brutus, S.A. Belomestnykh, I. Ben-Zvi, C. H. Boulware, T. L. Grimm, *et al.*, *Review of Scientific Instruments*, **87**, 093303 (2016).
- [12] I. Pinayev, V.N. Litvinenko, J. Tuozzolo, J.C. Brutus, S. Belomestnykh, *et al.*, “High-gradient High-charge CW Superconducting RF gun with CsK2Sb photocathode”, arXiv:1511.05595, 17 Nov 2015

# COMMISSIONING OF THE LOW ENERGY STORAGE RING FACILITY CRYRING@ESR

F. Herfurth, M. Lestinsky, Z. Andelkovic, M. Bai, A. Bräuning-Demian, V. Chetvertkova,  
O. Geithner, W. Geithner, O. Gorda, S. Litvinov, Th. Stöhlker, G. Vorobjev, U. Weinrich  
GSI Helmholtzzentrum für Schwerionenforschung, 64291 Darmstadt, Germany

A. Källberg

Fysikum, Stockholm University, SE-106 91 Stockholm, Sweden

## Abstract

CRYRING@ESR is the early installation of the low-energy storage ring LSR, a Swedish in kind contribution to FAIR, which was proposed as the central decelerator ring for antiprotons at the FLAIR facility. An early installation opens the opportunity to explore part of the low energy atomic physics with heavy, highly charged ions as proposed by the SPARC collaboration but also experiments of nuclear physics background much sooner than foreseen in the FAIR general schedule. Furthermore, the ring follows in large parts FAIR standards, and is used to test the FAIR control system.

CRYRING@ESR has been installed behind the existing experimental storage ring ESR starting in 2013. It has a local injector that is used for commissioning. In November 2016 the commissioning of the storage ring started and a first turn was achieved. After a complete bake out cycle and substantial developments of control system, diagnosis and others, commissioning was continued in late summer 2017. Stored as well as accelerated beam has been achieved by now. The remaining step is to take the electron cooler into operation, which is planned for November this year.

## INTRODUCTION

In Darmstadt, the facility for antiproton and ion research is being built. Based on the GSI accelerators for injection it will open up new areas of research with heavy ions and, new in Darmstadt, with antiprotons. When it comes to experiments with slow and stored heavy, highly charged ions and antiprotons, two collaborations, the Stored Particles Atomic Physics Research Collaboration - SPARC and the Facility for Low-Energy Antiproton and Ion Research - FLAIR, have been formed to move into one building complex, the FLAIR building.

The low energy storage ring LSR shall provide the highly charged ions and antiprotons at low energy at the FAIR facility for those two collaborations, SPARC and FLAIR. The LSR evolves from the heavy-ion storage ring CRYRING, which has been operated at the Manne Siegbahn Laboratory in Stockholm until 2010 [1]. The main-focus is on precision experiments, which requires low energy and well-controlled beam properties that is typically achieved by beam cooling. The LSR will be installed as intermediate step between the new experimental storage run NESR and the low energy facilities HITRAP and the ultra low energy storage ring USR. The LSR is a Swedish in-kind contribution to the FAIR facility in

Darmstadt, i.e. part of the investment done by the Swedish physics community into the FAIR project.

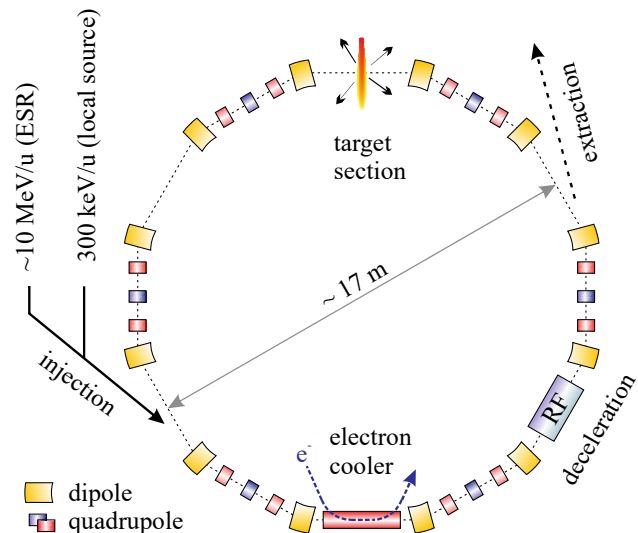


Figure 1: Schematic layout of CRYRING@ESR. The main components; injection, extraction, electron cooler, RF section, and the target section are indicated.

After careful cost evaluation a staged approach was put into place that does not include the NESR in its start version. However, contrary to the original plans the present storage ring at GSI, the ESR, will not be disassembled for component reuse but continue running. Consequently, instead of warehousing the ring components until installation at the Facility for Antiproton and Ion Research, FAIR, the immediate installation behind the existing Experimental Storage Ring, ESR [2, 3], has been proposed and worked out in detail by a Swedish-German working group. The estimated efforts for installation and operation of CRYRING at the ESR have been summarized in a report [4] published by that working group in 2012.

A schematic overview of the storage ring and its facilities is shown in Fig. 1. CRYRING as it is now installed behind the ESR can decelerate, cool and store heavy, highly charged ions from about 10 MeV/nucleon and antiprotons from about 30 MeV/nucleon down to a few 100 keV/nucleon. It provides a high performance electron cooler in combination with a gas jet target. It is equipped with its own injector and ion source, to allow for standalone commissioning. For more detailed ring parameters see also Table 1.

Table 1: Parameters for CRYRING@ESR

Description	Value
Circumference	54.17 m
Rigidity at injection	
<i>protons/antiprotons</i>	0.8 Tm
<i>ions</i>	1.44 Tm
Lowest Rigidity	0.054 Tm
Ramping rates	1.. 7 T/s

More details of the installation and ring characteristics can be found in the technical design report [1], earlier proceedings of this conference [5] and the most recent status report here [6].

## STATUS OF COMMISSIONING

During the last year, i.e. in 2016/17, the ring has been taken stepwise into operation until stored beam was achieved.

In a first step ions were transported from the ESR to CRYRING@ESR still in 2016. This is based on two assumptions that have been tested and validated on-line. First, fast extraction from the ESR had to be demonstrated using the existing kicker that was only designed for extraction into the reinjection beam line. To be able to use the existing kicker for extraction into the beam line towards CRYRING@ESR, a dedicated ion optic setup was developed and successfully tested [7].

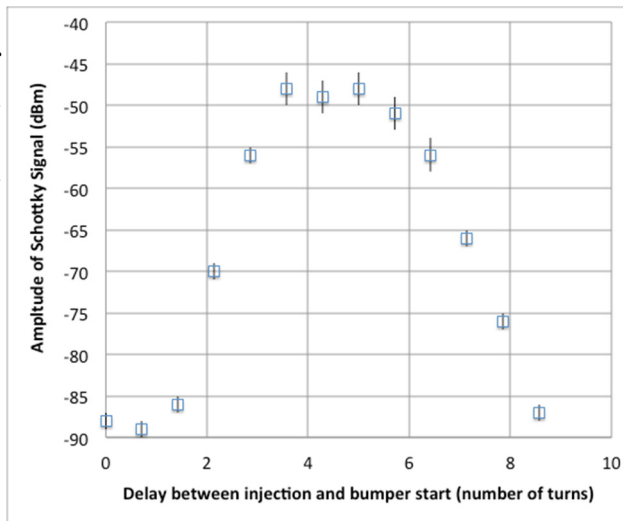


Figure 2: Present efficiency of the multiturn injection scheme. The amplitude of the Schottky noise signal is used as intensity monitor of the stored ion beam after injection at varying times after the bumper ramp start. This time is expressed in number of turns. One turn takes about 7  $\mu$ s at injection energy.

The second challenge was that the existing sections of that beam line are designed for 10 Tm ion beams – some even for 14 Tm. Here it was successfully tested if the

reminiscent magnetic field could be well enough controlled and understood to transport ions with a rigidity of only 0.8 Tm.

After the installation and commissioning of the local injector [6], this was used to deliver  $H_2^+$  ions for the commissioning of the ring itself. Those ions are accelerated to 300 keV/nucleon and then injected with the newly designed [1] multi turn injection system into the ring. This system, a combination of a magnetic and an electrostatic septum together with a electrostatic bump should allow for injection of both, ions from the local injector with at most 300 keV/nucleon, and ions from the ESR with a rigidity of up to 1.44 Tm.

The result of one optimisation cycle is displayed in Fig. 2. The equivalent of about three turns can be injected with steady efficiency while more turns are only injected and stored with lower efficiency. Expected was from theoretical investigations on the new injection scheme an accumulated efficiency of about 70 % for ten turns [1].

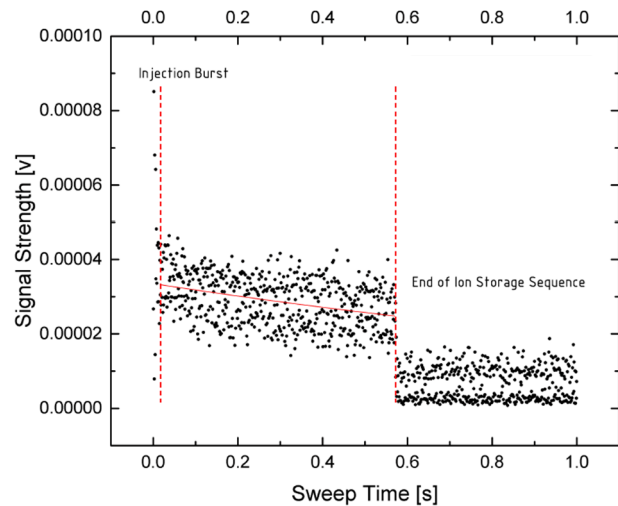


Figure 3: Storage time measurement using the Schottky noise signal. The moments in time when the ions are injected and dumped are marked with red dashed lines. The red line is an exponential fit to the data points that yields a storage time constant of 1.9(2) s.

Finally, stored beam has been achieved and the storage time constant has been measured (Fig. 3). For this the ion beam was injected, the Schottky noise signal recorded, and then the beam was dumped after about 0.7 s. The fit of an exponential to the data points yielded a storage time constant of 1.9(2) s. This storage time is dominated by the dissociation cross section of the hydrogen molecule over the scattering cross section with residual gas particles. The integrated residual pressure during the commissioning run was  $8 \cdot 10^{-11}$  mbar, which was measured with a number of extractor type vacuum pressure gauges.

Content from this work may be used under the terms of the CC BY 3.0 licence (© 2017). Any distribution of this work must maintain attribution to the author(s), title of the work, publisher, and DOI.

## SUMMARY AND FUTURE STEPS

Stored beam has been achieved, a major milestone on the way to the scientific applications with heavy, highly charged ions stored at low energy. The next steps are the commissioning of the electron cooler, the installation of first detectors and the installation and commissioning of the SPARC prototype gas jet target.

Eight experiment proposals have been evaluated positively by the GSI/FAIR general program advisory committee (GPAC) for the FAIR Phase Zero physics program. Those will be scheduled for the upcoming beam time period in 2018 and 2019.

## ACKNOWLEDGEMENT

We would like to thank for the tireless support this project received from the expert groups at GSI. Also worth mentioning is the interest of the scientific community, foremost the SPARC collaboration that is the driving factor behind this installation. Last but not least the help by our Swedish colleagues who used to run this ring in Stockholm should be gratefully acknowledged.

## REFERENCES

- [1] H. Danared *et al.*, “LSR - Low-energy Storage Ring”, Technical design report, Tech. Report version 1.3, Manne-Siegbahn Laboratory, Stockholm University, 2011.
- [2] B. Franzke, “The heavy ion storage and cooler ring project ESR at GSI”, B 24 (1987), 18–25.
- [3] M. Steck *et al.*, “Improved performance of the heavy ion storage ring ESR”, in *Proceedings of EPAC2004*, European Physical Society Accelerator Group (EPS-AG), 2004, ISBN 92-9083-231-2 (Web version), ISBN 92-9083-232-0 (CDROM), p. 1168.
- [4] M. Lestinsky *et al.*, “CRYRING@ESR: A study group report”, Project study, GSI Darmstadt.  
<https://www.gsi.de/fileadmin/SPARC/documents/Cryring/ReportCryring40ESR.PDF>, 2012.
- [5] F. Herfurth *et al.*, “The low energy storage ring CRYRING@ESR”, in *Proceedings of COOL'13*, Muerren, Switzerland, paper THPM1HA01, ISBN 978-3-95450-140-3.
- [6] W. Geithner *et al.*, “Status and outlook of the CRYRING@ESR project”, *Hyperfine Interact* (2017) 238: 13. <https://doi.org/10.1007/s10751-016-1383-5>
- [7] S. Litvinov *et al.*, “First Experimental Demonstration of the Extraction of Low Energy Beams from the ESR to the CRYRING@ESR”, in *Proceedings of the 25th Russian Particle Accelerator Conf. (RuPAC'16)*, St. Petersburg, Russia, pp.351-353, <https://doi.org/10.18429/JACoW-RuPAC2016-WEPSB002>

# NICA PROJECT: THREE STAGES AND THREE COOLERS

I. N. Meshkov<sup>†1,2</sup>, G.V. Trubnikov<sup>1,2</sup>

<sup>1</sup>Joint Institute for Nuclear Research, Dubna, Russia

<sup>2</sup>Sankt-Petersburg State University, Sankt-Petersburg, Russia

## Abstract

The Nuclotron-based Ion Collider Facility (NICA) project is being developed at JINR in three stages. The 1st stage, is a fixed target experiment with ions accelerated in the linac and tandem of two superconducting (SC) synchrotrons providing for ions  $^{197}\text{Au}^{79+}$  maximum kinetic energy of 4.5 GeV/u ( $\sqrt{s_{NN}} = 3.45$  GeV/u). The 2nd stage extends  $\sqrt{s_{NN}}$  to 11 GeV/u in colliding beams' mode. Both stages have a goal of experimental study of both hot and dense baryonic matter to search for so-called Mixed Phase formation in collisions of heavy relativistic ions and search for “new physics”. The third stage is spin physics studies in collisions of polarized protons ( $\sqrt{s_{NN}} = 27$  GeV) and deuterons. The report focuses on beam dynamics in the NICA and the cooling methods application.

## INTRODUCTION: THE NICA PROJECT AT JINR

The NICA project aims to design, construction and commissioning at the Joint Institute for Nuclear Research (Dubna, Russia) a modern accelerator complex Nuclotron-based Ion Collider Facility (NICA) equipped with two detectors: the MultiPurpose Detector (MPD) and the Spin Physics Detector (SPD). Experimental studies planned at NICA will be dedicated to search of the mixed phase of baryonic matter and the nature of nucleon/particle spin. The project development has three stages:

**Stage I:** the fixed target experiment on heavy ions generated in the ion source and accelerated in the chain Heavy-Ion Linac (HILAc) – Booster synchrotron – Nuclotron.

**Stage II:** development of the same accelerator chain and transfer of the accelerated ions to the Collider rings and performance of the experiments on the ion beams in collider mode.

**Stage III:** generation and acceleration of polarized protons and deuterons and performance of the experiments on the colliding beams of the polarized particles.

A study of hot and dense baryonic matter should shed light on in-medium properties of hadrons and the nuclear matter equation of state; onset of deconfinement and/or chiral symmetry restoration; phase transition, mixed phase and the critical end-point; and possible local parity violation in strong interactions [1]. It has been indicated in series of theoretical works, in particular, in [2], that heavy-ion collisions at the nucleon-nucleon center-of-mass energy  $\sqrt{s_{NN}} \sim 10$  GeV allow one to reach the highest possible net baryon density.

The NICA project is under development as a flagship JINR project [3] in high-energy physics. Its main goal is

construction of a collider facility providing ion collisions in collider mode at the energy range of  $\sqrt{s_{NN}} = 4 - 11$  GeV for  $\text{Au}^{79+}$  with luminosities up to  $L = 10^{27} \text{ cm}^{-2} \text{ s}^{-1}$ . NICA will also provide the polarized proton and deuteron beams up to  $\sqrt{s_{NN}} = 27$  GeV for pp collisions with luminosity up to  $L = 10^{32} \text{ cm}^{-2} \cdot \text{s}^{-1}$ . The high intensity and high polarization ( $> 50\%$ ) of the colliding beams will present a unique possibility for spin physics research, which is of crucial importance for the solution of the nucleon spin problem (“spin puzzle”) - one of the main tasks of the modern hadron physics.

## NICA – STAGE I

The program “The Baryonic Matter at Nuclotron” (BM@N) is complementary to that one of the Stage II. It is presently under active development and uses presently for testing experiment the existing Nuclotron facility. The last one currently consists of the “Old injector”, new Heavy Ion Linac (HILAc) and the Nuclotron. The “Old injector” contains a set of light ion sources including a source of polarized protons and deuterons and an Alvarez-type linac LU-20 (Fig. 1, pos. 1). In this year the old fore-injector of LU-20 – electrostatic generator of 625 kV voltage has been replaced by new RFQ fore-injector that provides output energy of 156 keV for all ions. The LU-20 is capable to accelerate protons at the second harmonics only. Therefore the output proton energy, as well as other ions at  $A/Z = 2$ , is of 5 MeV.

The “New injector” (pos. 2) contains the ESIS-type ion source, which provides  $^{197}\text{Au}^{32+}$  ions of intensity of  $2 \cdot 10^9$  ions per pulse of about  $7 \mu\text{s}$  duration at a repetition rate of 10 Hz, and the heavy ion linear accelerator (HILAc), consisting of RFQ and RFQ Drift Tube Linac sections. The HILAc accelerates the ions at  $A/Z \leq 8$  up to the energy of 3 MeV/u, at efficiency no less than 80% ( $A, Z$  are ion mass and charge numbers). It was fabricated by the BEVATECH Company (Germany) in 2014 - 2015 and has been commissioned at JINR in 2016.

The Stage I will be commissioned for experiments after construction of the Booster-synchrotron (pos. 4), transfer channels from HILAC to the Booster and from Booster to existing Nuclotron, and the BM@N detector.

### The NICA Booster

The ring of the SC Booster-synchrotron of the circumference of 215 m is housed inside the Synchrotron yoke (pos. 3). Its SC magnetic system provides a maximum magnetic rigidity of 25 Tm that allows us to accelerate ions  $^{197}\text{Au}^{31+}$  to the energy of 578 MeV/u. It is sufficient for stripping these ions up to state of bare nuclei. Then, after transfer to Nuclotron (see below) the nuclei can be accelerated up to maximum project energy of 4.5 GeV/u. This

<sup>†</sup> meshkov@jinr.ru

is the main reason for the Booster construction. Another reason is rather evident. A good vacuum, as high as 10 pTorr achievable in the Booster, allows one to reduce fast ion losses in collisions with residual gas atoms at low energy injection. In Nuclotron regular vacuum pressure is about 0.3 nTorr that leads to fast losses of injected ions.

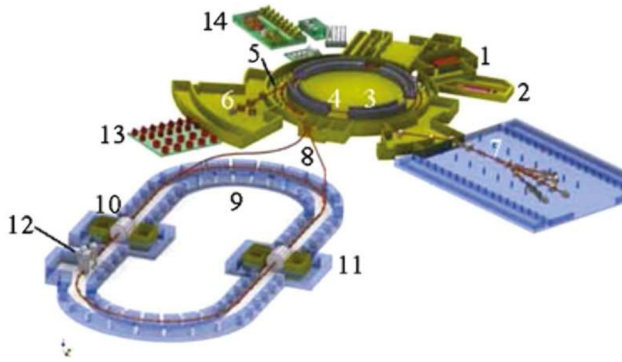


Figure 1: Scheme of the NICA facility. The description is given in the text.

The Booster SC magnets and other elements are being manufactured and passing through a “cold test” when necessary (Table 1).

Table 1: Booster SC Magnets’ Fabrication and Test

Magnet	Total number	Plan/Tested 12.09.2017
Dipole	40	28/25
Quad	48	20/26

The beginning of the machine commissioning is planned at the turn of 2018.

**Electron Cooler for the Booster** Electron cooling system (E-cooler) for the Booster is constructed by Budker INP [4] and is under commissioning presently at JINR/NICA (Fig. 2).



Figure 2: The BINP team with its leader V. Parkhomchuk (is taking photo) at E-cooler mounted at the Booster (May 2017).

The E-cooler will “compress” 6D emittance of the ion beam in the energy range from the injection energy up to 100MeV/u. The first regime of the lowest energy will be

used for multiturn and/or multicycle injection of the ion beam from HILAc. The highest cooling energy allows us preparing low emittance ion beam for injection into Nuclotron and have the emittance low at acceleration. It gives, particularly, some advantage at the beam slow extraction from Nuclotron (see below).

### **Ion Stripping and Beam Transfer Line to Nuclotron**

The ions are stripped at crossing a copper foil placed in the ion beam transfer line from the Booster to the Nuclotron. The stripping efficiency at the maximum Booster energy is no less than 80%. The Ion Beam Transfer Line (BTL), including ion stripping station, is under final design and fabrication at BINP. It is scheduled for commissioning in February 2019.

### *Nuclotron in the NICA Project*

The Nuclotron itself is a SC proton synchrotron (Fig.1, pos. 5) that has a maximum magnetic rigidity of 45 Tm and a circumference of 251.52 m. It can provide acceleration of completely stripped  $^{197}\text{Au}^{79+}$  ions up to a kinetic energy in the range of 1 – 4.5 GeV/u, and of protons up to a maximum kinetic energy of 12.6 GeV. It is used presently for fixed target experiments with extracted beams and experiments with an internal target. The experiments’ program includes experimental studies on relativistic nuclear physics, spin physics in few-body nuclear systems (with polarized deuterons), and physics of flavours.

**The Applied Research on Nuclotron Beams** is carried out presently in radiobiology and other subjects. Besides, the Nuclotron is used for testing the collider equipment and operational regimes of the elements and prototypes of the MPD at extracted beams ( $^{12}\text{C}^{6+}$  ions at 3.5 GeV/u and deuterons at 4 GeV/u). With the Booster commissioned the program of applied research at NICA will be enlarged significantly.

Both the applied researches and BM@N experiment require an efficient slow extraction of the particles accelerated in Nuclotron.

**Slow Resonant Extraction** from Nuclotron is accomplished using classical scheme of excitation of nonlinear resonance  $(Q_x)_{res} = n + 1/3$ . For Nuclotron  $n = 7$ ,  $Q_y = 7.4$ . The flux of extracted particles  $J(t)$  is determined by speed of variation of the betatron tune shift  $\delta(t)$ :

$$\delta(t) = Q_x - (Q_x)_{res}, \quad J(t) = \frac{dN}{d\delta} \cdot \frac{d\delta}{dt}. \quad (1)$$

Usually for experiment, the stretching in time of a slow extraction is preferably to be as long, as possible (Fig. 3).

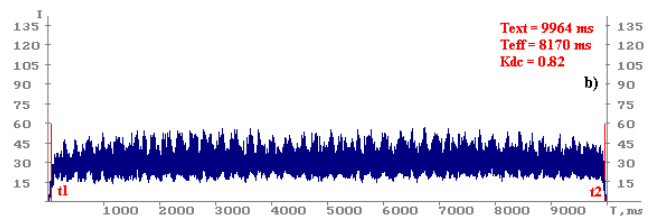


Figure 3: The spill of deuteron ions extracted from the Nuclotron; duration about 10 s.

Content from this work may be used under the terms of the CC BY 3.0 licence (© 2017). Any distribution of this work must maintain attribution to the author(s), title of the work, publisher, and DOI.

Another “desire” of experimenters is constant value of the extracted particle flux. A gain in this characteristic can be achieved at application of electron cooling in the Booster. It reduces the ion beam emittance that leads finally to a smaller emittance of the beam after its acceleration in Nuclotron. The numerical simulation of particle dynamics at slow resonant extraction (based on Ref. [5]) shows the increase of extraction time at constant flux of extracted particles when beam emittance is reduced. Besides the tune dependence on time  $\delta(t)$  is described with a definite function obtained by numerical simulation (Fig. 4). Details of these simulations will be published later.

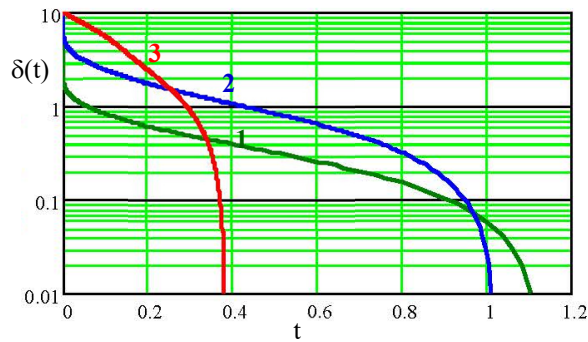


Figure 4: Dependence of  $\delta(t)$  on time at constant particle flux  $J(\delta)$  (arb. units) at slow resonant extraction of Gaussian beam of different values of the beam transverse ( $\sigma_x$ ) and longitudinal ( $\sigma_p$ ) emittances:

$$\sigma_x = \sigma_p = 0.1 \text{ (1), } 0.3 \text{ (2), } 1.0 \text{ (3) (arb. units).}$$

Thus, electron cooling gives us an additional control of parameters of an extracted ion flux.

### BM@N Detector

Presently the BM@N Detector is stage of fabrication and mounting its elements - subdetectors (Fig. 5), and testing them on ion beam from the Nuclotron.

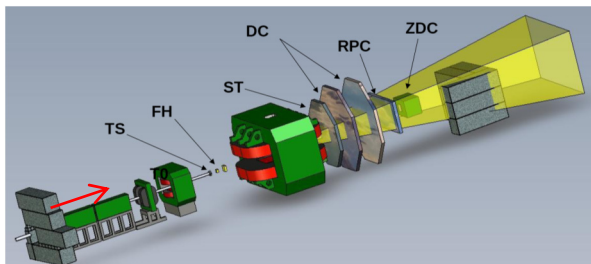


Figure 5: Scheme of the BM@N detector: TS – Target Station, FH – Forward Hodoscopes, ST – Straw tube Tracker, DC – Drift Chambers, RPC – Resistive Plate Chamber, ZDC – Zero Degree Calorimeter; arrow indicates the direction of the primary ion beam.

Full scale of BM@N experiment is scheduled for 2019. To be accomplished in time it demands construction and commissioning the Booster, BTL from the Booster to the Nuclotron and upgrading BTL from Nuclotron to BM@N experiment.

## NICA – STAGE II

Stage II of the NICA project includes the construction of the Collider, the BTL from the Nuclotron to the Collider, and the MultiPurpose Detector (MPD).

**The BTL from Nuclotron to the Collider Rings** after preliminary design by NICA group was, for ordered to SigmaPhi Co (France) for its final (working) design, fabrication and commissioning, with the request of the work completion at the 2019 end.

### The NICA Collider

NICA Collider consists of two SC rings (Fig. 1, pos. 9) of the racetrack shape have maximum magnetic rigidity of 45 Tm and a circumference of 503 m. The maximum rigidity of SC dipole magnets is of 1.8 T. The final design of the Collider is close to the completion and allows us to obtain its major parameters (Table 2).

Table 2: NICA Collider Major Parameters

Parameter	Value
Circumference, m	503.04
Heavy ions	
Energy range for Au <sup>79+</sup> , $\sqrt{s_{NN}}$ , GeV	4 - 11
Min. beta-function in IP, m	0.35
Max. luminosity, cm <sup>-2</sup> ·s <sup>-1</sup>	1·10 <sup>27</sup>
Polarized particles	
Max. proton energy, $\sqrt{s_{NN}}$ , GeV	27.0
Max. luminosity, cm <sup>-2</sup> ·s <sup>-1</sup>	1·10 <sup>32</sup>

**Collider Magnets** The first preserial prototype of the Collider “twin” dipole magnets (Fig. 6) was constructed and passed the “cold” test, where it has shown quality in accordance with the specification. Beginning of the magnet mass production is scheduled for the 2017 end.



Figure 6: Serial dipole magnet and quadrupole lens doublet for Booster and preserial “twin” dipole magnet for Collider Full energy range two parts of energy range.

**Collider RF System** consists of three different devices. RF-1 provides the “barrier” voltage for storage in the collider rings of the injected ions. The RF-2 and RF-3 providing the harmonic voltage of the 22<sup>nd</sup> and 66<sup>th</sup> harmonics of

the ion revolution frequency correspondingly are used for the formation of the bunched ion beams consisting of 22 bunches. The bunch number of 22 per ring is limited by the requirement of avoiding parasitic collisions in common parts of both rings in the large straight sections. Project length of a bunch in colliding beams is of 0.6 m (one sigma).

A possibility of slow acceleration/ deceleration of the ions stored in the Collider is foreseen. It may be necessary if the regime of ion storage will be optimized at certain fixed ion energy. Then ion energy change will be implemented with RF-1 system that has variable frequency.

**Collider Luminosity** For project luminosity achievement, the electron and stochastic cooling systems are constructed. Full energy range of Collider operation is divided in two parts of ion kinetic energy – so called “Space Charge Dominated Mode” (SCDM), for 1 to 3 GeV/u, and “IBS Dominated Mode” (IBS DM), from 3 to 4.5 GeV/u. To maintain Collider luminosity at project level the both electron and stochastic cooling methods are planned to be used. At SCD regime the electron cooling will be used alone, whereas at IBS DR both methods are applicable. Details of these regimes can be found in [6, 7].

**Electron Cooling for the Collider (ECC)** The electron cooler with the electron kinetic energy of 0.5–2.5 MeV will be placed in a special building at the Northern straight section of the Collider (Fig.1, pos. 12). Its design, construction, mounting on Collider and commissioning, including using in c the regime of the colliding ion beams, is entrusted to BINP team [8].

**Stochastic Cooling at the Collider** The development of the stochastic cooling system for the Collider is in stage of design and construction at JINR. This work is performed in close collaboration with the Forschungszentrum Juelich.

During 2011 – 2013, the first working version of the stochastic cooling system was designed, constructed, and tested at the Nuclotron at an ion kinetic energy of 3.5 GeV/u with deuteron and carbon ( $^{12}\text{C}^{+6}$ ) ion beams.

### The MPD

The MPD [6, 7] is located in the “North” straight section of NICA Collider (Fig. 1, pos.10). It is based on the superconducting solenoid (Fig. 7), with a magnetic field of 0.66T (6.623m in diameter and 9.010m in length). The major sub-detectors of the MPD are the time projection chamber (TPC), the inner tracker (IT), the time-of-flight (TOF) system, the electromagnetic calorimeter (ECal), the end cap tracker (ECT), and two forward spectrometers based on toroidal magnets (optional). Fast Forward Detector (FFD) and Fast Hadron Calorimeter (FHC). Two last ones will be used for tuning of the Collider luminosity. The MPD is under final design presently; prototypes of the sub-detectors are under construction and testing.

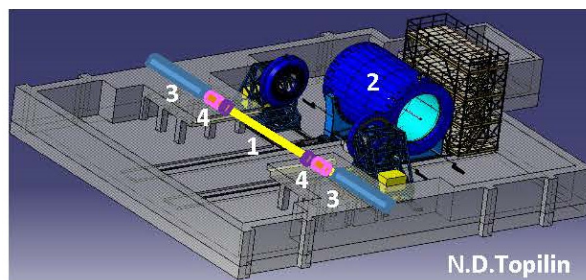


Figure 7: The MPD before final assembling: 1 - beam pipe, 2 – solenoid, 3 - final focus lenses, 4 - FFD and FHC for Collider luminosity tuning.

## NICA – STAGE III

The implementation of the Stage III of the NICA facility requires two significant developments.

1. Adopting of the NICA accelerator facility to acceleration in Nuclotron and Collider of polarized particles, protons and deuterons. It demands renewal the lattice of the collider inserting in both machines spin rotators allowing to provide a stable spin dynamics and control of the spin direction in the Collider.

Recently a group of expert from BINP joined the NICA team for fulfilment of these tasks.

2. Design and construction of Spin Physics Detector (SPD). The SPD is located in “Southern” straight section of the racetrack rings (Fig. 1, pos. 11). It is under conceptual design since 2012. To intensify the design process a new group of experts has been formed August 17, 2017 at the seminar at BVLHEP JINR with intention to spread it to international collaboration.

## CIVIL CONSTRUCTION AND INFRASTRUCTURE

The main civil construction works at NICA complex are carried out for building of the tunnels BTL NC and Collider and “rooms” for MPD, SPD and ECC. Strabag Co (Germany/Austria) and subcontractors from Russia started these works in November 2015. The Company execute the works in accordance with schedule. The mounting of the collider elements, transfer channel and MPD parts is planned to be started at the middle of 2019 when the corresponding parts of the collider building will be ready.

Cryogenics and the auxiliary equipment supply facility (Fig.1, pos. 13, 14) to provide LHe, LN2, electric power and cooling water for the accelerator complex and detectors is under construction.

## BASIC AND FINAL CONFIGURATIONS OF THE NICA STAGE II

The very important and difficult task of the NICA project development is to begin its commissioning in 2020. It is planned to be done in a reduced version of the facility and element parameters. Nevertheless, this will allow us to start experiments in the colliding beams’ mode, with the test and tuning of the MPD detector and the majority of the accelerators’ elements.

The basic configuration of the NICA assumes the following:

1. An increased length of colliding beams' bunches equal to  $\text{bunch} = 0.6 \text{ m}$  has been chosen to provide the "concentration" of the luminosity at the inner tracker area of the MPD.
2. The maximum ion number per bunch is limited by the value of the betatron tune shift  $Q \leq 0.05$ .
3. The maximum emittance of the colliding bunches is less than  $1.1 \pi\text{-mm}\cdot\text{mrad}$ ; the ratio of the horizontal emittance to the vertical one and the momentum spread of the ions is defined by the equilibrium state of the bunches in the presence of the intrabeam scattering (IBS).
4. The square of the separatrix for the RF-2 is 25 times larger than the longitudinal r.m.s. emittance of the bunch.
5. For suppression of the IBS, a stochastic cooling system of the Collider (SCSC) for each ring will be constructed in a reduced version: for longitudinal degree of freedom only (the "filter method").

As a result, the maximum peak luminosity can be provided at the level of  $5 \cdot 10^{25} \text{ cm}^{-2}\text{s}^{-1}$  at the kinetic energy of the  $^{197}\text{Au}^{79+}$  ions in the range of 3–4.5 GeV/u.

**The Final Configuration** of the NICA requires the construction of the third RF system of the 66th harmonics of the revolution frequency and high RF amplitude (RF-3). It will squeeze 22 bunches kept in the separatrices of RF-2 to the length of 60 cm. At that, each third separatrix is filled with ions when the two others remain empty.

The construction of the ECC and the completion of the SCSC will be produced.

The full configuration of the MPD will be commissioned as well.

## SUMMARY

The main characteristics of the NICA project, its status, and the principle problems related to the NICA creation have been considered in this report.

The BM@N and MPD experiments are competitive and, at the same time, complementary to experiments carried out at RHIC [9] and those planned within the FAIR project [10].

The NICA project as a whole has passed the phase of design and is currently in the stage of manufacturing and construction of the elements of accelerators and MPD and BM@N detectors.

The project realization plan foresees a staged construction and commissioning of the accelerator facility and the detector MPD and SPD.

## ACKNOWLEDGEMENT

Authors express the gratitude to the colleagues of the NICA accelerator team – A. Butenko, G. Khodzhibagiyev, T. Katayama, S. Kostromin, O. Kozlov, A. Sidorin, A. Smirnov, R. Stassen, E. Syresin, A. Philippov, and A. Tuzikov - for longstanding intense common work on the NICA project and (I. M.) to E. Levichev (BINP) for fruitful advises on nonlinear particle dynamics in cyclic accelerators.

## REFERENCES

- [1] <http://theor.jinr.ru/twiki-cgi/view/NICA/WebHome>
- [2] J. Cleymans and J. Randrup, *Phys. Rev. C* 74, 047901 (2006).
- [3] I. Meshkov, *Phys. At. Nucl.* 75, 594 (2012).
- [4] A. V. Bublei *et al.*, "Low Energy Electron Cooler for the NICA Booster", presented at COOL'17, Bonn, Germany, paper TUM11, this conference.
- [5] E. B. Levichev, "Lectures on Particle Nonlinear Dynamics in Cyclic Accelerators", Novosibirsk State Technical University (2009) (in Russian).
- [6] V. D. Kekelidze, R. Lednicky, V. A. Matveev, I. N. Meshkov, A. S. Sorin, and G. V. Trubnikov, *Eur. Phys. J. A* 52, 211 (2016).
- [7] V. D. Kekelidze, V. A. Matveev, I. N. Meshkov, A.S. Sorin, and G. V. Trubnikov, PEPAN 48, 727 (2017).
- [8] V.B. Reva *et al.*, "The High Voltage cooler for NICA, Status and Ideas", presented at COOL'17, Bonn, Germany, paper TUM21, this conference.
- [9] G.S. Stephans, *J. Phys. G* 32, 447 (2006) nucl-ex/0607030.
- [10] P. Senger, *J. Phys. G* 30, 1087 (2004).

# THE HESR STOCHASTIC COOLING SYSTEM, DESIGN, CONSTRUCTION AND TEST EXPERIMENTS IN COSY

R. Stassen\*, B. Breitschütz, N. Shurkhno, H. Stockhorst  
Forschungszentrum Jülich, 52425 Jülich, Germany  
L. Thorndahl, CERN, 1211 Geneva 23, Switzerland

## Abstract

The construction phase of the stochastic cooling tanks for the HESR has started. Meanwhile two pickups (PU) and one kicker (KI) are fabricated. One PU and one KI are installed into the COSY ring for testing the new stochastic cooling system with real beam at various momenta. Small test-structures were already successfully operated at the Nuclotron in Dubna for longitudinal filter cooling, but not for transverse cooling and as small PU in COSY. During the last COSY beam-time in 2017 additional transverse and ToF cooling were achieved. The first two series high power amplifiers were used for cooling and to test the temperature behaviour of the combinerboards at the KI. The system layout includes all components as planned for the HESR like low noise amplifier, switchable delay-lines and optical notch-filter. The HESR needs fast transmission-lines between PU and KI. Beside air-filled coax-lines, optical hollow fiber-lines are very attractive. First results with such a fiber used for the transverse signal path will be presented.

## STOCHASTIC COOLING SYSTEM OF HESR

Stochastic cooling at HESR is not only used to reduce beam size and momentum spread during the experiment, but also to accumulate antiprotons due to the postponed Recuperated Experimental Storage Ring (RESR) [1, 2] of the modularized start version of the FAIR project.

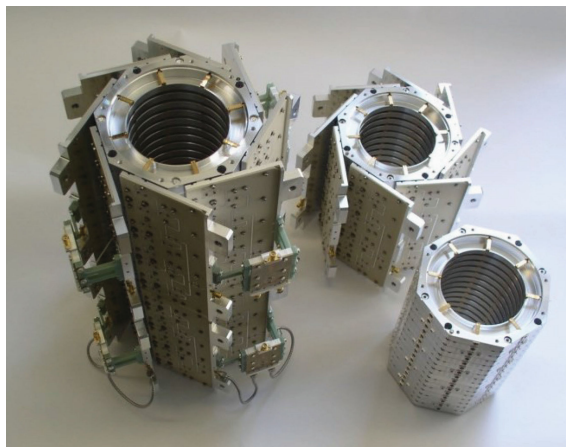


Figure 1: Stacks of slot ring couplers with and without 16:1 combiner-boards and two stacks mounted together including 2:1 combiner with heat-trap.

The system is based on dedicated structures. Each beam-surrounding slot of these so called slot-ring couplers covers the whole image current without a reduction of the HESR aperture [3]. Each resonant ring structure is heavily loaded with eight  $50\ \Omega$  electrodes for a broadband operation. The rings are screwed together to a selfsupporting structure in stacks of 16 rings. Four of these stacks will build the spindle for one tank. Figure 1 shows these stacks; one without combiner one with combinerboard and a combination of two stacks including additional 2:1 combiner especially designed to minimize the heat flow to the 16:1 combiners. Meanwhile a new structure has been designed for a special cooling system operating in the frequency range 350 – 700 MHz [4].

Beside the main 2 – 4 GHz system a 4 – 6 GHz system was planned for additional longitudinal cooling. This system will be substituted by an additional 2 – 4 GHz system with modified combiner-boards to cool heavy ions at lower energies [5].

The first HESR series pickup was installed into COSY during the winter-shutdown 2015/2016 and is used to measure routinely Schottky spectra for several experiments. Two cryo-pumps are installed to cool down the pickup and increase the signal to noise ratio. The inner structure of the pickup was cooled down to less than 20 K within 10 h and although the tank is not bakeable, the vacuum reached already  $5 \cdot 10^{-10}$  mbar. During the summer shutdown 2016 the first HESR kicker tank was installed in COSY at the position of the old vertical kicker.

First commissioning started in February 2017 after installing the new notch-filter, measurement system and prototype of the GaN power amplifiers.

The automated frequency adjustment of the notch-filter was successfully tested and takes less than a minute for frequency and gain - whereas with the old system the typical setup time was in the order of one hour. The program determines also the frequency error for each notch with respect to the fundamental frequency. The fluctuations of the Notch-frequency were within  $\pm 10$  Hz taking into account the harmonic number. This is pretty small and does not influence the cooling time and power, but can still increase the equilibrium momentum spread due to the small  $\eta$ -value in the HESR. These fluctuations are dominated by the transimpedance amplifiers in the optical receivers and can be further reduced by pairing the receivers.

The algorithms for automatic open-loop measurements and system delay adjustment were also successfully tested and refined. The open-loop measurements now can be carried out for the full bandwidth within single sweep or by

\* r.stassen@fz-juelich.de

Content from this work may be used under the terms of the CC BY 3.0 licence (© 2017). Any distribution of this work must maintain attribution to the author(s), title of the work, publisher, and DOI.

separate measurements of each harmonic. The latter had a problem of random phase jumps near  $\pm 180^\circ$ , which made it impossible to calculate phase in the center of the harmonic. The problem was solved with the fairly simple trick: for each harmonic the algorithm iteratively finds (by minimizing the standard deviation) the artificial delay that would shift the phase to zero, then it calculates the phase and restores the phase to its original value [6].

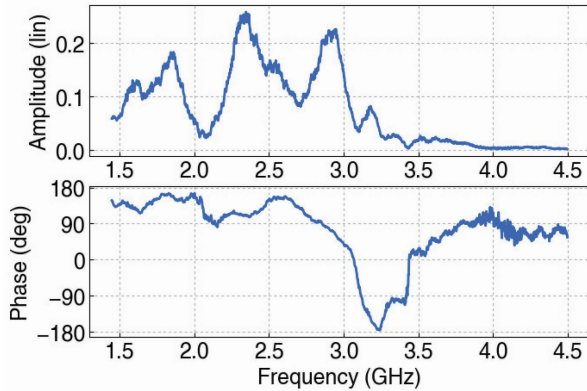


Figure 2: Amplitude (top) and phase (bottom) of system's hardware transfer function.

A lot of open-loop measurements were performed during first commissioning. The relative hardware transfer function from PU to K - derived from these open-loop measurements - is plotted in Fig. 2. Regions with high amplitude and good phase behaviour alternate with good phase and smaller gain and above 3 GHz with strong phase change and very low amplitude. The reason for this strange behaviour was found in a wrong orientation of the kicker with respect to the beam direction. Simulations of a rotated structure with CST Microwave Studio [7] have shown a similar behaviour.

Nevertheless first longitudinal cooling has been carried out using the ToF [8] cooling method and filter cooling (Fig. 3). The beam was initial heated and the particle numbers was about  $N = 1 \cdot 10^9$ . Figure 3 shows one longitudinal Schottky spectrum at about 3 GHz (blue: before cooling, green: after several minutes of cooling).

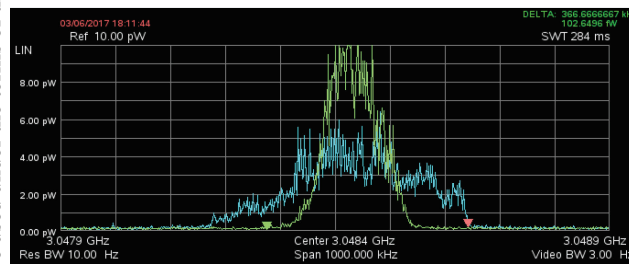


Figure 3: Longitudinal cooling with Filter method, blue: initial heated beam before cooling, green: after cooling.

The  $180^\circ$  phase shift between ToF and filter cooling was realized by adding a delay of 130 ps instead of an additional  $180^\circ$  phase shifter. Due to the small amplitude above 3 GHz the cooling works like a system with reduced bandwidth. Cooling simulations show similar cooling times when the

measured hardware transfer function is included into the simulations. The kicker tank has a symmetric layout and was easily rotated in the next shutdown. Figure 4 shows an open-loop measurement of the rotated tank. The plot shows the results for one group (group D) separated for both directions in sum-mode. Old Schottky measurements of the pickup tank have already shown that the maximum sensitivity is not at 3 GHz - as simulated with HFSS [9] - but at 2 GHz. Nevertheless the sensitivity in the whole frequency range is high enough for good cooling results. The constant decrease in the desired frequency range can be compensated by simple filter in a later stage.

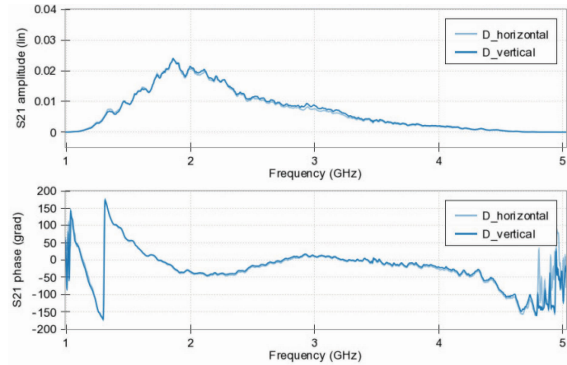


Figure 4: Open loop measurement with rotated kicker.

During the last beam-time in August 2017 a lot of different cooling experiments have been done with protons at a momentum of 2.425 GeV/c. The standard optic with zero dispersion in the straight sections was used. This gives an eta value of  $\eta = -0.07$ . This setting is comparable to the HESR working point taking into account the higher revolution frequency at COSY.

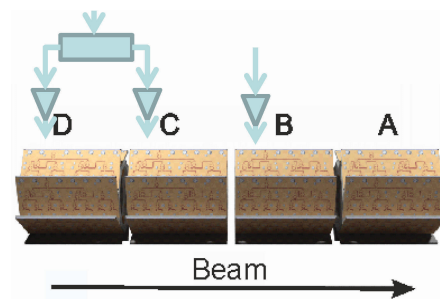


Figure 5: Kicker setup during last commissioning.

Two different signal paths were used. Group B with one high power amplifier was used for longitudinal cooling, while group D and C (each with one amplifier) combined with adjustable delay-lines were used to cool the beam in one transverse direction (Fig. 5).

## LONGITUDINAL COOLING WITH DIFFERENT PARTICLE NUMBERS

After reassembling the modified notch-filter and measurement system first open-loop measurements were carried out

using modified programs for a fast setup of notch frequency and system delay. Within several hours notch-frequency and system delay were adjusted using optical delay-lines. Even without phase-shifter to adjust the optimum phase, cooling was immediately visible after closing the loop. The momentum spread was reduced by a factor of 3 within about 2.3 min and  $7 \cdot 10^9$  particles (Fig. 6a) even without optimizing the gain. Figure 6b shows the longitudinal cooling of  $2 \cdot 10^8$  particles with the same setting of delay and gain. The cooling is only slightly faster than with  $7 \cdot 10^9$  particles, but the equilibrium is significantly smaller.

In both cases we can see instabilities in the cooled beam but without beam losses. The slight fast momentum change of some particles will be cooled again by the longitudinal cooling. It's the strongest stochastic cooling in COSY ever seen, although the system is not optimized. The use of one group with one amplifier limits the power and additional heating from Schottky noise outside the band was not reduced by additional filters.

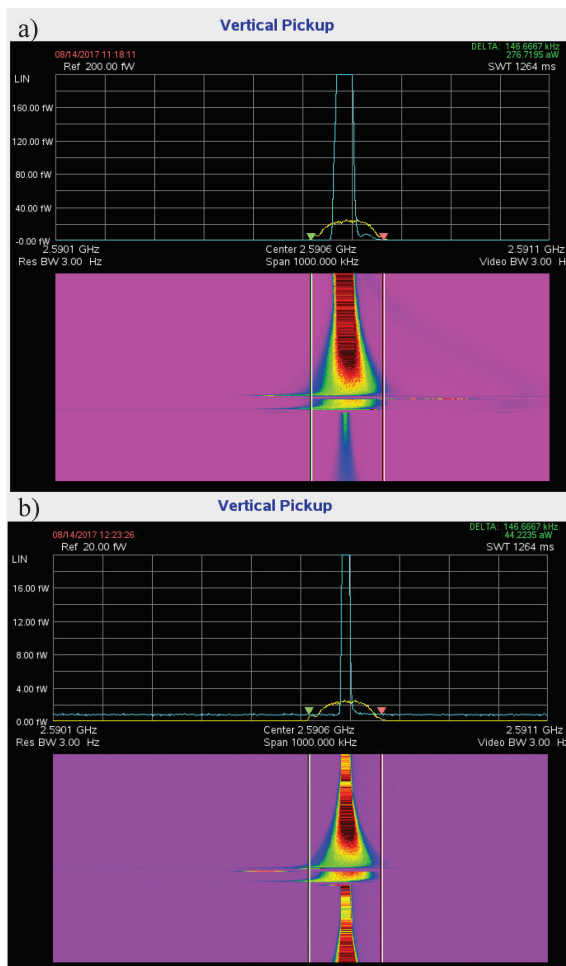


Figure 6: Longitudinal cooling of  $7 \cdot 10^9$  (a) and  $2 \cdot 10^8$  particles (b).

Even ToF [7] cooling was demonstrated after switching off the notch-filter and removing 150 ps delay to substitute the missing  $180^\circ$  phase shift.

## FIRST TRANSVERSE COOLING

Longitudinal cooling with this structure was already demonstrated 2013 at the Nuclotron in Dubna [10], but so far no transvers cooling. First transverse cooling was achieved by switching the hybrids of the first signal path from sum-mode to difference-mode.

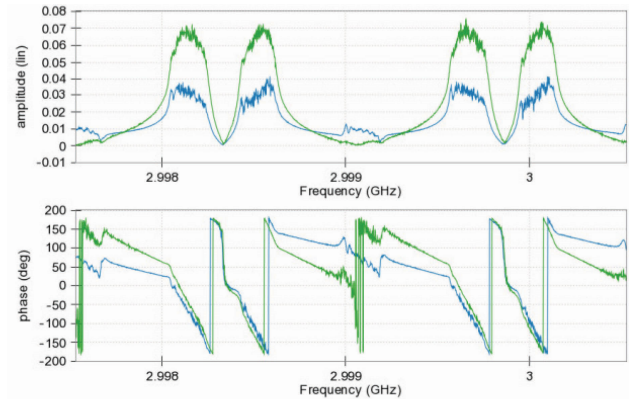


Figure 7: First transverse open loop measurement with and without notch-filter.

The sidebands are clearly visible in the open loop measurement (Fig. 7) with and without notch-filter. The notch-filter here helps to eliminate the unwanted longitudinal part – which is always there, even when the beam is centred – and reduce partly the Schottky noise. Only a few system delay corrections were needed to achieve horizontal cooling.

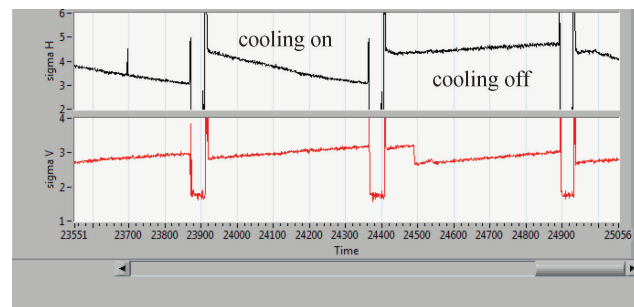


Figure 8: Profile measurements of horizontal cooled beam.

Profile measurements with the ion profile monitor (IPM [11]) verified the transverse cooling during the 5 minutes cycles (Fig. 8). Without cooling the beam is slightly heated by rest-gas scattering.

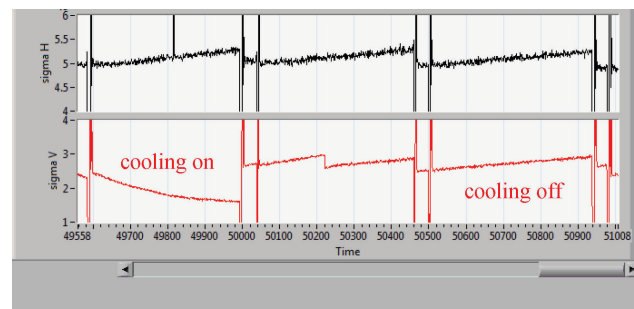


Figure 9: Profile measurement of vertical cooled beam.

Content from this work may be used under the terms of the CC BY 3.0 licence (© 2017). Any distribution of this work must maintain attribution to the author(s), title of the work, publisher, and DOI.

Figure 9 represents the other direction by switching manually from the horizontal into the vertical plane. A similar transverse cooling was measured without influence to the other plane.

## SECOND SIGNAL PATH WITH HOLLOW FIBER LINE

Optical fiber lines are very attractive to transmit broadband RF-signals over a wide distance. They are easy to install, have low attenuation and zero dispersion. But standard fibers have some disadvantages: The signal speed is only about 60% of speed of light and these lines have a high temperature-gradient. An alternative are hollow fiber lines, where the light is guided in a hollow core which is surrounded by a microstructured cladding [12]. 50 m of such a line was installed as transmission-line between pickup and kicker. The line acts very sensitive against movements, but once installed a stable operation was possible.

This second path was used for transverse cooling of the vertical plane. One original switchable delay-line – especially designed for the HESR including divider – was used to feed two amplifiers for two groups.

Single measurements of signal suppression at each of the two groups have shown that the delay difference between the groups is not optimized, but both groups show cooling.

Different gain settings were used to find the best cooling rate. Higher gains decreased the cooling rate (Fig. 10), but the equilibrium will be higher. Thus a gain control during cooling is useful and will be installed for the next beam time.

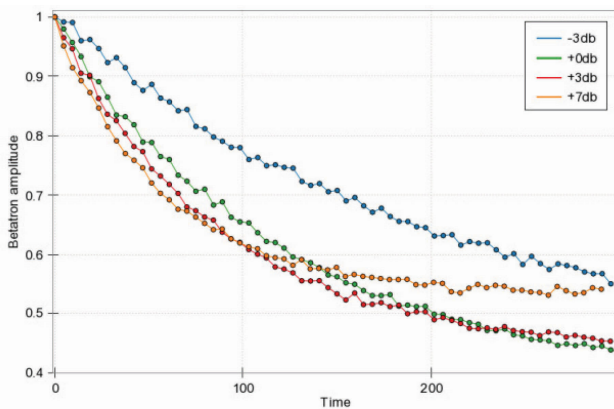


Figure 10: Vertical cooling with different gain settings.

With the second path it was possible to cool the beam in the longitudinal and vertical plane simultaneously. Figure 11 represents the difference signal of the vertical plane during cooling (blue curve: before cooling, yellow curve: after 5 min of cooling). The longitudinal parts demonstrate the longitudinal cooling with system one. Without transverse cooling the betatron sidebands would increase as well, but due to the vertical cooling with the second system the amplitudes decreased. Thus, first 2d cooling (longitudinal and vertical) was achieved although not all groups of the kicker were used.

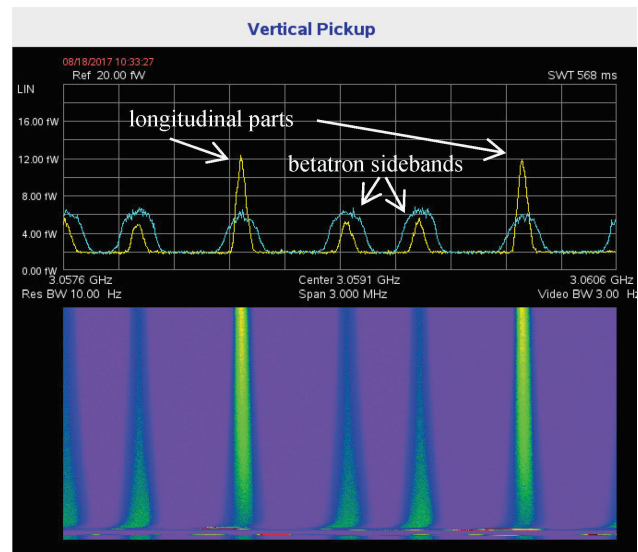


Figure 11: Difference signal of vertical plane.

Most of the power from the GaN amplifiers is dissipated in the Wilkinson resistors of the combiner-boards located inside the vacuum tank. Each combiner-board is connected to a fixed water-cooled pipe by thick copper ribbons. During the 2d cooling with three amplifiers the temperature at the combiner-boards rises only about 1-2°C. Thus the passive thermal cooling of the combinerboards is sufficient.

During the last hours of the beam-time a new measurement scheme was tested (see Fig. 12). The notch filter can be measured as well as an open loop measurement of the whole system. Most attractive is the possibility to perform measurements during cooling. Notch filter frequency and system delay can be checked without great influence of the cooling.

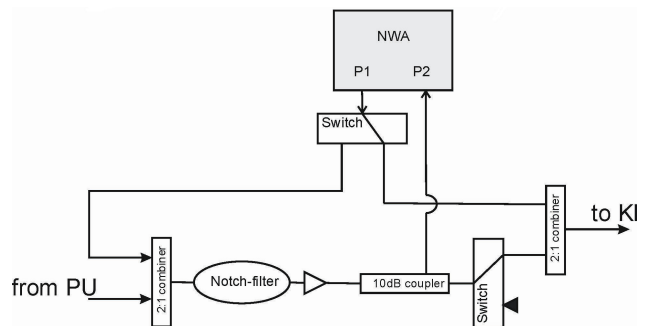


Figure 12: New measurement setup.

## SUMMARY

One pick-up and one kicker of the HESR stochastic cooling system can now be tested under real beam condition. Besides longitudinal cooling with filter and ToF method, transverse cooling in both directions has been achieved. A hollow fiber line as transmission line between pick-up and kicker was successfully used for the first time.

## OUTLOOK

The production of the high power amplifiers is ongoing with 2 amplifiers per month. We expect a full equipped kicker with eight amplifiers end of this year. First tests of a full 3d stochastic cooling with HESR pick-up and kicker can start beginning of 2018.

## REFERENCES

- [1] “FAIR - Facility for Antiproton and Ion Research”, Green Paper - The Modularized Start Version, October 2009; [http://www.faircenter.de/fileadmin/fair/publications\\_FAIR/FAIR\\_GreenPaper\\_2009.pdf](http://www.faircenter.de/fileadmin/fair/publications_FAIR/FAIR_GreenPaper_2009.pdf)
- [2] T. Katayama, T. Kikuchi, R. Maier, I. Meshkov, D. Prasuhn, R. Stassen, M. Steck, and H. Stockhorst, “Beam Accumulation with Barrier Voltage and Stochastic Cooling”, in *Proc. IPAC'10*, Kyoto, Japan, paper MOPD065, 2010.
- [3] R. Stassen *et al.*, “Recent Developments for the HESR Stochastic Cooling System”, in *Proc. COOL'07*, Bad Kreuznach, Germany, paper THAP13, 2007.
- [4] B. Breitmeyer, R. Greven, N. Shurkhno, R. Stassen, and H. Stockhorst, “Stochastic Cooling Hardware for Low Energy Deuterons at COSY”, in *Proc. IPAC'17*, Copenhagen, Denmark, doi: <https://doi.org/10.18429/JACoW-IPAC2017-TUPVA080>, 2017.
- [5] H. Stockhorst *et al.*, “Heavy ion storage and acceleration in the HESR with stochastic cooling and internal target”, in *Proc. STOR'14*, St. Goar, Germany, 2014.
- [6] N. Shurkhno and R. Stassen, “Algorithmic Control of Stochastic Cooling Systems”, presented at COOL'17, Bonn Germany, paper THA13, this conference.
- [7] CST Microwave Studio, 3D Electromagnetic Simulation Software, <https://www.cst.com/products/cstmws>
- [8] W. Kells, “Filterless Fast Momentum Cooling”, in *Proc. of the 11th Int. Conf. on High-Energy Accelerators*, Geneva, Switzerland, July 7-11, 1980, p. 777.
- [9] HFSS, High Frequency Structure Simulator, <http://www.ansys.com/products/electronics/ansys-hfss>
- [10] N. Shurkhno *et al.*, “Study for Stochastic Cooling at Nuclotron, JINR”, in *Proc. COOL'13*, Murren, Switzerland, paper TUPM1HA01, 2013.
- [11] V. Kamerzhiev *et al.*, “Beam Test of the FAIR IPM Prototype in COSY”, in *Proc. DIPAC'09*, Basel, Switzerland, paper TUPB12, 2009.
- [12] Hollow fiber lines, <http://www.nktpotonics.com/lasers-fibers/en/product/hollow-core-photonics-crystal-fibers/>



## List of Authors

**Bold** papercodes indicate primary authors; ~~crossed-out~~ papercodes indicate 'no submission'

### — A —

Alexander, I.	<b>TUP19</b>
Altinbas, Z.	<b>WEM22</b>
Andelkovic, Z.	<b>THM13</b>
Anderson, R.	<b>WEM22</b>
Aulenbacher, K.	<del>TUP07</del> , <b>TUP19</b> , <b>TUM23</b>

### — B —

Bai, M.	<b>THM13</b>
Bardonner, A.	<b>TUP16</b>
Bayes, R.	<b>MOA22</b>
Böhm, R.M.	<b>TUP16</b>
Beck, T.	<del>TUM12</del>
Beiser, Th.	<b>TUP07</b>
Belomestnykh, S.A.	<b>WEM22</b>
Benson, S.V.	<b>WEM12</b>
Biancacci, N.	<del>TUP10</del>
Birkel, G.	<del>TUM12</del>
Boine-Frankenheim, O.	<del>TUM12</del>
Boulware, C.H.	<b>WEM22</b>
Bradley, J.	<b>TUP04</b>
Bräuning-Demian, A.	<b>THM13</b>
Breitkreutz, B.	<b>TUP17</b> , <b>THA11</b>
Britten, V.A.	<b>TUP11</b>
Brown, K.A.	<b>WEM22</b>
Bruker, M.W.	<del>TUP07</del>
Brutus, J.C.B.	<b>WEM22</b>
Bryzgunov, M.I.	<b>TUM11</b> , <del>TUM13</del> , <b>TUM21</b> , <del>TUP19</del>
Bubley, A.V.	<b>TUM11</b> , <b>TUM21</b>
Buss, A.	<del>TUM12</del>
Bussmann, M.H.	<b>TUM12</b> , <del>TUP05</del>

### — C —

Caspers, F.	<b>TUP16</b>
Chekavinskiy, V.A.	<b>TUM11</b>
Chetvertkova, V.	<b>THM13</b>
Curcio, A.J.	<b>WEM22</b>

### — D —

Denisov, A.P.	<b>TUP09</b>
Derbenev, Y.S.	<b>WEM12</b>
Di Lieto, A.	<b>WEM22</b>
Dietrich, J.	<del>TUP19</del>
Dimopoulou, C.	<del>TUM12</del> , <b>TUP16</b> , <b>THM11</b>
Douglas, D.	<b>WEM12</b>
Drielsma, F.	<b>MOA13</b>
Droba, M.	<b>TUP11</b>
Du, Z.	<del>TUP18</del>

### — E —

Eidam, L.	<del>TUM12</del>
-----------	------------------

### — F —

Fedotov, A.V.	<b>WEM11</b>
Folz, C.	<b>WEM22</b>

### — G —

Gassner, D.M.	<b>WEM22</b>
Geithner, O.	<b>THM13</b>
Geithner, W.	<b>THM13</b>
Giacomini, T.	<del>TUM12</del>
Goncharov, A.D.	<b>TUM11</b> , <b>TUM21</b>
Gorchakov, K.	<b>TUM11</b>
Gorda, O.E.	<b>THM13</b>
Grimm, T.L.	<b>WEM22</b>
Gusev, I.A.	<b>TUM11</b>

### — H —

Hai, B.	<del>TUP05</del>
Halama, A.J.	<del>TUM13</del> , <b>TUM22</b>
Hannen, V.	<del>TUM12</del>
Hannon, F.E.	<b>WEM12</b>
Hayes, T.	<b>WEM22</b>
Henschel, J.	<b>THM22</b>
Herfurth, F.	<b>THM13</b>
Hess, R.	<b>THM11</b>
Hettrich, R.	<b>TUP16</b>
Hu, X.J.	<del>TUP18</del>
Huang, Z.	<del>TUP05</del> , <b>TUP08</b>
Hulsart, R.L.	<b>WEM22</b>
Hunt, J.R.	<del>TUP01</del> , <del>TUP02</del>
Hutton, A.	<b>TUP15</b> , <b>WEM12</b>

### — I —

Inacker, P.	<b>WEM22</b>
Ivanov, A.V.	<b>TUP13</b>

### — J —

Jamilkowski, J.P.	<b>WEM22</b>
Jing, L.	<del>TUP18</del>
Jing, Y.C.	<del>WEM21</del> , <b>WEM22</b>
Jørgensen, L.V.	<b>THM12</b>
Jordan, K.	<b>TUP15</b>

### — K —

Kamerdzhev, V.	<b>TUM13</b> , <b>TUM22</b>
Katayama, T.	<del>TUM13</del>
Kayran, D.	<b>WEM22</b>
Källberg, A.	<b>THM13</b>

Content from this work may be used under the terms of the CC BY 3.0 licence (© 2017). Any distribution of this work must maintain attribution to the author(s), title of the work, publisher, and DOI.

Kellermann, R. **WEM22**  
 Kiefer, D. **TUM12**  
 Klag, W. **TUP19**  
 Klammes, S. **TUM12**  
 Kozhuharov, C. **TUM12**  
 Kremnev, N.S. **TUM21**

— L —

Lambiase, R.F. **WEM22**  
 Latina, A. **TUP10**  
 Lestinsky, M. **THM13**  
 Li, J. **TUP05, TUP08, TUP09,**  
**TUP12, TUP13, TUP14,**  
**TUP15**  
 Li, R. **WEM12**  
 Li, X.N. **TUP05**  
 Litvinenko, V. **WEM21, WEM22**  
 Litvinov, S.A. **THM13**  
 Litvinov, Yu.A. **TUM12**  
 Lochmann, M. **TUM12**  
 Löser, M. **TUM12**  
 Lu, H.J. **TUP13**

— M —

Ma, J. **WEM21, WEM22**  
 Ma, X. **TUM12, TUP05, TUP09**  
 Ma, X.M. **TUP13, TUP14, TUP15**  
 Mahler, G.J. **WEM22**  
 Maletic, D. M. **MOA13**  
 Mao, L.J. **TUP05, TUP08, TUP09,**  
**TUP12, TUP13, TUP14,**  
**TUP15**  
 Mao, R.S. **TUP05**  
 Mapes, M. **WEM22**  
 Marusic, A. **WEM22**  
 Meng, W. **WEM22**  
 Mernick, K. **WEM22**  
 Meshkov, I.N. **THM21**  
 Meusel, O. **TUP11**  
 Michnoff, R.J. **WEM22**  
 Mihara, K. **WEM22**  
 Miller, T.A. **WEM22**  
 Minty, M.G. **WEM22**

— N —

Narayan, G. **WEM22**  
 Neuffer, D.V. **TUP04**  
 Nörtershäuser, W. **TUM12**  
 Nolden, F. **TUM12**  
 Nugent, J.C. **MOA22**

— O —

Orfin, P. **WEM22**

— P —

Panasyuk, V.M. **TUM11, TUM21**  
 Parkhomchuk, V.V. **TUM11, TUM13, TUM21,**  
**TUP09, TUP19**  
 Peschke, C. **TUP16**  
 Petrushina, I. **WEM22**  
 Phillips, D. **WEM22**  
 Pinayev, I. **WEM21, WEM22**  
 Podlech, H. **TUP11**  
 Polukhin, V.A. **TUM21**  
 Powers, T. **TUP15**  
 Putmakov, A.A. **TUM21, TUP09**

— R —

Rao, T. **WEM22**  
 Ravikumar, D. **WEM22**  
 Reich, J. **WEM22**  
 Resta-López, J. **TUP01, TUP02**  
 Reva, V.B. **TUM11, TUM13, TUM21,**  
**TUP09, TUP19**  
 Rimmer, R.A. **TUP15, WEM12**  
 Robert-Demolaize, G. **WEM22**  
 Roblin, Y. **WEM12**  
 Roser, T. **WEM22**

— S —

Samulyak, V. **WEM21**  
 Sanchez Alarcon, R.M. **TUM12**  
 Sanjari, M.S. **TUM12**  
 Schempp, A. **TUP11**  
 Schramm, U. **TUM12**  
 Schulte, K. **TUP11**  
 Seberg, S.K. **WEM22**  
 Senkov, D.V. **TUM11**  
 Severino, F. **WEM22**  
 Sheehy, B. **WEM22**  
 Shih, K. **WEM22**  
 Shurkhno, N. **TUP06, THA11, THA13**  
 Siebold, M. **TUM12**  
 Skaritka, J. **WEM22**  
 Skorobogatov, D.N. **TUP09**  
 Smart, L. **WEM22**  
 Smirnov, A.V. **TUM11**  
 Smith, K.S. **WEM22**  
 Snydstrup, L. **WEM22**  
 Soler, P. **MOA22**  
 Soria, V. **WEM22**  
 Spata, M. **TUP15**  
 Spiller, P.J. **TUM12**  
 Stassen, R. **TUP17, THA11, THA13**  
 Steck, M. **TUM12, THM11**  
 Stockhorst, H. **TUP17, THA11**  
 Stöhlker, T. **TUM12, THM13**  
 Stratakis, D. **TUP04**  
 Stuhl, A. **TUP16**

— T —

Tang, M.T.	TUP08, TUP12, TUP13, TUP14, TUP15
Tennant, C.	WEM12
Than, R.	WEM22
Theisen, C.	WEM22
Thorndahl, L.	THA11
Tichelmann, S.	TUM12
Trubnikov, G.V.	THM21
Tuozzolo, J.E.	WEM22

— U —

Uchida, M.A.	MOA12, MOA21
Ullmann, J.	TUM12

— V —

Veglia, B.	TUP01, TUP02
Vorobjev, G.	THM13

— W —

Walsh, J.	WEM22
Walther, T.	TUM12
Wang, E.	WEM22
Wang, G.	WEM21, WEM22
Wang, H.	TUP15, WEM12
Wang, H.B.	TUM12, TUP05
Wang, S.	TUP15
Wang, S. X.	TUP08
Wei, W.	TUP18
Weilbach, T.	TUP07
Weinrich, U.	THM13
Weiss, D.	WEM22
Welsch, C.P.	TUP01, TUP02
Wen, W.Q.	TUM12, TUP05

Wilhelm, P.	WEM13
Winters, D.F.A.	TUM12, TUP05
Winzen, D.	TUM12
Wu, J.X.	TUP05, TUP18, THA12
Wunderlich, S.	TUP16

— X —

Xia, J.W.	TUP18
Xiao, B. P.	WEM22
Xie, H.M.	TUP18
Xin, T.	WEM22
Xu, W.	WEM22

— Y —

Yan, T.L.	TUP13, TUP14
Yang, J.	TUM12
Yang, J.C.	TUP05, TUP08, TUP12, TUP15
Yang, X.D.	TUP08, TUP12, TUP13, TUP14, TUP15
Yuan, Y.J.	TUP05

— Z —

Zaltsman, A.	WEM22
Zhang, D.	TUP05
Zhang, H.	TUP15, WEM12
Zhang, Y.	TUP15, WEM12, THM14
Zhang, Y.	TUP18
Zhao, D.	TUP05
Zhao, H.	TUP08, TUP12, TUP13, TUP14, TUP15
Zhao, H.W.	TUP15
Zhao, L.X.	TUP08, TUP13
Zhao, Z.	WEM22
Zhu, G.	TUP18

Content from this work may be used under the terms of the CC BY 3.0 licence (© 2017). Any distribution of this work must maintain attribution to the author(s), title of the work, publisher, and DOI.

## *Institutes List*

### **Belgrade Institute of Physics**

Belgrade, Serbia

- Maletic, D. M.

### **BINP SB RAS**

Novosibirsk, Russia

- Bryzgunov, M.I.
- Bubley, A.V.
- Chekavinskiy, V.A.
- Denisov, A.P.
- Goncharov, A.D.
- Gorchakov, K.
- Gusev, I.A.
- Ivanov, A.V.
- Kremnev, N.S.
- Panasyuk, V.M.
- Parkhomchuk, V.V.
- Polukhin, V.A.
- Putmakov, A.A.
- Reva, V.B.
- Senkov, D.V.
- Skorobogatov, D.N.

### **BNL**

Upton, Long Island, New York, USA

- Altinbas, Z.
- Anderson, R.
- Belomestnykh, S.A.
- Brown, K.A.
- Brutus, J.C.B.
- Curcio, A.J.
- Di Lieto, A.
- Fedotov, A.V.
- Folz, C.
- Gassner, D.M.
- Hayes, T.
- Hulsart, R.L.
- Inacker, P.
- Jamilkowski, J.P.
- Jing, Y.C.
- Kayran, D.
- Kellermann, R.
- Lambiase, R.F.
- Litvinenko, V.
- Mahler, G.J.
- Mapes, M.
- Marusic, A.
- Meng, W.
- Mernick, K.
- Michnoff, R.J.
- Mihara, K.
- Miller, T.A.
- Minty, M.G.
- Narayan, G.
- Orfin, P.
- Phillips, D.
- Pinayev, I.

- Rao, T.
- Ravikumar, D.
- Reich, J.
- Robert-Demolaize, G.
- Roser, T.
- Samulyak, V.
- Seberg, S.K.
- Severino, F.
- Sheehy, B.
- Shih, K.
- Skaritka, J.
- Smart, L.
- Smith, K.S.
- Snyderstrup, L.
- Soria, V.
- Than, R.
- Theisen, C.
- Tuozzolo, J.E.
- Walsh, J.
- Wang, E.
- Wang, G.
- Weiss, D.
- Xiao, B. P.
- Xin, T.
- Xu, W.
- Zaltsman, A.
- Zhao, Z.

### **CERN**

Geneva, Switzerland

- Biancacci, N.
- Caspers, F.
- Jørgensen, L.V.
- Latina, A.
- Thorndahl, L.

### **Cockcroft Institute**

Warrington, Cheshire, United Kingdom

- Hunt, J.R.
- Resta-López, J.
- Veglia, B.
- Welsch, C.P.

### **DPNC**

Genève, Switzerland

- Drielsma, F.

### **ESI**

Archamps, France

- Caspers, F.

### **Fermilab**

Batavia, Illinois, USA

- Bradley, J.
- Neuffer, D.V.

- Stratakis, D.

#### FZJ

Jülich, Germany

- Breitschütz, B.
- Halama, A.J.
- Kamerzhiev, V.
- Shurkhno, N.
- Stassen, R.
- Stockhorst, H.

#### GSI

Darmstadt, Germany

- Andelkovic, Z.
- Bai, M.
- Bardonnier, A.
- Boine-Frankenheim, O.
- Bräuning-Demian, A.
- Böhm, R.M.
- Chetvertkova, V.
- Dimopoulou, C.
- Eidam, L.
- Geithner, O.
- Geithner, W.
- Giacomini, T.
- Gorda, O.E.
- Henschel, J.
- Herfurth, F.
- Hess, R.
- Hettrich, R.
- Kozhuharov, C.
- Lestinsky, M.
- Litvinov, S.A.
- Litvinov, Yu.A.
- Lochmann, M.
- Nörtershäuser, W.
- Nolden, F.
- Peschke, C.
- Sanchez Alarcon, R.M.
- Sanjari, M.S.
- Spiller, P.J.
- Steck, M.
- Stöhlker, T.
- Stuhl, A.
- Ullmann, J.
- Vorobjev, G.
- Weinrich, U.
- Winters, D.F.A.
- Wunderlich, S.

#### Helmholtz-Zentrum Dresden-Rossendorf (HZDR), Institute of Radiation Physics

Dresden, Germany

- Siebold, M.

#### HIJ

Jena, Germany

- Stöhlker, T.

#### HIM

Mainz, Germany

- Aulenbacher, K.
- Bruker, M.W.
- Dietrich, J.
- Weilbach, T.

#### HZDR

Dresden, Germany

- Bussmann, M.H.
- Löser, M.
- Schramm, U.

#### IAP

Frankfurt am Main, Germany

- Britten, V.A.
- Droba, M.
- Meusel, O.
- Podlech, H.
- Schempp, A.
- Schulte, K.

#### IKP

Mainz, Germany

- Alexander, I.
- Aulenbacher, K.
- Beiser, Th.
- Klag, W.

#### IMP/CAS

Lanzhou, People's Republic of China

- Du, Z.
- Hai, B.
- Hu, X.J.
- Huang, Z.
- Jing, L.
- Li, J.
- Li, X.N.
- Lu, H.J.
- Ma, X.M.
- Ma, X.
- Mao, L.J.
- Mao, R.S.
- Tang, M.T.
- Wang, H.B.
- Wang, S. X.
- Wei, W.
- Wen, W.Q.
- Wu, J.X.
- Xia, J.W.
- Xie, H.M.
- Yan, T.L.
- Yang, J.C.
- Yang, J.
- Yang, X.D.
- Yuan, Y.J.
- Zhang, D.
- Zhang, Y.
- Zhao, D.

- Zhao, H.W.
- Zhao, H.
- Zhao, L.X.
- Zhu, G.

**Imperial College of Science and Technology, Department of Physics**

London, United Kingdom

- Uchida, M.A.

**JINR**

Dubna, Moscow Region, Russia

- Meshkov, I.N.
- Smirnov, A.V.
- Trubnikov, G.V.

**JLab**

Newport News, Virginia, USA

- Benson, S.V.
- Derbenev, Y.S.
- Douglas, D.
- Hannon, F.E.
- Hutton, A.
- Jordan, K.
- Li, R.
- Powers, T.
- Rimmer, R.A.
- Roblin, Y.
- Spata, M.
- Tennant, C.
- Wang, H.
- Wang, S.
- Zhang, H.
- Zhang, Y.

**Laurentian University, Campus Sudbury**

Sudbury, Ontario, Canada

- Bayes, R.

**MPI-K**

Heidelberg, Germany

- Wilhelm, P.

**Nihon University**

Narashino, Chiba, Japan

- Katayama, T.

**Niowave, Inc.**

Lansing, Michigan, USA

- Boulware, C.H.
- Grimm, T.L.

**SBU**

Stony Brook, New York, USA

- Ma, J.
- Samulyak, V.

**Stockholm University**

Stockholm, Sweden

- Källberg, A.

**Stony Brook University**

Stony Brook, USA

- Litvinenko, V.

**SUNY SB**

Stony Brook, New York, USA

- Petrushina, I.

**TEMF, TU Darmstadt**

Darmstadt, Germany

- Boine-Frankenheim, O.
- Eidam, L.

**TU Darmstadt**

Darmstadt, Germany

- Beck, T.
- Birkel, G.
- Kiefer, D.
- Klammes, S.
- Nörtershäuser, W.
- Tichelmann, S.
- Ullmann, J.
- Walther, T.

**TU Dresden**

Dresden, Germany

- Schramm, U.

**University of Glasgow**

Glasgow, United Kingdom

- Nugent, J.C.
- Soler, P.

**Westfälische Wilhelms-Universität Münster, Institut für Kernphysik**

Münster, Germany

- Buss, A.
- Hannen, V.
- Winzen, D.

# COOL 2017 Participant List

<u>name</u>	<u>institution</u>	<u>position</u>	<u>city</u>	<u>country/region</u>
Mr. ALEXANDER, Igor	Institute of Nuclear Physics	PhD student	Mainz	Germany
Dr. AULENBACHER, Kurt	Helmholtz Institut Mainz	Leader section ACID-II	Mainz	Germany
Prof. BAI, Mei	GSI Helmholtzzentrum für Schwerionenforschung GmbH	Head of Accelerator Operations	Darmstadt	Germany
Mr. BEISER, Thomas	Helmholtz-Institut Mainz	PhD Student	Mainz	Germany
Dr. BENSON, Stephen	Jefferson Lab	Senior Research Scientist	Newport News	United States
Dr. BREITKREUTZ, Bernd	FZ Juelich		Juelich	Germany
Ms. BRITTEN, Virginia	IAP, Goethe-Universität Frankfurt		Frankfurt am Main	Germany
Dr. BUBLEI, Aleksandr	BINP SB RAS		Novosibirsk	Russian Federation
Dr. BUSSMANN, Michael	Helmholtz-Zentrum Dresden - Rossendorf		Dresden	Germany
Dr. CASPERS, Fritz	CERN/ESI	"retired"/user	Geneve	Switzerland
Prof. DIETRICH, Jürgen	Helmholtz Institut Mainz		Jülich	Germany
Dr. DIMOPOULOU, Christina	GSI		Darmstadt	Germany
Dr. FRANZKE, Bernhard	GSI Darmstadt	retired	Darmstadt	Germany
GEBEL, Ralf	FZ Jülich, IKP		Jülich	Germany
Dr. GORDA, Oleksii	GSI		Darmstadt	Germany
Mr. HALAMA, Arthur	FZ Jülich, IKP	Engineer	Juelich	Germany
HERFURTH, Frank	GSI		Darmstadt	Germany
Mr. HETRICH, Rainer	GSI		Darmstadt	Germany
Dr. HEB, Regina	GSI		Darmstadt	Germany
Dr. JORGENSEN, Lars	CERN		Geneva	Switzerland
Dr. KAMERDZHIEV, Vsevolod	FZ Jülich, IKP-4		Jülich	Germany
Dr. KATAYAMA, Takeshi	Nihon University		Chiba	Japan
Dr. LATINA, Andrea	CERN		Geneva	Switzerland
Mr. LI, J.	Institute of Modern Physics, CAS		Lanzhou	China
Prof. LITVINENKO, Vladimir	Department of Physics and Astronomy, Stony Brook University	Tenured Professor of Physics	Stony Brook, NY 11794-3800	United States
Ms. LI, xiaoni	IMPCAS		Lanzhou	China
Dr. MALETIC, Dimitrije	Institute of Physics Belgrade	Senior Research Associate	Zemun- Belgrade	Serbia
Dr. MAO, Lijun	IMP Lanzhou		Lanzhou	China
Prof. MESHKOV, Igor	JINR	Directorate adviser	Dubna,	Russian Federation
Dr. NEUFFER, David	Fermilab		Batavia IL	United States
Dr. NOLDEN, Fritz	GSI	retired	Darmstadt	Germany
Dr. PINAYEV, Igor	BNL		Upton, NY	United States
Dr. PRASUHN, Dieter	FZ Jülich, IKP-4		Jülich	Germany
Dr. RESTA LOPEZ, Javier	The University of Liverpool		Liverpool	United Kingdom

Content from this work may be used under the terms of the CC BY 3.0 licence (© 2017). Any distribution of this work must maintain attribution to the author(s), title of the work, publisher, and DOI.

# COOL 2017 Participant List

<u>name</u>	<u>institution</u>	<u>position</u>	<u>city</u>	<u>country/region</u>
Mr. SHURKHNO, Nikolay	FZ Juelich		Juelich	Germany
Ms. SIMONSEN, Hannah	FZ Jülich, IKP		Juelich	Germany
Dr. STASSEN, Rolf	FZ Jülich, IKP		Jülich	Germany
Dr. STECK, Markus	GSI Helmholtzzentrum		Darmstadt	Germany
Dr. STOCKHORST, Hans	none		Bonn	Germany
Mr. TANG, Mei Tang	Institute of Modern Physics, CAS		Lanzhou	China
Dr. TOELLE, Raimund	FZ Jülich, IKP-4		Jülich	Germany
TRANQUILLE, Gerard	CERN		Geneva	Switzerland
Dr. TRUBNIKOV, Grigory	JINR		Dubna	Russian Federation
Dr. UCHIDA, Melissa	Imperial College London		London	United Kingdom
VALDAU, Yury	Forschungszentrum Jülich		Jülich	Germany
Dr. WANG, Gang	Brookhaven National Laboratory		Upton	United States
Dr. WANG, Hanbing	Institute of Modern Physics, CAS		Lanzhou	China
Mr. WILHELM, Patrick	Max Planck Institute for Nuclear Physics	PhD student	Heidelberg	Germany
Dr. WINTERS, Danyal	GSI Helmholtzzentrum für Schwerionenforschung		Darmstadt	Germany
Dr. WOLF, Andreas	Max-Planck-Institut für Kernphysik		Heidelberg	Germany
Dr. WU, Junxia	Institute of Modern Physics, CAS		Lanzhou	China
Prof. XIAODONG, Yang	Institute of Modern Physics, CAS		Lanzhou	China
Dr. ZHANG, Yuhong	Jefferson Lab	Senior scientist	Newport News	United States
Mr. ZHAO, He	Institute of Modern Physics, CAS		Lanzhou	China
Mr. ZHU, Guangyu	Institute of Modern Physics, CAS		Lanzhou	China